Quantifying Atmospheric CO_2 From Space-Based Observations and Air Transport Simulations – Focusing on Ocean and Permafrost

by

Yifan Guan

A dissertation submitted in partial fulfillment
of the requirements for the degree of
Doctor of Philosophy
(Climate and Space Sciences and Engineering)
in the University of Michigan
2023

Doctoral Committee:

Associate Professor Gretchen Keppel-Aleks, Chair
Professor Rose Cory
Associate Professor Eric A. Kort
Professor Allison L. Steiner

Yifan Guan

guanyf@umich.edu

ORCID iD: 0000-0001-8175-3765

Dedication

To all that I have met.

Acknowledgement

Thanks to my family for supporting me to explore learning opportunities and encouraging me to continuously develop myself in multiple aspects. Thanks to all the fellow students – all my friends met at UMich for your kindness and goodness. Especially, I would like to express my gratefulness to my advisor Prof. Gretchen Keppel-Aleks over the last five years – her patience and understanding made me went through the whole PhD studying process, her mentorship and guidance lead me to reflect, think deeply and strive to become more constructively critical. Thanks to all the co-authors who offer great suggestions and who provide assistance to this dissertation work.

I would also thank the participants of the NASA OCO-2 mission for providing the OCO-2 data used in this thesis, and acknowledges NASA support through the OCO Science team and grants 80NSSC18K0897, 80NSSC21K1071 to the University of Michigan. The computing resources were provided by the University of Michigan Information and Technology Services (ITS) Advanced Research Computing (ARC) division and the Department of Climate and Space Sciences and Engineering (CLaSP) IT services.

Table of Contents

List of Tables

List of Figures

List of Appendices

Abstract

Atmospheric carbon dioxide (CO_2) accounts for the largest radiative forcing among anthropogenic greenhouse gases. There is a pressing need to understand the rate at which CO_2 accumulates in the atmosphere, in both the seasonal and the interannual timescales (mainly driven by terrestrial and oceanic carbon flux), because of their relationship with climatic variations that may provide insights into long-term carbon-climate feedback. Given advances in space-based measurements of atmospheric CO_2, which enables us to monitor atmospheric CO_2 abundance over open ocean, and in techniques to estimate ocean air-sea exchange based on sparse surface ocean observations, we have novel opportunities to refine our understanding of the ocean influence on atmospheric CO_2 variation at the interannual timescale. Meanwhile, it remains challenging for current satellite missions to quantify and separate emissions of old carbon from permafrost from labile high-latitude carbon. This dissertation focuses on space-based observations over ocean and permafrost. In the first and second case study on the ocean, we estimate the likely range of IAV in the atmospheric CO_2 owing to air-sea carbon exchange by simulating three-dimensional atmospheric CO_2 using the GEOS-Chem atmospheric transport model. The ocean carbon fluxes we use are from state-of-the-art products that report calculated air-sea fluxes. In addition to global integration, we separately label CO_2 from individual ocean regions, aiming to identify the fingerprints of ocean subregions and the whole ocean on atmospheric total column CO_2 dry mole fraction (XCO_2). These simulations were analyzed in conjunction with observed atmospheric CO_2 IAV from NASAs OCO-2 satellite mission, which detects the combined imprint of the ocean, terrestrial ecosystem, and human activities. The case

study on the ocean suggests that OCO-2 IAV provides new opportunities to monitor climate-driven variations in CO_2 over open ocean and remote regions; and over remote ocean regions, simulations suggest that ocean fluxes contribute a large proportion of IAV. In the third study, we quantify permafrost-driven atmospheric CO_2 enhancement using the GEOS-Chem atmospheric transport model with tagged CO_2 species originating from permafrost sources in North America, Europe, and Asia. We then explore the detectability of these perturbations using an Observing System Simulation Experiment based upon a hypothetical satellite mission that employs a multi-spectral imaging spectrometer with channels in the thermal infrared and shortwave infrared, capable of providing two pieces of vertical information about the CO_2 abundance. Our analysis points toward and provides preliminary estimates of observational requirements to identify signals from the Northern Permafrost regions using space-based observations.

Chapter 1 Introduction

1.1 The Earth's global Carbon Cycle Under Climate Change

Carbon is stored in the atmosphere, the ocean and freshwater, the soils and terrestrial biomass, the rocks and sediments (Fig 1.1). The processes and reservoirs in the carbon cycle can be placed into groups: the slow carbon cycle, and the fast carbon cycle, with intergrate with one another but have different timescales. The slow carbon cycle moves carbon between the atmosphere, lithosphere, and oceans with a timescale of 100 to 200 million years, while the fast carbon cycle happens over years or decades, especially between the atmosphere and terrestrial or marine ecosystems. The largest reservoir of carbon is the deep water of the ocean, which contains about 37000 GtC - 80% of the Earth's carbon; oceanic sediments contain about 1750 GtC - 4%; ocean surface waters hold about 1000 GtC. Oil, gas, and coal contribute about 1300 GtC which is 3%; soil and permafrost hold 5%(~2200 GtC) and 4%(~1750 GtC); vegetation adds about 1%(~400GtC); atmosphere holds 2%(~750GtC) (IPCC AR6; IPCC 2021). CO_2 could transfer among these reservoirs through physical, chemical, and biological processes. The three most important repositories associated with anthropogenic climate change are the atmosphere, terrestrial biosphere, and ocean. These repositories are constantly exchanging carbon over time spans of up to centuries or as relatively rapid interannual to seasonal timescales.

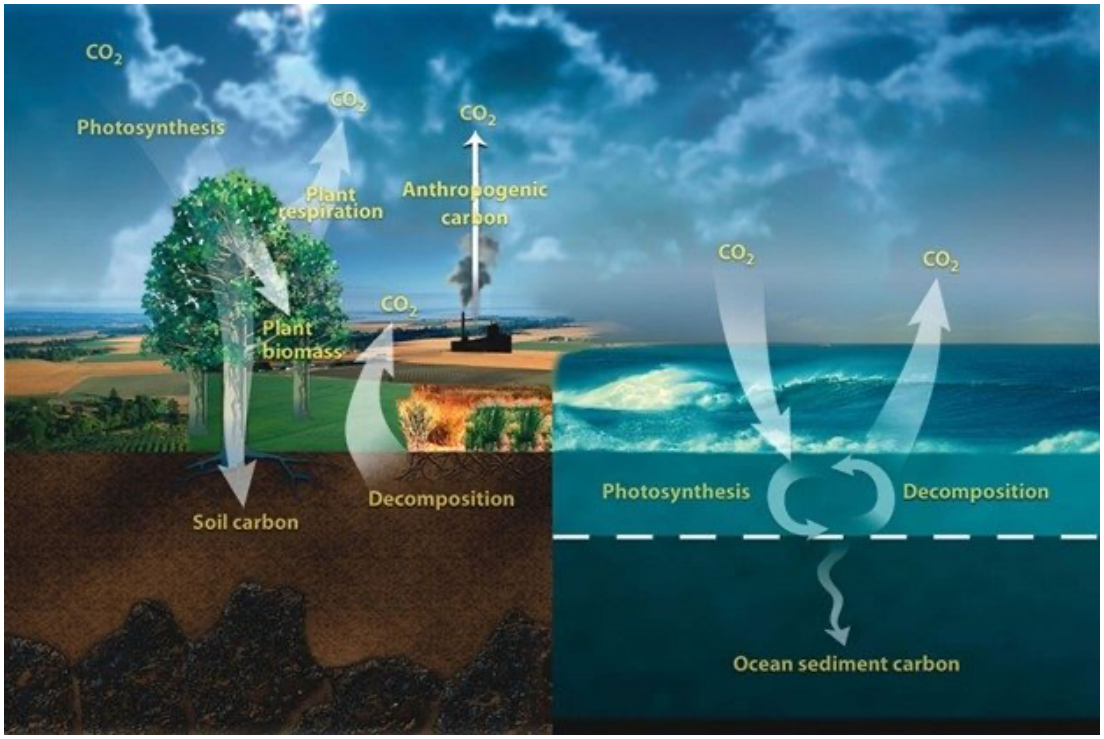

Figure 1.1: *Fast carbon cycle showing the movement of carbon between land, atmosphere, and oceans. The effects of the slow carbon cycle, such as volcanic and tectonic activity are not included. Obtained from "The Carbon Cycle" (2011).*

The concentration of carbon dioxide (CO_2) in the atmosphere has increased from approximately 278 parts per million (ppm) in the Industrial Era to 414.7 ± 0.1 ppm in 2021 (Dlugokencky and Tans, 2022). Global emissions and their partitioning among the atmosphere, ocean, and land are in balance in the real world. The CO_2 emissions are from (1) fossil fuel combustion and oxidation from all energy and industrial processes, including cement production and carbonation (E_{FOS}), and (2) the emissions resulting from human activities on land, including those leading to land-use change (E_{LUC}), which could partition among (3) the growth rate of atmospheric CO_2 concentration (G_{ATM}), (4) the ocean sink (S_{OCEAN}) and (5) the land sink (S_{LAND}) (Friedlingstein et al., 2022; Jackson et al., 2022). In the global carbon cycle, the former five quantities shall sum to zero. However, the estimates of these quantities do not balance due to the

limitation of our knowledge of the carbon pools and carbon fluxes, which generates a carbon budget imbalance (B_{IM}) with the following equation:

$$B_{IM} = E_{FOS} + E_{LUC} - (G_{ATM} + S_{OCEAN} + S_{LAND})$$

The B_{IM}, also demonstrate by the discrepancies between the red dashed line and blue bold line in Fig 1.2, is about 3% of emissions (Friedlingstein et al., 2022). Although the small percentage of imbalance in the global carbon cycle suggests the partitioning of emissions among the components of the carbon cycle is almost complete, the discrepancy can reach up to 1 GtC yr^{-1} – which is still a large variability in CO_2 fluxes in seasonal to interannual timescale. With a persistent low agreement between the magnitude of the land CO_2 flux in the northern extra-tropics and an apparent discrepancy between the ocean sink outside the tropics - particularly in the Southern Ocean based on the different methods and approaches, yet a scientific consensus on the source of the imbalance has not been reached.

In the global carbon cycle, the five components listed here shall sum to zero. However, due to the limitation of our knowledge, the quantities do not really balance. Such discrepancies are demonstrated by the gap between the red dashed line which reflects the sum of human-induced emissions, and the blue edge, which accounts for the total balance ability of land, ocean and atmosphere. Although this imbalance is small in terms of percentage compared to the cumulative change since the 19th century. The discrepancy can reach up to 1GtC per year, which is large in seasonal to interannual timescale. We especially would like to understand what is happening with the ocean and the permafrost component which tracks a large portion of Northern extra-tropical land – those are prominent source of where uncertainty lies.

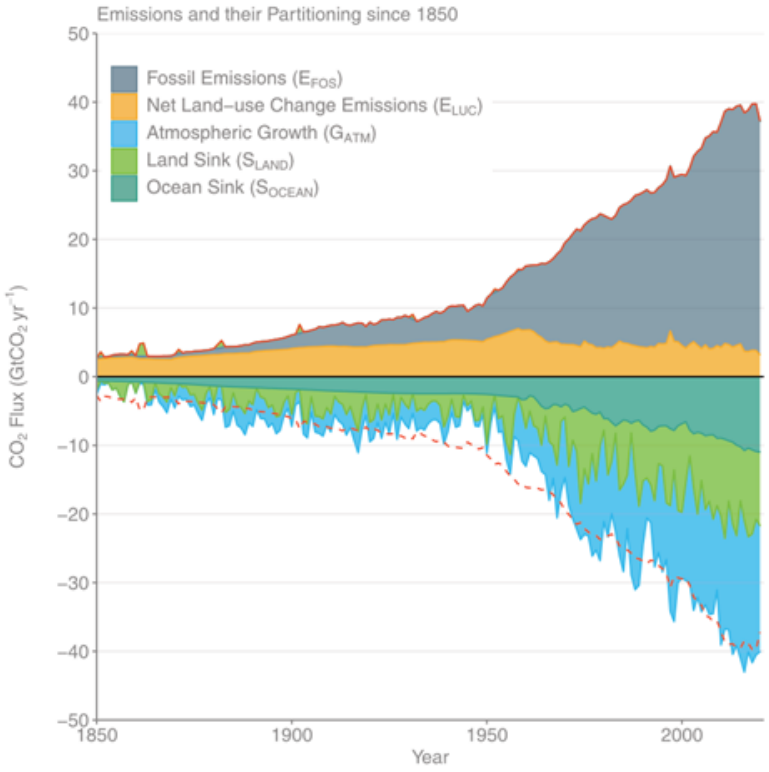

Figure 1.2: *Combined components of the global carbon budget as a function of time, for fossil CO_2 emissions and emissions from land-use change, as well as their partitioning among the atmosphere, ocean, and land. Source: Global Carbon Budget 2021.*

1.1.1 Ocean

One source of the uncertainties in the understanding of carbon cycle points toward the ocean sink. Ocean covers 70% of the Earth and is one of the most essential Earth System Components in the removal (~2.5 PgC/yr) of the anthropogenic emissions (Friedlingstein et al., 2022). Oceans have a large capacity to absorb CO_2, mainly through three ocean processes that draw down CO_2 into the oceans: the physical carbon pump, the biological carbon pump, and the carbonate pump, thus balancing the amount of CO_2 in the atmosphere and exchange with the ocean system.

The physical pump makes CO_2 constantly exchange between the ocean and the atmosphere. When warm water in oceanic surface currents is carried from low latitudes to high

latitudes and cooled, surface waters loaded with dissolved CO_2 move to the deeper ocean through vertical mixing of the ocean. Inversely, when cold water returns to the surface and warms up again, CO_2 is emitted to the atmosphere. The oceanic biological carbon pump is driven by organisms like phytoplankton and heterotrophic zooplankton, through photosynthesis, respiration, eating, producing waste products, decay and decomposition, helping transform carbon compounds into new forms, moving carbon throughout the ocean or down to seafloor sediments. In the carbonate pump, CO_2 can combine with water molecules and then enters into reversible chemical reactions that produce bicarbonate ions(H^+ CO_3^-) hydrogen ions (H^+), and carbonate (CO_3^{2-}) ions. The carbonate ions could combine with calcium ions (Ca^{2+}) and form calcium carbonate ($CaCO_3$), which is used by Shell-building organisms such as coral.

1.1.2 Permafrost

Another source of the uncertainties in the understanding of carbon cycle points toward the Northern extra-tropics, with ¼ of the land area consisting of permafrost and spans an area of ~18.8 million km^2. Permafrost is soil, sediment, or rock that is perennially frozen and may or may not contain a significant amount of ice. The permafrost contains large amounts of organic carbon, which are the remnants of plants, animals, and microbes that have lived and died in the tundra and boreal ecosystems, accumulating in frozen soil over hundreds to thousands of years (Schuur et al., 2016). The current estimated inventory of organic soil carbon within the northern circumpolar permafrost region is approximately 1,460–1,600 petagrams of carbon. From 0 to 3m depth, the permafrost region represents 33% of the global pool stored in only 15% of the total global soil area. Substantial permafrost carbon exists below 3-m depth - the Yedoma deposits of Siberia and Alaska contain 327–466 Pg C, and Arctic River deltas contain 96 ± 55 Pg C (Strauss et al., 2017).

Warming is causing perennially frozen permafrost to thaw, with permafrost in many locations currently reaching record-high temperatures (Biskaborn et al. 2019). Active layer (portion of the soil above permafrost that thaws and freezes seasonally) thickening is the most important mechanism in permafrost thawing as warming affects the surface permafrost. When active-layer thickening has become deep enough so that the entire summer-thawed layer does not re-freeze in the winter, talik (year-round unfrozen ground that lies in permafrost areas) formation occurs and deeper permafrost thawing occurs through talik expansion. Organic carbon contained in soils of the permafrost region represents a climate-sensitive carbon reservoir that is affected by warming air and ground temperatures and permafrost thaw. Additional net releases of CO_2 to the atmosphere from permafrost thaw as a result of warming and faster microbial decomposition of permafrost carbon have the potential to accelerate climate warming. (illustrated in Fig 1.4, Schuur and Hugelius, 2016).

Regional atmospheric measurements like the Carbon in Arctic Reservoirs Vulnerability Experiment (CARVE) (Miller and Dinardo, 2012) and the Arctic and Boreal Vulnerability Experiment (ABoVE) consist of a combination of in situ and remote measurements (Parazoo et al. 2016). However, the NASA aircraft campaign operates from April through November and ground-based measurements, which have 80 study-years of summer measurements yet only 9 study-years of non-summer measurements available for upscaling (McGuire et al. 2012). With large uncertainty in the stability of permafrost carbon and the accelerated positive feedback, it would be valuable to complement the existing networks, and campaigns with a satellite-based approach to monitoring CO_2 from Arctic permafrost.

Permafrost thawing and increased microbial decomposition due to warming in the Northern Artic cause intensive release of stored organic carbon into the atmosphere. Across the

landscape, the arctic carbon cycle is also influenced by disturbances, such as wildfires and abrupt permafrost thaw. During non-growing seasons, the ecosystem CO_2 fluxes across the circumpolar region, were 2 to 3 times higher than previously estimated from ground-based measurements (Natali et al. 2019), which suggests that during the cold season when microbes remain metabolically active, CO_2 release could even offset CO_2 uptake during the growing season and serve as a source of 0.6 Pg C annually to the atmosphere. The heterogeneity of permafrost and its changing conditions make the exact balance of CO_2 difficult to predict, with a wide range, from a low of ~9 PgC (Schneider von Deimling et al., 2012), under a scenario that includes negative anthropogenic emissions to a high of 104 ± 37 PgC (Schaefer et al., 2011) for the remaining 21st century.

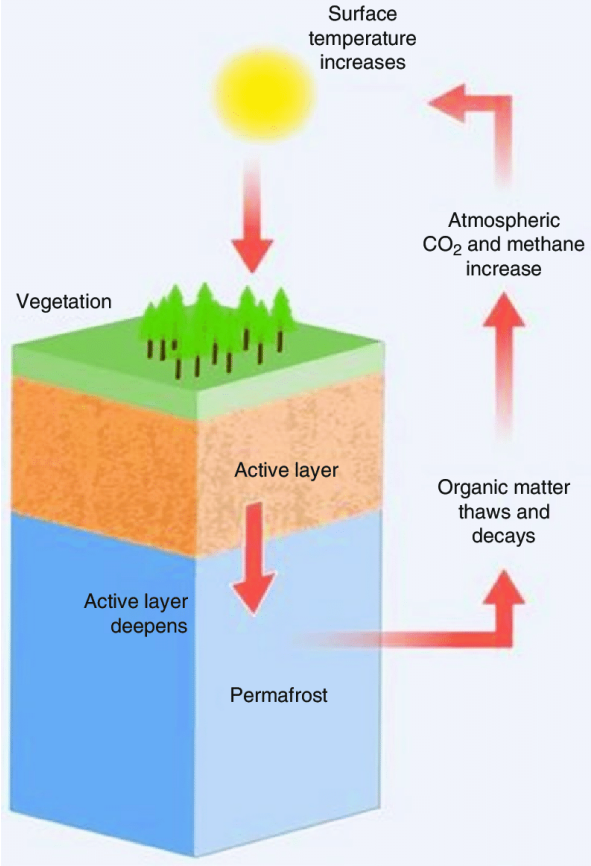

Figure 1.3: *The positive feedback from thawing permafrost amplifies existing atmospheric warming due to human activities. Source: UNEP report "Policy Implications of Warming Permafrost".*

1.2 The Observing System of CO_2

Now we understand the mechanism of the carbon cycle in the ocean and permafrost, and we also care about what effect they have on the atmosphere. To monitor atmospheric CO_2 concentration so as we can trace back of the influence of ocean and permafrost, traditionally, we have access to the surface network such as the NOAA ESRL measurement stations at the ground surface, the FLUXNET to help quantify photosynthesis or evapotranspiration of the terrestrial ecosystem, or Argos/research vessels/commercial ships over the ocean regions are utilized to create observation records (Fig 1.5 and Fig 1.6). The National Oceanic and Atmospheric Administration Earth System Research Laboratory (NOAA ESRL) network has ~155 CO_2 measurement stations monitoring atmospheric CO_2 at the surface (GLOBALVIEW, 2010). FLUXNET can identify trace gases fluxes in the boundary layer, and help quantify photosynthesis, evapotranspiration, soil moisture, and respiration (Pastorello et al., 2020; Euskirchen et al., 2017). The Total Carbon Column Observing Network (TCCON) has used a ground-based Fourier transform spectrometer to measure column CO_2 (Washenfelder et al. 2006, Wunch et al. 2011).

Oceanic regions are visited by research vessels and commercial ships of opportunity (SOOP) equipped with underway pCO_2 systems that also make routine measurements of CO_2 in the Marine Boundary Layer – MBL (Sutton et al., 2014). The international GO-SHIP network collects high-quality, high spatial and vertical resolution of ocean interior carbon measurements to determine changes in anthropogenic CO_2 inventories over the full water column below the depth of Argo floats.

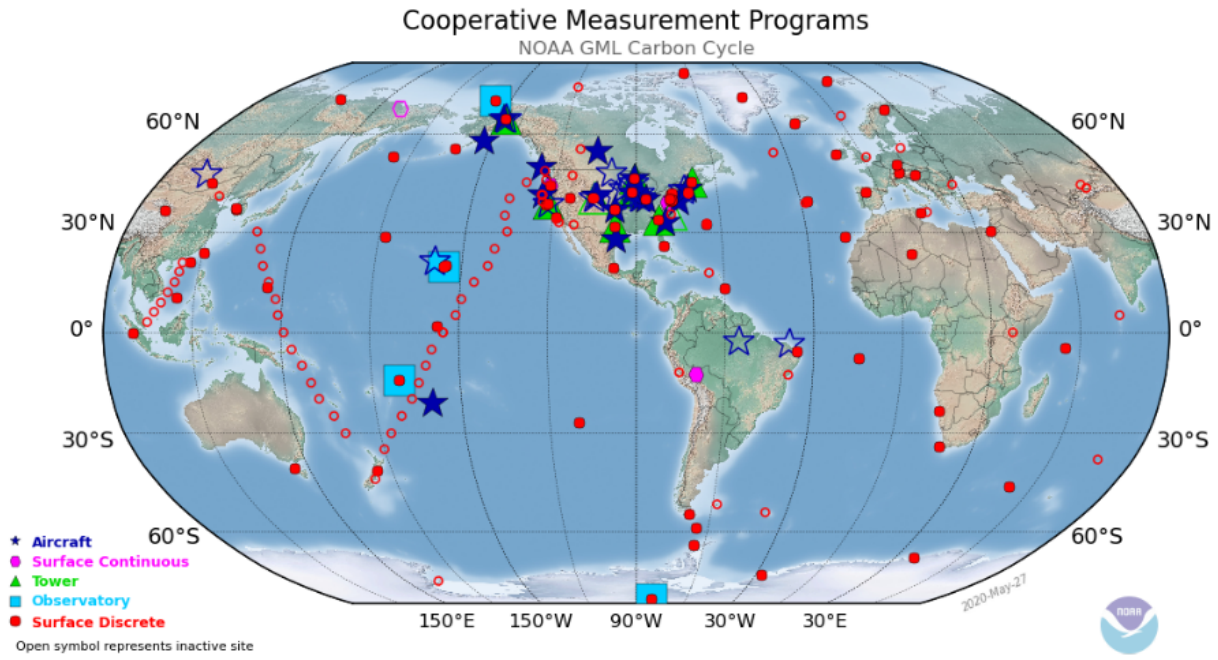

Figure 1.4: *NOAA GML Carbon Cycle measurement programs.*

Using ensembles of models and inventories, as well as CO_2 surface measurements, different components of the global emissions of CO_2 can be estimated. Retrieval of atmospheric CO_2 vertical profiles from ground-based near-infrared spectra can serve as a validation tool for these estimates. The space-based measurements of XCO_2 have great potential to provide additional constraints on sources and sinks of CO_2.

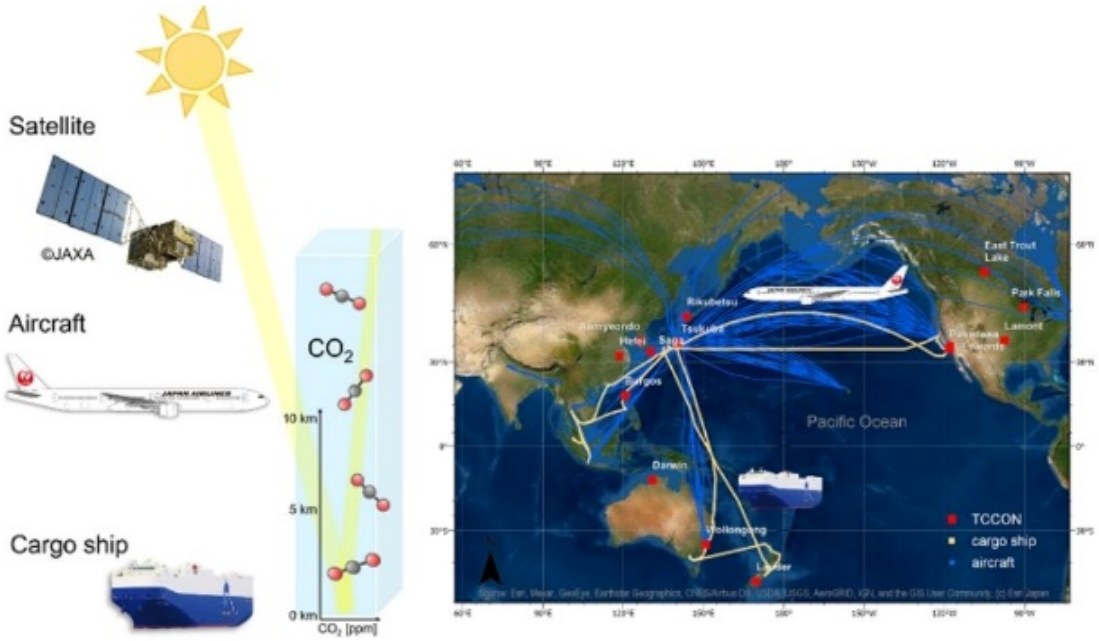

Figure 1.5: *Illustration of the satellite, aircraft, and cruise observation. Obtained from the National Institute for Environmental Studies (NIES).*

The atmospheric CO_2 surface network shows a decadal-average growth rate of reaching 2.41±0.26 ppm/y (mean ± 2 std dev) on an annual basis due to the impacts of interannual climate variability (Buchwitz et al., 2018). This IAV has been shown to reflect, primarily, variations in the rate of terrestrial CO_2 uptake due to climate stressors (Luo et al., 2022) and disturbance (Keppel-Aleks et al., 2014), but also embodies IAV in net ocean carbon exchange and fossil fuel emissions (Doney et al., 2009). Although studies have suggested that ocean flux IAV may impart an observable impact on atmospheric CO_2 IAV (Crisp et al., 2022), gaps remain in quantifying the influence from the ocean since most atmospheric CO_2 observations are made on land. As for the permafrost, previous studies focused on CO_2 flux measurements have produced results that have not been fully agreed upon. The differential response of individual ecosystem types and the relative scarcity of measurement sites across the Arctic region makes it difficult to upscale the aggregated effect of ecosystems, including tundra, boreal forests, and wetland/lake/fresh water

(Belshe et al., 2013; Commane et al., 2017), and the long cold Arctic winter season limits ground-based observations due to operating difficulties. Given advances in space-based measurements of atmospheric CO_2, which enables us to monitor atmospheric CO_2 abundance over open ocean and remote areas, we have novel opportunities to refine our understanding of the regional ocean and permafrost influence on atmospheric CO_2 variation at the interannual to seasonal timescale.

1.3 Monitoring CO_2 with Satellite Remote Sensing

Atmospheric carbon dioxide abundance can be indirectly observed by various satellite instruments, which give measurements of spectrally resolved near-infrared or infrared radiation reflected or emitted by the atmosphere. Through the analysis of molecular absorption signals in the radiance observations, the averaged CO_2 concentration in the sampled atmospheric column can be identified. The space-based measurements of total column CO_2 have great potential to provide knowledge on sources and sinks of CO_2, due to its better coverage on spatial scales, especially over remote regions. Increased research has led to the monitoring of CO_2 from more than 200 locations on the earth's surface, and a growing development of space-based satellites with near-global coverage, which increased our opportunities to understand climate change and the carbon cycle. Satellite observations dedicated to monitoring the carbon cycle, including GOSAT (Kuze et al.,2016), the Orbiting Carbon Observatory-2 (OCO-2, Eldering et al., 2017), the Orbiting Carbon Observatory-3 (OCO-3), circulating in the low Earth orbit, are giving the hourly to daily to seasonal coverage, and helping to create multi-year dataset records for the research community.

Satellites retrieve XCO_2, which is the column-averaged dry air mole fraction of CO_2 (Crisp, 2015). To estimate XCO_2, satellites use high-resolution spectroscopic observations of

reflected sunlight, and monitor atmospheric oxygen (O_2) and CO_2 concentrations by measuring absorption spectra in three bands, including the molecular O_2 A-band (approximately 0.765 μm, Visible), a weak CO_2 band (1.61 μm, short-wave IR), and a strong CO_2 band (approximately 2.06 μm) (Crisp, 2017). A variety of algorithms have been developed for retrievals of CO_2 from NIR and SWIR spectra, including the Differential Optical Absorption Spectroscopy (DOAS) approach for SCIAMACHY (Reuter et al., 2010), the retrieval algorithm from short-wavelength infrared spectral observations for CO_2 by the GOSAT TANSO-FTS described by Yoshida et al. (2011), the Atmospheric CO_2 Observations from Space (ACOS) algorithm applied to GOSAT, OCO-2 and OCO-3 measurements (O'Dell et al., 2018), etc.

The algorithms developed by different institutions to retrieve CO_2 concentrations are based on a general inverse method, which begins such that the initial guess and the a priori values, and based on an optimal estimation method to yield a weighted mean value of the actual state and an a priori state. Using an inverse model coupled with the forward model and constrained by a priori, the initial state vector is modified by minimizing the difference between the simulated and observed radiance spectra through iteration. Specifically, the ACOS optimal estimation algorithm, is a full physics algorithm that takes into account XCO_2 and other physical parameters, including 100 surface pressure, surface albedo, temperature, and water vapor profile in its state vector (O'Dell et al., 2018).

GOSAT, OCO-2, and OCO-3 – can provide higher CO_2 sensitivity in total column measurements that include near surface emissions (Buchwitz et al., 2010; Liu et al., 2018). The weighting function in the algorithm ensures that the signal from surface emissions in the lower troposphere is stronger than earlier CO_2 detecting instruments (Crisp et al., 2017). Mainly dedicated for measuring natural CO_2 fluxes in the global scale, they also have the potential to

monitor strong anthropogenic emission sources at a local scale. GOSAT has an resolution of ~10 × 10 km^2, while OCO-2 performs a relatively better combination of high precision and fine spatial resolution (1.29 × 2.25 km^2), and OCO-3 has similar precision and spatial resolution (Eldering et al., 2019). After validation with ground-based FTIR measurements (such as TCCON), they can provide seasonal and annual variation by smoothing its sampling pixels, and their global emission results have in good agreement with global CO_2 emission inventories. However, it was planned to sample a small proportion of a large region with a 16-day repeat cycle (Miller et al., 2007) thus has limitations to detecting a broad region simultaneously. Compared with ground-based monitoring methods, the top-down space-based observing approach offer widely distributed measurements and high monitoring density.

1.4 Motivations

The overarching question of the dissertation is "How could space-based observations give insight into our better understanding of the carbon cycle?" This question is driven the opportunity by provided by satellite remote sensing to obtain a more complete, precise, and timely measurement of CO_2 emissions, and distinguish the natural sources of CO_2. In this case, we need to employ various tools and approaches including numerical models for the underlying physical processes. By presenting a comparison of observation and fluxes-driven forward atmospheric chemical transport model simulations, we could assess and determine the importance of fluxes from a different component of the carbon cycle in multiple timescales. Besides, the numerical model is an essential component of observing system simulation experiments (OSSEs), which is a powerful tool used to evaluate the potential impact of the future observing system (Masutani et al., 2010). We could know the "true" state, which is usually a standard model simulation driven by the assimilated meteorological data and generate simulated

observations of a potential observing system (e.g., satellite), then evaluate the value of a new observing system when actual observational data are not available. We especially focus on ocean and permafrost, with the timescales from annual to interannual, since uncertainties in the measurements of the ocean and land surface sink point to the gap in the understanding of the imbalance in the carbon cycle.

1.5 Organization of Dissertation

The dissertation explores the CO_2 using satellite remote sensing observations from multiple aspects and in different components of the global carbon cycle, and is divided into 3 principal chapters:

Chapter 2 leverages the new opportunity provided by observations from the Orbiting Carbon Observatory-2 (OCO-2) mission, and examined the interannual variability (IAV) in OCO-2 data to determine whether the small variations that result from interannual flux variations can be detected in light of other sources of variance in the space-based dataset. We especially focus on remote terrestrial regions and the open ocean where traditional in situ CO_2 monitoring is difficult, yet space-based OCO-2 provides better spatial coverage compared to ground-based monitoring techniques. The IAV is tied to climatic variations (e.g. ENSO), and characterizing the temporal-spatial pattern can provide insights into long-term carbon-climate feedback.

Chapter 3 expands on the work of Chapter 2, and further evaluates the imprint that sea-air CO_2 fluxes from the whole ocean and different oceanic subregions leave on the atmospheric XCO_2 IAV, by quantifying more than 7 years of XCO_2 IAV based on the OCO-2 total column CO_2 observation from late 2014 to 2022 and comparing against the simulated ocean-driven XCO_2 derived from the GEOS-Chem simulation using ocean carbon flux products as input.

Chapter 4 investigates atmospheric XCO_2 increase driven by permafrost thawing using the GEOS-Chem atmospheric transport model with tagged CO_2 species originating from permafrost sources in North America, Europe, and Asia, and explores the detectability of regional flux perturbations and local atmospheric CO_2 enhancements. This analysis points toward and provides preliminary estimates of observational requirements to identify signals from the Northern Permafrost regions using space-based observations.

Chapter 5 summarizes the key findings from the above chapters and discusses the implications for future work.

1.6 References

Belshe, E. F., E. a. G. Schuur, and B. M. Bolker. "Tundra Ecosystems Observed to Be CO2 Sources Due to Differential Amplification of the Carbon Cycle." *Ecology Letters* 16, no. 10 (2013): 1307–15. https://doi.org/10.1111/ele.12164.

Biskaborn, Boris K., Sharon L. Smith, Jeannette Noetzli, Heidrun Matthes, Gonçalo Vieira, Dmitry A. Streletskiy, Philippe Schoeneich, et al. "Permafrost Is Warming at a Global Scale." *Nature Communications* 10, no. 1 (January 16, 2019): 264. https://doi.org/10.1038/s41467-018-08240-4.

Buchwitz, Michael, Maximilian Reuter, Oliver Schneising, Stefan Noël, Bettina Gier, Heinrich Bovensmann, John P. Burrows, et al. "Computation and Analysis of Atmospheric Carbon Dioxide Annual Mean Growth Rates from Satellite Observations during 2003–2016." *Atmospheric Chemistry and Physics* 18, no. 23 (December 7, 2018): 17355–70. https://doi.org/10.5194/acp-18-17355-2018.

Commane, Róisín, Jakob Lindaas, Joshua Benmergui, Kristina A. Luus, Rachel Y.-W. Chang, Bruce C. Daube, Eugénie S. Euskirchen, et al. "Carbon Dioxide Sources from Alaska Driven by Increasing Early Winter Respiration from Arctic Tundra." *Proceedings of the National Academy of Sciences* 114, no. 21 (May 23, 2017): 5361–66. https://doi.org/10.1073/pnas.1618567114.

Crisp, David, Han Dolman, Toste Tanhua, Galen A. McKinley, Judith Hauck, Ana Bastos, Stephen Sitch, Simon Eggleston, and Valentin Aich. "How Well Do We Understand the Land-Ocean-Atmosphere Carbon Cycle?" *Reviews of Geophysics* 60, no. 2 (2022): e2021RG000736. https://doi.org/10.1029/2021RG000736.

Crisp, David, Harold R. Pollock, Robert Rosenberg, Lars Chapsky, Richard A. M. Lee, Fabiano A. Oyafuso, Christian Frankenberg, et al. "The On-Orbit Performance of the Orbiting

Carbon Observatory-2 (OCO-2) Instrument and Its Radiometrically Calibrated Products." *Atmospheric Measurement Techniques* 10, no. 1 (January 5, 2017): 59–81. https://doi.org/10.5194/amt-10-59-2017.

Eldering, A., P. O. Wennberg, D. Crisp, D. S. Schimel, M. R. Gunson, A. Chatterjee, J. Liu, et al. "The Orbiting Carbon Observatory-2 Early Science Investigations of Regional Carbon Dioxide Fluxes." *Science* 358, no. 6360 (October 13, 2017): eaam5745. https://doi.org/10.1126/science.aam5745.

Eldering, Annmarie, Thomas E. Taylor, Christopher W. O'Dell, and Ryan Pavlick. "The OCO-3 Mission: Measurement Objectives and Expected Performance Based on 1 Year of Simulated Data." *Atmospheric Measurement Techniques* 12, no. 4 (April 15, 2019): 2341–70. https://doi.org/10.5194/amt-12-2341-2019.

Euskirchen, Eugénie S., Colin W. Edgar, M. Syndonia Bret-Harte, Anja Kade, Nikita Zimov, and Sergey Zimov. "Interannual and Seasonal Patterns of Carbon Dioxide, Water, and Energy Fluxes From Ecotonal and Thermokarst-Impacted Ecosystems on Carbon-Rich Permafrost Soils in Northeastern Siberia." *Journal of Geophysical Research: Biogeosciences* 122, no. 10 (2017): 2651–68. https://doi.org/10.1002/2017JG004070.

Friedlingstein, Pierre, Michael O'Sullivan, Matthew W. Jones, Robbie M. Andrew, Luke Gregor, Judith Hauck, Corinne Le Quéré, et al. "Global Carbon Budget 2022." *Earth System Science Data* 14, no. 11 (November 11, 2022): 4811–4900. https://doi.org/10.5194/essd-14-4811-2022.

Jackson, R. B., P. Friedlingstein, C. Le Quéré, S. Abernethy, R. M. Andrew, J. G. Canadell, P. Ciais, et al. "Global Fossil Carbon Emissions Rebound near Pre-COVID-19 Levels." *Environmental Research Letters* 17, no. 3 (March 2022): 031001. https://doi.org/10.1088/1748-9326/ac55b6.

Kuze, A., Y. Nakamura, T. Oda, J. Yoshida, N. Kikuchi, F. Kataoka, H. Suto, and K. Shiomi. "Examining Partial-Column Density Retrieval of Lower-Tropospheric CO2 from GOSAT Target Observations over Global Megacities." *Remote Sensing of Environment* 273 (May 1, 2022): 112966. https://doi.org/10.1016/j.rse.2022.112966.

Liu, Junjie, Kevin Bowman, Nicholas C. Parazoo, A. Anthony Bloom, Debra Wunch, Zhe Jiang, Kevin R. Gurney, and Dave Schimel. "Detecting Drought Impact on Terrestrial Biosphere Carbon Fluxes over Contiguous US with Satellite Observations." *Environmental Research Letters* 13, no. 9 (September 2018): 095003. https://doi.org/10.1088/1748-9326/aad5ef.

Luo, Yiqi, Yuanyuan Huang, Carlos A. Sierra, Jianyang Xia, Anders Ahlström, Yizhao Chen, Oleksandra Hararuk, et al. "Matrix Approach to Land Carbon Cycle Modeling." *Journal of Advances in Modeling Earth Systems* 14, no. 7 (2022): e2022MS003008. https://doi.org/10.1029/2022MS003008.

Masutani, Michiko, John S. Woollen, Stephen J. Lord, G. David Emmitt, Thomas J. Kleespies, Sidney A. Wood, Steven Greco, et al. “Observing System Simulation Experiments at the National Centers for Environmental Prediction.” *Journal of Geophysical Research: Atmospheres* 115, no. D7 (2010). https://doi.org/10.1029/2009JD012528.

McGuire, A. D., T. R. Christensen, D. Hayes, A. Heroult, E. Euskirchen, J. S. Kimball, C. Koven, et al. “An Assessment of the Carbon Balance of Arctic Tundra: Comparisons among Observations, Process Models, and Atmospheric Inversions.” *Biogeosciences* 9, no. 8 (August 17, 2012): 3185–3204. https://doi.org/10.5194/bg-9-3185-2012.

Miller, C. E., D. Crisp, P. L. DeCola, S. C. Olsen, J. T. Randerson, A. M. Michalak, A. Alkhaled, et al. “Precision Requirements for Space-Based Data.” *Journal of Geophysical Research: Atmospheres* 112, no. D10 (2007). https://doi.org/10.1029/2006JD007659.

O’Dell, Christopher W., Annmarie Eldering, Paul O. Wennberg, David Crisp, Michael R. Gunson, Brendan Fisher, Christian Frankenberg, et al. “Improved Retrievals of Carbon Dioxide from Orbiting Carbon Observatory-2 with the Version 8 ACOS Algorithm.” *Atmospheric Measurement Techniques* 11, no. 12 (December 11, 2018): 6539–76. https://doi.org/10.5194/amt-11-6539-2018.

Olefeldt, D., S. Goswami, G. Grosse, D. Hayes, G. Hugelius, P. Kuhry, A. D. McGuire, et al. “Circumpolar Distribution and Carbon Storage of Thermokarst Landscapes.” *Nature Communications* 7, no. 1 (October 11, 2016): 13043. https://doi.org/10.1038/ncomms13043.

Parazoo, Nicholas C., Roisin Commane, Steven C. Wofsy, Charles D. Koven, Colm Sweeney, David M. Lawrence, Jakob Lindaas, Rachel Y.-W. Chang, and Charles E. Miller. “Detecting Regional Patterns of Changing CO2 Flux in Alaska.” *Proceedings of the National Academy of Sciences* 113, no. 28 (July 12, 2016): 7733–38. https://doi.org/10.1073/pnas.1601085113.

Pastorello, Gilberto, Carlo Trotta, Eleonora Canfora, Housen Chu, Danielle Christianson, You-Wei Cheah, Cristina Poindexter, et al. “The FLUXNET2015 Dataset and the ONEFlux Processing Pipeline for Eddy Covariance Data.” *Scientific Data* 7, no. 1 (July 9, 2020): 225. https://doi.org/10.1038/s41597-020-0534-3.

Reuter, M, M Buchwitz, O Schneising, J Heymann, H Bovensmann, and J P Burrows. “A Method for Improved SCIAMACHY CO2 Retrieval in the Presence of Optically Thin Clouds,” 2009.

Schaefer, Kevin, Tingjun Zhang, Lori Bruhwiler, and Andrew P. Barrett. “Amount and Timing of Permafrost Carbon Release in Response to Climate Warming.” *Tellus B* 63, no. 2 (2011): 165–80. https://doi.org/10.1111/j.1600-0889.2011.00527.x.

Schneider von Deimling, T., M. Meinshausen, A. Levermann, V. Huber, K. Frieler, D. M. Lawrence, and V. Brovkin. “Estimating the Near-Surface Permafrost-Carbon Feedback on

Global Warming." *Biogeosciences* 9, no. 2 (February 3, 2012): 649–65. https://doi.org/10.5194/bg-9-649-2012.

Strauss, Jens, Lutz Schirrmeister, Guido Grosse, Daniel Fortier, Gustaf Hugelius, Christian Knoblauch, Vladimir Romanovsky, et al. "Deep Yedoma Permafrost: A Synthesis of Depositional Characteristics and Carbon Vulnerability." *Earth-Science Reviews* 172 (September 1, 2017): 75–86. https://doi.org/10.1016/j.earscirev.2017.07.007.

Sutton, A. J., C. L. Sabine, S. Maenner-Jones, N. Lawrence-Slavas, C. Meinig, R. A. Feely, J. T. Mathis, et al. "A High-Frequency Atmospheric and Seawater pCO_2 Data Set from 14 Open-Ocean Sites Using a Moored Autonomous System." *Earth System Science Data* 6, no. 2 (November 6, 2014): 353–66. https://doi.org/10.5194/essd-6-353-2014.

Washenfelder, R. A., G. C. Toon, J.-F. Blavier, Z. Yang, N. T. Allen, P. O. Wennberg, S. A. Vay, D. M. Matross, and B. C. Daube. "Carbon Dioxide Column Abundances at the Wisconsin Tall Tower Site." *Journal of Geophysical Research: Atmospheres* 111, no. D22 (2006). https://doi.org/10.1029/2006JD007154.

Wunch, D., P. O. Wennberg, G. C. Toon, B. J. Connor, B. Fisher, G. B. Osterman, C. Frankenberg, et al. "A Method for Evaluating Bias in Global Measurements of CO_2 Total Columns from Space." *Atmospheric Chemistry and Physics* 11, no. 23 (December 9, 2011): 12317–37. https://doi.org/10.5194/acp-11-12317-2011.

Chapter 2 Characteristics of Interannual Variability in Space-Based XCO_2 Global Observations

This chapter was published as Guan, Y., Keppel-Aleks, G., Doney, S. C., Petri, C., Pollard, D., Wunch, D., Hase, F., Ohyama, H., Morino, I., Notholt, J., Shiomi, K., Strong, K., Kivi, R., Buschmann, M., Deutscher, N., Wennberg, P., Sussmann, R., Velazco, V. A., and Té, Y.: Characteristics of interannual variability in space-based XCO_2 global observations, Atmos. Chem. Phys., 23, 5355–5372, https://doi.org/10.5194/acp-23-5355-2023, 2023.

Abstract

Atmospheric carbon dioxide (CO_2) accounts for the largest radiative forcing among anthropogenic greenhouse gases. There is, therefore, a pressing need to understand the rate at which CO_2 accumulates in the atmosphere, including the interannual variations (IAV) in this rate. IAV in the CO_2 growth rate is a small signal relative to the long-term trend and the mean annual cycle of atmospheric CO_2, and IAV is tied to climatic variations that may provide insights into long-term carbon-climate feedbacks. Observations from the Orbiting Carbon Observatory-2 (OCO-2) mission offer a new opportunity to refine our understanding of atmospheric CO_2 IAV since the satellite can measure over remote terrestrial regions and the open ocean where traditional in situ CO_2 monitoring is difficult, providing better spatial coverage compared to ground-based monitoring techniques. In this study, we analyze the IAV of column-averaged dry air CO_2 mole fraction (XCO_2) from OCO-2 between September 2014 to June 2021. The amplitude of IAV variations, which is calculated as the standard deviation of the timeseries, is up to 1.2 ppm over the continents and around 0.4 ppm over the open ocean. Across all latitudes, the

OCO-2 detected XCO_2 IAV shows a clear relationship with ENSO-driven variations that originate in the tropics and are transported poleward. Similar, but smoother, zonal patterns of OCO-2 XCO_2 IAV timeseries compared to ground-based in situ observations and with column observations from the Total Carbon Column Observing Network (TCCON) and the Greenhouse Gases Observing Satellite (GOSAT) show that OCO-2 observations can be used reliably to estimate IAV. Furthermore, the extensive spatial coverage of the OCO-2 satellite data leads to smoother IAV timeseries than those from other datasets, suggesting that OCO-2 provides new capabilities for revealing small IAV signals despite sources of noise and error that are inherent to remote sensing datasets.

2.1 Introduction

Increasing atmospheric CO_2 concentration from anthropogenic emissions is the major driver of the observed warming of Earth's climate since the industrial revolution (IPCC, 2021). Although CO_2 accumulation in the atmosphere generally is ~45% of anthropogenic emissions on a multi-year average (Ciais et al., 2013; Friedlingstein et al., 2019), the growth rate shows substantial interannual variability (Conway et al., 1994). The difference between emissions and the atmospheric CO_2 growth rate results from net CO_2 uptake by oceans and terrestrial ecosystems (Prentice et al., 2001; Doney et al., 2009), and the fluctuations reflect variations in the strength of those sinks due to climate variations (Peters et al., 2017; Friedlingstein et al., 2019). Much research has suggested that interannual variability (IAV) in the growth rate is predominantly due to variations in terrestrial ecosystem carbon uptake (Marcolla et al., 2017), even though the average uptake is roughly comparable between land and ocean (Le Quéré et al., 2009). Existing atmospheric CO_2 observations from surface flask sampling and in situ networks have been used to estimate global- and regional-scale interannual variability in CO_2 fluxes

(Gurney et al., 2008; Peylin et al., 2013; Keppel-Aleks et al., 2014; Piao et al., 2020). We note, however, that the surface observing network is located primarily on land and coastal sites, and more subtle ocean flux signals may be obscured by the large IAV in terrestrial fluxes.

Previous analyses of surface CO_2 IAV has shown a strong relationship with the phase and intensity of El Niño–Southern Oscillation (ENSO) (Le Quéré et al., 2009; Schwalm et al., 2011). ENSO variations originate from coupled ocean-atmosphere dynamics that are reflected in large wind and sea surface temperature anomalies over the central and eastern Pacific Ocean. ENSO affects the climate of much of the tropics and subtropics via atmospheric teleconnections on timescales of 2-7 years (Timmermann et al., 2018). On land, suppressed precipitation and high temperature associated with positive phases of ENSO (El Niño conditions) suppress CO_2 uptake by tropical ecosystems, while promoting fires that further reduce the CO_2 uptake by lands (Feely et al., 2002; McKinley et al., 2004; Piao et al., 2009; Wang et al., 2014). Although of smaller magnitude, the equatorial Pacific Ocean experiences weakening of the easterly trade winds and suppression of ventilation of deep, cold, carbon-rich waters to the surface during an El Niño, reducing the efflux of natural CO_2 to the atmosphere (Patra et al., 2005 ; Chatterjee et al., 2017).

Chatterjee et al. (2017) were able to directly observe the ocean flux-driven signal on atmospheric CO_2 from El Niño for the first-time using XCO_2 (column-averaged dry air CO_2 mole fraction) observed over the ocean by NASA's OCO-2 satellite. Space-based observations from OCO-2, which launched in July 2014, provide novel opportunities to characterize the patterns of IAV in XCO_2 in areas that were previously not directly observed by existing monitoring networks. The IAV in XCO_2 is being used implicitly for flux attribution in inverse modeling studies (Nassar et. al, 2011). These exciting results, however, must be tempered by an awareness that atmospheric CO_2 IAV is a relatively small signal. For example, IAV in the

surface network is about 1 ppm in scale compared to a seasonal amplitude of around 10 ppm in northern high latitudes. OCO-2 measures column averaged CO_2, so its measurements are sensitive to variations in the boundary layer mole fraction, which is in direct contact with the land or atmospheric fluxes, but also variations in the free troposphere and stratosphere, where flux signals are generally smaller than those observed at the surface (Olsen and Randerson, 2004). Furthermore, variations in the free troposphere are expected to have relatively long correlation length scales due to efficient mixing, making it important to consider the spatial scales at which XCO_2 observations provide unique information. This is especially important in light of analysis which suggests that the error variance budget in OCO-2 observations is large and contains substantial spatially coherent signal (Baker et al., 2022; Torres et al., 2019; Mitchell et al., 2023).

In this paper, we analyze XCO_2 from OCO-2 to characterize spatiotemporal patterns in IAV at near-global scale, over both land and ocean, and relate XCO_2 variations to ENSO conditions. We contextualize the information contained in OCO-2 observations by comparing with space-based GOSAT and ground-based TCCON XCO_2 and with surface measurements of CO_2. Finally, we use these comparisons to emphasize the spatial scales at which the IAV signal emerges from instrumental noise.

2.2 Data and Methods

2.2.1 Datasets

2.2.1.1 OCO-2 observatory

We analyzed IAV in dry air, column-average mole fraction XCO_2 inferred from OCO-2 satellite observations. The OCO-2 observatory was launched in July 2014 and has measured passive, reflected solar near infrared CO_2 and O_2 absorption spectra using grating spectrometers

since September 2014 (Eldering et al., 2017). XCO_2 data are retrieved from the measured spectra using the Atmospheric CO_2 Observations from Space (ACOS) optimal estimation algorithm, which is a full physics algorithm that takes into account XCO_2 and other physical parameters, including surface pressure, surface albedo, temperature, and water vapor profile in its state vector (O'Dell et al., 2018). The satellite flies in a polar and sun-synchronous orbit that repeats every 16 days, with three different observing modes of OCO-2, namely nadir (land only, views the ground directly below the spacecraft), glint (over ocean and land, views just off the peak of the specularly reflected sunlight), and target (typically for comparison with specific ground-based or airborne measurements) (Crisp et al., 2012; Crisp et al., 2017). We use the version 10 OCO-2 Level 2 bias-corrected XCO_2 data product from Goddard Earth Sciences Data and Information Services Center (GES DISC) Archive: https://disc.gsfc.nasa.gov/datasets/OCO_2_L2_Lite_FP_10r/summary), which has been validated with collocated ground-based measurements from the Total Carbon Column Observing Network (TCCON; discussed in more detail in Section 2.2). After filtering and bias correction, the OCO-2 XCO_2 retrievals agree well with TCCON in nadir, glint, and target observation modes, and generally have absolute median differences less than 0.4 ppm and Root Mean Square differences less than 1.5 ppm (O'Dell et al., 2018; Wunch et al., 2017).

2.2.1.2 TCCON

We corroborate patterns of XCO_2 IAV from OCO-2 with those from TCCON, a ground-based network of Fourier transform spectrometers that measure direct solar absorption spectra in the near infrared (Wunch et al., 2011). Retrievals of XCO_2 and other gases are computed using the GGG algorithm, a nonlinear least-squares spectral fitting algorithm. The TCCON retrievals are tied to the World Meteorological Organization (WMO) X2007 CO_2 scale via calibration with

aircraft and AirCore profiles above the TCCON sites (Karion et al., 2010; Wunch et al., 2010). This ensures an accuracy and precision of ~0.6 ppm (1-sigma) throughout the network (Washenfelder et al., 2006; Messerschmidt et al., 2010; Deutscher et al., 2010, Wunch et al., 2010). TCCON has been used widely as a validation standard by providing independent measurements to compare with multiple satellite XCO_2 retrievals including OCO-2. In previous work Sussmann and Rettinger (2020) have demonstrated a concept to retrieve annual growth rates of XCO_2 from TCCON data, which are regionally to hemispherically representative in spite of the non-uniform sampling in time and space inherent to the ground-based network. In our study, we focus on IAV in the XCO_2 timeseries from 26 TCCON sites (Table 2.1, Fig 2.1) that have at least 3 years of observational coverage within the period from September 2014 to June 2021. These TCCON data have been filtered using the standard filter that is based on a measure of cloudiness and limits the solar zenith angle. Data are publicly available from the TCCON GGG2014 Data Archive (https://tccondata.org/) hosted by the California Institute of Technology.

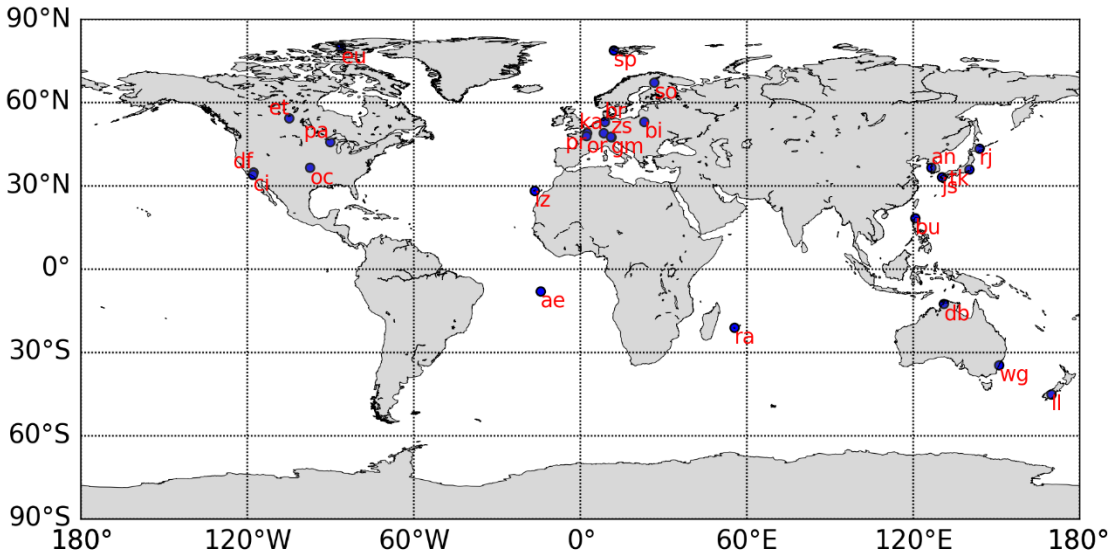

Figure 2.1: *Map showing the locations and the acronyms of the TCCON sites.*

Table 2.1: *TCCON Column-Averaged Dry-Air Mole Fractions of CO_2 (GGG2014 Data)*

Region	Site	Acronym	Latitude	Longitude	Start Date	End Date	Publication
Polar Northern Hemisphere (60-90°N)	Eureka (NU)	eu	80.05	-86.42	2010-07	2020-07	Strong, K. et al., 2017
	Ny Ålesund	sp	78.90	11.90	2014-04	2019-09	Notholt, J. et al., 2019
	Sodankylä (FI)	so	67.37	26.63	2009-05	2020-10	Kivi, R. et al., 2017
Temperate Northern Hemisphere (20-60°N)	East Trout Lake(SK)	et	54.35	-104.99	2016-10	2020-09	Wunch, D., et al., 2017
	Bialystok (PL)	bi	53.23	23.03	2009-03	2018-10	Deutscher, N. et al., 2017
	Bremen (DE)	br	53.10	8.85	2010-01	2020-06	Notholt, J. et al., 2017
	Karlsruhe (DE)	ka	49.10	8.44	2010-04	2020-11	Hase, F. et al., 2017
	Paris (FR)	pr	48.97	2.37	2014-09	2020-06	Te, Y. et al., 2017
	Orléans (FR)	or	47.97	2.11	2009-08	2020-06	Warneke, T. et al., 2017
	Garmisch (DE)	gm	47.48	11.06	2007-07	2020-06	Sussmann, R. et al., 2017
	Zugspitze (DE)	zs	47.42	10.98	2015-04	2020-06	Sussmann, R. et al., 2018
	Park Falls (US)	pa	45.95	-90.27	2004-06	2020-12	Wennberg, P. O. et al., 2017
	Rikubetsu (JP)	rj	43.46	143.77	2013-11	2019-09	Morino, I. et al., 2017
	Lamont (US)	oc	36.60	-97.49	2008-07	2020-12	Wennberg, P. O. et al., 2017
	Anmyeondo (KR)	an	36.58	126.33	2015-02	2018-04	Goo, T.-Y. et al., 2017
	Tsukuba (JP)	tk	36.05	140.12	2011-08	2019-09	Morino, I. et al., 2017
	Edwards (US)	df	34.96	-117.88	2013-07	2020-12	Iraci, L. et al., 2017
	Caltech (US)	ci	34.14	-118.13	2012-09	2020-12	Wennberg, P. O. et al., 2017
	Saga (JP)	js	33.24	130.29	2011-07	2020-12	Shiomi, K.et al., 2017
	Izana (ES)	iz	28.30	-16.50	2007-05	2021-02	Blumenstock, T. et al., 2017
Tropical Northern Hemisphere (0-20°N)	Burgos (PH)	bu	18.53	120.65	2017-03	2020-03	Morino, I., et al., 2018
Tropical Southern Hemisphere (0-20°S)	Ascension Island (SH)	ae	-7.92	-14.33	2012-05	2018-10	Feist, D. G. et al., 2017
	Darwin (AU)	db	-12.46	130.94	2005-08	2020-04	Griffith, D. W. T., et al., 2017
Temperate Southern Hemisphere (20-60°S)	Réunion Island (RE)	ra	-20.90	55.49	2011-09	2020-07	De Maziere, M. et al., 2017
	Wollongong (AU)	wg	-34.41	150.88	2008-06	2020-06	Griffith, D. W. T. et al., 2017
	Lauder (NZ)	ll	-45.04	169.68	2010-02	2018-10	Sherlock, V. et al., 2017

2.2.1.3 Marine Boundary Layer Observations

To explore differences in surface and column-average CO_2 IAV, we analyze IAV in the surface CO_2 mole fraction at marine boundary layer (MBL) sites in the NOAA (National Oceanic and Atmospheric Administration) cooperative sampling network (https://gml.noaa.gov/dv/site/?program=ccgg). At these sites, boundary layer CO_2 is measured

using weekly flask samples (Masarie and Tans, 1995; Dlugokencky et al., 2021). MBL sites are typically far away from anthropogenic sources and regions of active terrestrial exchange, so they provide an estimate for large-scale patterns in the global background CO_2 concentration. The surface MBL dry air mole fraction data has an accuracy level of about 0.1 ppm. In this study, we select 16 sites with at least 80% data coverage for the approximately 7-year period overlapping with OCO-2 (Table 2.2, Fig 2.2), and the data are aggregated into four north-south zones for comparison with OCO-2 XCO_2: northern and southern hemisphere tropical (0 - 20°) and Northern Hemisphere/Southern Hemisphere extratropical zones (20-60°). Each belt contains at least three MBL sites. Higher latitudes (60-90°) are not considered in this comparison due to the gaps remaining in the OCO-2 XCO_2 record in high latitudes during wintertime and shouldering seasons.

Table 2.2: *Marine Boundary Layer stations within the NOAA Earth System Research Laboratory CO_2 sampling network*

Region	Station	Acronym	Latitude	Longitude	Start Date	End Date
Temperate Northern Hemisphere (20-60°N)	Mace Head, Ireland	MHD	53.3	-9.9	2014-01	2020-07
	Shemya, AK	SHM	52.7	174.1	2014-01	2020-07
	Terceira Island Azores	AZR	38.8	-27.4	2014-01	2020-07
	Tudor Hill, Bermuda	BMW	32.3	-64.9	2014-01	2020-07
	Sand Island, Midway	MID	28.2	-177.4	2014-01	2020-07
	Key Biscayne, FL	KEY	25.7	-80.2	2014-01	2020-07
Tropical Northern Hemisphere (0-20°N)	Cape Kumukahi, HI	KUM	19.5	-154.8	2014-01	2020-07
	Mariana Islands, Guam	GMI	13.5	144.7	2014-01	2019-08
	Ragged Pointed, Barbados	RPB	13.2	-59.4	2014-01	2020-07
	Christmas Island, Republic of Kiribati	CHR	1.7	157.2	2014-01	2019-08
Tropical Southern Hemisphere (0-20°S)	Seychelles	SEY	-4.7	55.2	2014-01	2020-07
	Ascension Island	ASC	-8.0	-14.4	2014-01	2020-07
	Tutuila, America Samoa	SMO	-14.2	-170.6	2014-01	2020-07
Temperate Southern Hemisphere (20-60°S)	Cape Grim, Australia	CGO	-40.7	144.7	2014-01	2020-07
	Baring Head	BHD	-41.4	174.9	2014-01	2020-07
	Crozet Island	CRZ	-46.5	51.9	2014-01	2020-07

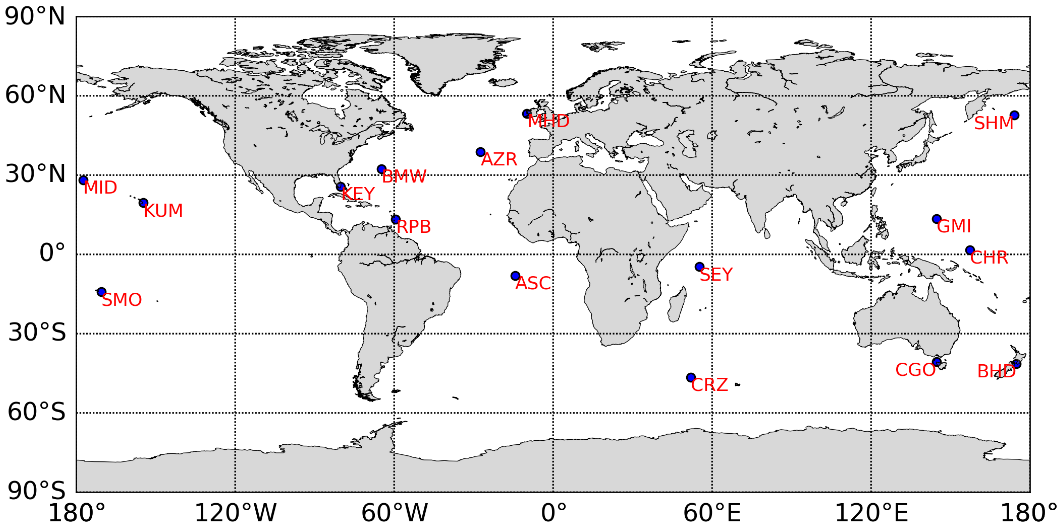

Figure 2.2: *Map showing the locations and the acronyms of the Marine Boundary Layer stations within the NOAA Earth System Research Laboratory CO_2 sampling network.*

2.2.1.4 GOSAT

We compare patterns of XCO_2 IAV from OCO-2 with those from GOSAT. Also known as Ibuki, GOSAT is the world's first satellite dedicated to greenhouse gas monitoring, measuring global total column CO_2 and CH_4 since 2009. With the Thermal and Near infrared Sensor for carbon Observation (TANSO) - Fourier Transform Spectrometer (FTS) onboard for greenhouse gas monitoring using three SWIR bands and one TIR band (Cogan et al., 2012; Yoshida et al., 2013). Column-averaged dry mole fraction are obtained at a circular footprint of approximately 10.5 km. GOSAT has a regional biased of about approximately 0.3 ppm and 1.7 ppm single observation error versus the TCCON (Kulawik et al., 2016). We utilize the FTS SWIR Level 3 data global monthly 2.5° resolution mean CO_2 mixing ratio products from 2009 June to 2021 December to generate IAV and make comparisons with OCO-2. L3 products are generated by interpolating, extrapolating, and smoothing the FTS SWIR column-averaged mixing ratios of CO_2 and apply the geostatistical calculation technique Kriging method. GOSAT observation

datasets are available to public at NIES GOSAT website (https://www.gosat.nies.go.jp/en/about_5_products.html).

2.2.1.5 Multivariate ENSO Index (MEI)

We use the bi-monthly Multivariate El Niño/Southern Oscillation (ENSO) index (MEI; downloaded from Physical Sciences Laboratory: https://psl.noaa.gov/enso/mei/) to explore the relationship between CO_2 IAV and ENSO. The MEI is the time series of the leading combined Empirical Orthogonal Function of five different variables (sea level pressure, sea surface temperature, zonal and meridional components of the surface wind, and outgoing longwave radiation) over the tropical Pacific basin. Positive values in the MEI indicate El Niño conditions, while negative values indicate La Niña conditions, and the magnitude reflects the relative strength. Unlike other ENSO indices which use only one climate metric (e.g., the sea level pressure difference between Tahiti and Darwin or the sea surface temperature anomaly within a pre-defined box), the MEI provides for a more complete and flexible description of the ENSO phenomenon than traditional single variable ENSO indices and has less vulnerability to errors (Klaus Wolter et. al, 2011).

2.2.2 Methods

2.2.2.1 Spatial Aggregation

We aggregate daily XCO_2 observations from the version 10 OCO-2 Level 2 lite product to monthly scale, exploring patterns of IAV at three spatial scales: gridcell-level, zonal averages over 5° of latitude, and broad zonal belts. Aggregating soundings reduces random noise in the observations, mitigates the impact of data gaps due to cloud cover, and partly mitigates effect from low winter sunlight levels in polar regions. For gridcell level analysis, we aggregate data equatorward of 45° to 5°x5° bins since these data are not limited by polar night or degraded by

high solar zenith angles during winter. Poleward of 45° in both hemispheres, we aggregate the satellite observation to a latitude-longitude resolution of 5°x10° to compensate for fewer and noisier soundings in these latitudes, especially during winter and its shoulder seasons. Within each 5°x5° or 5°x10° gridcell, only months that have more than 5 soundings are included in the analysis. Our criteria for aggregation are based on sensitivity experiments in which we modulated the grid cell resolution from 1°x1° to 15°x15° (Fig A.1 and Fig A.2) and varied the threshold on the required number of soundings within a month from 1 to 25 (Fig A.3, Fig A.4 and Fig A.5). Our goal was to reduce noise but maintain high spatial coverage (Fig A.6 and Fig A.7). The 5°x5° and 5°x10° aggregation strike the necessary balance of reducing noise (evidenced by the smoother IAV amplitude fields as aggregation increases in Fig A.1) but maintaining spatial information by not oversmoothing (evidenced by the fact that the aggregation occurs at spatial scales finer than the "elbow" where correlations among 1° gridcells stop changing with separation distance in Fig A.8)

In our analysis, we also aggregate data to zonal averages. At intermediate spatial scales, we average all data around the 5° latitude bins described above. For comparison with TCCON and MBL data, which are spatially sparse, we further aggregate XCO_2 data into four broad zonal belts – each of which contains at least 1 TCCON or 3 MBL stations -- (delineated in Table 2.1 and Table 2.2) to assess IAV patterns among the datasets. Keppel-Aleks et al., (2014) showed that drivers of IAV (i.e., temperature, drought stress, or fire) could be attributed when surface CO_2 were aggregated into similar broad zonal belts, whereas process-level attribution was not possible with global averaging. We therefore analyze broad zonal belts to gain a large-scale understanding of how three CO_2 datasets are similar and where differences lie.

2.2.2.2 Deriving Interannual Variations

We use a consistent process to calculate IAV (Equation 1) from the raw OCO-2, TCCON and MBL timeseries. The methodology is based on approaches used in Keppel-Aleks et al. (2013) and NOAA curve fitting methodology (Thoning et al, 1989). We decompose the raw time-series data into a long-term trend (which is a function of location (x,y) and time (t)), a seasonal cycle (which is a function of location and calendar month (m)), and IAV anomalies using Equation 1:

$$IAV(x,y,t) = Raw(x,y,t) - Trend(x,y,t) - Seasonal(x,y,m) \quad \text{Equation 1}$$

We first fit a third order polynomial to the Raw timeseries to calculate the observed trend at each location (Fig 2.3a). After removing the trend calculated at each gridcell (Fig 2.3b), we calculate a mean seasonal cycle by taking the mean value of all January, February, etc. data (Fig 2.3c). Particularly at high latitudes, some months are systematically under sampled. For these gridcells, we must have at least two years with sufficient observations to calculate a climatological mean for that month, otherwise, that calendar month is assumed to have insufficient data to infer the IAV. Finally, we remove the mean seasonal cycle from the detrended timeseries at each gridcell to obtain the IAV anomaly timeseries (Fig 2.3d). Given the short data record, we quantify the uncertainty in our calculation of the climatological seasonal cycle as the standard error for each calendar month (blue shading in Fig 2.3c), and this uncertainty is propagated to the corresponding IAV timeseries (Fig 2.3d). We fit a third order polynomial to the raw timeseries since the GOSAT, MBL and TCCON timeseries extend over a decade in length. We confirm that the use of a third-order polynomial, versus a second-order polynomial, does not remove the IAV signal from the shorter OCO-2 timeseries (Fig A.9).

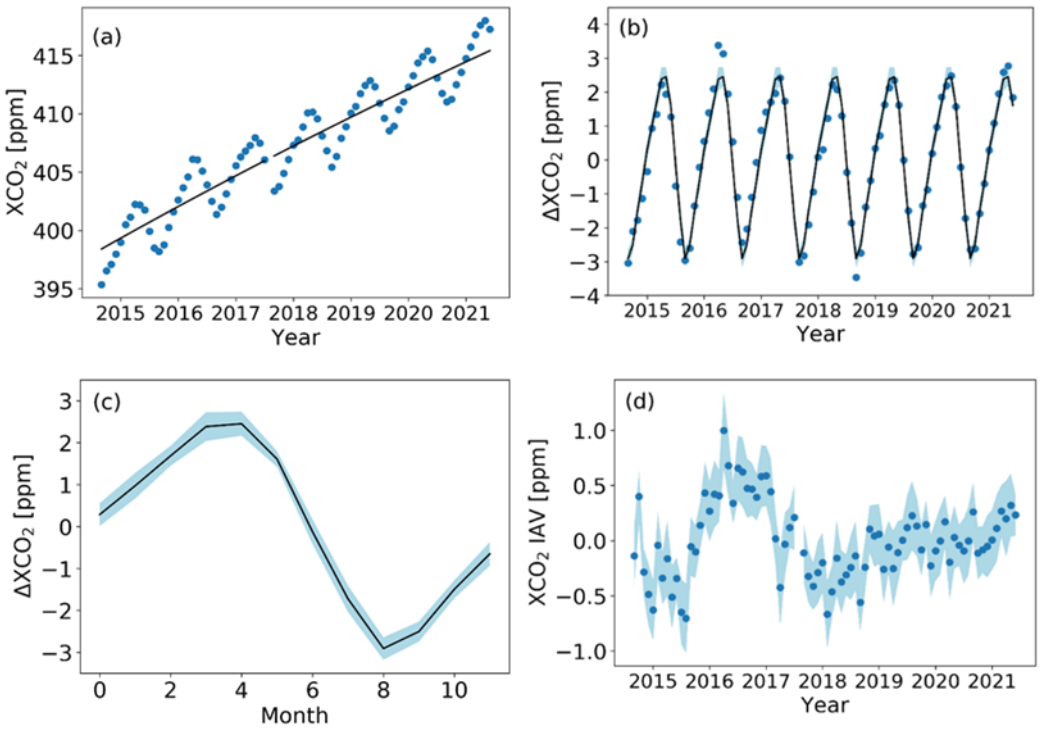

Figure 2.3: *Methodology to calculate the CO_2 interannual variability timeseries, using OCO-2 XCO_2 data at the 5° grid cell at 20°N, 155°W, which contains Moana Loa, as an example. (a) 5°resolution monthly mean raw OCO-2 XCO_2 and the associated 3rd order polynomial trend. (b) detrended monthly XCO_2 after removing the long-term trend with a repeating 12-month annual cycle obtained from calculating the mean for each month. The light blue shading gives the uncertainty of the seasonal cycle, which is derived by calculating the standard deviation across all Januarys, Februarys, etc. (c) 12-month mean annual cycle together with the uncertainty range plotted in (b). (d) Resulting interannual variability, when mean annual cycle is removed from detrended timeseries.*

2.3 Results

2.3.1 Spatiotemporal Variations Based on OCO-2 Observation

When averaged into broad zonal belts representing the tropics and mid-latitudes, the OCO-2 XCO_2 IAV timeseries anomalies range between -0.5 to 0.75 ppm (Fig 2.4a). All latitude bands show increasing IAV during positive MEI (El Niño) and decreasing IAV during negative MEI (La Niña), although the phasing varies among latitudes. During the strong 2015–2016 El Niño, which began around March 2015 and reached its peak at the start of 2016, XCO_2 showed the largest IAV. The Southern Hemisphere extratropical region (Fig 2.4d) have larger and more

rapid response in the IAV associated with ENSO compared to other zones, especially for the smaller El Niño that peaked at the beginning of 2020. At this time, the XCO_2 IAV timeseries (Fig 2.4d) had an anomaly nearly twice as large as that of other latitude belts (Fig 2.4a to 2.4c). During both El Niño events, the IAV timeseries in the NH tropics zone peaks nearly six months after the maximum MEI value.

We assess the spatial correlation patterns with no time lag, 3-month, 6-month lag between the IAV timeseries and MEI (Fig 2.8a). The XCO_2 IAV timeseries have strong correlation coefficient with the MEI index in both Southern Hemisphere and Northern Hemisphere low latitudes from 0° to 30°N at lag 0, whereas in the Northern Hemisphere extratropics, the maximum positive correlation occurs at month 4 (Fig 2.8b). The positive correlation between MEI and the IAV timeseries is gradually attenuated, with no clear correlation at six months lag (Fig 2.8c).

The differences in temporal phasing between the broad zonal belts (Fig 2.4a) associated with El Niño events can be linked to transport of El Niño-driven CO_2 flux anomalies away from the tropics when zonal means are calculated from OCO-2 observations at 5° latitude resolution (Fig 2.5). For the two El Niño periods in 2015-2017 and late-2018 to 2021, high IAV values originate in the tropics and a smooth transition to high IAV values is seen at higher latitudes as time progresses (Fig 2.5a). We note that fluxes outside the tropics may also be influenced by ENSO-related climate variability, yet the transport of tropical-driven anomalies appears to dominate. This 7-year study period also captures the half-year lags for atmospheric transport or climate-ecological teleconnections that impacts XCO_2 variations in the far North. While the OCO-2 patterns largely conform with variability expected based on ENSO and are in broad agreement with other observational networks, there are some anomalies that cannot be explained,

such as the high XCO_2 in early 2020 around 60°S (Fig 2.5a). Even with more aggressive data filtering, this episode persists, requiring more investigation of unknown geophysical drivers of high XCO_2 or potential retrieval issues that could cause a high bias.

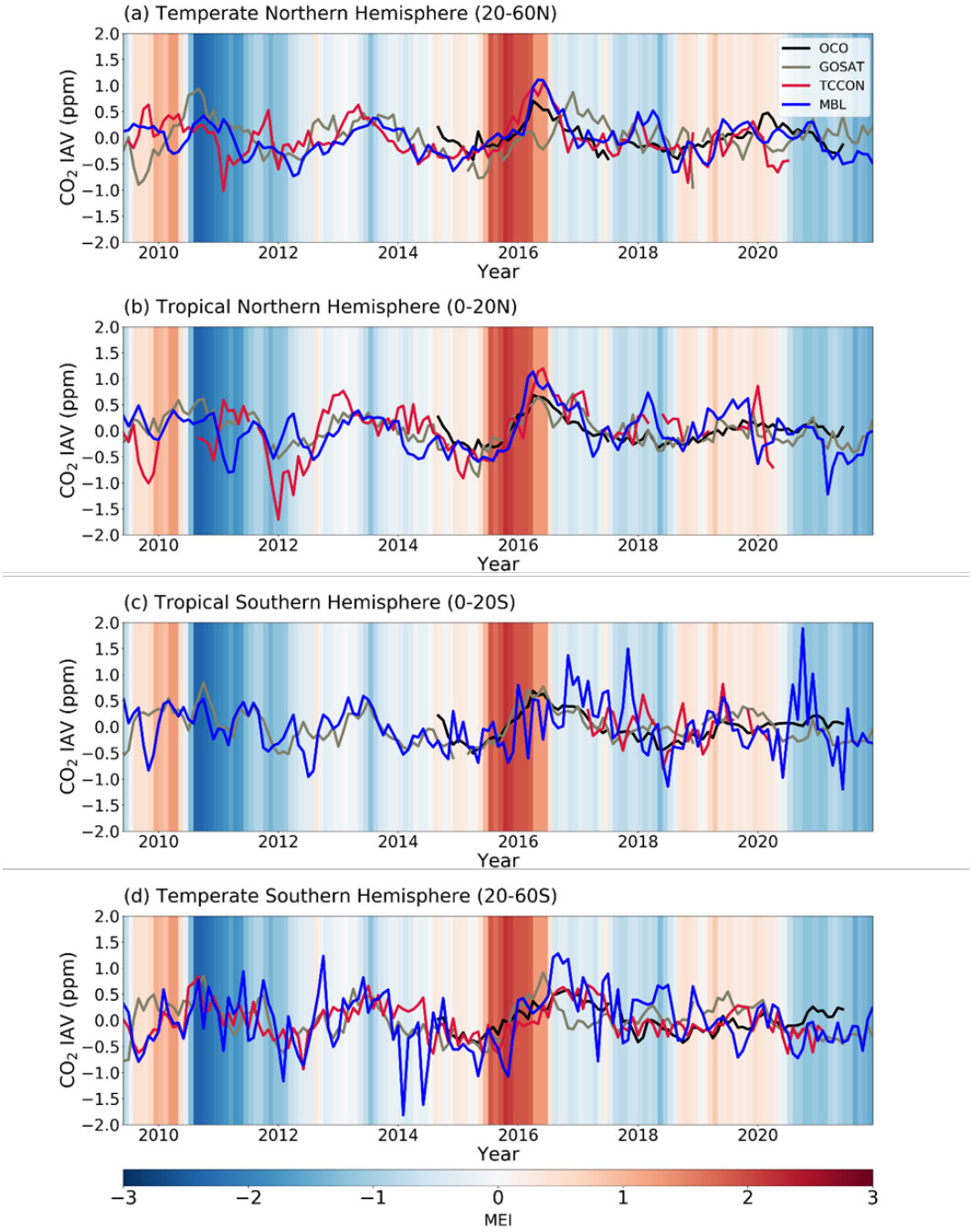

Figure 2.4: *IAV timeseries averaged for zonal bands between 60 °N and 60 °S from four different observing strategies: Space-based OCO-2 XCO_2 (Black), Surface CO_2 observations from NOAA's marine boundary layer (MBL) sites (Blue), Ground-based TCCON XCO_2 (Red), Space-based GOSAT XCO_2*

(Gray). (a) temperate northern hemisphere (20°N-60°N), (b) tropical northern hemisphere (0° - 20°N), (c) tropical southern hemisphere (0°-20°S), (d) temperate southern hemisphere (20°S-60°S). For all panels, the background shading indicates the Multivariate ENSO Index (MEI), which is positive during El Niño phases.

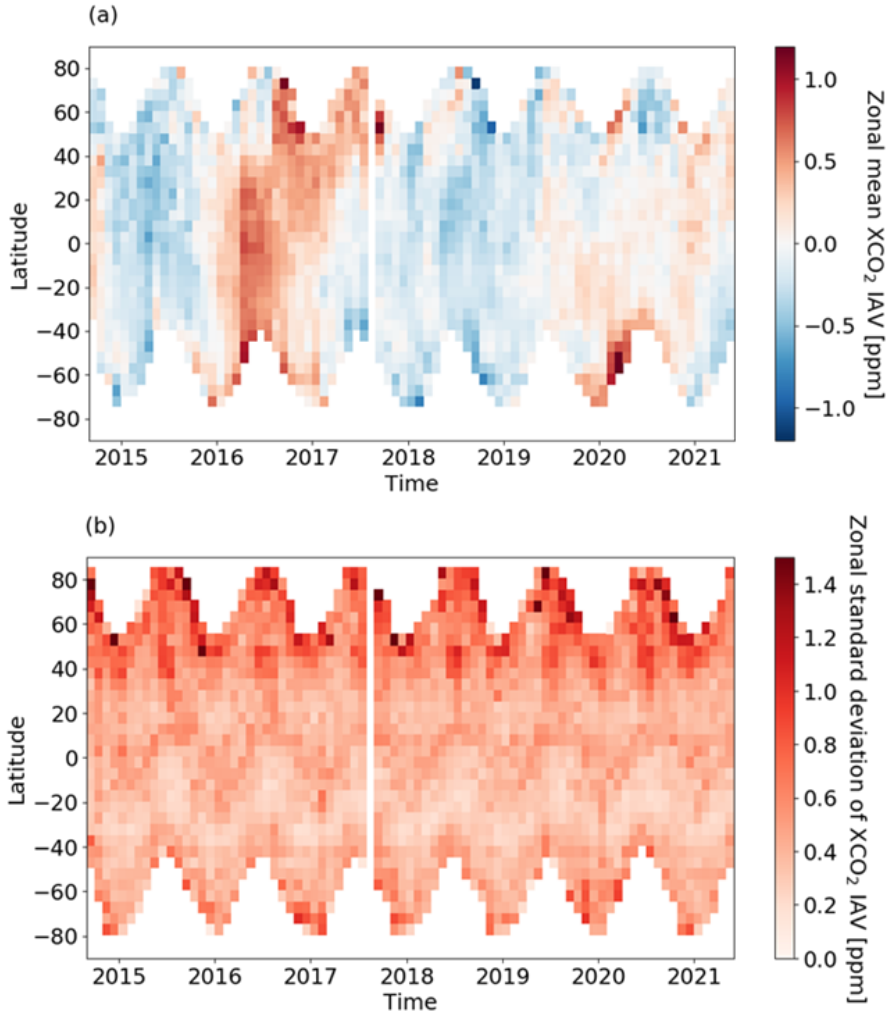

Figure 2.5: *Hovmöller Diagrams diagram showing zonal mean OCO-2 XCO_2 IAV timeseries for 5° latitude bins (a) and the zonal standard deviation of XCO_2 IAV (b), which gives an estimate of coherence in the IAV patterns among grid cells in the 5° zonal belt.*

We quantify coherence in CO_2 IAV within a latitude circle by taking the standard deviation across gridcell-level IAV anomalies within each 5° latitude zone. The standard deviation among gridcells is highest in the far North, with values as high as 1 ppm poleward of 45°N and as low as 0.2 ppm in the Southern Tropical bands (Fig 2.5b), indicating that IAV is

less spatially coherent in the Northern Hemisphere. This may be consistent with studies that show greater IAV in terrestrial ecosystem fluxes (concentrated in the northern hemisphere) (Zeng et al., 2005) relative to ocean fluxes, or may reflect that our IAV timeseries also retains the imprint of sampling, measurement, and retrieval errors, which become more pronounced at higher latitudes. In general, there is not a time-dependent or ENSO-related pattern for the longitudinal variation of IAVs (no obvious changes during the two El Niño periods), which suggests the variation within each 5° band may be approximately stable and does not change substantially with interannual climate events.

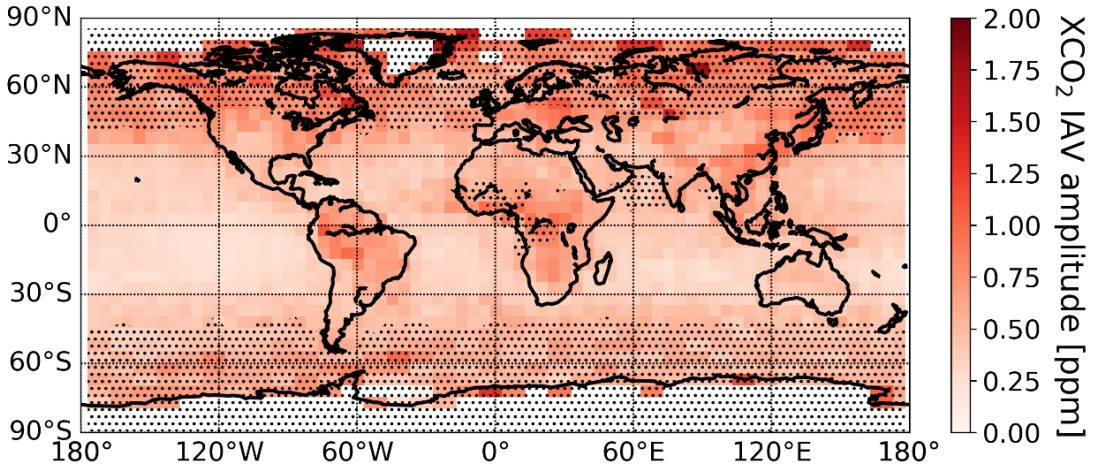

Figure 2.6: *OCO-2 XCO_2 IAV amplitude, determined as the standard deviation of the IAV timeseries. Data equatorward of 45° are averaged at 5°by 5° resolution , and data poleward of 45° are averaged at 5°by 10° resolution. Shaded regions indicate gridcells that lack mean annual cycle data for at least two calendar months due to polar night or related retrieval challenges.*

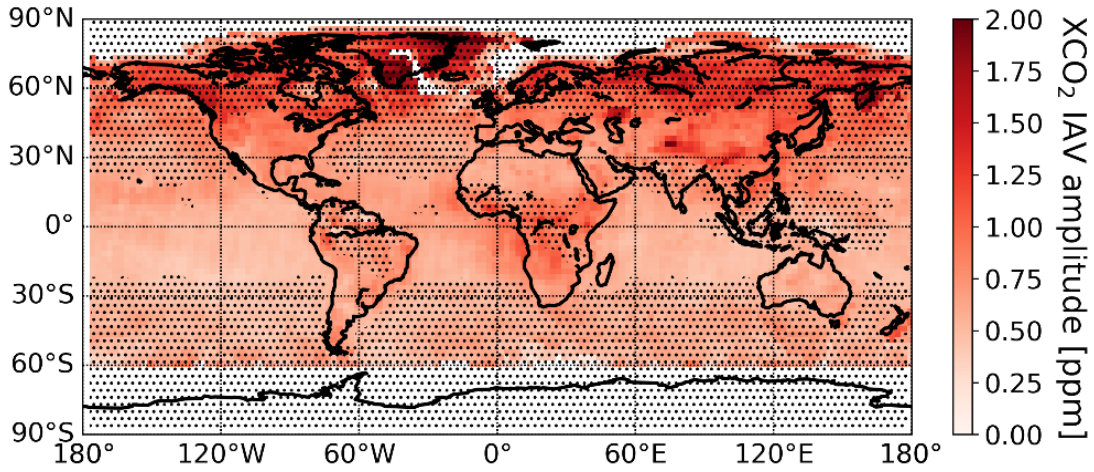

Figure 2.7: *Similar as Figure 2.6 but based on GOSAT data.*

The XCO_2 IAV amplitude (the standard deviation of the IAV timeseries) is notably larger over continental gridcells compared to ocean gridcells (Fig 2.6). In both hemispheres, the IAV amplitude over subtropical ocean basins is less than 0.4 ppm, while the IAV amplitude over tropical land in Southeast Asia, Congo forests and Amazon Basin is about 1 ppm. In higher latitudes, the XCO_2 IAV amplitude can exceed 1.2 ppm above deciduous and boreal forests in North America and Eurasia. Higher values over land likely occur due to the active CO_2 exchange between terrestrial ecosystem and the atmosphere, but we cannot rule out that retrievals over land show more variance due to complex topography, albedo, etc., which are elements of the retrieval state vector. Nevertheless, over land areas with low carbon exchange (e.g., Australia, the Middle East, the Sahara Desert), the XCO_2 IAV amplitude is nearly of the same low level as the ocean basins. It is worth noting that for high latitude regions, including both Northern continents and Southern Ocean, OCO-2 does not obtain observations over a full calendar year (stippled gridcells in Fig 2.6) due to polar nights, low light levels, and high solar zenith angles.

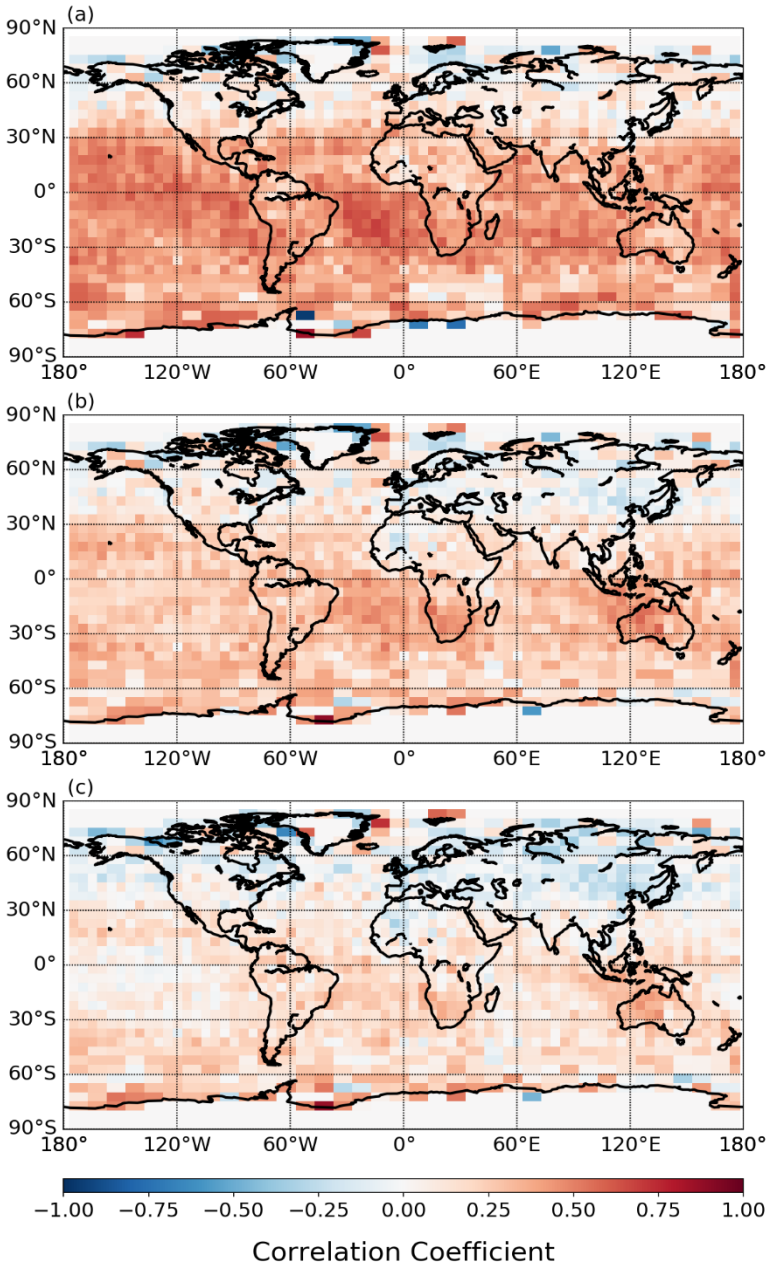

Figure 2.8: *Correlation coefficient between local grid cell OCO-2 XCO_2 IAV timeseries and MEI, for (a) synchronous timeseries, (b) with 3-month lags, (c) with 6-month lags.*

The XCO_2 IAV amplitudes are less zonally coherent through these regions than those in the tropics and mid-latitudes, for both land and ocean. When averaging all ocean or land grid cells around a latitude circle, the zonal mean IAV amplitude over the ocean ranges from 0.3 to 1.0 ppm, while the land IAV amplitude ranges from 0.4 to 1.1 ppm (Fig 2.9). Both the land and

ocean profiles have similar north-south patterns, with higher IAV amplitude in the Northern Hemisphere and lower IAV amplitude in the Southern Hemisphere, and the small IAV amplitudes in the subtropics of both hemispheres, with more scatter among land gridcells than ocean (Fig. 2.5b and Fig 2.9), suggesting either the influence of local flux IAV on land or greater error associated with retrievals on land. We note better coherence between the XCO_2 IAV timeseries of each local grid cell and that of zonal mean XCO_2 IAV timeseries for ocean, with correlation coefficients of approximately 0.8. In contrast, land gridcells are generally correlated with the zonal mean at around 0.4 to 0.6 (Fig 2.10).

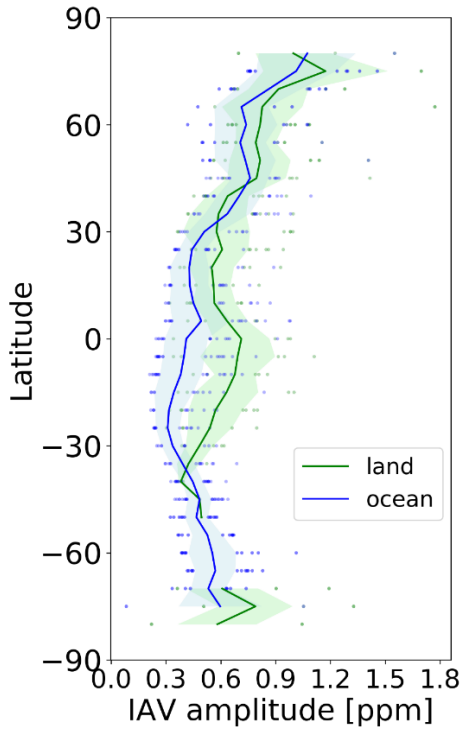

Figure 2.9: *Latitudinal profile for zonal mean of IAV amplitude and the standard deviation among land (green) or ocean (blue) gridcells in each latitude band (shaded area). Individual points represent all grid cells valid IAV record within the certain zonal band.*

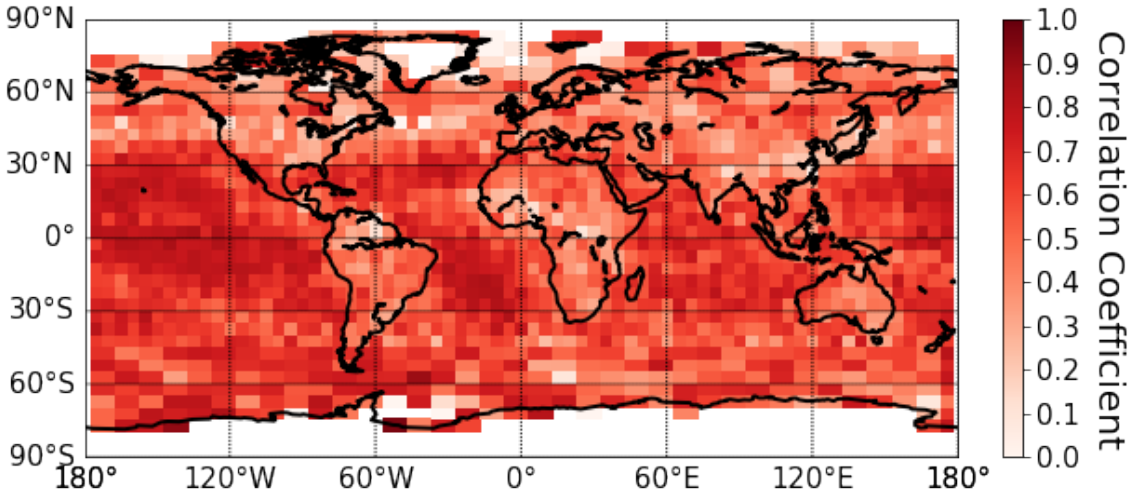

Figure 2.10: *Correlation coefficient between local grid cell IAV timeseries and the corresponding 5° zonal mean OCO-2 XCO_2 IAV timeseries.*

2.3.2 OCO-2 XCO_2 IAV compared to GOSAT XCO_2 IAV

We carried out comparisons between the global spatiotemporal pattern of XCO_2 IAV between OCO-2 and GOSAT, since GOSAT has data beginning in 2009. The XCO_2 timeseries from OCO-2 provides higher coverage over mid-latitude oceans and tropical rainforests (stippling in Fig 2.6, 2.7). The IAV amplitude of OCO-2 is generally smaller than that of GOSAT worldwide (Fig 2.6, 2.7), which may be due to greater data volume and reduced noise in the OCO-2 dataset (Wu et al., 2020). OCO-2 and GOSAT zonal mean IAV timeseries generally share the same feature from 2014 to 2021 (Fig 2.4a-d), with an increasing trend during El Niño and decreasing trend during La Niña, however the GOSAT XCO_2 shows a delayed response in the northern midlatitudes, by almost 9 months, to the strong 2015 El Niño compared to the other datasets. Generally, GOSAT IAV timeseries are nosier, from month-to-month, compared to those from OCO-2.

2.3.3 XCO_2 IAV compared to surface and TCCON ground-based sites

Given that the small IAV signal (up to 1 ppm over land, and smaller over ocean) is similar in magnitude to noise and systematic bias in OCO-2 soundings (Torres et al., 2019), we corroborate patterns of IAV from OCO-2 with other datasets. The OCO-2 IAV timeseries in broad latitudinal belts share similarities with those of TCCON XCO_2 and MBL surface CO_2 ground-based IAV timeseries, with all timeseries showing similar relationships to MEI. Especially striking is that all timeseries capture the lagged response in the NH midlatitude belt to the strong 2015/16 El Niño (Fig 2.4a-d). Although the patterns are similar, the magnitude of IAV at the MBL sites is almost double the IAV in the OCO-2 XCO_2 timeseries. Given that the atmospheric boundary layer, where surface observations are made, is on average 10% of the total column, this suggests that much IAV in total column observations is present within the free troposphere. For TCCON, the amplitude of IAV is similar to that of OCO-2, since both methods capture total column variations. We note that the zonal IAV timeseries for MBL and TCCON appear to have more high frequency variations than those from OCO-2 (Fig A.10, Fig A.11 & Fig A.12), which likely stems from the fact that the zonal composites are developed from sparse ground-based sites (between 1 and 12 observatories) within each latitude belt, whereas the satellite measures at all longitudes within a belt, though with more limited time resolution. The zonal mean OCO-2 observations are correlated with MBL sites within the same latitude band with R between 0.5 and 0.75 (diagonal elements on Fig 2.13b). Correlations between zonal TCCON and OCO-2 observations range between 0.15 and 0.55. The correlations are weakest in the northern tropics band, where TCCON data were unavailable during the strong El Niño (Fig 2.3c). It is noteworthy that OCO-2 zonal averages are more correlated among different latitudes than are MBL or TCCON observations (off-diagonal elements in Fig 2.13c, d, e). The greater

correlation across latitudes for OCO-2 compared to MBL sites is likely due to the sensitivity of the OCO-2 XCO_2 observations to the free troposphere, where meridional transport is more rapid than at the surface. While TCCON data are also sensitive to the free troposphere, we hypothesize that the zonal belt averages for TCCON, constructed from only a few sites, are more affected by noise, both instrumental and geophysical, and thus show lower coherence than the OCO-2 XCO_2 averages constructed from the whole latitudinal bands.

We further compared the IAV from OCO-2 XCO_2 with TCCON stations at the site level (Fig 2.12). Across all sites, the IAV amplitude generally shows good agreement and lies between 0.4 to 1.2 ppm. We note a slight low IAV amplitude in OCO-2 relative to TCCON for all five sites in the Southern Hemisphere which lie below the one-to-one line. Low OCO-2 IAV amplitudes may be due to the fact that a 5x5 ° gridcell encompassing these near-coastal locations includes both land and ocean OCO-2 soundings, and may be due to specific sources of variance from retrieval bias affected by surface type for the OCO-2 (e.g., Fig 2.9). It is also worth noting that OCO-2 is looking at a region of 5° by 5° gridcell (or 5° by 10° in higher latitudes) around TCCON sites, so there are different signals affecting the variance between the two types of observations.

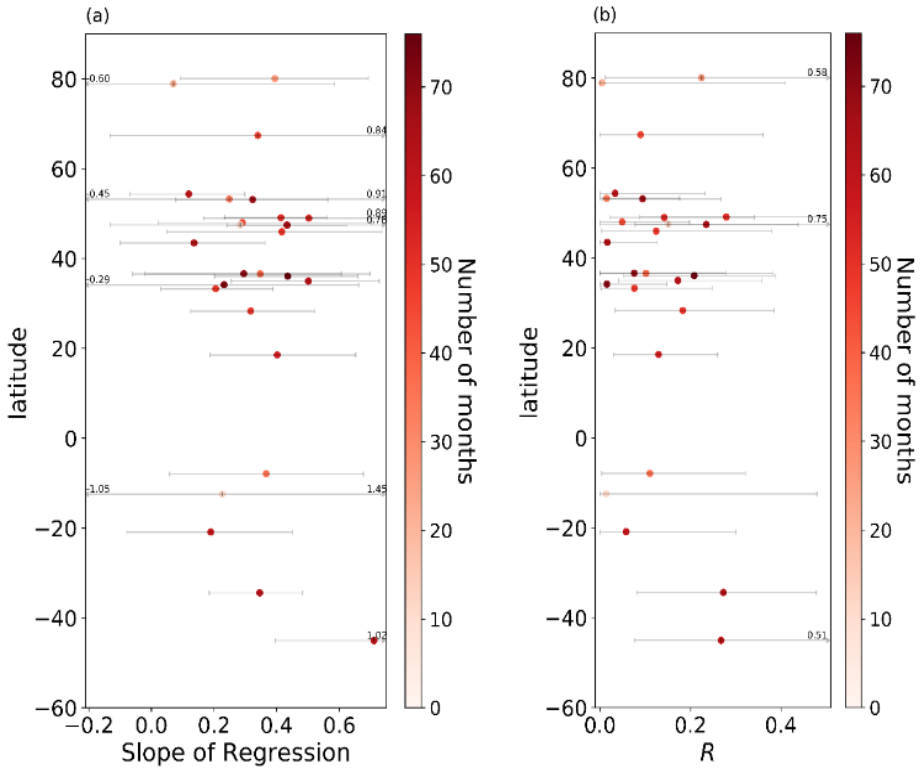

Figure 2.11: *Latitudinal profile of regression Slope (panel a) and correlation coefficient (R, panel b) of OCO-2 versus TCCON XCO_2 IAV. The Slope and R values are based on using monthly XCO_2 IAV. The error bars result from a Monte Carlo bootstrapping approach. The colours represent the number of months data which used for the regression calculation, given gaps in both the OCO-2 and TCCON datasets.*

We derive the regression slopes and Correlation Coefficient R between OCO-2 and monthly averaged TCCON IAV through bootstrapping Linear Regression fitting techniques to investigate the coherence between IAV signals from space-based and in-situ ground-based observations. We compute the linear regression 1000 times, by iteratively resampling the IAV timeseries with replacement, and calculate the 95% significant level for regression slopes based on the histogram of the sample distributions during the bootstrapping (Fig A.13). Despite having similar IAV amplitudes, the IAV timeseries from OCO-2 are only moderately correlated with those from TCCON (Fig 2.11). The regression slopes range from 0.1- 0.6 and R values are generally around 0.1 – 0.5, indicating that less than 25% of the IAV in OCO-2 is explained by

IAV measured by TCCON. These R values are, as expected, smaller than the zonal averages shown in Fig 2.11b, which average some of the site-level noise for TCCON and gridcell-level noise for OCO-2. The detailed XCO_2 IAV timeseries of each site (Fig A.10) for OCO-2 and TCCON show that the IAV timeseries in the NH are more variable, which can partly explain the hemispheric difference in amplitude, slope, and correlation coefficients.

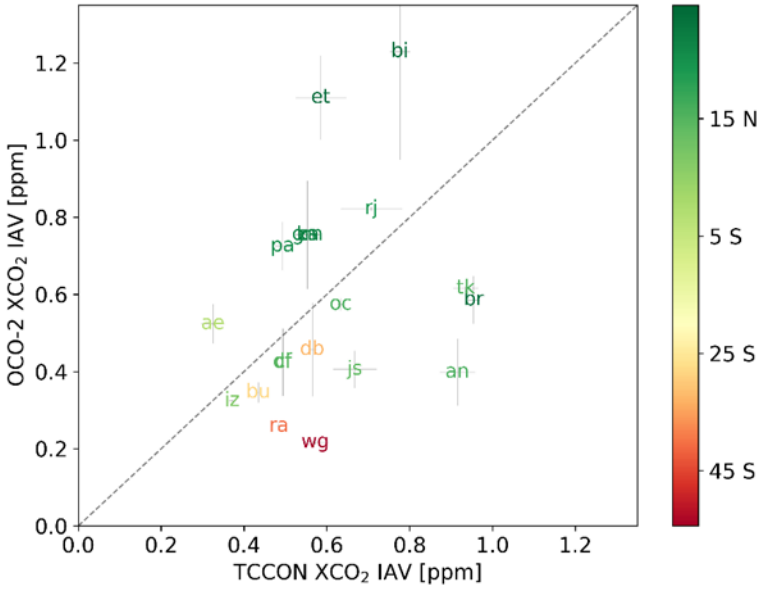

Figure 2.12: *Comparison of OCO-2 and TCCON XCO_2 IAV amplitude at individual sites. Colours reflect site latitudes. The grey dashed line is the one-to-one identity line. The grey solid line is the error bar of the IAV amplitude.*

2.4 Discussion

We use seven years of OCO-2 total column carbon dioxide observations from late 2014 to mid-2021 to illustrate the global temporal-spatial patterns of atmospheric XCO_2 interannual variations. OCO-2 and GOSAT showed reasonable agreement (Fig 2.4) in northern and southern hemisphere tropical zones (0-20°), although there were some notable phase differences during the strong 2015 El Niño for GOSAT compared to the other timeseries in both the northern and southern extratropic regions. In contrast, OCO-2 shows good temporal agreement with the ground-based observations from MBL and TCCON. The temporal agreement of the OCO-2 and

TCCON XCO_2 IAV timeseries and the MBL surface CO_2 IAV timeseries in broad zonal belts improves our confidence that we can quantify IAV timeseries from the satellite record. We note that amplitude differences remain among the timeseries, owing to two major factors: first, compared to MBL surface observations, we expect XCO_2 timeseries to have smaller amplitudes of variability since it integrates over the entire atmospheric column (Olsen and Randerson 2004), and second, the fact that the OCO-2 timeseries averages around a full latitude circle rather than a few discrete sites reduces some of the IAV contained in site-level records. From the space-based and ground-based detection, we are able to characterize the global response of OCO-2 and TCCON XCO_2 or MBL surface CO_2 IAV to ENSO, and track the CO_2 IAV against the positive/negative phase of ENSO, together with the transport of the signal from South to North (Fig 2.4). All datasets show consistent patterns in the response to the El Niño periods, although we note that the IAV amplitude is a factor of almost two smaller in the column average mole fraction compared to the boundary layer CO_2, which reflects the fact that IAV variations emerge due to surface fluxes in the lower part of the atmosphere (Olsen & Randerson, 2004), but are efficiently transported into the free troposphere which comprises the bulk of the column. When taken together, the use of surface and column data may allow better separation of transport-driven versus local flux driven variations at the interannual timescale. In the future, as partial column retrievals (e.g., Kulawik et al., 2017) mature, intercomparisons of lowermost tropospheric partial columns may provide a useful bridge between variations in surface MBL observations and total column observations.

Our results, however, underscore the difficulty in detecting IAV signals from remote sensing of XCO_2 -- while northern hemisphere seasonal amplitudes are typically 10 ppm scale (Basu et al., 2011), the magnitude of OCO-2 detected XCO_2 IAV is almost an order of

magnitude smaller (less than 0.4 ppm over ocean and about 1ppm over continents). The magnitude of IAV is therefore comparable to other components of the XCO_2 variance budget; for instance, Torres et al. (2019) show random noise in individual OCO-2 soundings of about 0.3 ppm in the southern hemisphere and of about 0.7 ppm in the northern hemisphere, and spatially coherent errors in the retrievals ranging from 0.3 to 0.8 ppm (Torres et al., 2019). Moreover, the uncertainty which originally comes from the varying climatological seasonal cycle, can also reach the level of 0.5ppm (Fig 2.3d). Therefore, robust partitioning of IAV from the observed XCO_2 signal at a given location requires a comprehensive variance budget (Mitchell et al., 2023), and efforts to infer interannual variations in fluxes from OCO-2 must take gridcell-level variance into account or leverage zonally averaged data, which is characterized by greater separation between IAV signal and noise.

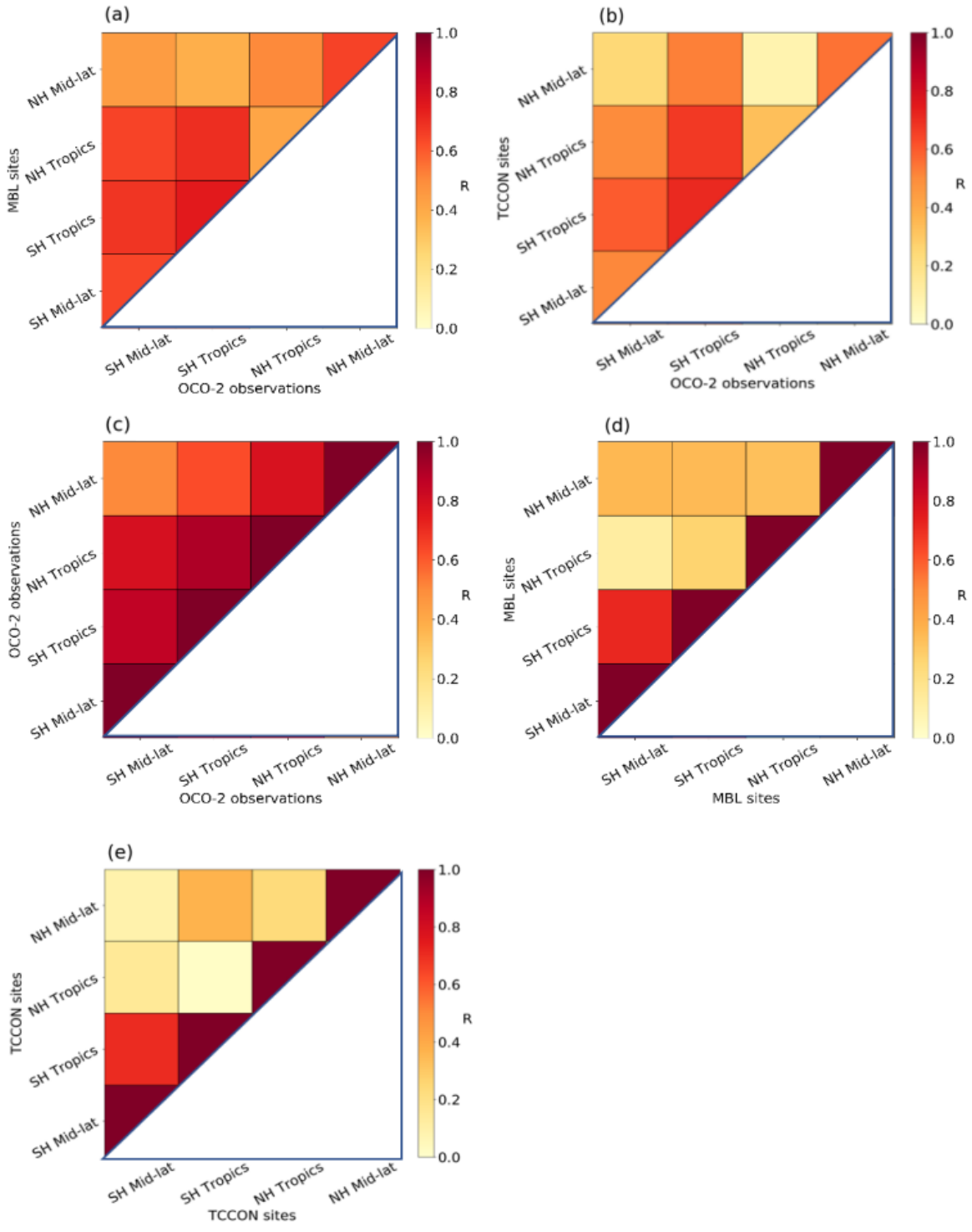

Figure 2.13: *Correlation coefficient (R) between among mean CO_2 timeseries using three observing strategies. Panel (a) shows the correlation between zonal mean OCO-2 XCO_2 IAV and zonal mean marine boundary layer CO_2. Panel (b) shows the correlation between zonal mean XCO_2 IAV from OCO-2 and TCCON. Panels (c-e) show the correlation in zonal mean IAV timeseries across four latitude bands for a single observing strategy. Panel (c) shows OCO-2 XCO_2, Panel (d) shows MBL CO_2 and Panel (e)*

shows TCCON XCO_2. For Panels c-e, the diagonal elements are 1 by construction. Zonal bands include tropical (0°-20°) and NH/SH temperate zone (20°-60°).

Our analysis shows that proper spatial averaging of the monthly XCO_2 signal can mitigate the imprint of random noise and systematic effects from weather systems at sub-monthly timescales. Based on sensitivity tests, we recommend averaging low to mid-latitude of XCO_2 (equatorward of 45°) to 5°x5° bins, and 5° latitude x 10° longitude grid cell poleward of 45°, ensuring that each gridcell aggregates at least 5 soundings within a month. At these levels of spatial averaging, the XCO_2 IAV amplitude was comparable to that of the co-located ground based XCO_2 IAV amplitude measured by TCCON (Fig 2.12). However, the moderate to low correlation between the IAV timeseries from each monitoring platform reveals the discrepancies of the two measurements in sampling, detection or retrieval, suggesting that one or both is still convolving another source of variance with the calculated IAV signal. Based on the good agreement between the two timeseries in broad zonal belts, we expect that random noise in both observations may degrade the comparison.

The smaller coherence in the IAV timeseries in nearby land and ocean gridcells may be due to larger error over land or may reflect that XCO_2 observations over land contain information about heterogeneous local flux IAV. Complete analysis of the variance budget for OCO-2 observations (Mitchell et al., 2023) will elucidate the likely imprint of each process. When using IAV timeseries for flux inference, it will be crucial to account for non-flux imprints such as imprint from atmospheric transport, random errors, systematic errors, and remote geophysical coherence on the timeseries (e.g., Torres et al., 2019; Mitchell et al., 2023), since spurious attribution of IAV will lead to biased fluxes.

2.5 Conclusions

We examined IAV in OCO-2 data to determine whether the small variations that result from interannual flux variations can be detected in light of other sources of variance in the space-based dataset. Our results show that zonal averages reveal relationships with ENSO that are consistent with those from established ground-based monitoring network. Zonal averages greatly reduce random noise in XCO_2 compared to 5x5^o averages. In general, OCO-2 can successfully monitor CO_2 IAV over both land and ocean, contributing important spatial coverage beyond inferences of IAV from existing ground-based networks.

2.6 References

Baker, D. F., Bell, E., Davis, K. J., Campbell, J. F., Lin, B., and Dobler, J.: A new exponentially decaying error correlation model for assimilating OCO-2 column-average CO_2 data using a length scale computed from airborne lidar measurements, Geosci. Model Dev., 15, 649–668, https://doi.org/10.5194/gmd-15-649-2022, 2022.

Basu, S., Houweling, S., Peters, W., Sweeney, C., Machida, T., Maksyutov, S., Patra, P. K., Saito, R., Chevallier, F., Niwa, Y., Matsueda, H., and Sawa, Y.: The seasonal cycle amplitude of total column CO_2: Factors behind the model-observation mismatch, J. Geophys. Res.-Atmos., 116, D23306, https://doi.org/10.1029/2011JD016124, 2011.

Blumenstock, T., Hase, F., Schneider, M., García, O. E., and Sepúlveda, E.: TCCON data from Izana (ES), Release GGG2014.R1 (R1), https://doi.org/10.14291/TCCON. GGG2014.IZANA01.R1, 2017.

Chatterjee, A., Gierach, M. M., Sutton, A. J., Feely, R. A., Crisp, D., Eldering, A., Gunson, M. R., O'Dell, C. W., Stephens, B. B., and Schimel, D. S.: Influence of El Niño on atmospheric CO_2 over the tropical Pacific Ocean: Findings from NASA's OCO-2 mission, Science, 358, eaam5776, https://doi.org/10.1126/science.aam5776, 2017.

Ciais, P., Sabine, C., Bala, G., and Peters, W.: Carbon and Other Biogeochemical Cycles, in: Climate Change 2013: The Physical Science Basis. Contribution of Working Group I to the Fifth Assessment Report of the Intergovernmental Panel on Climate Change, Cambridge University Press, 465–570, https://doi.org/10.1017/CBO9781107415324.015, 2013.

Cogan, A. J., Boesch, H., Parker, R. J., Feng, L., Palmer, P. I., Blavier, J.-F. L., Deutscher, N. M., Macatangay, R., Notholt, J., Roehl, C., Warneke, T., and Wunch, D.: Atmospheric carbon dioxide retrieved from the Greenhouse gases Observing SATellite (GOSAT):

Comparison with ground-based TCCON observations and GEOS-Chem model calculations, J. Geophys. Res.-Atmos., 117, D21301, https://doi.org/10.1029/2012JD018087, 2012.

Conway, T. J., Tans, P. P., Waterman, L. S., Thoning, K. W., Kitzis, D. R., Masarie, K. A., and Zhang, N.: Evidence for interannual variability of the carbon cycle from the National Oceanic and Atmospheric Administration/Climate Monitoring and Diagnostics Laboratory Global Air Sampling Network, J. Geophys. Res.-Atmos., 99, 22831-22855, https://doi.org/10.1029/94JD01951, 1994.

Crisp, D., Fisher, B. M., O'Dell, C., Frankenberg, C., Basilio, R., Bösch, H., Brown, L. R., Castano, R., Connor, B., Deutscher, N. M., Eldering, A., Griffith, D., Gunson, M., Kuze, A., Mandrake, L., McDuffie, J., Messerschmidt, J., Miller, C. E., Morino, I., Natraj, V., Notholt, J., O'Brien, D. M., Oyafuso, F., Polonsky, I., Robinson, J., Salawitch, R., Sherlock, V., Smyth, M., Suto, H., Taylor, T. E., Thompson, D. R., Wennberg, P. O., Wunch, D., and Yung, Y. L.: The ACOS CO_2 retrieval algorithm – Part II: Global data characterization, Atmos. Meas. Tech., 5, 687–707, https://doi.org/10.5194/amt-5-687-2012, 2012.

Crisp, D., Pollock, H. R., Rosenberg, R., Chapsky, L., Lee, R. A. M., Oyafuso, F. A., Frankenberg, C., O'Dell, C. W., Bruegge, C. J., Doran, G. B., Eldering, A., Fisher, B. M., Fu, D., Gunson, M. R., Mandrake, L., Osterman, G. B., Schwandner, F. M., Sun, K., Taylor, T. E., Wennberg, P. O., and Wunch, D.: The on-orbit performance of the Orbiting Carbon Observatory-2 (OCO-2) instrument and its radiometrically calibrated products, Atmos. Meas. Tech., 10, 59–81, https://doi.org/10.5194/amt-10-59-2017, 2017.

De Mazière, M., Sha, M. K., Desmet, F., Hermans, C., Scolas, F., Kumps, N., Metzger, J.-M., Duflot, V., and Cammas, J.-P.: TCCON data from Réunion Island (RE), Release GGG2014.R1 (R1), https://doi.org/10.14291/TCCON.GGG2014.REUNION01.R1, 2017.

Deutscher, N. M., Griffith, D. W. T., Bryant, G. W., Wennberg, P. O., Toon, G. C., Washenfelder, R. A., Keppel-Aleks, G., Wunch, D., Yavin, Y., Allen, N. T., Blavier, J.-F., Jiménez, R., Daube, B. C., Bright, A. V., Matross, D. M., Wofsy, S. C., and Park, S.: Total column CO_2measurements at Darwin, Australia – site description and calibration against in situ aircraft profiles, Atmospheric Measurement Techniques, 3, 947–958, https://doi.org/10.5194/amt-3-947-2010, 2010.

Deutscher, N. M., Notholt, J., Messerschmidt, J., Weinzierl, C., Warneke, T., Petri, C., and Grupe, P.: TCCON data from Bialystok (PL), Release GGG2014.R2 (R2), https://doi.org/ 10.14291/TCCON.GGG2014.BIALYSTOK01.R2, 2019.

Dlugokencky, E. J., Crotwell, A. M., Mund, J. W., Crotwell, M. J., and Thoning, K. W.: Atmospheric Nitrous Oxide Dry Air Mole Fractions from the NOAA GML Carbon Cycle Cooperative Global Air Sampling Network, 1997–2020, Version: 2021-07-30, NOAA Global Monitoring Laboratory Data Repository [data set], https://doi.org/10.14291/TCCON. GGG2014.BIALYSTOK01.R2, 2021.

Doney, S. C., Lima, I., Feely, R. A., Glover, D. M., Lindsay, K., Mahowald, N., Moore, J. K., and Wanninkhof, R.: Mechanisms governing interannual variability in upper-ocean inorganic carbon system and air–sea CO_2 fluxes: Physical climate and atmospheric dust, Deep-Sea Res. Pt. II, 56, 640–655, https://doi.org/10.1016/j.dsr2.2008.12.006, 2009.

Eldering, A., O'Dell, C. W., Wennberg, P. O., Crisp, D., Gunson, M. R., Viatte, C., Avis, C., Braverman, A., Castano, R., Chang, A., Chapsky, L., Cheng, C., Connor, B., Dang, L., Doran, G., Fisher, B., Frankenberg, C., Fu, D., Granat, R., Hobbs, J., Lee, R. A. M., Mandrake, L., McDuffie, J., Miller, C. E., Myers, V., Natraj, V., O'Brien, D., Osterman, G. B., Oyafuso, F., Payne, V. H., Pollock, H. R., Polonsky, I., Roehl, C. M., Rosenberg, R., Schwandner, F., Smyth, M., Tang, V., Taylor, T. E., To, C., Wunch, D., and Yoshimizu, J.: The Orbiting Carbon Observatory-2: first 18 months of science data products, Atmos. Meas. Tech., 10, 549–563, https://doi.org/10.5194/amt-10-549-2017, 2017.

Feely, R. A., Boutin, J., Cosca, C. E., Dandonneau, Y., Etcheto, J., Inoue, H. Y., Ishii, M., Quéré, C. L., Mackey, D. J., McPhaden, M., Metzl, N., Poisson, A., and Wanninkhof, R.: Seasonal and interannual variability of CO_2 in the equatorial Pacific, Deep-Sea Res. Pt. II, 49, 2443–2469, https://doi.org/10.1016/S0967-0645(02)00044-9, 2002.

Feist, D. G., Arnold, S. G., John, N., and Geibel, M. C.: TCCON data from Ascension Island (SH), Release GGG2014.R0 (GGG2014.R0),https://doi.org/10.14291/TCCON.GGG2014. ASCENSION01.R0/1149285, 2014.

Friedlingstein, P., Jones, M. W., O'Sullivan, M., Andrew, R. M., Hauck, J., Peters, G. P., Peters, W., Pongratz, J., Sitch, S., Le Quéré, C., Bakker, D. C. E., Canadell, J. G., Ciais, P., Jackson, R. B., Anthoni, P., Barbero, L., Bastos, A., Bastrikov, V., Becker, M., Bopp, L., Buitenhuis, E., Chandra, N., Chevallier, F., Chini, L. P., Currie, K. I., Feely, R. A., Gehlen, M., Gilfillan, D., Gkritzalis, T., Goll, D. S., Gruber, N., Gutekunst, S., Harris, I., Haverd, V., Houghton, R. A., Hurtt, G., Ilyina, T., Jain, A. K., Joetzjer, E., Kaplan, J. O., Kato, E., Klein Goldewijk, K., Korsbakken, J. I., Landschützer, P., Lauvset, S. K., Lefèvre, N., Lenton, A., Lienert, S., Lombardozzi, D., Marland, G., McGuire, P. C., Melton, J. R., Metzl, N., Munro, D. R., Nabel, J. E. M. S., Nakaoka, S.-I., Neill, C., Omar, A. M., Ono, T., Peregon, A., Pierrot, D., Poulter, B., Rehder, G., Resplandy, L., Robertson, E., Rödenbeck, C., Séférian, R., Schwinger, J., Smith, N., Tans, P. P., Tian, H., Tilbrook, B., Tubiello, F. N., van der Werf, G. R., Wiltshire, A. J., and Zaehle, S.: Global Carbon Budget 2019, Earth Syst. Sci. Data, 11, 1783–1838, https://doi.org/10.5194/essd-11-1783-2019, 2019.

GES DISC: OCO-2 Level 2 bias-corrected XCO_2 and other select fields from the full-physics retrieval aggregated as daily files, Retrospective processing V10r (OCO_2_L2_Lite_FP 10r), GES DISC [data set], https://disc.gsfc.nasa.gov/datasets/OCO_2_L2_Lite_FP_10r/summary?keywords=OCO-2, last access: 1 March 2022.

Goo, T.-Y., Oh, Y.-S., and Velazco, V. A.: TCCON data from Anmeyondo (KR), Release GGG2014.R0 (GGG2014.R0),https://doi.org/10.14291/TCCON.GGG2014.ANMEYONDO01. R0/1149284, 2014.

Griffith, D. W. T., Deutscher, N. M., Velazco, V. A., Wennberg, P. O., Yavin, Y., Keppel-Aleks, G., Washenfelder, R. A., Toon, G. C., Blavier, J.-F., Paton-Walsh, C., Jones, N. B., Kettlewell, G. C., Connor, B. J., Macatangay, R. C., Roehl, C., Ryczek, M., Glowacki, J., Culgan, T., and Bryant, G. W.: TCCON data from Darwin (AU), Release GGG2014.R0 (GGG2014.R0), https://doi.org/10.14291/TCCON.GGG2014.DARWIN01.R0/1149290, 2014a.

Griffith, D. W. T., Velazco, V. A., Deutscher, N. M., Paton-Walsh, C., Jones, N. B., Wilson, S. R., Macatangay, R. C., Kettlewell, G. C., Buchholz, R. R., and Riggenbach, M. O.: TCCON data from Wollongong (AU), Release GGG2014.R0 (GGG2014.R0),https://doi.org/10.14291/TCCON.GGG2014. WOLLONGONG01.R0/1149291, 2014b.

Gurney, K. R., Baker, D., Rayner, P., and Denning, S.: Interannual variations in continental-scale net carbon exchange and sensitivity to observing networks estimated from atmospheric CO_2 inversions for the period 1980 to 2005, Global Biogeochem. Cy., 22, GB3025, https://doi.org/10.1029/2007GB003082, 2008.

Hase, F., Blumenstock, T., Dohe, S., Groß, J., and Kiel, M. ä.: TCCON data from Karlsruhe (DE), Release GGG2014.R1 (GGG2014.R1),https://doi.org/10.14291/TCCON.GGG2014. KARLSRUHE01.R1/1182416, 2015.

IPCC: Carbon and Other Biogeochemical Cycles, https://www.ipcc.ch/report/ar5/wg1/carbon-and-other-biogeochemical-cycles/, last access: 4 April 2023.

Iraci, L. T., Podolske, J. R., Hillyard, P. W., Roehl, C., Wennberg, P. O., Blavier, J.-F., Landeros, J., Allen, N., Wunch, D., Zavaleta, J., Quigley, E., Osterman, G. B., Albertson, R., Dunwoody, K., and Boyden, H.: TCCON data from Edwards (US), Release GGG2014.R1 (GGG2014.R1), https://doi.org/10.14291/TCCON.GGG2014.EDWARDS01.R1/ 1255068, 2016.

Japan Aerospace Exploration Agency (JAXA), National Institute for Environmental Studies (NIES) and Ministry of the Environment (MOE): Data products distributed from GOSAT DHF, GOSAT [data set], https://www.gosat.nies.go.jp/en/about_5_products.html, last access: 5 August 2022.

Karion, A., Sweeney, C., Tans, P., and Newberger, T.: AirCore: An Innovative Atmospheric Sampling System, J. Atmos. Ocean. Tech., 27, 1839–1853, https://doi.org/10.1175/2010JTECHA1448.1, 2010.

Kawakami, S., Ohyama, H., Arai, K., Okumura, H., Taura, C., Fukamachi, T., and Sakashita, M.: TCCON data from Saga (JP), Release GGG2014.R0 (GGG2014.R0), https://doi.org/10.14291/ TCCON.GGG2014.SAGA01.R0/1149283, 2014.

Keppel-Aleks, G., Wolf, A. S., Mu, M., Doney, S. C., Morton, D. C., Kasibhatla, P. S., Miller, J. B., Dlugokencky, E. J., and Randerson, J. T.: Separating the influence of temperature, drought, and fire on interannual variability in atmospheric CO_2, Global Biogeochem. Cy., 28, 1295–1310, https://doi.org/10.1002/2014GB004890, 2014.

Kivi, R., Heikkinen, P., and Kyrö, E.: TCCON data from Sodankylä (FI), Release GGG2014.R1 (R1), https://doi.org/10.14291/TCCON.GGG2014.SODANKYLA01.R1, 2022.

Kulawik, S., Wunch, D., O'Dell, C., Frankenberg, C., Reuter, M., Oda, T., Chevallier, F., Sherlock, V., Buchwitz, M., Osterman, G., Miller, C. E., Wennberg, P. O., Griffith, D., Morino, I., Dubey, M. K., Deutscher, N. M., Notholt, J., Hase, F., Warneke, T., Sussmann, R., Robinson, J., Strong, K., Schneider, M., De Mazière, M., Shiomi, K., Feist, D. G., Iraci, L. T., and Wolf, J.: Consistent evaluation of ACOS-GOSAT, BESD-SCIAMACHY, CarbonTracker, and MACC through comparisons to TCCON, Atmos. Meas. Tech., 9, 683–709, https://doi.org/10.5194/amt-9-683-2016, 2016.

Kulawik, S. S., O'Dell, C., Payne, V. H., Kuai, L., Worden, H. M., Biraud, S. C., Sweeney, C., Stephens, B., Iraci, L. T., Yates, E. L., and Tanaka, T.: Lower-tropospheric CO_2 from near-infrared ACOS-GOSAT observations, Atmos. Chem. Phys., 17, 5407–5438, https://doi.org/10.5194/acp-17-5407-2017, 2017.

Le Quéré, C., Raupach, M. R., Canadell, J. G., Marland, G., Bopp, L., Ciais, P., Conway, T. J., Doney, S. C., Feely, R. A., Foster, P., Friedlingstein, P., Gurney, K., Houghton, R. A., House, J. I., Huntingford, C., Levy, P. E., Lomas, M. R., Majkut, J., Metzl, N., Ometto, J. P., Peters, G. P., Prentice, I. C., Randerson, J. T., Running, S. W., Sarmiento, J. L., Schuster, U., Sitch, S., Takahashi, T., Viovy, N., van der Werf, G. R., and Woodward, F. I.: Trends in the sources and sinks of carbon dioxide, Nat. Geosci., 2, 831–836, https://doi.org/10.1038/ngeo689, 2009.

Marcolla, B., Rödenbeck, C., and Cescatti, A.: Patterns and controls of inter-annual variability in the terrestrial carbon budget, Biogeosciences, 14, 3815–3829, https://doi.org/10.5194/bg-14-3815-2017, 2017.

Masarie, K. A. and Tans, P. P.: Extension and integration of atmospheric carbon dioxide data into a globally consistent measurement record, J. Geophys. Res.-Atmos., 100, 11593–11610, https://doi.org/10.1029/95JD00859, 1995.

McKinley, G. A., Rödenbeck, C., Gloor, M., Houweling, S., and Heimann, M.: Pacific dominance to global air-sea CO_2 flux variability: A novel atmospheric inversion agrees with ocean models, Geophys. Res. Lett., 31, L22308, https://doi.org/10.1029/2004GL021069, 2004.

Messerschmidt, J., Macatangay, R., Notholt, J., Petri, C., Warneke, T., and Weinzierl, C.: Side by side measurements of CO_2 by ground-based Fourier transform spectrometry (FTS), 62, 749–758, https://doi.org/10.1111/j.1600-0889.2010.00491.x, 2010.

Mitchell, K. A., Doney, S. C., and Keppel-Aleks, G.: Characterizing Average Seasonal, Synoptic, and Finer Variability in Orbiting Carbon Observatory-2 XCO_2 Across North America and Adjacent Ocean Basins, J. Geophys. Res.-Atmos., 128, e2022JD036696, https://doi.org/10.1029/2022JD036696, 2023.

Morino, I., Matsuzaki, T., and Horikawa, M.: TCCON data from Tsukuba (JP), 125HR, Release GGG2014.R1 (GGG2014.R1),https://doi.org/10.14291/TCCON.GGG2014.TSUKUBA02.R1/ 1241486, 2016a.

Morino, I., Yokozeki, N., Matsuzaki, T., and Horikawa, M.: TCCON data from Rikubetsu (JP), Release GGG2014.R1 (GGG2014.R1),https://doi.org/10.14291/TCCON.GGG2014. RIKUBETSU01.R1/12422 65, 2016b.

Morino, I., Velazco, V. A., Hori, A., Uchino, O., and Griffith, D. W. T.: TCCON data from Burgos, Ilocos Norte (PH), Release GGG2020.R0 (R0), https://doi.org/10.14291/TCCON. GGG2020.BURGOS01.R0, 2023.

Mudelsee, M.: Climate Time Series Analysis, Springer Netherlands, Dordrecht, https://doi.org/10.1007/978-90-481-9482-7, 2010.

Nassar, R., Jones, D. B. A., Kulawik, S. S., Worden, J. R., Bowman, K. W., Andres, R. J., Suntharalingam, P., Chen, J. M., Brenninkmeijer, C. A. M., Schuck, T. J., Conway, T. J., and Worthy, D. E.: Inverse modeling of CO_2 sources and sinks using satellite observations of CO_2 from TES and surface flask measurements, Atmos. Chem. Phys., 11, 6029–6047, https://doi.org/10.5194/acp-11-6029-2011, 2011.

NOAA GML CCGG Group: NOAA Global Greenhouse Gas Reference Network Continuous Insitu Measurements of CO_2, CH_4, and CO at Global Background Sites, 1973–Present, Global Monitoring Laboratory [data set], https://doi.org/10.15138/YAF1-BK21, 2019.

Notholt, J., Warneke, T., Petri, C., Deutscher, N. M., Weinzierl, C., Palm, M., and Buschmann, M.: TCCON data from Ny Ålesund, Spitsbergen (NO), Release GGG2014.R1 (R1), https://doi. org/10.14291/TCCON.GGG2014.NYALESUND01.R1, 2019a.

Notholt, J., Petri, C., Warneke, T., Deutscher, N. M., Palm, M., Buschmann, M., Weinzierl, C., Macatangay, R. C., and Grupe, P.: TCCON data from Bremen (DE), Release GGG2014.R1 (R1), https://doi.org/10.14291/TCCON.GGG2014.BREMEN01.R1, 2019b.

O'Dell, C. W., Eldering, A., Wennberg, P. O., Crisp, D., Gunson, M. R., Fisher, B., Frankenberg, C., Kiel, M., Lindqvist, H., Mandrake, L., Merrelli, A., Natraj, V., Nelson, R. R., Osterman, G. B., Payne, V. H., Taylor, T. E., Wunch, D., Drouin, B. J., Oyafuso, F., Chang, A., McDuffie, J., Smyth, M., Baker, D. F., Basu, S., Chevallier, F., Crowell, S. M. R., Feng, L., Palmer, P. I., Dubey, M., García, O. E., Griffith, D. W. T., Hase, F., Iraci, L. T., Kivi, R., Morino, I., Notholt, J., Ohyama, H., Petri, C., Roehl, C. M., Sha, M. K., Strong, K., Sussmann, R., Te, Y., Uchino, O., and Velazco, V. A.: Improved retrievals of carbon dioxide from Orbiting Carbon Observatory-2 with the version 8 ACOS algorithm, Atmos. Meas. Tech., 11, 6539–6576, https://doi.org/10.5194/amt-11-6539-2018, 2018.

Olsen, S. C. and Randerson, J. T.: Differences between surface and column atmospheric CO_2 and implications for carbon cycle research, J. Geophys. Res.-Atmos., 109, D02301, https://doi.org/10.1029/2003JD003968, 2004.

Patra, P. K., Maksyutov, S., Ishizawa, M., Nakazawa, T., Takahashi, T., and Ukita, J.: Interannual and decadal changes in the sea-air CO_2 flux from atmospheric CO_2 inverse modeling, Global Biogeochem. Cy., 19, GB4013, https://doi.org/10.1029/2004GB002257, 2005.

Peters, G. P., Le Quéré, C., Andrew, R. M., Canadell, J. G., Friedlingstein, P., Ilyina, T., Jackson, R. B., Joos, F., Korsbakken, J. I., McKinley, G. A., Sitch, S., and Tans, P.: Towards real-time verification of CO_2 emissions, Nature Clim. Change, 7, 848–850, https://doi.org/10.1038/s41558-017-0013-9, 2017

Peylin, P., Law, R. M., Gurney, K. R., Chevallier, F., Jacobson, A. R., Maki, T., Niwa, Y., Patra, P. K., Peters, W., Rayner, P. J., Rödenbeck, C., van der Laan-Luijkx, I. T., and Zhang, X.: Global atmospheric carbon budget: results from an ensemble of atmospheric CO_2inversions, Biogeosciences, 10, 6699–6720, https://doi.org/10.5194/bg-10-6699-2013, 2013.

Piao, S., Fang, J., Ciais, P., Peylin, P., Huang, Y., Sitch, S., and Wang, T.: The carbon balance of terrestrial ecosystems in China, Nature, 458, 1009–1013, https://doi.org/10.1038/nature07944, 2009.

Piao, S., Wang, X., Wang, K., Li, X., Bastos, A., Canadell, J. G., Ciais, P., Friedlingstein, P., and Sitch, S.: Interannual variation of terrestrial carbon cycle: Issues and perspectives, Glob. Change Biol., 26, 300–318, https://doi.org/10.1111/gcb.14884, 2020.

Prentice, I., Farquhar, G., Fasham, M., Goulden, M., Heimann, M., Jaramillo, V., Kheshgi, H., Le Quéré, C., Scholes, R., and Wallace, D.: The carbon cycle and atmospheric carbon dioxide, in: Climate Change 2001: The Scientific Basis, edited by: Houghton, J. T., Ding, Y., Griggs, D. J., Noguer, M., Linden, P. J. van der, Dai, X., Maskell, K., and Johnson, C. A., Cambridge University Press, 183–237, 2001.

Schwalm, C. R., Williams, C. A., Schaefer, K., Baker, I., Collatz, G. J., and Rödenbeck, C.: Does terrestrial drought explain global CO_2flux anomalies induced by El Niño?, Biogeosciences, 8, 2493–2506, https://doi.org/10.5194/bg-8-2493-2011, 2011.

Sherlock, V., Connor, B., Robinson, J., Shiona, H., Smale, D., and Pollard, D. F.: TCCON data from Lauder (NZ), 125HR, Release GGG2014.R0 (GGG2014.R0), https://doi.org/10.14291/ TCCON.GGG2014.LAUDER02.R0/1149298, 2014.

Strong, K., Roche, S., Franklin, J. E., Mendonca, J., Lutsch, E., Weaver, D., Fogal, P. F., Drummond, J. R., Batchelor, R., and Lindenmaier, R.: TCCON data from Eureka (CA), Release GGG2014.R2 (R2), https://doi.org/10.14291/TCCON.GGG2014.EUREKA01.R2, 2017.

Sussmann, R. and Rettinger, M.: TCCON data from Garmisch (DE), Release GGG2014.R1 (R1), https://doi.org/10.14291/TCCON.GGG2014.GARMISCH01.R1, 2017.

Sussmann, R. and Rettinger, M.: TCCON data from Zugspitze (DE), Release GGG2014.R1 (R1), https://doi.org/10.14291/TCCON.GGG2014.ZUGSPITZE01.R1, 2018.

Sussmann, R. and Rettinger, M.: Can We Measure a COVID-19-Related Slowdown in Atmospheric CO_2 Growth? Sensitivity of Total Carbon Column Observations, Remote Sens.-Basel, 12, 2387, https://doi.org/10.3390/rs12152387, 2020.

Té, Y., Jeseck, P., and Janssen, C.: TCCON data from Paris (FR), Release GGG2014.R0 (GGG2014.R0), https://doi.org/10.14291/TCCON.GGG2014.PARIS01.R0/1149279, 2014.

Thoning, K. W., Tans, P. P., and Komhyr, W. D.: Atmospheric carbon dioxide at Mauna Loa Observatory: 2. Analysis of the NOAA GMCC data, 1974–1985, J. Geophys. Res.-Atmos., 94, 8549–8565, https://doi.org/10.1029/JD094iD06p08549, 1989.

Timmermann, A., An, S. I., Kug, J. S., Jin, F. F., Cai, W., Capotondi, A., Cobb, K. M., Lengaigne, M., McPhaden, M. J., Stuecker, M. F., Stein, K., Wittenberg, A. T., Yun, K. S., Bayr, T., Chen, H. C., Chikamoto, Y., Dewitte, B., Dommenget, D., Grothe, P., Guilyardi, E., Ham, Y. G., Hayashi, M., Ineson, S., Kang, D., Kim, S., Kim, W. M., Lee, J. Y., Li, T., Luo, J. J., McGregor, S., Planton, Y., Power, S., Rashid, H., Ren, H. L., Santoso, A., Takahashi, K., Todd, A., Wang, G., Wang, G., Xie, R., Yang, W. H., Yeh, S. W., Yoon, J., Zeller, E., and Zhang, X.: El Niño–Southern Oscillation complexity, Nature, 559, 535–545, https://doi.org/10.1038/s41586-018-0252-6, 2018.

Torres, A. D., Keppel-Aleks, G., Doney, S. C., Fendrock, M., Luis, K., De Mazière, M., Hase, F., Petri, C., Pollard, D. F., Roehl, C. M., Sussmann, R., Velazco, V. A., Warneke, T., and Wunch, D.: A Geostatistical Framework for Quantifying the Imprint of Mesoscale Atmospheric Transport on Satellite Trace Gas Retrievals, J. Geophys. Res.-Atmos., 124, 9773–9795, https://doi.org/10.1029/2018JD029933, 2019.

Total Carbon Column Observing Network (TCCON) Team: 2014 TCCON Data Release (GGG2014), Caltech Data [data set], https://doi.org/10.14291/TCCON.GGG2014, 2017.

Wang, X., Piao, S., Ciais, P., Friedlingstein, P., Myneni, R. B., Cox, P., Heimann, M., Miller, J., Peng, S., Wang, T., Yang, H., and Chen, A.: A two-fold increase of carbon cycle sensitivity to tropical temperature variations, Nature, 506, 212–215, https://doi.org/10.1038/nature12915, 2014.

Warneke, T., Messerschmidt, J., Notholt, J., Weinzierl, C., Deutscher, N. M., Petri, C., and Grupe, P.: TCCON data from Orléans (FR), Release GGG2014.R1 (R1), https://doi.org/10.14291/TCCON.GGG2014.ORLEANS01.R1, 2019.

Washenfelder, R. A., Toon, G. C., Blavier, J.-F., Yang, Z., Allen, N. T., Wennberg, P. O., Vay, S. A., Matross, D. M., and Daube, B. C.: Carbon dioxide column abundances at the Wisconsin Tall Tower site, J. Geophys. Res.-Atmos., 111, D22305, https://doi.org/10.1029/2006JD007154, 2006.

Wennberg, P. O., Wunch, D., Roehl, C. M., Blavier, J.-F., Toon, G. C., and Allen, N. T.: TCCON data from Caltech (US), Release GGG2014.R1 (GGG2014.R1), https://doi.org/10.14291/ TCCON.GGG2014.PASADENA01.R1/11824 15, 2015.

Wennberg, P. O., Wunch, D., Roehl, C. M., Blavier, J.-F., Toon, G. C., and Allen, N. T.: TCCON data from Lamont (US), Release GGG2014.R1 (GGG2014.R1), https://doi.org/10.14291/ TCCON.GGG2014.LAMONT01.R1/1255070, 2016.

Wennberg, P. O., Roehl, C. M., Wunch, D., Toon, G. C., Blavier, J.-F., Washenfelder, R., Keppel-Aleks, G., Allen, N. T., and Ayers, J.: TCCON data from Park Falls (US), Release GGG2014.R1 (GGG2014.R1), https://doi.org/10.14291/TCCON.GGG2014.PARKFALLS01.R1, 2017.

Wolter, K. and Timlin, M. S.: El Niño/Southern Oscillation behaviour since 1871 as diagnosed in an extended multivariate ENSO index (MEI.ext), International Journal of Climatology, 31, 1074–1087, https://doi.org/10.1002/joc.2336, 2011.

Wu, L., aan de Brugh, J., Meijer, Y., Sierk, B., Hasekamp, O., Butz, A., and Landgraf, J.: XCO_2 observations using satellite measurements with moderate spectral resolution: investigation using GOSAT and OCO-2 measurements, Atmos. Meas. Tech., 13, 713–729, https://doi.org/10.5194/amt-13-713-2020, 2020.

Wunch, D., Toon, G. C., Wennberg, P. O., Wofsy, S. C., Stephens, B. B., Fischer, M. L., Uchino, O., Abshire, J. B., Bernath, P., Biraud, S. C., Blavier, J.-F. L., Boone, C., Bowman, K. P., Browell, E. V., Campos, T., Connor, B. J., Daube, B. C., Deutscher, N. M., Diao, M., Elkins, J. W., Gerbig, C., Gottlieb, E., Griffith, D. W. T., Hurst, D. F., Jiménez, R., Keppel-Aleks, G., Kort, E. A., Macatangay, R., Machida, T., Matsueda, H.,

Moore, F., Morino, I., Park, S., Robinson, J., Roehl, C. M., Sawa, Y., Sherlock, V., Sweeney, C., Tanaka, T., and Zondlo, M. A.: Calibration of the Total Carbon Column Observing Network using aircraft profile data, Atmos. Meas. Tech., 3, 1351–1362, https://doi.org/10.5194/amt-3-1351-2010, 2010.

Wunch, D., Toon, G. C., Blavier, J.-F. L., Washenfelder, R. A., Notholt, J., Connor, B. J., Griffith, D. W. T., Sherlock, V., and Wennberg, P. O.: The total carbon column observing network, Philos. T. Roy. Soc. A, 369, 2087–2112, https://doi.org/10.1098/rsta.2010.0240, 2011.

Wunch, D., Toon, G. C., Sherlock, V., Deutscher, N. M., Liu, C., Feist, D. G., and Wennberg, P. O.: Documentation for the 2014 TCCON Data Release, https://doi.org/10.14291/TCCON. GGG2014.DOCUMENTATION.R0/1221662, 2015.

Wunch, D., Mendonca, J., Colebatch, O., Allen, N. T., Blavier, J.-F., Roche, S., Hedelius, J., Neufeld, G., Springett, S., Worthy, D., Kessler, R., and Strong, K.: TCCON data from East Trout Lake, SK (CA), Release GGG2014.R1 (R1), https://doi.org/10.14291/TCCON.GGG2014.EASTTROUTLAKE01.R1, 2018.

Yoshida, Y., Kikuchi, N., Morino, I., Uchino, O., Oshchepkov, S., Bril, A., Saeki, T., Schutgens, N., Toon, G. C., Wunch, D., Roehl, C. M., Wennberg, P. O., Griffith, D. W. T., Deutscher, N. M., Warneke, T., Notholt, J., Robinson, J., Sherlock, V., Connor, B., Rettinger, M., Sussmann, R., Ahonen, P., Heikkinen, P., Kyrö, E., Mendonca, J., Strong, K., Hase, F., Dohe, S., and Yokota, T.: Improvement of the retrieval algorithm for GOSAT SWIR XCO_2 and XCH_4 and their validation using TCCON data, Atmos. Meas. Tech., 6, 1533–1547, https://doi.org/10.5194/amt-6-1533-2013, 2013.

Zeng, N., Mariotti, A., and Wetzel, P.: Terrestrial mechanisms of interannual CO_2 variability: Interannual CO_2 Variability, Global Biogeochem. Cy., 19, GB1016, https://doi.org/10.1029/2004GB002273, 2005.

Chapter 3 Quantifying Atmospheric CO_2 Interannual Variability Driven by Ocean From OCO-2 Observations and Atmospheric Transport Simulations

Abstract

Interannual variability (IAV) in the atmospheric CO_2 growth rate is caused by variation in the balance between uptake by land and ocean and accumulation of anthropogenic emissions in the atmosphere. While variations in terrestrial fluxes are thought to drive most of the observed atmospheric CO_2 IAV, the ability to characterize ocean impacts has been limited by the fact that most sites in the surface CO_2 monitoring network are located on coasts or islands or within the continental interior. NASA's Orbiting Carbon-Observatory 2 (OCO-2) mission has observed the atmospheric total column carbon dioxide mole fraction (XCO_2) from space since September 2014. With a near-global coverage, this dataset provides a first opportunity to directly observe IAV in atmospheric CO_2 over remote ocean regions. We assess the impact of ocean flux IAV on the OCO-2 record using atmospheric transport simulations with underlying gridded air-sea CO_2 fluxes from observation-based products. We use three observation-based products to bracket the likely range of ocean air-sea flux contributions to XCO_2 variability (over both land and ocean) within the GEOS-Chem atmospheric transport model. We find that the magnitude of XCO_2 IAV generated by the whole ocean is between 0.1-1 ppm throughout the world. Depending on location and flux product, between 20-80% of the IAV from the ocean flux-GEOS-Chem simulations is caused by IAV in air-sea CO_2 fluxes, with the remainder due to IAV in atmospheric dynamics acting on climatological ocean flux-driven XCO_2 gradients. The Southern Hemisphere mid-latitudes and low-latitudes are the dominant ocean regions in generating the

XCO_2 IAV globally, showing substantial imprints on ocean-driven IAV in the Northern Hemisphere across all three flux products. Nevertheless, the small magnitude of the air-sea flux impacts on XCO_2 presents a substantial challenge for detection of ocean-driven IAV from OCO-2. Although the IAV amplitude arising from ocean fluxes and transport is 20 to 50% of the total observed XCO_2 IAV amplitude of 0.4 to 1.6 ppm in the Southern Hemisphere and the tropics, ocean-driven IAV represents only 10% of the observed amplitude in the Northern Hemisphere. We find that for all three products, the simulated ocean-driven XCO_2 IAV is weakly anti-correlated with OCO-2 observations, suggesting that even over ocean basins, terrestrial IAV obscures the ocean signal.

3.1 Introduction

The ocean regulates the uptake, storage, and release to the atmosphere of carbon on annual to millennial timescales, helping mitigate climate change by significantly modulating the long-term trend in the atmospheric CO_2 growth rate. The ocean took up on average, 3.0 ± 0.4 PgC yr^{-1} or 29% of the total anthropogenic CO_2 emissions for the decade beginning in 2011, and cumulatively has sequestered over 1/3 of fossil emissions since the industrial era (Le Quéré et al., 2018; Friedlingstein et al., 2022). When also taking into account land-use change emissions to the atmosphere, which counteracts the residual terrestrial sink, the ocean is the only long-term sink for anthropogenic carbon (Ballantyne et al., 2012, Crisp et al. 2022).

Interannual variability (IAV) in the atmospheric CO_2 growth rate is superimposed on the long-term positive trend. The atmospheric CO_2 surface network shows a decadal-average growth rate of 2.41±0.26 ppm/y (mean ± 2 std dev) on an annual basis due to the impacts of internal climate variability during 2003–2016 (Buchwitz et al., 2018). This IAV has been shown to reflect, primarily, variations in the rate of terrestrial CO_2 uptake due to climate stressors (Luo et

al., 2022) and disturbance (Keppel-Aleks et al., 2014), but also embodies IAV in net ocean carbon exchange and fossil fuel emissions (Doney et al., 2009, Crisp et al. 2022). The global ocean carbon flux IAV is estimated at about 0.3 PgC/yr (equivalent to about 0.15 ppm CO_2 mixed into the global atmosphere), with the tropical Pacific Ocean, which is modulated by El Niño-Southern Oscillation (ENSO), accounting for a large fraction of variability (Rodenbeck et al., 2014, Bennington et al. 2022). Considering only a global value, however, may obscure key regions of ocean flux IAV and its impact on spatial patterns of atmospheric CO_2 IAV.

The net flux of CO_2 between the atmosphere and the ocean is a function of (1) wind-driven gas exchange kinetic rates and (2) the difference of the partial pressure of CO_2 in the air and the ocean surface (ΔpCO_2), with the ocean component being far more regionally heterogeneous. Local variations in oceanic pCO_2 are related to physical or biogeochemical processes including sub-surface water upwelling, which can enrich the surface water in CO_2, temperature-driven solubility variations, alkalinity (which is closely related to salinity and controls the speciation of dissolved inorganic carbon), and phytoplankton photosynthesis and respiration (Doney et. al, 2009, Crisp et al. 2022). These variables are all affected by interannual climate variability (McKinley et al. 2020). Because the response of the global carbon cycle to climate fluctuations may provide insight into the long-term response to climate change, understanding the global and regional characteristics of ocean-driven atmosphere CO_2 IAV can help to improve our understanding of the climate–carbon cycle processes and our ability to project the fate of the ocean CO_2 sink in the future.

Although studies have suggested that ocean flux IAV may impart an observable impact on atmospheric CO_2 IAV (Crisp et al., 2022), gaps remain in quantifying the influence from the ocean since most atmospheric CO_2 observations are made on land and coasts, with fewer island

and ship-based measurements in the remote open ocean. Early research deduced that the CO_2 flux variation over the ocean, especially the equatorial Pacific Ocean, is one of the main causes of the atmospheric CO_2 IAV (Francey et al., 1995). Later studies based on inverse models, seawater system measurements, and air-sea CO_2 flux estimates (Rodenbeck et al., 2003; Feely et al., 2002) suggested air-sea CO_2 flux is not the primary driver for interannual to seasonal variations in atmospheric CO_2. Nevison et al. (2008) used an atmospheric transport model with an underlying mechanistic ocean flux model to show that the amplitude of atmospheric IAV owing to ocean fluxes was around 10% of the IAV amplitude at northern hemisphere surface stations, and up to 50% of the observed IAV in the Southern Hemisphere. In neither hemisphere, however, was the IAV owing to ocean fluxes highly correlated with the observations (Nevison et al., 2008). Setting aside uncertainties within the atmosphere, there remain substantial uncertainties as to the magnitude of air-sea CO_2 flux variability itself based on ocean biogeochemical models (Hauck et al. 2020), observation-based flux products (McKinley et al. 2020, Bennington et al. 2022, Hauck et al. 2023) and atmospheric CO_2 inverse models (Peylin et al., 2013).

Quantifying ocean-driven atmospheric CO_2 IAV remains challenging since direct observations of pCO_2 in surface waters and the corresponding difference with the atmosphere are sparse, and there are large spatiotemporal gaps. CO_2 fluxes can be estimated from observation-based pCO_2 products, which use statistical or mechanistic approaches to interpolate oceanic partial pressure measurements (Rödenbeck et al., 2014, Landschutzer et al. 2014, 2016, Denvil-Somier et al 2019. These observation-based products estimate near global 1^{o}x1^{o}, monthly pCO_2 fields from sparse pCO_2 data using various techniques, including statistical interpolation, linear and non-linear regressions, and machine learning-based methodologies. The CO_2 flux is then

calculated from the interpolated pCO_2 fields (Fay et al., 2021). Robust estimates of mean and seasonality can be derived from observation-based products (Gloege et al. 2021, Fay and McKinley 2021), while significant uncertainties in terms of higher and lower frequency variability remain (Rodenbeck et al. 2015, Hauck et al. 2020, Bennington et al. 2022).

New space-based observations of the column-integrated CO_2 mole fraction, XCO_2, from NASA's Orbiting Carbon Observatory 2 (OCO-2) mission may provide a unique vantage to observe the atmospheric imprint of IAV in air-sea CO_2 fluxes. OCO-2 is NASA's first dedicated Earth remote sensing satellite to study atmospheric carbon dioxide from space (Eldering et al., 2017). It was designed to collect space-based measurements of atmospheric CO_2 with high precision and near-global coverage (Crisp et al., 2012; Crisp et al., 2017). Compared to surface in-situ CO_2 observations, such as from the NOAA greenhouse gas network, which is mostly sited in coastal, island, and inland locations, OCO-2 can observe directly over the open ocean, which may improve the spatiotemporal attribution of ocean fluxes.

The research presented here leverages these two advances in carbon cycle data products to answer the following scientific questions: (1) What are the fingerprints of ocean carbon fluxes on IAV of atmospheric CO_2, and from what regions are these imprints most prominent? (2) What differences emerge from different observation-based products, and how large are these differences compared to the IAV owing from atmospheric transport? (3) How detectible is the IAV signal from ocean fluxes in surface or column CO_2? To answer these questions, we run atmospheric transport simulations with underlying air-sea fluxes from several observation-based products. We use the output from these simulations to quantify the imprint of regional and global sea-air CO_2 fluxes on atmospheric CO_2 IAV. As a final step, we use OCO-2 observations of XCO_2 to contextualize the simulated ocean-driven XCO_2 variations.

3.2 Data and Methods

3.2.1 Datasets

3.2.1.1 SOCOM Fluxes

Gridded air-sea CO_2 fluxes estimated from observation-based products for near-global surface ocean pCO_2 have been developed from the same sparse in situ pCO_2 data using a variety of interpolation / mapping methods (Rodenbeck et al. 2015, Fay et al., 2021). In this study, we choose 3 data products that use different spatial interpolation methods and provide the best temporal and spatial coverage over the past 4 decades from 1982 to 2021. We use the JENA product (Rödenbeck et al., 2014), which is a temporally and spatially resolved estimate of the global surface-ocean CO_2 partial pressure field and the sea–air CO_2 flux obtained by fitting a simple data-driven diagnostic model of ocean mixed-layer biogeochemistry to surface-ocean CO_2 partial pressure data from the SOCAT database. Second, we use the Self-Organizing Map Feed-Forward Neural Network (SOMFFN) product, which is based on a combination of self-organizing maps (Landschutzer et al., 2013, 2014, 2016). Finally, we use the Copernicus Environment Monitoring Service product (CMEMS; LSCE-FFNN-v1), which is a two-step neural network model for the reconstruction of surface ocean pCO_2 over the global ocean (Denvil-Sommer et al., 2019). In these networks of models, the information travels forward in the neural network, through the input nodes then through the hidden layers (single or multiple), and finally through the output nodes. JENA has a resolution of about $4^\circ \times 5^\circ$ spatially at daily time scale, while SOMFFN and CMEMS are reported at $1^\circ \times 1^\circ$ on a monthly basis. Each product covers the global ocean but excludes some coastal areas and/or the Arctic. Based on surface water pCO_2 measurements of surface water, for each product, the sea–air CO_2 flux is calculated through gas exchange parameterization, which uses a calculated value of the gas

transfer velocity and the solubility of CO_2 in seawater near-surface salinity, and observed values of sea surface temperature and dry air mixing ratio of atmospheric CO_2. Our analysis is based on the overlapping ocean region of the three products, and we mask-out high latitude ocean in the Arctic and Antarctic regions as well as the coastal areas in order to have intercomparability among the three products.

We divide the ocean into 7 subregions (Fig 3.1) based on the oceanic biome regions defined by climatological criteria (Fig B.1) and analyze these flux products (Fig B.2) aggregated to the ocean subregions. Oceanic biomes are classified from sea surface temperature, spring/summer chlorophyll-a concentrations, ice fraction, and maximum mixed layer depth (Fay and McKinley, 2014). The biome regions partition the surface ocean into regions of common biogeochemical function and are consistent with a variety of observational and modeling studies assessing air-sea CO_2 fluxes and primary productivity.

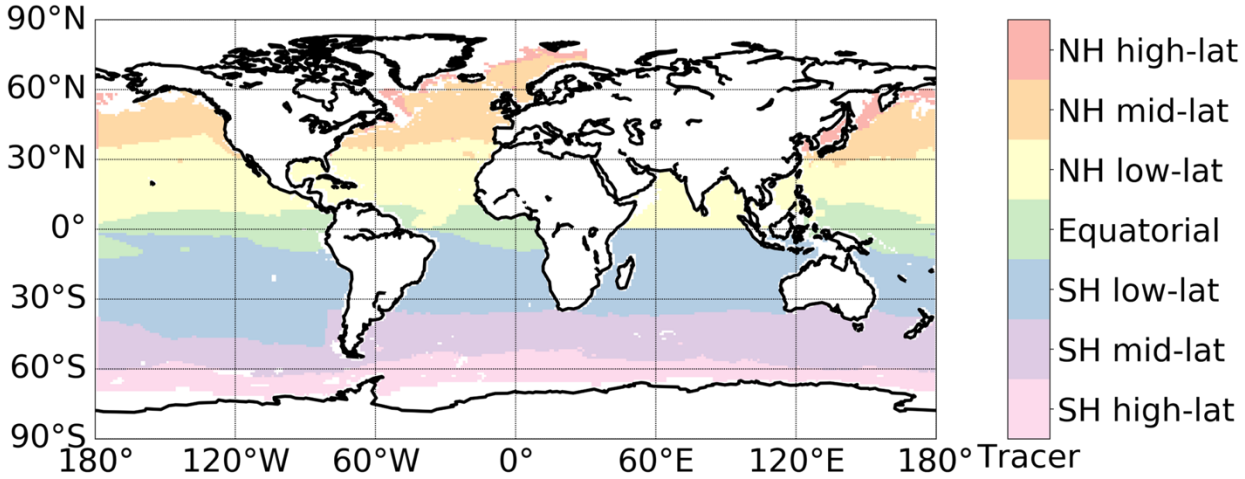

Figure 3.1: *The tracers defined for the tagged simulations based on ocean biome regions in Fay and McKinley, 2014.*

3.2.1.2 OCO-2 Observations

We analyze IAV in dry air, column-average mole fraction XCO_2 inferred from OCO-2 satellite observations. The OCO-2 observatory was launched in July 2014 and has measured passive, reflected solar near-infrared CO_2 and O_2 absorption spectra using grating spectrometers since September 2014 (Eldering et al., 2017). XCO_2 data are retrieved from the measured spectra using the Atmospheric CO_2 Observations from Space (ACOS) optimal estimation algorithm, which is a full physics algorithm that solves for XCO_2 and other physical parameters, including surface pressure, surface albedo, temperature, and water vapor profile in its state vector (O'Dell et al., 2018). The satellite is in a polar and sun-synchronous orbit that repeats every 16 days, with three different observing modes of OCO-2, namely nadir (land only, views the ground directly below the spacecraft with insufficient signal to noise over the ocean), glint (ocean and land, views the spot with directly reflected sunlight resulting in a higher ocean signal), and target (sites of specific interest, primarily for validation) (Crisp et al., 2012; Crisp et al., 2017). We use the version 10 OCO-2 Level 2 bias-corrected XCO_2 data product from 2014 September to 2022, (From Goddard Earth Sciences Data and Information Services Center Archive: https://disc.gsfc.nasa.gov/datasets/OCO_2_L2_Lite_FP_10r/summary), which has been validated with collocated ground-based measurements from the Total Carbon Column Observing Network (TCCON). After filtering and bias correction, the OCO-2 XCO_2 retrievals agree well with TCCON in nadir, glint, and target observation modes, and generally have absolute median differences less than 0.4 ppm and RMS differences less than 1.5 ppm (O'Dell et al., 2012; Wunch et al., 2017).

We characterize IAV from OCO-2 XCO_2 in Guan et al. (2023). In that analysis, we determined optimal spatiotemporal scales for aggregating the observations to detect IAV

variability in light of other sources of error. We evaluated IAV signals against the TCCON ground-truth network, confirming that the IAV inferred from OCO-2 is robust given the small magnitude of IAV compared to other sources of variance (Mitchell et al., 2023). Further, the OCO-2 IAV timeseries show similar zonal patterns of OCO-2 XCO_2 IAV timeseries compared to GOSAT space-based observation and ground-based NOAA ESRL in situ data. The analysis by Guan et al. (2023) validates that the OCO-2 satellite provides new capabilities for discerning atmospheric XCO_2 IAV.

3.2.2 Methods

3.2.2.1 GEOS-Chem simulations

We simulate atmospheric XCO_2 generated by ocean carbon fluxes using GEOS-Chem (Bey et al., 2001), an offline global chemical transport model driven by meteorological input from the Goddard Earth Observing System (GEOS) of the NASA Global Modeling and Assimilation Office (GMAO) and developed by an extensive global community of researchers. It has been widely used for gas flux inversion and source attribution studies, including for CO_2, CH_4, and CO (e.g., Nassar et al., 2010; Fisher et al., 2017). We use the version 12.0.0 of GEOS-Chem, released in Aug 2018.

To simulate atmospheric CO_2 fields from individual subregions, we modify the GEOS-Chem code base to tag the source regions and separately track different CO_2 tracers originating from each region (Lin et al., 2020). This approach is possible since CO_2 is a passive tracer that is not involved in atmospheric chemical reactions. In the simulation, each CO_2 tracer corresponds to the influence of ocean CO_2 fluxes from one tagged region, and the simulation using the JENA product has two more tracers than SOMFFN and CMEMS since the JENA product has slightly larger data coverage in both the far North and the far South.

The meteorological inputs for GEOS-Chem come from the Modern-Era Retrospective analysis for Research and Applications, 80 Version 2 (MERRA2) reanalysis. We run simulations for 1982-2021 at 2° latitude by 2.5° longitude resolution with 47 vertical levels up to 0.01 hPa on a hybrid eta (sigma-pressure) grid. Convective transport in GEOS-Chem is simulated with a single-plume scheme (Wu et al., 2007) while boundary layer mixing in GEOS-Chem uses the non-local parameterization (Lin and McElroy, 2010) which draws on the mixing depths, temperature, latent and sensible heat fluxes, and specific humidity. Although some bias in the vertical distribution of CO_2 has been shown in GEOS-Chem for northern high latitudes (Schuh et al., 2019), similar tagged transport runs have been shown to generally capture seasonal cycles in surface CO_2 as well as gradients between surface and mid-tropospheric CO_2 across a range of latitudes (Lin et al., 2020). We initialize all tracers with a 3-year spin-up. We calculate XCO_2 in the GEOS-Chem runs by integrating the dry air mole fraction for the 47 model layers accounting for pressure differences with height.

In a sensitivity study, we isolate the impact of atmospheric transport IAV, rather than air-sea flux IAV, on the resulting IAV in XCO_2. For this analysis, we simulate XCO_2 from the seasonal climatology of air-sea CO_2 fluxes averaged over the 40-year period of the GEOS-Chem simulation, maintaining time-varying atmospheric transport from the MERRA2 reanalysis. Together with the baseline experiment using time-varying air-sea fluxes and time-varying transport, we can distinguish the effect of dynamical-driven variation, flux-driven variation, and the combination of both.

3.2.2.2 Timeseries analysis

We characterize spatiotemporal patterns of OCO-2 detected XCO_2 by first aggregating OCO-2 observations to monthly averages on a 5° by 5° grid equatorward of 45° and to a 5°

by10° grid poleward of 45° from 2014.08 (August) to 2021, which overlaps with the simulation time period. Our analysis shows that averaging XCO_2 observations at these scales minimizes the effect of retrieval error and mitigates influences caused by missing measurements due to cloud cover in the tropics and weak winter sunlight in polar regions (Guan et al., 2023). We similarly aggregate GEOS-Chem model output at this scale when compared to OCO-2. We use a consistent process to calculate IAV from the OCO-2 XCO_2 (Equation 1), and GEOS-Chem XCO_2 (Equation 2), noting that we must account for an additional term in the multi-decadal GEOS-Chem simulations since curvature in the long-term atmospheric growth trend must be taken into account. The methodology is based on approaches used in Keppel-Aleks et al. (2014) and NOAA curve fitting methodology (Thoning et al, 1989).

$$IAV_{OCO\text{-}2}(x,y,t) = Raw(x,y,t) - Long\ Term\ Trend(x,y,t) - Seasonal(x,y,m) \quad \text{Equation 1}$$

$$IAV_{GEOS\text{-}Chem}(x,y,t) = Raw(x,y,t) - Long\ Term\ Trend(x,y,t) - Multi\text{-}Decadal\ (x,y,t) - Seasonal(x,y,m) \quad \text{Equation 2}$$

In these equations, (x,y) denotes a specific gridcell, t denotes a specific time, and m denotes a monthly average. We first fit a third-order polynomial to the Raw timeseries to calculate the observed trend at each location. For the GEOS-Chem simulation, since polynomial fitting does not fully capture the long-term trend over multiple decades, we apply a Fast Fourier Transform 10-year low-pass filter to remove decadal-scale variability. We calculate a mean seasonal cycle by taking the average value of all January, February, etc. data after removing the long-term trends. Finally, we remove the mean seasonal cycle from the detrended timeseries at each gridcell to obtain the IAV anomaly timeseries. We calculate the IAV amplitude as the standard deviation of the IAV anomaly timeseries. An identical method is used to calculate IAV from the gridded fluxes.

3.3 Results

Figure 3.2 shows the global distribution of air-sea CO_2 flux IAV amplitude (calculated as the standard deviation of IAV anomalies) over 40 years from 1982 to 2021 in the observation-based products. The three observation-based products show broadly similar magnitudes and spatial patterns in air-sea flux IAV (Fig B.3). The flux IAV amplitude is highest over the northern midlatitude ocean, Eastern Pacific, and Southern Ocean, with the largest inter-product differences in the northern hemisphere. In the Southern Hemisphere, the zonally integrated air-sea flux IAV is largest at 60°, around 0.6-0.7 mol m^{-2} y^{-1}. The flux IAV decreases by almost a factor of three in the subtropical regions in both hemispheres to around 0.2 mol m^{-2} s^{-1}. The large zonal IAV and the small zonal standard deviation around a latitude circle in the Southern Ocean, especially for SOMFFN and CMEMS (shading in Fig 3.2d,f), is due to the fact that the flux IAV is more uniform across the whole latitudinal band while in the Northern Hemisphere, the larger positive and negative flux IAV at the gridcell level partially cancels when integrated around a latitude band. (shading in Fig 3.2d-f). Consequently, the Southern Hemisphere has a bigger imprint of atmospheric XCO_2 IAV, as we will show below.

The XCO_2 timeseries simulated from global air-sea fluxes (i.e., the sum of all tagged regions) shows small IAV that ranges from +/-0.2 ppm for Jena (Fig 3.3) with smaller variations for SOMFFN and CMEMS. Both spatially averaged timeseries (Fig 3.3) and maps of IAV (Fig B.4) are notably different across the three observation-based flux product when propagated through an atmospheric transport model. The simulated XCO_2 from Jena is also somewhat phase shifted compared to that that derived from the other two observation-based flux products, although XCO_2 simulated from any one flux product is generally coherent across latitude bands. The corresponding globally averaged XCO_2 IAV amplitude is about 0.11 ppm for Jena, but less

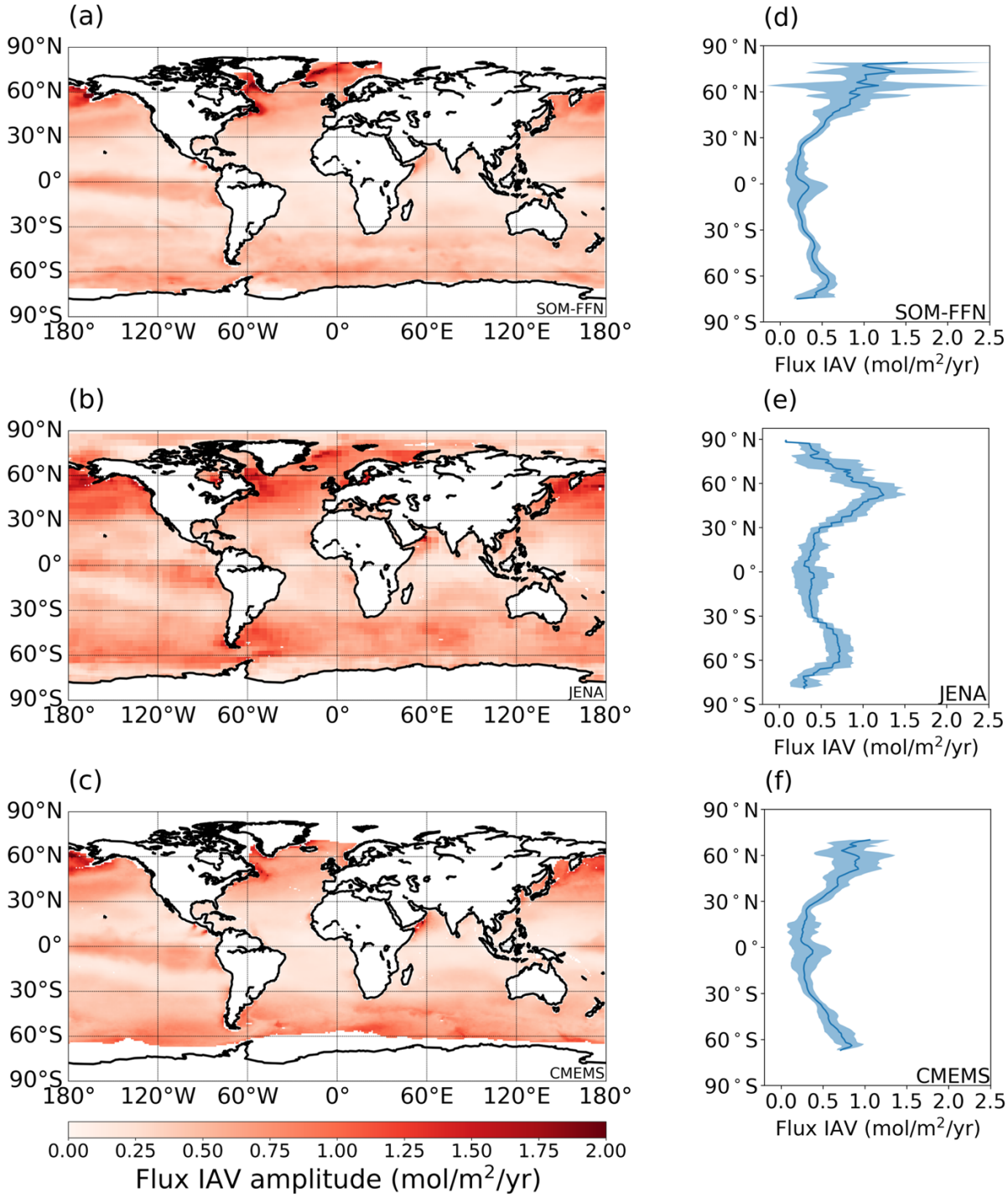

Figure 3.2: *Map of ocean flux IAV amplitude (a-c) and latitudinal profile of zonal mean flux IAV amplitude (d-f). Warmer colors signify more IAV while cooler colors indicate lower IAV regions. The IAV amplitude is calculated from the standard deviation of the IAV timeseries. The zonal mean IAV is obtained by averaging the IAV timeseries for all longitudes within the specified latitude band, while the shading shows the standard deviation of the IAV timeseries among all longitudes, indicating the coherence of flux IAV around a latitude circle. Panels (a, d) show results for SOMFFN; panels (b, e) show results for JENA and (c,f) show results for CMEMS (e,f) product.*

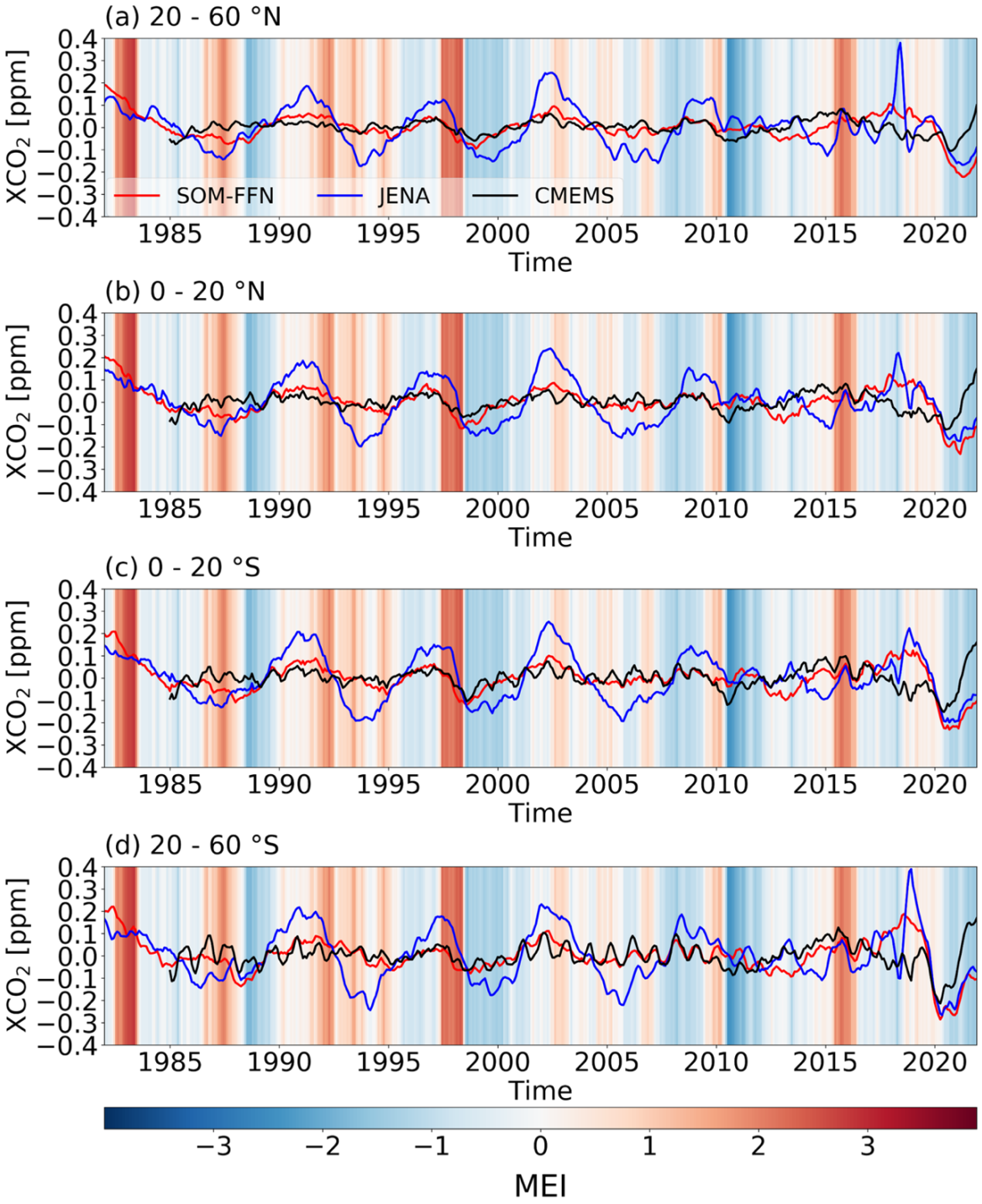

Figure 3.3: *XCO_2 IAV timeseries averaged for zonal bands between 60 °N and 60 °S from three different observation-based products. (a) 20 – 60 °N, (b) 0 – 20 °N, (c) 0 – 20 °S, (d) 20 – 60 °S. The background shading indicates the Multivariate ENSO Index (MEI), which is positive during El Niño phases.*

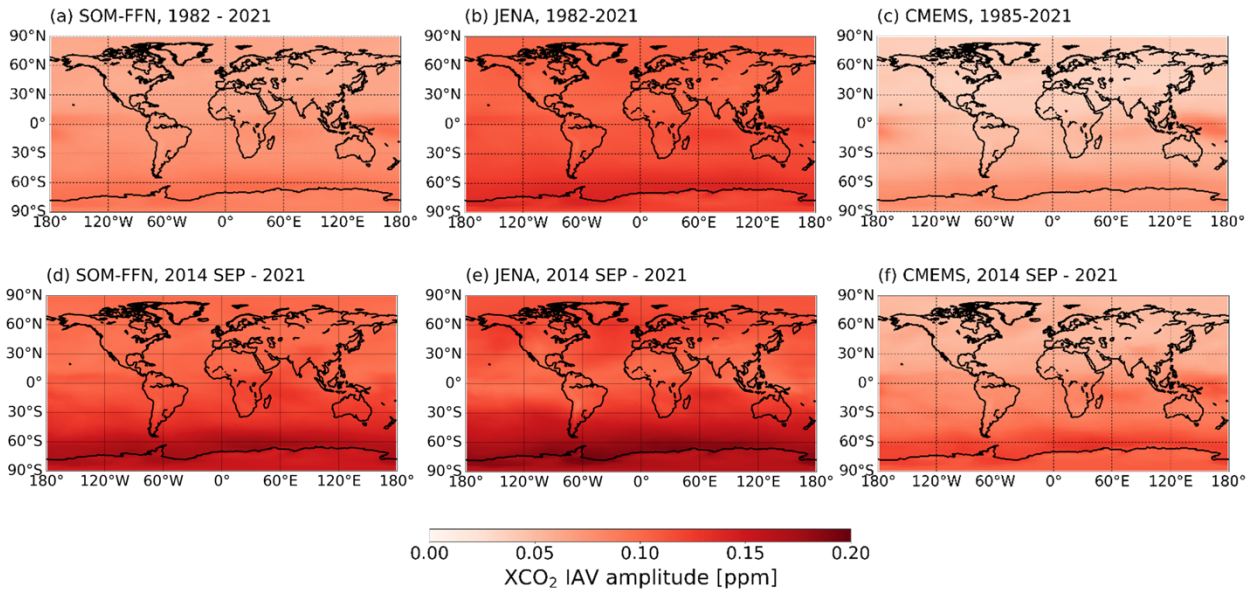

Figure 3.4: *XCO_2 IAV amplitude based on simulation from 1982 to 2021, using SOMFFN (a) JENA (b) and CMEMS (c) ocean observation-based products as input surface CO_2 fluxes to GEOS-Chem atmospheric transport runs. Modeled XCO_2 IAV amplitude based on simulation during the period of overlap with OCO-2 (September 2014 through the end of 2021), using SOMFFN (d), JENA (e), and CMEMS (f) as input fluxes.*

Flux	Contribution	Percentage of Global	NH high-lat	NH mid-lat	NH low-lat	Equatorial	SH low-lat	SH mid-lat	SH high-lat
SOMFFN	1st contributor	Area		1%		3.2%	4.8%	91%	
		Gridcells		1.6%		2%	3.1%	93.3%	
	2nd contributor	Area		25.9%	2.2%	3.8%	48.1%	7.2%	12.8%
		Gridcells		33.2%	1.5%	2.5%	35.5%	5.5%	21.8%
JENA	1st contributor	Area		12.1%	18.2%	1%	54.3%	14.4%	
		Gridcells		22.6%	14.2%	0.6%	37.6%	25%	
	2nd contributor	Area		3.6%	15.7%	2%	28%	50.7%	
		Gridcells		3.4%	25%	1.3%	34.7%	35.6%	
CMEMS	1st contributor	Area		16.4%	1.4%	5.9%	12.3%	64%	
		Gridcells		25.5%	0.9%	3.8%	8%	61.8%	
	2nd contributor	Area		13.4%	2.6%	3.4%	47.1%	30.9%	2.6%
		Gridcells		11.3%	1.7%	2.2%	46.3%	34.9%	3.6%

Table 3.1: *The percentage of global area or global gridcells for which each ocean flux region is the dominant driver of IAV in simulations with time-varying ocean fluxes and time-varying atmospheric transport.*

than 0.07 ppm for SOMFFN and CMEMS (Fig 3.4 a-c). Each data product shows the ocean-driven XCO_2 IAV amplitude largest over the tropical Pacific and the Southern Ocean. When the IAV amplitude is calculated for the period from September 2014 to 2021, the overlapping period between OCO-2 observations and observation-based products, the amplitude is similar for

SOMFFN and JENA (around 0.12 ppm globally averaged), and similar for CMEMS (around 0.08 ppm). The difference in simulated IAV for a given observation-based product calculated across two different time periods suggests that the ocean may leave a larger imprint on XCO_2 IAV in recent years compared to historical averages.

The Southern Hemisphere oceanic regions are the dominant contributors to XCO_2 IAV across the three models. We calculated the XCO_2 IAV amplitude arising separately from each regional tracer, then determined the region that contributes the largest and second largest IAV amplitude to each global atmospheric gridcell (left-hand column of Fig 3.5, and Fig B.5-7). Across all three models, the Southern Hemisphere low- and mid-latitude regions are the primary contributors to IAV over 70-95% of the global area (Table 3.1), including large swaths of the Northern Hemisphere for SOMFFN and CMEMS. In fact, the SOMFFN simulation shows that Northern Hemisphere ocean regions are not a dominant contributor to XCO_2 IAV even locally. In contrast, the XCO_2 IAV from the simulation with JENA and CMEMS fluxes show a modest contribution from the Northern Hemisphere, with the mid latitude region emerging as the dominant contributor to about 15% of the global area. The dominant region in each gridcell accounts for up to 60% of the atmospheric XCO_2 IAV amplitude for CMEMS (Fig 3.5f), and roughly 35-50% of the IAV amplitude for SOMFFN and JENA (Fig 3.5b and Fig 3.5d), suggesting more equable contributions from different regions. The second most-dominant contributors to atmospheric CO_2 IAV are similarly the Southern Hemisphere, or tropics or Northern Hemisphere mid-latitude across all three ocean-flux-GEOS-Chem simulations (Table 3.2).

Not all IAV in XCO_2 arises from IAV in surface fluxes; IAV in patterns of atmospheric transport is also an important contributor to XCO_2 IAV. We calculate the relative contributions of ocean flux variability and IAV in atmospheric transport from GEOS-Chem simulations with climatological monthly-mean cyclostationary ocean CO_2 fluxes as surface boundary conditions. IAV in these simulations arises only from IAV in atmospheric transport acting on the spatial gradients in XCO_2 set up by the climatological annual cycle of ocean air-sea CO_2 exchange. All three models show nearly identical spatial patterns in the XCO_2 amplitude arising from cyclostationary air-sea CO_2 fluxes (Fig 3.6 a-c), suggesting that seasonal flux patterns result in similar atmospheric gradients across the three models. The western Pacific warm pool is a hotspot for dynamics-driven variability, likely due to ENSO-driven changes in atmospheric

transport, and this region has an IAV amplitude of 0.07-0.08 ppm across all three simulations. Given the large variability in the magnitude of IAV among SOMFFN, JENA, and CMEMS (Fig 3.4), the ratio of dynamics-driven variations to total IAV diverged among the ocean-flux-GEOS-Chem simulations (Fig 3.6 d-f). For SOMFFN and CMEMS, which showed smaller IAV when driven with interannually varying fluxes, transport contributes about 50% of IAV in the Southern Hemisphere subtropics and subpolar regions, and 50-80% of IAV in the tropics and high latitudes of both hemispheres. For JENA, which had high IAV in the full simulations (Fig 3.4b), transport contributes less than 20% of total IAV except in the tropical Pacific, where it contributes 50%.

In the atmospheric transport simulations with cyclostationary fluxes, the Southern Hemisphere mid-latitude region is the dominant contributor to IAV for about 60% to 96% of the global area. Consistent across the three observation-based products, the second dominant contributor is the Southern Hemisphere low-latitude region. These results suggest that IAV in transport interacts most strongly with atmospheric gradients set up by Southern Hemisphere fluxes. Jena and CMEMS show that the Northern Hemisphere mid latitude regions are also important contributors when run with cyclostationary fluxes, and are the dominant contributor to roughly 15% to 25% of the global area. Fig 3.7 shows that in the cyclostationary simulations, the influence of Northern and Southern Hemisphere regions are more localized to the originating hemisphere. Taken together with the results from the time-varying fluxes, these results suggest that IAV in the Southern Hemisphere fluxes is synergistic with IAV from atmospheric transport, whereas, in the Northern hemisphere, IAV in the fluxes counteracts the IAV due to transport alone.

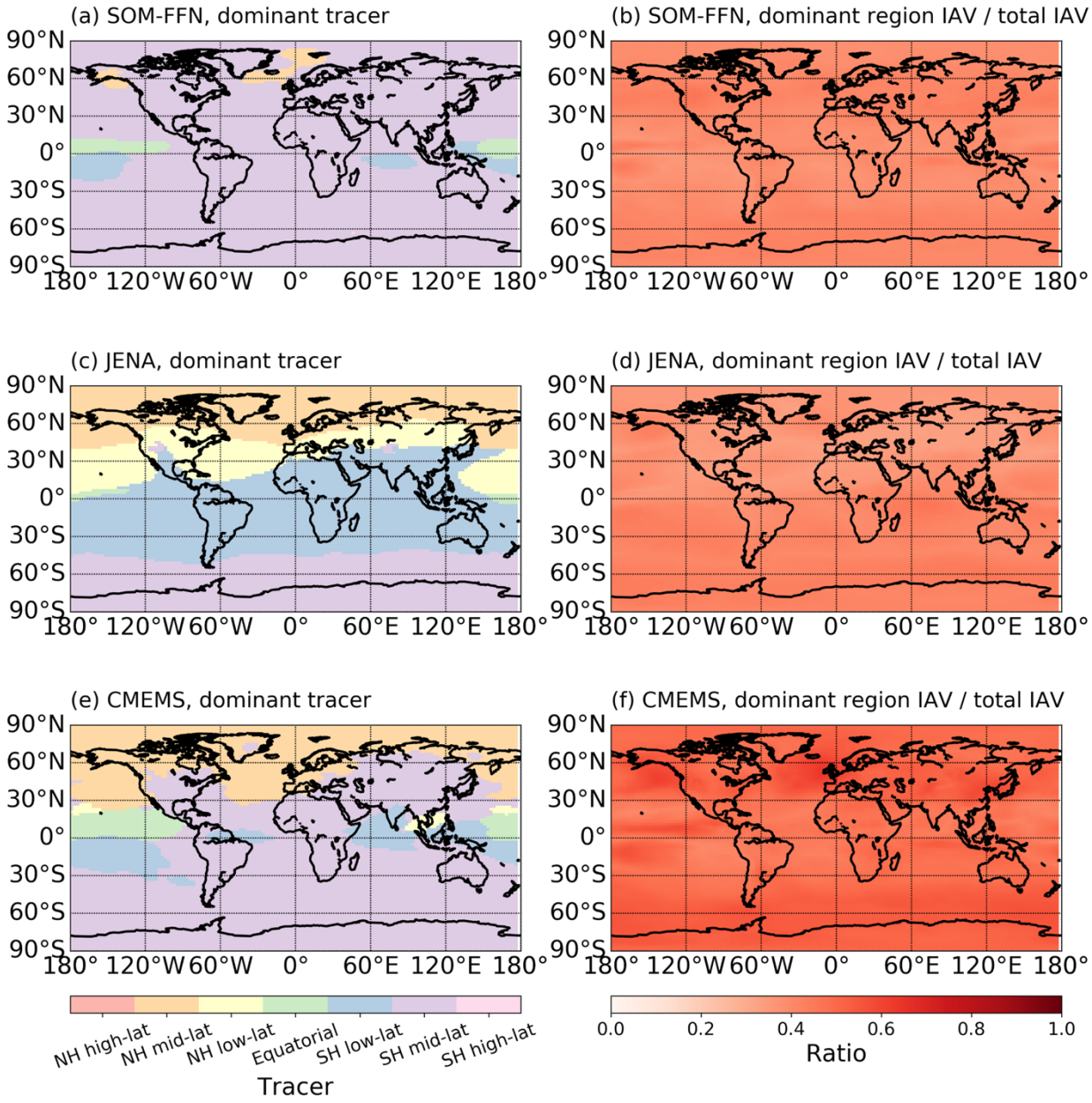

Figure 3.5: *The most influential ocean subregions at different locations based on simulations from 1982 to 2021 with time-varying SOMFFN (a), JENA (c), and CMEMS (e) fluxes. The dominant tracer is identified by calculating the XCO_2 IAV amplitude for each gridcell caused by a single tracer and then ranking them. The fraction of the overall IAV amplitude accounted for by the dominant tracer is shown in the left-hand column for SOMFFN (b), JENA (d), and CMEMS (f).*

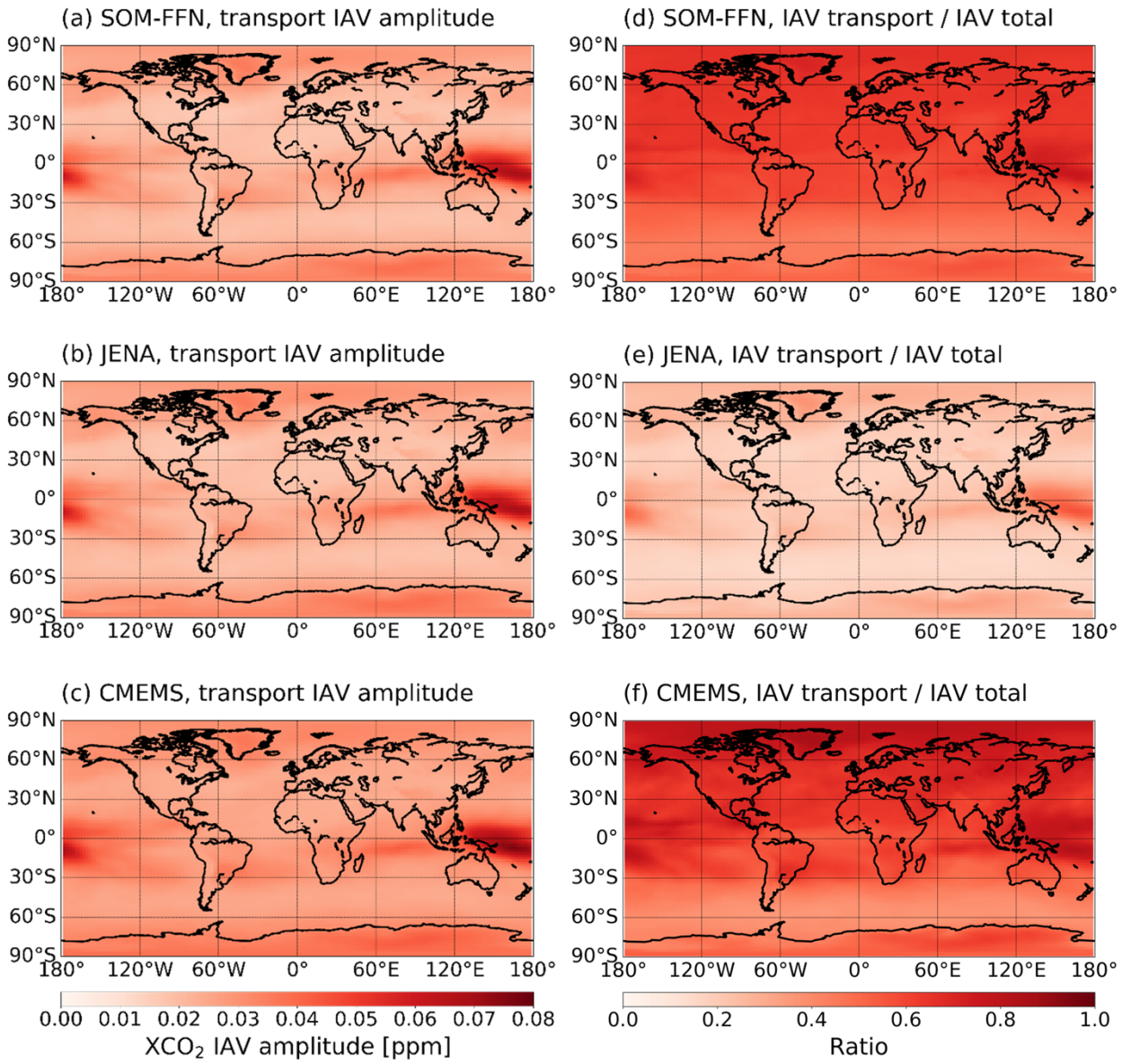

Figure 3.6: *The XCO_2 IAV amplitude from transport only simulations based on (a) SOMFFN, (b) JENA, and (c) CMEMS. The ratio of total IAV generated by transport alone for (d) SOMFFN, (e) JENA, and (f) CMEMS.*

Products	Contribution	Percentage of global	NH high-lat	NH mid-lat	NH low-lat	Equatorial	SH low-lat	SH mid-lat	SH high-lat
SOMFFN	1st contributor	Area				1%	3%	96%	
		Gridcells				0.6%	1.9%	97.4%	
	2nd contributor	Area		42.6%		3.4%	50.5%	3.5%	
		Gridcells		45.2%		2.1%	50.4%	2.3%	
JENA	1st contributor	Area		16.3%		6.2%	2.9%	74.6%	
		Gridcells		23%		3.9%	1.9%	71.2%	
	2nd contributor	Area		30.5%		2.3%	45.7%	21.5%	
		Gridcells		25.5%		1.5%	46.7%	26.3%	
CMEMS	1st contributor	Area		25.8%		6%	10.2%	58%	
		Gridcells		31.2%		3.8%	6.7%	58.3%	
	2nd contributor	Area		16.9%	0.2%	4.8%	45.4%	32.5%	0.2%
		Gridcells		14%	0.1%	3.1%	46.9%	35.6%	0.3%

Table 3.2: *Same as Table 3.1, except for simulations with cyclostationary ocean fluxes and time-varying atmospheric transport.*

The ocean-driven XCO_2 IAV simulated by the three observation-based products is largely unrelated to observed patterns of IAV as observed by OCO-2, which includes other sources of IAV. The OCO-2 IAV amplitude for the 2014-2021 period was an order of magnitude larger than that simulated from any of the three ocean observation-based products (Fig 3.4, Fig 3.8), although we note that the OCO-2 observations contain the imprint not only of ocean fluxes but also land and fossil emissions. The OCO-2 XCO_2 IAV amplitude, calculated as the standard deviation of the IAV timeseries, suggests that XCO_2 interannual variability over ocean basins is smaller than that over continent (around 0.4 ppm vs 1.2 ppm; Fig 3.8), although this may be due to larger error variance due to complex topography and land surface albedo variations (Guan et al., 2023; Mitchell et al., 2023). We calculate the correlation coefficient, slope, and fractional ratio between simulated XCO_2 IAV and OCO-2 XCO_2 IAV (Fig 3.9, Fig B.8) at the gridscale to explore where the imprint of the ocean might be detectible. Over most of the planet, the observed XCO_2 IAV is only weakly correlated with the XCO_2 IAV simulated from ocean fluxes, with many regions showing a slight negative correlation. Simulations from the three different flux products show different meridional patterns of correlation, with Jena

simulations showing slight positive correlations within the tropics and CMEMS showing slight positive correlations in the Southern Hemisphere, although we note these relationships are not statistically significant. Across all regions, the slope between the observed and simulated XCO_2 IAV is less than 0.2, consistent with the magnitude of the observed IAV being dominated by terrestrial signals. The maps of correlations and slopes suggest that detecting ocean IAV directly from space-based measurements is challenging given other sources of variability. Disentangling these multiple impacts to differentiate between plausible ocean flux products, such as the three analyzed here, will require a combination of observations and modeling.

Previous analysis of OCO-2 observations over the tropical Pacific suggested that space-based observations can detect an ocean-driven decrease in XCO_2 , potentially as large as 0.5 ppm, during the initial phases of the strong 2015 El Niño (Chatterjee et al., 2017). Our simulations show that atmospheric XCO_2 decreases over the Nino 3.4 region during the strong 1997-1998 El Niño (by about 0.3 ppm), but show a weaker decrease (about 0.1ppm) during 2015-2016 El Niño. The decrease in the atmospheric XCO_2 IAV timeseries corresponds to the reduced ocean outgassing over the Niño 3.4 region (up to 1.5 mol/m^2/y) (Fig 3.10), which is roughly similar between the two El Niño periods and leads to similar decreases in the tropical XCO_2 tracer (Fig B.9). During the strong 1997-98 El Niño, however, a temporary reduction in Northern Hemisphere CO_2 outgassing also reduced XCO_2 over the Niño.4 region, amplifying the apparent response (Fig B.9). As expected, XCO_2 anomalies during the two El Niño events are

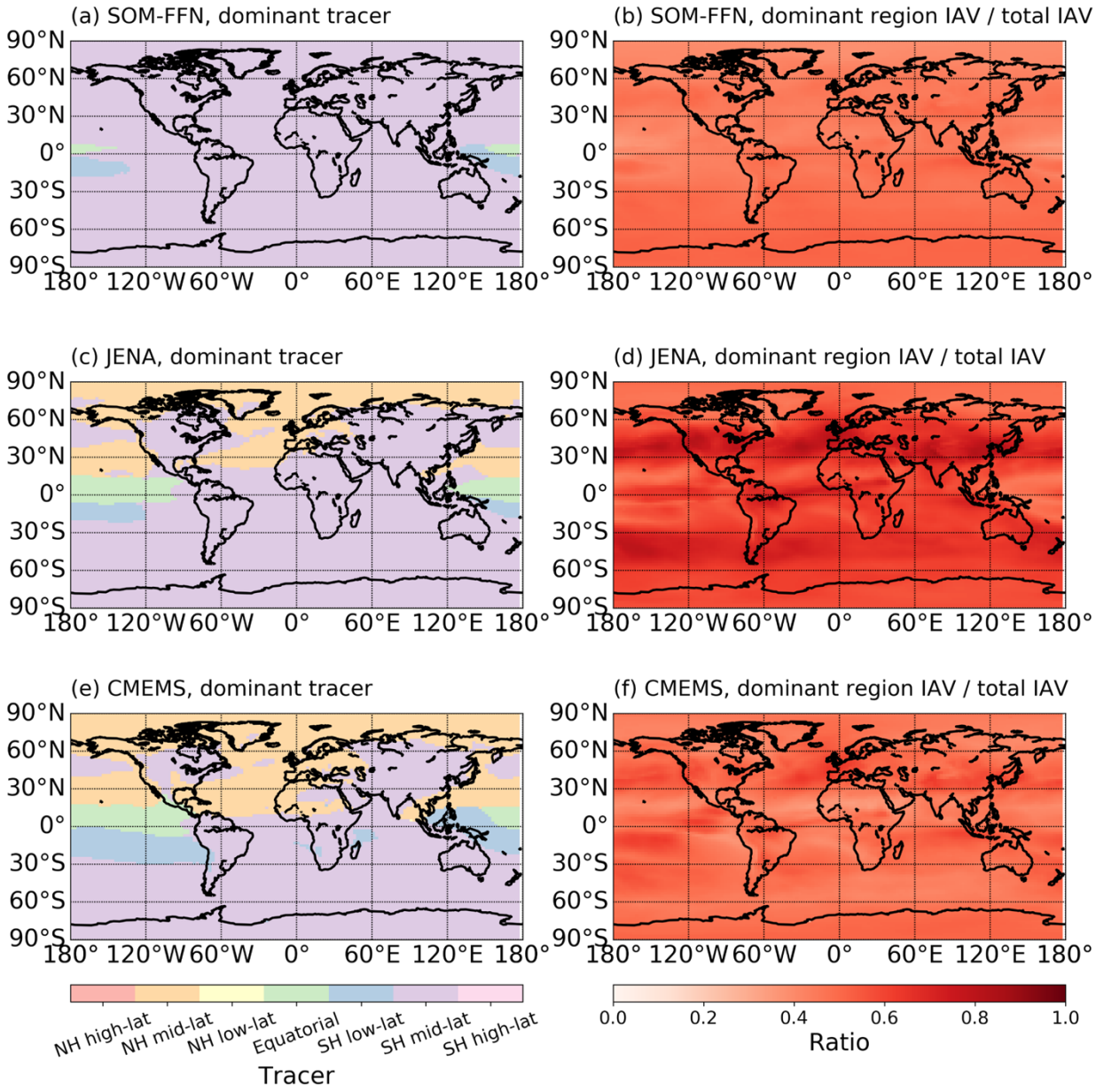

Figure 3.7: *The most influential ocean subregions at different locations based on simulations with cyclostationary SOMFFN (a), JENA (c), and CMEMS (e) ocean fluxes. The dominant tracer is identified by calculating the XCO_2 IAV amplitude for each gridcell caused by each region and then ranking them. The fraction of the overall IAV amplitude accounted for by the dominant region is shown in the left-hand column for SOMFFN (b), JENA (d), and CMEMS (f).*

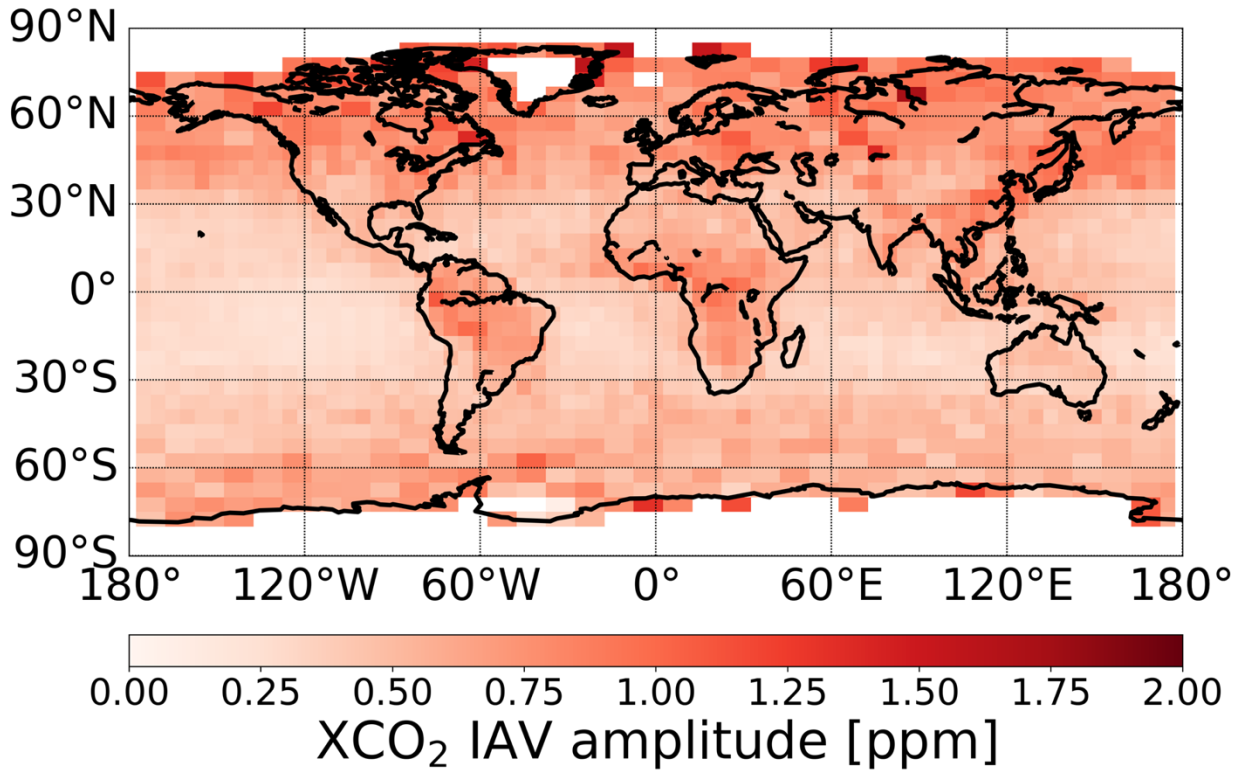

Figure 3.8: *Observed OCO-2 XCO_2 IAV amplitude, determined as the standard deviation of the IAV timeseries. Data equatorward of 45° are averaged at 5° by 5° resolution, and data poleward of 45° are averaged at 5° by 10° resolution based on Guan et al., (2022).*

mainly driven by changes in the air-sea CO_2 flux rather than changes in the atmospheric circulation (Fig B.10). These simulations suggest that even during strong El Niño events, detecting the direct atmospheric imprint of changes in ocean outgassing within the tropics will be challenging given the small direct signal predicted from all three observational flux products, compounding variability from other ocean and terrestrial regions, and retrieval uncertainties in XCO_2.

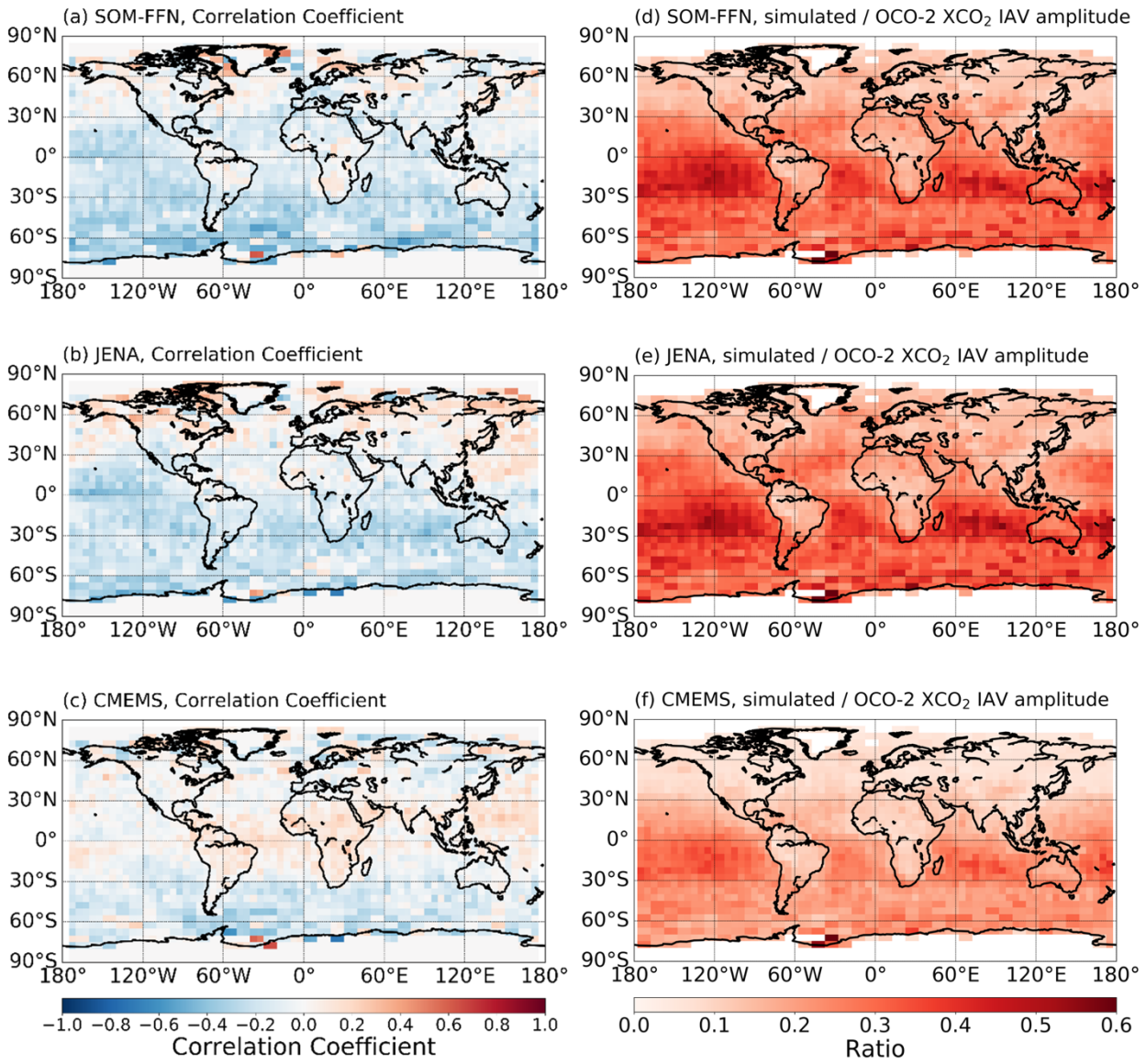

Figure 3.9: *(a-c) The correlation coefficient between simulated XCO_2 IAV and OCO-2 IAV for (a) SOMFFN, (b) JENA, and (c) CMEMS data products. (d-f) The ratio of IAV amplitude between simulated oceanic XCO_2 IAV and OCO-2 XCO_2 IAV, for (d) SOMFFN, (e) JENA, (f) CMEMS*

3.4 Discussion

We simulate ocean-driven IAV in atmospheric CO_2 based on three estimates of air-sea CO_2 fluxes from interpolated observation-based products. Although these observation-based products all use the same ocean pCO_2 data to estimate gridded fluxes and show largely similar

spatial patterns of flux IAV, they result in very different estimates of atmospheric XCO_2 IAV over the 40 year period from 1982-2021 (Fig 3.3; Fig 3.4 a-c). The inter-model spread was much reduced when looking at the four years from 2014-2021 overlapping with OCO-2 observations (Fig 3.4 d-f). During this period, all three observation-based flux products show a multi-year decrease in the net ocean flux. These results, together with the low correspondence with total IAV from OCO-2, suggest that multi-decadal variability in air-sea CO_2 fluxes may be more detectable in atmospheric XCO_2 than year-to-year variability. Our results largely corroborate the results from Nevison et al. (2008), who showed a small imprint for the ocean on atmospheric CO_2 IAV. Our results show that even in the remote Southern Ocean, which shows large IAV in the fluxes, the atmospheric IAV signature imparted by the ocean is small.

Further, our simulations show that a large fraction of the IAV in atmospheric XCO_2 results from IAV in atmospheric transport acting on atmospheric gradients derived from cyclostationary ocean fluxes (Fig 3.6), not from IAV in the ocean fluxes themselves. The three observation-based products showed a very similar pattern of transport-induced IAV, with the dominant spatial contributors showing high consistency among the three data products (Table 3.1). This is somewhat expected, since the MERRA/GEOS-Chem atmospheric transport patterns were common among all three simulations, but also requires that the three observation-based products simulate similar mean spatial seasonal patterns in atmospheric XCO_2 (Fig B.11).

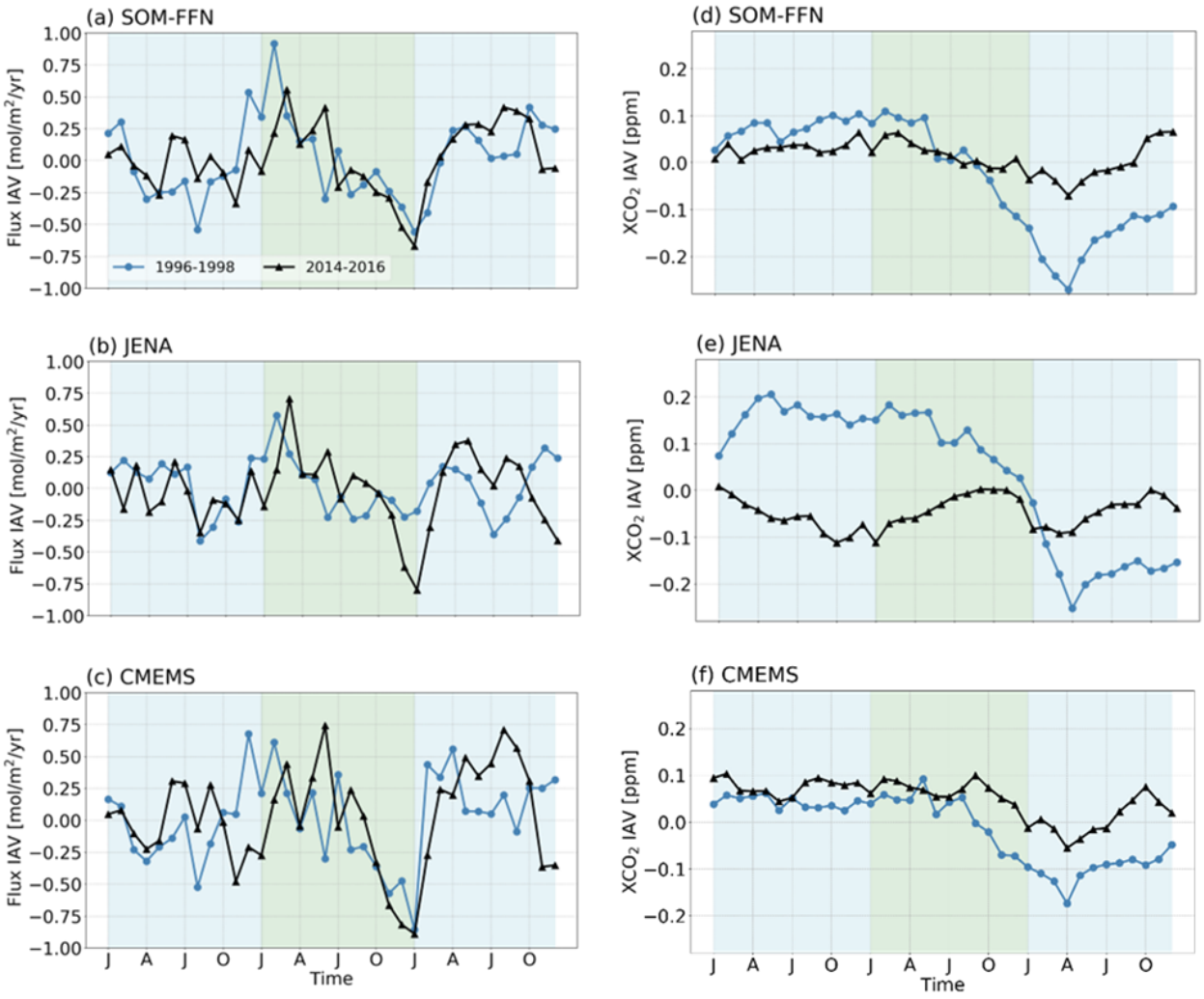

Figure 3.10: *IAV timeseries averaged over the Niño 3.4 region for three years centered on two strong El Niño events: 1997-1998 in blue; 2015-2016 in black. Year 1 and Year 3 are shaded blue, and Year 2 is shaded with green. Left Column shows the Ocean Flux IAV whereas the right column shows the simulated XCO_2 IAV. (a)(d) SOMFFN, (b)(e) JENA, (c)(f) CMEMS.*

Our study shows that atmospheric XCO_2 IAV is affected most strongly by air-sea CO_2 fluxes in the Southern Hemisphere (Fig 3.7), although the observation-based products show tradeoffs between the Southern Hemisphere low- and mid-latitude regions in terms of which region dominates. In the simulations with time-varying air-sea fluxes, the Southern Hemisphere, and to a lesser extent the tropics, dominate ocean-driven XCO_2 IAV even in the Northern

Hemisphere. This pattern generally holds in the simulations with cyclostationary fluxes, although the Northern Hemisphere regions have a relatively larger contribution.

Given the small signature of ocean fluxes on atmospheric XCO_2 IAV, attributing ocean-induced IAV based on space-based observations will be challenging. Mitchell et al. (2023) provides a detailed assessment of time and space scales of variation in OCO-2 XCO_2 over North American land and coastal ocean using a geostatistical approach. They identify synoptic scale variations as contributing up to 2 ppm^2 variance, mesoscale transport, and correlated error as contributing up to 1 ppm variance, and random noise as up to 1 ppm. Given that our simulations suggest the imprint of ocean IAV is less than 0.1 ppm, these results suggest that directly observing ocean IAV is not possible with the current technology for space-based remote sensing of atmospheric CO_2. Rather, XCO_2 observations will require precision better than 0.1 ppm, or 0.025% on a ~400 ppm background to detect and attribute ocean-driven variation. Furthermore, because transport is an important contributor to the patterns of atmospheric CO_2 IAV, using methods such as atmospheric inversions to back out ocean fluxes in an optimal estimation framework requires fidelity in atmospheric transport modeling (Schuh et al., 2019). Here, patterns of atmospheric transport-induced IAV from cyclostationary air-sea CO_2 fluxes (Fig 3.6) are similar because all flux products were transported through the same GEOS-Chem transport model. The choice of a different transport model would likely result in different spatial patterns, albeit with a similarly small magnitude compared to the IAV amplitude of the observations.

Our results temper the optimistic results from Chatterjee et al. (2017), who showed that a large ocean flux signal could be discerned from space-based XCO_2 data. We note that this study targeted the area with the largest ocean-driven XCO_2 IAV in our simulations (Fig 3.4), as well as

the region that was most sensitive to IAV in atmospheric transport (Fig 3.6). Nevertheless, all three ocean products we analyze suggest a smaller XCO_2 IAV than what was observed for the 2015-16 El Niño. These results suggest that flux anomalies associated with changing modes in ocean oscillations in other basins may impart smaller variations in the atmosphere that are difficult to detect using OCO-2 or a similar satellite.

3.5 Conclusions

We evaluate the imprint that air-sea CO_2 fluxes from the whole ocean and different oceanic subregions leave on the atmospheric XCO_2 interannual variation. We quantify the observed total XCO_2 IAV based on OCO-2 column-mean CO_2 observation from late 2014 to 2022 and compare against the simulated ocean-driven XCO_2 derived from the GEOS-Chem simulation using air-sea CO_2 fluxes estimated from observation-based surface pCO_2 products as input. The ocean-driven IAV in atmospheric XCO_2 caused by air-sea CO_2 exchange and IAV in atmospheric transport is about 0.1 ppm (standard deviation). While this magnitude is up to 40% of the total IAV in OCO-2 XCO_2 over the tropical and subtropical ocean basins, this magnitude is well below random noise in individual OCO-2 soundings and systematic errors in the satellite observations themselves. These results indicate that direct observation of air-sea CO_2 flux variations from total column XCO_2 would be very challenging with current space-based sensors.

3.6 References

Ballantyne, A. P., Alden, C. B., Miller, J. B., Tans, P. P., and White, J. W. C.: Increase in observed net carbon dioxide uptake by land and oceans during the past 50 years, Nature, 488, 70–72, https://doi.org/10.1038/nature11299, 2012.

Bennington, V., Gloege, L., and McKinley, G. A.: Variability in the Global Ocean Carbon Sink From 1959 to 2020 by Correcting Models With Observations, Geophysical Research Letters, 49, e2022GL098632, https://doi.org/10.1029/2022GL098632, 2022.

Bey, I., Jacob, D. J., Yantosca, R. M., Logan, J. A., Field, B. D., Fiore, A. M., Li, Q., Liu, H. Y., Mickley, L. J., and Schultz, M. G.: Global modeling of tropospheric chemistry with

assimilated meteorology: Model description and evaluation, Journal of Geophysical Research: Atmospheres, 106, 23073–23095, https://doi.org/10.1029/2001JD000807, 2001.

Buchwitz, M., Reuter, M., Schneising, O., Noël, S., Gier, B., Bovensmann, H., Burrows, J. P., Boesch, H., Anand, J., Parker, R. J., Somkuti, P., Detmers, R. G., Hasekamp, O. P., Aben, I., Butz, A., Kuze, A., Suto, H., Yoshida, Y., Crisp, D., and O'Dell, C.: Computation and analysis of atmospheric carbon dioxide annual mean growth rates from satellite observations during 2003–2016, Atmospheric Chemistry and Physics, 18, 17355–17370, https://doi.org/10.5194/acp-18-17355-2018, 2018.

Crisp, D., Fisher, B. M., O'Dell, C., Frankenberg, C., Basilio, R., Bösch, H., Brown, L. R., Castano, R., Connor, B., Deutscher, N. M., Eldering, A., Griffith, D., Gunson, M., Kuze, A., Mandrake, L., McDuffie, J., Messerschmidt, J., Miller, C. E., Morino, I., Natraj, V., Notholt, J., O'Brien, D. M., Oyafuso, F., Polonsky, I., Robinson, J., Salawitch, R., Sherlock, V., Smyth, M., Suto, H., Taylor, T. E., Thompson, D. R., Wennberg, P. O., Wunch, D., and Yung, Y. L.: The ACOS CO_2 retrieval algorithm – Part II: Global XCO_2 data characterization, Atmospheric Measurement Techniques, 5, 687–707, https://doi.org/10.5194/amt-5-687-2012, 2012.

Crisp, D., Pollock, H. R., Rosenberg, R., Chapsky, L., Lee, R. A. M., Oyafuso, F. A., Frankenberg, C., O'Dell, C. W., Bruegge, C. J., Doran, G. B., Eldering, A., Fisher, B. M., Fu, D., Gunson, M. R., Mandrake, L., Osterman, G. B., Schwandner, F. M., Sun, K., Taylor, T. E., Wennberg, P. O., and Wunch, D.: The on-orbit performance of the Orbiting Carbon Observatory-2 (OCO-2) instrument and its radiometrically calibrated products, Atmospheric Measurement Techniques, 10, 59–81, https://doi.org/10.5194/amt-10-59-2017, 2017.

Crisp, D., Dolman, H., Tanhua, T., McKinley, G. A., Hauck, J., Bastos, A., Sitch, S., Eggleston, S., & Aich, V.: How Well Do We Understand the Land-Ocean-Atmosphere Carbon Cycle? Rev Geophys, 60(2), e2021RG000736. https://doi.org/10.1029/2021RG000736, 2022.

Denvil-Sommer, A., Gehlen, M., Vrac, M., and Mejia, C.: LSCE-FFNN-v1: a two-step neural network model for the reconstruction of surface ocean pCO_2 over the global ocean, Geoscientific Model Development, 12, 2091–2105, https://doi.org/10.5194/gmd-12-2091-2019, 2019.

Doney, S. C., Fabry, V. J., Feely, R. A., and Kleypas, J. A.: Ocean Acidification: The Other CO_2 Problem, Annual Review of Marine Science, 1, 169–192, https://doi.org/10.1146/annurev.marine.010908.163834, 2009.

Eldering, A., O'Dell, C. W., Wennberg, P. O., Crisp, D., Gunson, M. R., Viatte, C., Avis, C., Braverman, A., Castano, R., Chang, A., Chapsky, L., Cheng, C., Connor, B., Dang, L., Doran, G., Fisher, B., Frankenberg, C., Fu, D., Granat, R., Hobbs, J., Lee, R. A. M., Mandrake, L., McDuffie, J., Miller, C. E., Myers, V., Natraj, V., O'Brien, D., Osterman,

G. B., Oyafuso, F., Payne, V. H., Pollock, H. R., Polonsky, I., Roehl, C. M., Rosenberg, R., Schwandner, F., Smyth, M., Tang, V., Taylor, T. E., To, C., Wunch, D., and Yoshimizu, J.: The Orbiting Carbon Observatory-2: first 18 months of science data products, Atmospheric Measurement Techniques, 10, 549–563, https://doi.org/10.5194/amt-10-549-2017, 2017.

Fay, A. R., McKinley, G. A., and Lovenduski, N. S.: Southern Ocean carbon trends: Sensitivity to methods, Geophysical Research Letters, 41, 6833–6840, https://doi.org/10.1002/2014GL061324, 2014.

Fay, A. R., Gregor, L., Landschützer, P., McKinley, G. A., Gruber, N., Gehlen, M., Iida, Y., Laruelle, G. G., Rödenbeck, C., Roobaert, A., and Zeng, J.: SeaFlux: harmonization of air–sea CO_2 fluxes from surface pCO_2 data products using a standardized approach, Earth System Science Data, 13, 4693–4710, https://doi.org/10.5194/essd-13-4693-2021, 2021.

Fay, A. R. and McKinley, G. A.: Observed Regional Fluxes to Constrain Modeled Estimates of the Ocean Carbon Sink, Geophysical Research Letters, 48, e2021GL095325, https://doi.org/10.1029/2021GL095325, 2021.

Fisher, J. A., Murray, L. T., Jones, D. B. A., and Deutscher, N. M.: Improved method for linear carbon monoxide simulation and source attribution in atmospheric chemistry models illustrated using GEOS-Chem v9, Geoscientific Model Development, 10, 4129–4144, https://doi.org/10.5194/gmd-10-4129-2017, 2017.

Francey, R. J., Tans, P. P., Allison, C. E., Enting, I. G., White, J. W. C., and Trolier, M.: Changes in oceanic and terrestrial carbon uptake since 1982, Nature, 373, 326–330, https://doi.org/10.1038/373326a0, 1995.

Friedlingstein, P., O'Sullivan, M., Jones, M. W., Andrew, R. M., Hauck, J., Olsen, A., Peters, G. P., Peters, W., Pongratz, J., Sitch, S., Le Quéré, C., Canadell, J. G., Ciais, P., Jackson, R. B., Alin, S., Aragão, L. E. O. C., Arneth, A., Arora, V., Bates, N. R., Becker, M., Benoit-Cattin, A., Bittig, H. C., Bopp, L., Bultan, S., Chandra, N., Chevallier, F., Chini, L. P., Evans, W., Florentie, L., Forster, P. M., Gasser, T., Gehlen, M., Gilfillan, D., Gkritzalis, T., Gregor, L., Gruber, N., Harris, I., Hartung, K., Haverd, V., Houghton, R. A., Ilyina, T., Jain, A. K., Joetzjer, E., Kadono, K., Kato, E., Kitidis, V., Korsbakken, J. I., Landschützer, P., Lefèvre, N., Lenton, A., Lienert, S., Liu, Z., Lombardozzi, D., Marland, G., Metzl, N., Munro, D. R., Nabel, J. E. M. S., Nakaoka, S.-I., Niwa, Y., O'Brien, K., Ono, T., Palmer, P. I., Pierrot, D., Poulter, B., Resplandy, L., Robertson, E., Rödenbeck, C., Schwinger, J., Séférian, R., Skjelvan, I., Smith, A. J. P., Sutton, A. J., Tanhua, T., Tans, P. P., Tian, H., Tilbrook, B., van der Werf, G., Vuichard, N., Walker, A. P., Wanninkhof, R., Watson, A. J., Willis, D., Wiltshire, A. J., Yuan, W., Yue, X., and Zaehle, S.: Global Carbon Budget 2020, Earth System Science Data, 12, 3269–3340, https://doi.org/10.5194/essd-12-3269-2020, 2020.

Gloege, L., McKinley, G. A., Landschützer, P., Fay, A. R., Frölicher, T. L., Fyfe, J. C., Ilyina, T., Jones, S., Lovenduski, N. S., Rodgers, K. B., Schlunegger, S., and Takano, Y.:

Quantifying Errors in Observationally Based Estimates of Ocean Carbon Sink Variability, Global Biogeochemical Cycles, 35, e2020GB006788, https://doi.org/10.1029/2020GB006788, 2021.

Guan, Y., Keppel-Aleks, G., Doney, S. C., Petri, C., Pollard, D., Wunch, D., Hase, F., Ohyama, H., Morino, I., Notholt, J., Shiomi, K., Strong, K., Kivi, R., Buschmann, M., Deutscher, N., Wennberg, P., Sussmann, R., Velazco, V. A., and Té, Y.: Characteristics of interannual variability in space-based XCO_2 global observations, Atmospheric Chemistry and Physics, 23, 5355–5372, https://doi.org/10.5194/acp-23-5355-2023, 2023.

Hauck, J., Nissen, C., Landschützer, P., Rödenbeck, C., Bushinsky, S., and Olsen, A.: Sparse observations induce large biases in estimates of the global ocean CO_2 sink: an ocean model subsampling experiment, Philos Trans A Math Phys Eng Sci, 381, 20220063, https://doi.org/10.1098/rsta.2022.0063, 2023.

Hauck, J., Zeising, M., Le Quéré, C., Gruber, N., Bakker, D. C. E., Bopp, L., Chau, T. T. T., Gürses, Ö., Ilyina, T., Landschützer, P., Lenton, A., Resplandy, L., Rödenbeck, C., Schwinger, J., and Séférian, R.: Consistency and Challenges in the Ocean Carbon Sink Estimate for the Global Carbon Budget, Frontiers in Marine Science, 7, 2020.

Keppel-Aleks, G., Wolf, A. S., Mu, M., Doney, S. C., Morton, D. C., Kasibhatla, P. S., Miller, J. B., Dlugokencky, E. J., and Randerson, J. T.: Separating the influence of temperature, drought, and fire on interannual variability in atmospheric CO_2, Global Biogeochemical Cycles, 28, 1295–1310, https://doi.org/10.1002/2014GB004890, 2014.

Landschützer, P., Gruber, N., Bakker, D. C. E., Schuster, U., Nakaoka, S., Payne, M. R., Sasse, T. P., and Zeng, J.: A neural network-based estimate of the seasonal to inter-annual variability of the Atlantic Ocean carbon sink, Biogeosciences, 10, 7793–7815, https://doi.org/10.5194/bg-10-7793-2013, 2013.

Landschützer, P., Gruber, N., Bakker, D. C. E., and Schuster, U.: Recent variability of the global ocean carbon sink, Global Biogeochemical Cycles, 28, 927–949, https://doi.org/10.1002/2014GB004853, 2014.

Landschützer, P., Gruber, N., and Bakker, D. C. E.: Decadal variations and trends of the global ocean carbon sink, Global Biogeochemical Cycles, 30, 1396–1417, https://doi.org/10.1002/2015GB005359, 2016.

Le Quéré, C., Andrew, R. M., Friedlingstein, P., Sitch, S., Hauck, J., Pongratz, J., Pickers, P. A., Korsbakken, J. I., Peters, G. P., Canadell, J. G., Arneth, A., Arora, V. K., Barbero, L., Bastos, A., Bopp, L., Chevallier, F., Chini, L. P., Ciais, P., Doney, S. C., Gkritzalis, T., Goll, D. S., Harris, I., Haverd, V., Hoffman, F. M., Hoppema, M., Houghton, R. A., Hurtt, G., Ilyina, T., Jain, A. K., Johannessen, T., Jones, C. D., Kato, E., Keeling, R. F., Goldewijk, K. K., Landschützer, P., Lefèvre, N., Lienert, S., Liu, Z., Lombardozzi, D., Metzl, N., Munro, D. R., Nabel, J. E. M. S., Nakaoka, S., Neill, C., Olsen, A., Ono, T., Patra, P., Peregon, A., Peters, W., Peylin, P., Pfeil, B., Pierrot, D., Poulter, B., Rehder,

G., Resplandy, L., Robertson, E., Rocher, M., Rödenbeck, C., Schuster, U., Schwinger, J., Séférian, R., Skjelvan, I., Steinhoff, T., Sutton, A., Tans, P. P., Tian, H., Tilbrook, B., Tubiello, F. N., van der Laan-Luijkx, I. T., van der Werf, G. R., Viovy, N., Walker, A. P., Wiltshire, A. J., Wright, R., Zaehle, S., and Zheng, B.: Global Carbon Budget 2018, Earth System Science Data, 10, 2141–2194, https://doi.org/10.5194/essd-10-2141-2018, 2018.

Lin, J.-T. and McElroy, M. B.: Impacts of boundary layer mixing on pollutant vertical profiles in the lower troposphere: Implications to satellite remote sensing, Atmospheric Environment, 44, 1726–1739, https://doi.org/10.1016/j.atmosenv.2010.02.009, 2010.

Lin, X., Rogers, B. M., Sweeney, C., Chevallier, F., Arshinov, M., Dlugokencky, E., Machida, T., Sasakawa, M., Tans, P., and Keppel-Aleks, G.: Siberian and temperate ecosystems shape Northern Hemisphere atmospheric CO_2 seasonal amplification, Proc. Natl. Acad. Sci. U.S.A., 117, 21079–21087, https://doi.org/10.1073/pnas.1914135117, 2020.

Luo, Y., Huang, Y., Sierra, C. A., Xia, J., Ahlström, A., Chen, Y., Hararuk, O., Hou, E., Jiang, L., Liao, C., Lu, X., Shi, Z., Smith, B., Tao, F., and Wang, Y.-P.: Matrix Approach to Land Carbon Cycle Modeling, Journal of Advances in Modeling Earth Systems, 14, e2022MS003008, https://doi.org/10.1029/2022MS003008, 2022.

McKinley, G. A., Fay, A. R., Eddebbar, Y. A., Gloege, L., & Lovenduski, N. S.: External Forcing Explains Recent Decadal Variability of the Ocean Carbon Sink. AGU Advances, 1(2), e2019AV000149. Retrieved from https://doi.org/10.1029/2019AV000149, 2020.

Mitchell, K. A., Doney, S. C., and Keppel-Aleks, G.: Characterizing Average Seasonal, Synoptic, and Finer Variability in Orbiting Carbon Observatory-2 XCO_2 Across North America and Adjacent Ocean Basins, Journal of Geophysical Research: Atmospheres, 128, e2022JD036696, https://doi.org/10.1029/2022JD036696, 2023.

Nassar, R., Jones, D. B. A., Suntharalingam, P., Chen, J. M., Andres, R. J., Wecht, K. J., Yantosca, R. M., Kulawik, S. S., Bowman, K. W., Worden, J. R., Machida, T., and Matsueda, H.: Modeling global atmospheric CO_2 with improved emission inventories and CO_2 production from the oxidation of other carbon species, Geoscientific Model Development, 3, 689–716, https://doi.org/10.5194/gmd-3-689-2010, 2010.

Nevison, C. D., Mahowald, N. M., Doney, S. C., Lima, I. D., and Cassar, N.: Impact of variable air-sea O_2 and CO_2 fluxes on atmospheric potential oxygen (APO) and land-ocean carbon sink partitioning, Biogeosciences, 5, 875–889, https://doi.org/10.5194/bg-5-875-2008, 2008.

O'Dell, C. W., Connor, B., Bösch, H., O'Brien, D., Frankenberg, C., Castano, R., Christi, M., Eldering, D., Fisher, B., Gunson, M., McDuffie, J., Miller, C. E., Natraj, V., Oyafuso, F., Polonsky, I., Smyth, M., Taylor, T., Toon, G. C., Wennberg, P. O., and Wunch, D.: The ACOS CO_2 retrieval algorithm – Part 1: Description and validation against synthetic

observations, Atmospheric Measurement Techniques, 5, 99–121, https://doi.org/10.5194/amt-5-99-2012, 2012.

O'Dell, C. W., Eldering, A., Wennberg, P. O., Crisp, D., Gunson, M. R., Fisher, B., Frankenberg, C., Kiel, M., Lindqvist, H., Mandrake, L., Merrelli, A., Natraj, V., Nelson, R. R., Osterman, G. B., Payne, V. H., Taylor, T. E., Wunch, D., Drouin, B. J., Oyafuso, F., Chang, A., McDuffie, J., Smyth, M., Baker, D. F., Basu, S., Chevallier, F., Crowell, S. M. R., Feng, L., Palmer, P. I., Dubey, M., García, O. E., Griffith, D. W. T., Hase, F., Iraci, L. T., Kivi, R., Morino, I., Notholt, J., Ohyama, H., Petri, C., Roehl, C. M., Sha, M. K., Strong, K., Sussmann, R., Te, Y., Uchino, O., and Velazco, V. A.: Improved retrievals of carbon dioxide from Orbiting Carbon Observatory-2 with the version 8 ACOS algorithm, Atmospheric Measurement Techniques, 11, 6539–6576, https://doi.org/10.5194/amt-11-6539-2018, 2018.

Peylin, P., Law, R. M., Gurney, K. R., Chevallier, F., Jacobson, A. R., Maki, T., Niwa, Y., Patra, P. K., Peters, W., Rayner, P. J., Rödenbeck, C., van der Laan-Luijkx, I. T., and Zhang, X.: Global atmospheric carbon budget: results from an ensemble of atmospheric CO_2 inversions, Biogeosciences, 10, 6699–6720, https://doi.org/10.5194/bg-10-6699-2013, 2013.

Rödenbeck, C., Houweling, S., Gloor, M., and Heimann, M.: CO_2 flux history 1982–2001 inferred from atmospheric data using a global inversion of atmospheric transport, Atmospheric Chemistry and Physics, 3, 1919–1964, https://doi.org/10.5194/acp-3-1919-2003, 2003.

Rödenbeck, C., Bakker, D. C. E., Metzl, N., Olsen, A., Sabine, C., Cassar, N., Reum, F., Keeling, R. F., and Heimann, M.: Interannual sea–air CO_2 flux variability from an observation-driven ocean mixed-layer scheme, Biogeosciences, 11, 4599–4613, https://doi.org/10.5194/bg-11-4599-2014, 2014.

Rödenbeck, C., Bakker, D. C. E., Gruber, N., Iida, Y., Jacobson, A. R., Jones, S., Landschützer, P., Metzl, N., Nakaoka, S., Olsen, A., Park, G.-H., Peylin, P., Rodgers, K. B., Sasse, T. P., Schuster, U., Shutler, J. D., Valsala, V., Wanninkhof, R., and Zeng, J.: Data-based estimates of the ocean carbon sink variability – first results of the Surface Ocean pCO_2 Mapping intercomparison (SOCOM), Biogeosciences, 12, 7251–7278, https://doi.org/10.5194/bg-12-7251-2015, 2015.

Schuh, A. E., Jacobson, A. R., Basu, S., Weir, B., Baker, D., Bowman, K., Chevallier, F., Crowell, S., Davis, K. J., Deng, F., Denning, S., Feng, L., Jones, D., Liu, J., and Palmer, P. I.: Quantifying the Impact of Atmospheric Transport Uncertainty on CO_2 Surface Flux Estimates, Global Biogeochemical Cycles, 33, 484–500, https://doi.org/10.1029/2018GB006086, 2019.

Thoning, K. W., Tans, P. P., and Komhyr, W. D.: Atmospheric carbon dioxide at Mauna Loa Observatory: 2. Analysis of the NOAA GMCC data, 1974–1985, Journal of Geophysical Research: Atmospheres, 94, 8549–8565, https://doi.org/10.1029/JD094iD06p08549, 1989.

Wanninkhof, R.: Relationship between wind speed and gas exchange over the ocean revisited, Limnology and Oceanography: Methods, 12, 351–362, https://doi.org/10.4319/lom.2014.12.351, 2014.

Wanninkhof, R., Park, G.-H., Takahashi, T., Sweeney, C., Feely, R., Nojiri, Y., Gruber, N., Doney, S. C., McKinley, G. A., Lenton, A., Le Quéré, C., Heinze, C., Schwinger, J., Graven, H., and Khatiwala, S.: Global ocean carbon uptake: magnitude, variability and trends, Biogeosciences, 10, 1983–2000, https://doi.org/10.5194/bg-10-1983-2013, 2013.

Wu, S., Mickley, L. J., Jacob, D. J., Logan, J. A., Yantosca, R. M., and Rind, D.: Why are there large differences between models in global budgets of tropospheric ozone?, Journal of Geophysical Research: Atmospheres, 112, https://doi.org/10.1029/2006JD007801, 2007.

Wunch, D., Wennberg, P. O., Osterman, G., Fisher, B., Naylor, B., Roehl, C. M., O'Dell, C., Mandrake, L., Viatte, C., Kiel, M., Griffith, D. W. T., Deutscher, N. M., Velazco, V. A., Notholt, J., Warneke, T., Petri, C., De Maziere, M., Sha, M. K., Sussmann, R., Rettinger, M., Pollard, D., Robinson, J., Morino, I., Uchino, O., Hase, F., Blumenstock, T., Feist, D. G., Arnold, S. G., Strong, K., Mendonca, J., Kivi, R., Heikkinen, P., Iraci, L., Podolske, J., Hillyard, P. W., Kawakami, S., Dubey, M. K., Parker, H. A., Sepulveda, E., García, O. E., Te, Y., Jeseck, P., Gunson, M. R., Crisp, D., and Eldering, A.: Comparisons of the Orbiting Carbon Observatory-2 (OCO-2) XCO_2 measurements with TCCON, Atmospheric Measurement Techniques, 10, 2209–2238, https://doi.org/10.5194/amt-10-2209-2017, 2017.

Yin, L., Tao, F., Zhai, R., Chen, Y., Hu, J., Wang, Z., and Fu, B.: Impacts of Future Climate Change and Atmospheric CO_2 Concentration on Ecosystem Water Retention Service, Earth's Future, 10, e2021EF002138, https://doi.org/10.1029/2021EF002138, 2022.

Chapter 4 Quantifying the Potential Influence of Arctic Permafrost Thawing on Atmospheric CO_2

Abstract

The Northern permafrost region covers a quarter of the Northern Hemisphere's land and contains nearly twice the amount of carbon (~1600 PgC) currently stored in the Earth's atmosphere. The warming due to anthropogenic carbon emissions, which for the Arctic is over twice as fast as the global mean, is causing permafrost to thaw and microbial decomposition release – with a potential for positive carbon-climate feedbacks on par with anticipated emission reductions. Despite the critical role of Arctic permafrost degradation in the global carbon budget, it remains challenging to quantify and separate emissions of old carbon from permafrost from labile high-latitude carbon.

In this study, we quantify permafrost-driven atmospheric CO_2 enhancement using the GEOS-Chem atmospheric transport model with tagged CO_2 species originating from permafrost sources in North America, Europe, and Asia. Land-atmosphere net ecosystem CO_2 exchange from an atmospheric inversion was adjusted by adding 1 Pg C/y of additional carbon release to North American, European, and Asian Arctic regions. We conduct two sensitivity tests (1) in which the additional 1 Pg C/y is uniformly released across the annual cycle and (2) in which the additional carbon release follows the seasonal cycle of heterotrophic respiration from labile carbon. CO_2 tagging to individual Arctic regions enables quantification of fingerprints of each subregion and the whole Northern Permafrost on atmospheric partial column CO_2 dry mole fraction in the lower or upper troposphere.

We explore the detectability of these perturbations using an Observing System Simulation Experiment based upon a hypothetical satellite mission that employs a multi-spectral imaging spectrometer with channels in the thermal infrared and shortwave infrared, capable of providing two pieces of vertical information about the CO_2 abundance. We sampled the GEOS-Chem transport simulations using a realistic sampling pattern to generate pseudo-observations. During summertime, 1 Pg C/y of additional carbon release from North American permafrost can cause a mean of 3.5ppm and as large as 6ppm partial XCO_2 increase in the lower troposphere, which is potentially detectable from space. The CO_2 release from the permafrost has a much larger influence on the lower troposphere than the upper troposphere - the difference is as large as 3.5 ppm near the source region and as low as 0.5 ppm in a remote area.

4.1 Introduction

The northern hemisphere permafrost area is approximately 14 million km^2 – equal to 15% of the exposed land surface area, yet permafrost soils store about 60% of the world's soil carbon (Turetsky et al., 2020). Much of this permafrost is critically vulnerable to climatic and disturbance-induced changes. Since 1981, the global temperature warming rate is 0.32° F (0.18° C) per decade (IPCC, 2021), and in high latitudes of the Northern Hemisphere, temperatures have been rising twice as fast as the global average - which is a phenomenon known as arctic amplification (Previdi et al., 2021). Such rapid warming and shifting climatic conditions are causing Arctic permafrost to become a substantial carbon source to the atmosphere (Turner et al., 2020).

Current estimates report 1200 Pg C in the active layer (where the soil freezes and thaws seasonally) and around 500 PgC in deeper Yedoma (carbon-rich Pleistocene-age permafrost with 50–90% ice content by volume) and deposits (Strauss et al. 2013; Biskaborn et al., 2019).

Seasonal thawing of the active layer begins in spring when air temperatures rise above 0 °C and snow cover is removed. The temporal and spatial variations of these seasonal freeze-thaw processes within the active layer are a major determinant of permafrost vulnerability and can be influenced by factors including temperature, snow depth, vegetation coverage, land topography, soil moisture, precipitation, and disturbance such as wildfire and land-use change (Douglas et al., 2020; Neumann et al., 2019). Systematic climate warming and related climatic changes are the main cause of gradual permafrost thaw, while extreme temperature or episodic events such as wildfires (Scholten et al., 2021; Mack et al., 2021) can cause abrupt thaw. Both the abrupt and gradual thawing of permafrost can expose larger quantities of organic carbon to aerobic conditions to decompose, and carbon can also be mobilized by erosion from upland soils into water systems (Schwab et al., 2020; Vonk et al., 2015). In this way, human-induced climate warming cause Northern Hemisphere permafrost regions to emit greenhouse gases into the atmosphere, generating positive feedback to make climate change happen faster than expected based on projected emissions from human activities alone (Natali et al., 2019; Schuur et al., 2015).

The need to understand these emissions is critical given that climate simulations indicate that by next century, permafrost area could decrease by 3 to 5 million km^2 (4PgC) under the Representative Concentration Pathway 4.5 (RCP4.5) scenario and by 6 to 16 million km^2 (341PgC) under the Representative Concentration Pathway 8.5 (RCP8.5) scenario, and abrupt thaw over the twenty-first century will lead to a CO_2 feedback of 3.1PgC per °C global temperature increase based on RCP8.5 projection, and RCP4.5 CO_2 feedback from abrupt thaw is 2.3PgC per °C increase, but increases to 11.6PgC per °C increase beyond the twenty-first century (Walter et al., 2018). Currently, the Earth system models framework applied to the

northern permafrost region mainly focuses on how the thickness and changing of the hydrological state of the permafrost active layer (Fisher et al., 2018; Burke et al., 2020). However, there are considerable uncertainties in the thawing rate and extent, the vegetation response, the characteristics of regional heterogeneities in soil properties, the decomposition timescales, and the effect of arctic amplification of global warming on permafrost degradation, which may result in an underestimate of the carbon emissions from thawing permafrost (Jin et al., 2021; Mishra et al., 2021).

Detailed monitoring and characterization are required to better understand permafrost vulnerability, seasonal and interannual changes, and the thawing and degrading processes. In-situ observations such as NOAA Earth System Research Laboratories Global Monitoring Laboratory and FLUXNET eddy covariance towers can quantify trace gas concentrations in the boundary layer or help quantify net carbon fluxes. Atmospheric CO_2 observations, however, are sensitive to large concentration footprints (>1000 km). Flux towers are localized data with few locations, limited coverage, and sensitivity (Schimel, D. & Schneider, F. D, 2019), thus have limitation in detecting carbon release from permafrost, especially episodic events. Airborne campaigns such as HIAPER Pole-to-Pole Observations (HIPPO) target measurements in the troposphere provides regional coverage and vertical profiles from several hours to days, and can bridge spatial scales between in-situ and satellite observations. Yet the campaigns are usually offering short-term snapshots, not routine monitoring. Previous studies focused on CO_2 flux measurements have produced results that have not been fully agreed upon. For instance, Belshe et al. (2013) suggested that the tundra remained a general carbon source of 0.462 Pg C per year. The recent NASA campaign (Commane et al. 2017) found tundra Alaska to be a consistent net CO_2 source to the atmosphere, whereas the boreal forest region was either neutral or a net CO_2 sink due to

the interannual variation of photosynthesis and respiration and the combustion emissions by wildfire. The differential response of individual ecosystem types and the relative scarcity of measurement sites across the Arctic region makes it difficult to upscale the aggregated effect of ecosystems, including tundra, boreal forests, and wetland/lake/fresh water. The long cold Arctic winter season limits both Airborne and ground-based observations, due to operating difficulties. Space-based shortwave infrared satellite observations dedicated to monitoring the carbon cycle, including GOSAT (Kuze et al.,2016), OCO-2 (Eldering et al., 2017), GHGSat, CO_2M, Sentinel-5 circulating in the low Earth orbit, provide monthly to seasonal coverage, and are creating multi-year dataset records for the research community. However, carbon loss in winter and shoulder seasons (fall and spring) is difficult to observe given the high solar viewing angles and the fact that all the missions above use reflected solar sunlight in the NIR. Microbes rely on fresh plant matter in summer but older organic matter from fall to winter to spring, and the polar night can serve as a critical period for climate-vulnerable permafrost Carbon pools (Pedron et al.,2022). Moreover, the current satellites, either operating with a low Earth orbit (LEO) or geosynchronous orbit (GEO), are not especially well suited to provide observations for carbon cycle studies at northern high latitudes. LEO is sun-synchronous – a satellite passes over a given point on the Earth at a fixed time of day, but obtaining adequate temporal coverage requires multiple LEO satellites (Velazco et al., 2011). GEO can offer continuous coverage, yet observations are limited to ~55°S–55°N, and the difficulty remains when viewing higher latitudes caused by the large nadir viewing angles.

In this study, we quantify the detectability of permafrost thaw using a hypothetical observing system that represents the next generation of space-based carbon observations, to determine the observable atmospheric CO_2 enhancement owing to permafrost thawing by

simulating three-dimensional atmospheric CO_2 using the GEOS-Chem atmospheric transport model with tagged CO_2 species originating from boreal and Arctic regions across North America, Europe, and Asia. Our analysis points toward and provides preliminary estimates of observational requirements to identify signals from the Northern Permafrost regions using space-based observations.

4.2. Data and Methods

We perform an Observing System. Simulation Experiment (OSSE) to determine the feasibility of detecting permafrost carbon losses from space. Our OSSE is based on a multispectral imaging spectrometer (Natraj et al., 2022) in a highly elliptical Molniya orbit, with an inclination of 63.4 degrees, an argument of perigee of 270 degrees, and an orbital period of approximately half a sidereal day (Trichtchenko et al., 2019). In this orbit, the spacecraft would see the Pan-Arctic (north of 48N) for at least 8 hours of every 12-hour period. For this study, we make a conservative assumption that the spacecraft would be able to image the Pan-Arctic only twice per day. This observing system is used to sample atmospheric CO_2 in the GEOS-Chem atmospheric transport model in simulations with and without enhanced permafrost carbon emissions. We analyze pseudo observations based on our simulations to quantify CO_2 enhancements that could be seen given a perfect sampling system and a realistic sampling system based on the orbit and instrument characteristics. The observing system and atmospheric simulations are described below.

4.2.1 Multispectral Imaging Spectrometer

The multispectral imager would measure CO_2 absorption spectra in the shortwave infrared (SWIR) region at 1.6 and 2.0 μm, and those in the thermal infrared (TIR) regions at 4.6, 10, and 15 μm. Observations in these two spectral bands provide the potential for two vertical

pieces of information since SWIR observations are sensitive to the near-surface where carbon exchange occurs and TIR observations are sensitive to the upper free troposphere. TIR observations do not require reflected sunlight and therefore may provide observational constraints on carbon losses during winter and shoulder seasons.

Similar to Natraj et al., (2022) synthetic retrievals were performed to determine the precision and vertical sensitivity of the information from these spectral channels. Briefly, the averaging kernel as a function of altitude defines the relation between the retrieved quantities and the true atmospheric state. The averaging kernels are computed for every scene as part of the retrieval algorithm, starting with an estimate of the initial state of the atmosphere and the surface, then using the Jacobians and the retrieval constraint in the forward model, which would account for the radiative transfer in the atmosphere, satellite observation geometry (solar zenith angle, viewing angle), properties of clouds, surface properties, the presence of other tracers and aerosols, spectral line strengths and instrument aspects. As an output of this algorithm, the averaging kernel (defined as AK) is a valid concept for interpreting the optimal estimation retrieval. Figure 4.3 and Figure 4.4 show the Pseudo averaging Kernel for TIR and SW band detections for different months, AK = 1,2,21,22 are for OCT to MAY (assuming solar zenith delta T = 0.72); AK = 4,5,24,25 are for JUN and JUL (assuming solar zenith delta T = 1.2); AK = 5,7,25,27 (assuming solar zenith delta T = 1.5) are for AUG and SEP. AK = 2, 5, 22, 25 are based on the assumption that land is covered by snow; AK = 1,4,7,21,24,27 are based on the assumption that land is covered by forest. The TIR AK (Fig 4.3) peaks at 0.2hPa, but the SWIR (Fig 4.4) peaks from the low to mid-troposphere, and more rapid increases in the lower troposphere.

In the analysis described below, we apply the averaging kernels to the simulated atmospheric CO_2 to generate "realistic" pseudo observations. Because only a limited number of synthetic retrievals were conducted, we map the AKs to all locations and seasons in the Pan-Arctic based on presence or absence of snow, vegetation type of the underlying surface, and mean solar zenith angle of a particular location and month.

4.2.2 GEOS-Chem Simulations

We simulate atmospheric CO_2 using GEOS-Chem (Bey et al., 2001), an offline global chemical transport model driven by meteorological input from the Goddard Earth Observing System (GEOS) of the NASA Global Modeling and Assimilation Office (GMAO) and developed by an extensive global community of researchers. It has been widely used for carbon gas flux inversion and source attribution (Nassar et al., 2010; Fisher et al., 2017). We use version 12.0.0 of GEOS-Chem which was released in Aug 2018.

The meteorological inputs for GEOS-Chem come from the Modern-Era Retrospective analysis for Research and Applications, 80 Version 2 (MERRA2) reanalysis, with the dynamic time step set to be 600s. The model is initialized with a globally uniform atmospheric CO_2 mole fraction equal to 410 ppm. We run simulations at 2° in latitude by 2.5° in longitude with 47 vertical levels up to 0.01 hPa on a hybrid eta (sigma-pressure) grid. Convective transport in GEOS-Chem is simulated with a single-plume scheme (Wu et al., 2007); while boundary layer mixing in GEOS-Chem uses the non-local parameterization (Lin and McElroy, 2010) which draws on the mixing depths, temperature, latent and sensible heat fluxes, and specific humidity. Although bias in the vertical distribution of CO_2 has been shown in GEOS-Chem for northern high latitudes (Schuh et al., 2019), similar tagged transport runs have been shown to agree favorably with observations (Lin et al., 2020).

To simulate CO_2 fields, we use realistic net ecosystem exchange (NEE) as the lower boundary condition to the atmospheric model. In this study, we follow the patterns of monthly land fluxes from the CAMS CO_2 global inversion v17r1 (Chevallier et al., 2019), which covers 1979 to 2017 with a spatial resolution of 1.875° in latitude by 3.75° in the longitude to get the estimates of net ecosystem exchange, and represents the carbon balance of the land. The net fluxes include contributions from the natural biosphere including vegetation and wetlands. Based on the comprehensive synthesis estimation for CO_2 emissions from thawing permafrost across the Arctic region, which shall be between 5 and 15% of the permafrost carbon pool over decades and centuries under RCP 8.5 pathway, the magnitude of annual CO_2 release of ~0.5–2 Pg C/yr (Schuur and Mack, 2018). Therefore, we adopt a setting that the carbon fluxes exchange between the permafrost and the atmosphere to be 1PgC/yr for each of the Arctic terrestrial ecosystems region in each single simulation run, in which we consider permafrost thawing as an important accelerator to climate change on a similar scale to land-use change.

We simulate atmospheric CO_2 contributions from individual subregions, from 2011 to 2016, including a 3-year spin-up, by modifying the GEOS-Chem code base to tag the source regions and separately track different CO_2 species originating from each region (Lin et al., 2020). This approach is possible since CO_2 is a passive tracer that is not involved in chemical reactions. In this baseline simulation, each CO_2 tracer corresponds to the influence of NEE CO_2 fluxes from one tagged region, which is defined as 10 tagged regions for terrestrial ecosystems (Fig 4.1), including North America Arctic, European Arctic, Siberian Arctic, four boreal, two temperate ecosystems, with the combined regions of Equatorial and Southern Hemisphere Terrestrial. The delineation of these ecosystems was mostly according to the dominant plant functional types (PFTs), together with the climate zones into account (Lin et al., 2020). We

calculate XCO_2 in the GEOS-Chem runs by integrating the dry air mole fraction for the 47 model layers.

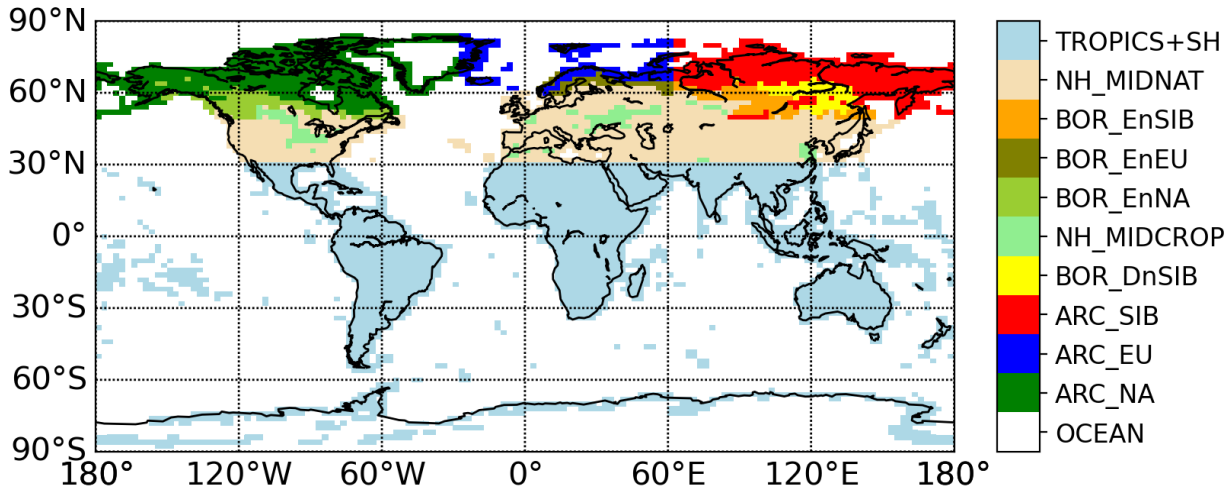

Figure 4.1: *The tracers defined for the tagged GEOS-CHEM 3D atmospheric transport simulations based on different vegetation types.*

4.2.3 Perturbations to Represent Permafrost Loss

We perturb the NEE fluxes from CAMS in two ways to represent additional carbon losses from permafrost (Fig 4.2). First, we use heterotrophic respiration (Rh) from the Carnegie-Ames-Stanford Approach (CASA; Olsen and Randerson 2003) model at 1 by 1° resolution to represent the baseline mean annual cycle of respiration. Rh fluxes of the CASA model are based on a compartmental pool structure, which simulates the loss of CO_2 from decomposing plant residue and surface soil organic matter (SOM) pools. We add a monthly enhancement to the CASA Rh, distributing 1 Pg C of total annual increase over the annual cycle proportional to the CASA Rh estimate for any given month (Fig 4.5). This enhanced Rh is added to the original NEE fluxes in Arctic North America, or Arctic Europe, or Arctic Siberian so that there is a net source of carbon to the atmosphere from the individual regions. In the second type of

configuration, we add a uniform monthly Rh enhancement, again with 1 Pg C of total annual increase, for each of the 3 Arctic Regions. As a following step, we execute six enhanced respiration simulations, separately quantifying the atmospheric imprint of permafrost thaw in the 3 source regions, with type 1 (Fig 4.2 a-c) or type 2 (Fig 4.2 d-f) thawing settings. We then separately track and attribute the enhancement of atmospheric CO_2 by comparing results from the perturbation simulation with those from the baseline simulation.

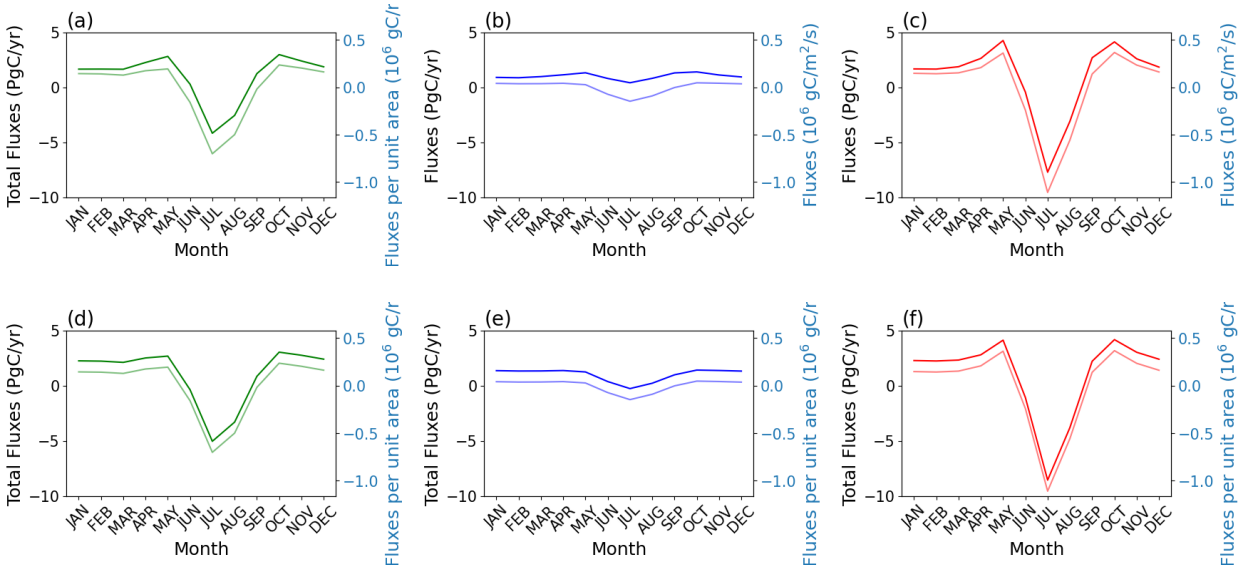

Figure 4.2: *The input fluxes in the 2 types of the simulation run mirroring the permafrost thawing process. (a)-(c) shows the fluxes reflecting thawing with a seasonal cycle; (d)-(f) shows the fluxes with uniform thawing throughout the year.*

4.2.4 Analysis Framework

Starting with the GEOS-Chem nature run and enhanced emissions runs described above, we sample the simulations to produce pseudo-observations. First, we integrate total column XCO_2 and lower tropospheric (LT) and upper tropospheric (UT) partial columns. The LT is sensitive to pressures greater than 500 hPa and the UT is sensitive to pressures less than 500 hPa. For a "perfect" observing system, we assume that the AKs equal unity for all pressures. For a

"realistic" observing system, we apply the SWIR and TIR AKs (Fig 4.3 and Fig 4.4). We also calculate a ΔCO_2 value, which represents the difference between the LT and UT partial columns and may reflect the magnitude of the underlying surface fluxes.

We propagate error in our estimates of the CO_2 enhancements based on the synthetic retrieval precisions. We assume a 4 km footprint; thus 3850 observations can be detected within a 2x2.5 degree gridcell, of approximately 220 km (north to south) by 280 km (east to west). Error is calculated as the square root of the sum of lower troposphere CO_2 enhancement error, upper troposphere CO_2 enhancement error, and total column CO_2 enhancement standard deviation, over the number of the cloud free pixels.

We also apply a cloud mask, since clouds can corrupt both the shortwave infrared reflectance and thermal infrared emission signal, therefore we mask our sampling. We apply a mask generated from the cloud fraction based on the MODerate-resolution Imaging Spectroradiometer (MODIS) Cloud Product Daily Global Level 2 data at 1-km spatial resolutions resolution and hourly temporal resolution to mask for the presence of clouds. The algorithm combines infrared and visible techniques to determine both physical and radiative cloud properties, specify confidence for an unobstructed view, and identify scenes where land and ocean should be retrieved based upon the degree of surface obstruction caused by cloud.

Throughout the rest of the paper, we analyze only the simulation with enhanced Rh from North America distributed according to the seasonal cycle of Rh (Fig 4.6 – Fig 4.12).

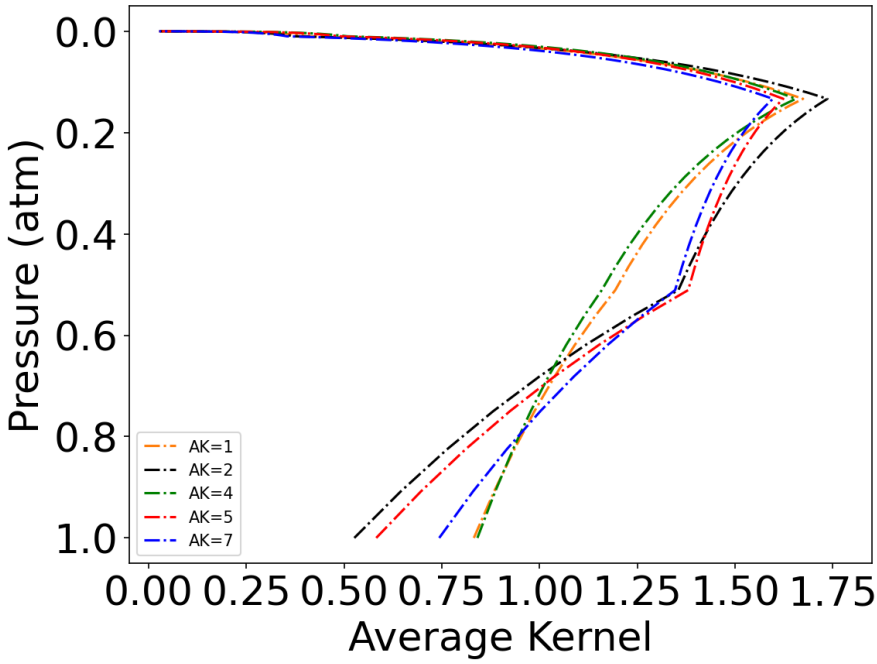

Figure 4.3: *The Pseudo averaging Kernel of the space-based satellite TIR band detections for different months, AK = 1 and AK = 2 are for OCT to MAY (assuming solar zenith delta T = 0.72); AK = 4 and AK = 5 are for JUN and JUL (assuming solar zenith delta T = 1.2); AK = 5 and AK = 7 (assuming solar zenith delta T = 1.5); are for AUG and SEP. AK = 2, 5 are based on the assumption that land is covered by snow; AK = 1,4,7 are based on the assumption that land is covered by forest.*

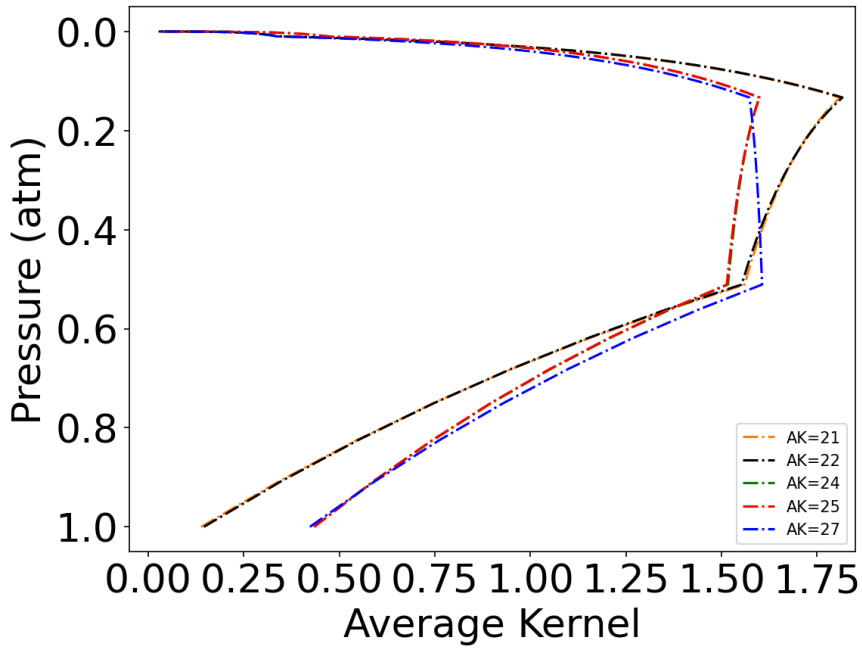

Figure 4.4: *The Pseudo averaging Kernel of the space-based satellite TIR band detections for different months, AK = 21 and AK = 22 are for OCT to MAY (assuming solar zenith delta T = 0.72); AK = 24 and*

AK = 25 are for JUN and JUL (assuming solar zenith delta T = 1.2); AK = 25 and AK = 27 (assuming solar zenith delta T = 1.5); are for AUG and SEP. AK = 22, 25 are based on the assumption that land is covered by snow; AK = 21,24,27 are based on the assumption that land is covered by forest.

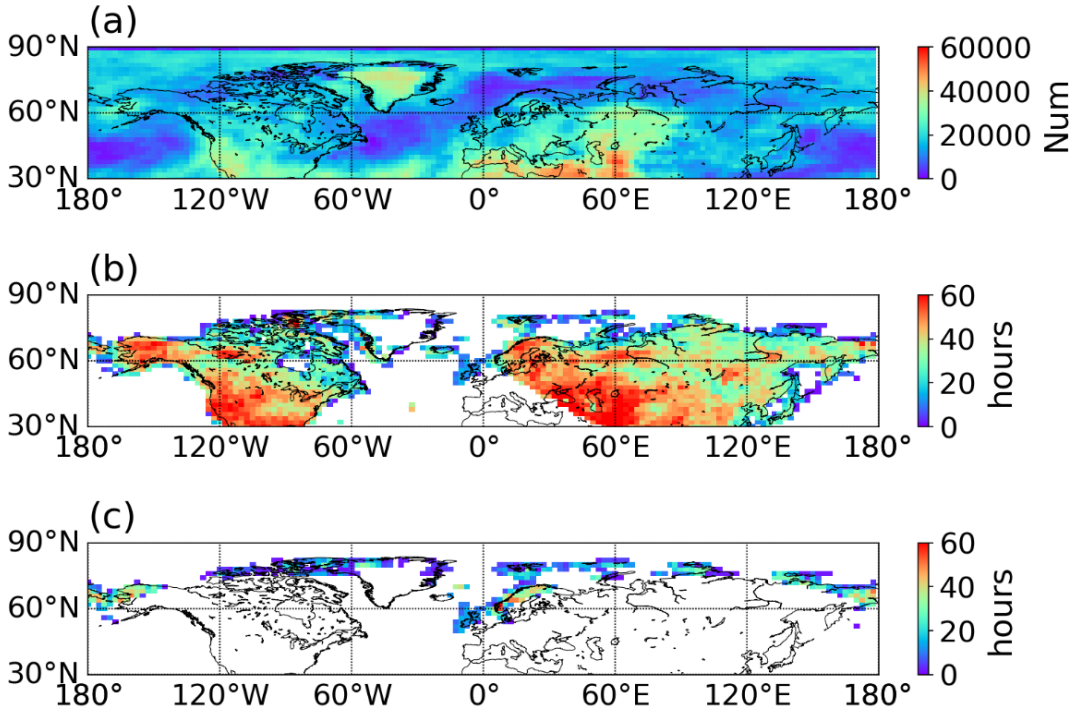

Figure 4.5: *(a) Cloud-free pixels of the space-based satellite detections for July based on MODIS 0.25 degree cloud mask and assumption of a 4x4 km satellite footprint. (b) Number of hours favorable to TIR sampling assuming a possibility of two satellite overpasses per day, where and how many hours that TIR band has detectability, (c) shows the regions where and how many hours that SWIR band has detectability.*

4.3 Results

Given a perfect observing system (AK=1 and no cloud masking), the total column XCO_2 enhancement for July is typically around 3 ppm over the North American source region given a 1 Pg C y^{-1} enhancement distributed according to the seasonal cycle of heterotrophic respiration (Fig 4.6a). In the upper troposphere, less than 0.6 ppm of increase can be generated in the summertime July, when the emission is the strongest and most intense (Fig 4.6b). By contrast, the lower troposphere can have an increase of up to 4.5 ppm over the Arctic North America

emission sourcing region (Fig 4.6c). The influence from the upper troposphere is subtle – since the difference in the CO_2 enhancement between the lower and upper troposphere is nearly as large as that of the total column (Fig 4.6c). We highlight a longitudinal and a latitudinal transect that intersects over boreal Canada, which shows that most of the enhancement is below 500 hPa (Fig 4.6e and Fig 4.6f).

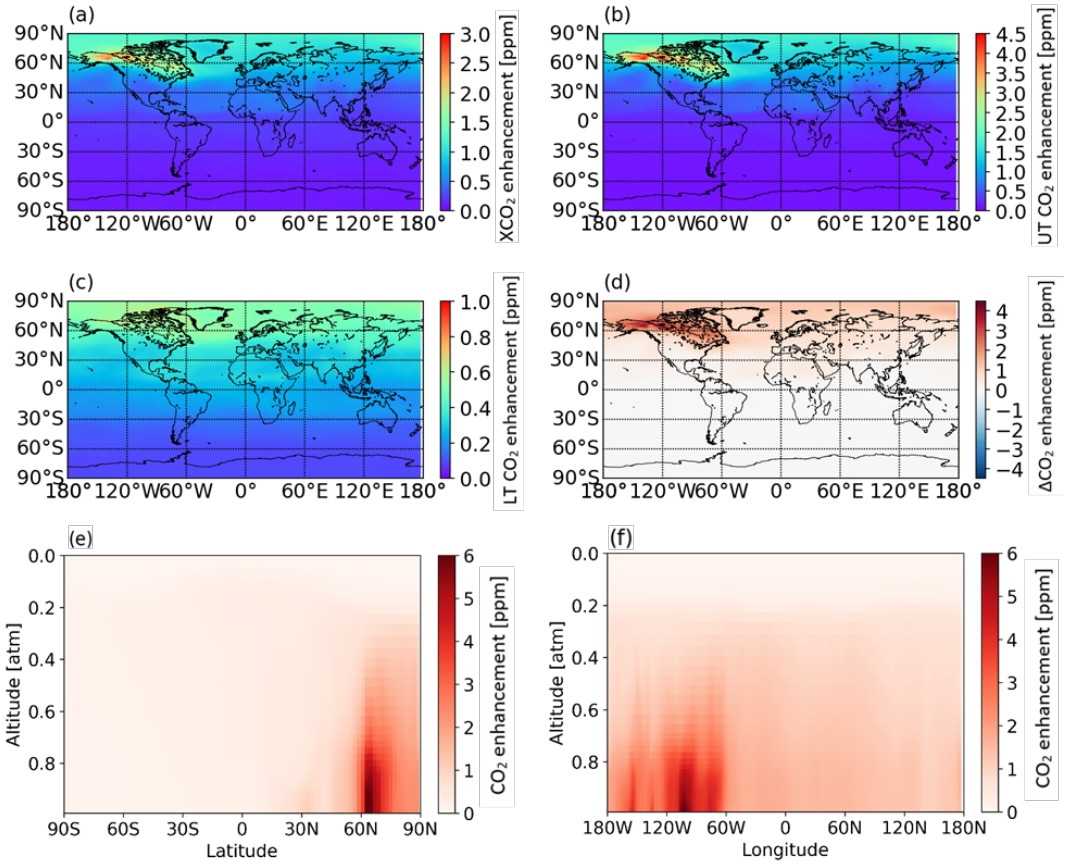

Figure 4.6: *Difference (enhancement) in CO_2 variables between simulations with enhanced respiration and baseline NEE. All panels show monthly mean data for July. (a) Total Column XCO_2 enhancement, (b) Lower Tropospheric Partial Column, (c) Upper Tropospheric Partial Column UT CO_2 enhancement, (d) Δ(UT-LT) CO_2 enhancement, (e) north-south cross-section in the CO_2 mole fraction enhancement along 120°W (f) east-west cross-section in the CO_2 mole fraction enhancement along 60°.*

The time series of monthly mean XCO_2 enhancement for our simulation show a summer peak, consistent with the period of maximum emissions, with a secular increase over the 12 months simulated due to the continued accumulation of the 1 Pg anomalous flux (Fig 4.7). The

partial column CO_2 in the lower troposphere shares the same pattern, albeit with a stronger signal up to 1 ppm larger than for XCO_2. The upper partial column has an increasing trend throughout the year, with minimal seasonality arising from the seasonality of fluxes at the surface. The vertical contrast ΔCO_2 between upper and lower troposphere peaks with surface emissions, and notably shows a larger decrease after peak emissions compared to the total column, more closely tracking fluxes (Fig 4.7c vs 4.7a).

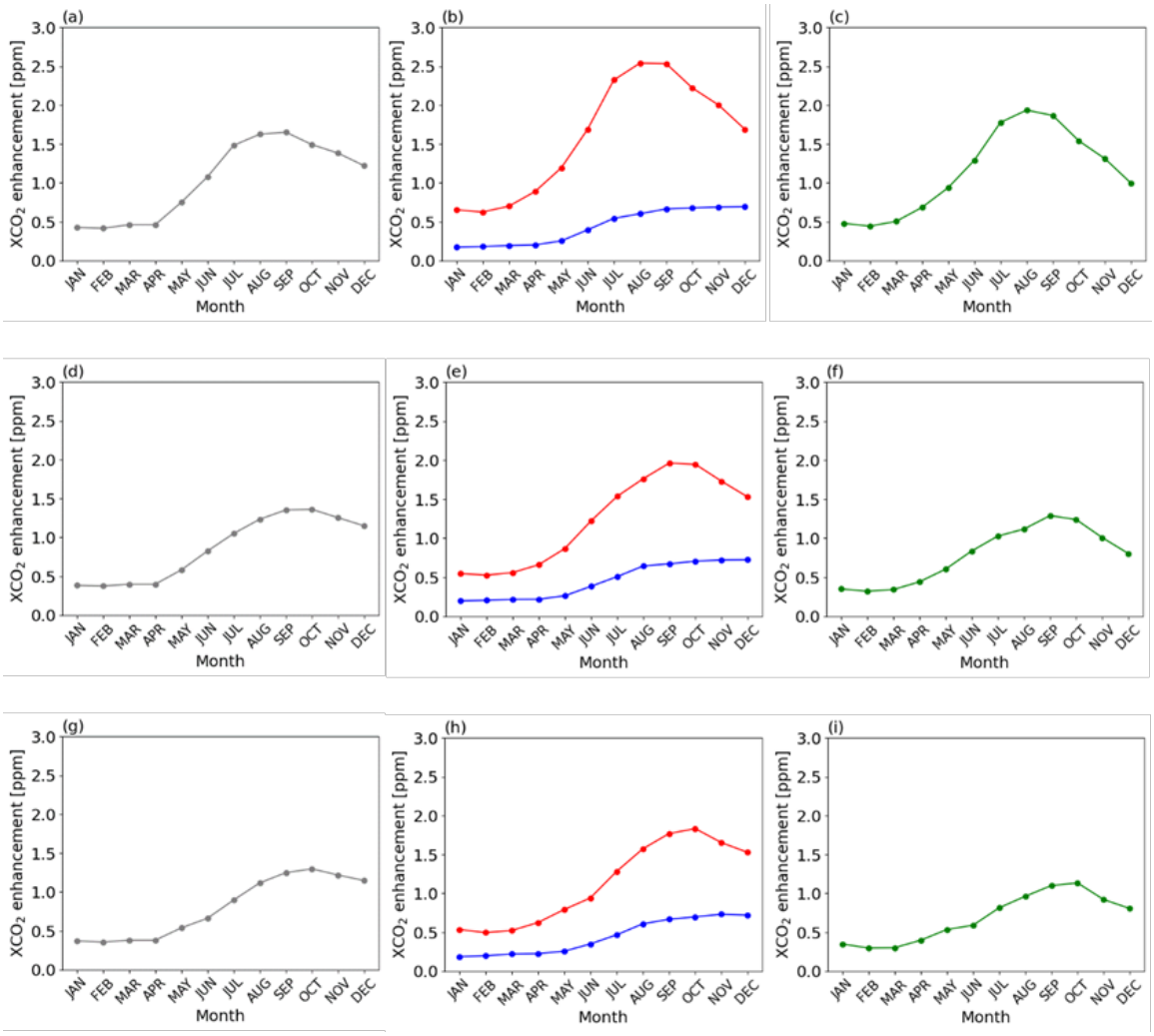

Figure 4.7: *Simulated Monthly Mean CO_2 enhancement over NA arctic Region for 2015 JAN to DEC, with model input fluxes from North America, for Total Column (a), Lower (Blue) and Upper Troposphere (RED) (b), and the difference between Upper and Lower Troposphere (c). (d)-(f) is over EU arctic Region, (g)-(h)is over SIB arctic Region.*

Histograms of hourly CO_2 enhancement at 12 sample locations within the Arctic (Fig 4.8) show substantial variation in LT CO_2 enhancement over the North American source region (Fig 4.9). During the 744 hours in July, the sites within the North American source region show a flat distribution of LT CO_2 within the month, with enhancements up to 3 ppm (Fig 4.9a-d, Fig 4.10a-d). Outside the source region, sites closer to the source (e.g. MBC and TER, in Fig 4.9e-f, Fig 4.10e-f) show smaller mean enhancements, albeit with a heavy tail between 2-3 ppm enhancement. In contrast, sites in Europe and Asia show reduced variability with hourly enhancements typically less than 1.5 ppm with a tighter distribution (Fig 4.9g-n).

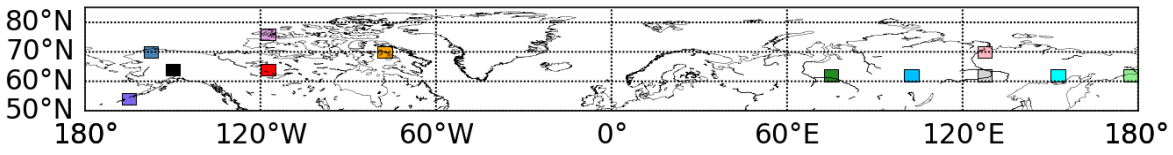

Figure 4.8: *Maps of the selected sample locations in the mid-lat to the high-lat Northern Hemisphere.*

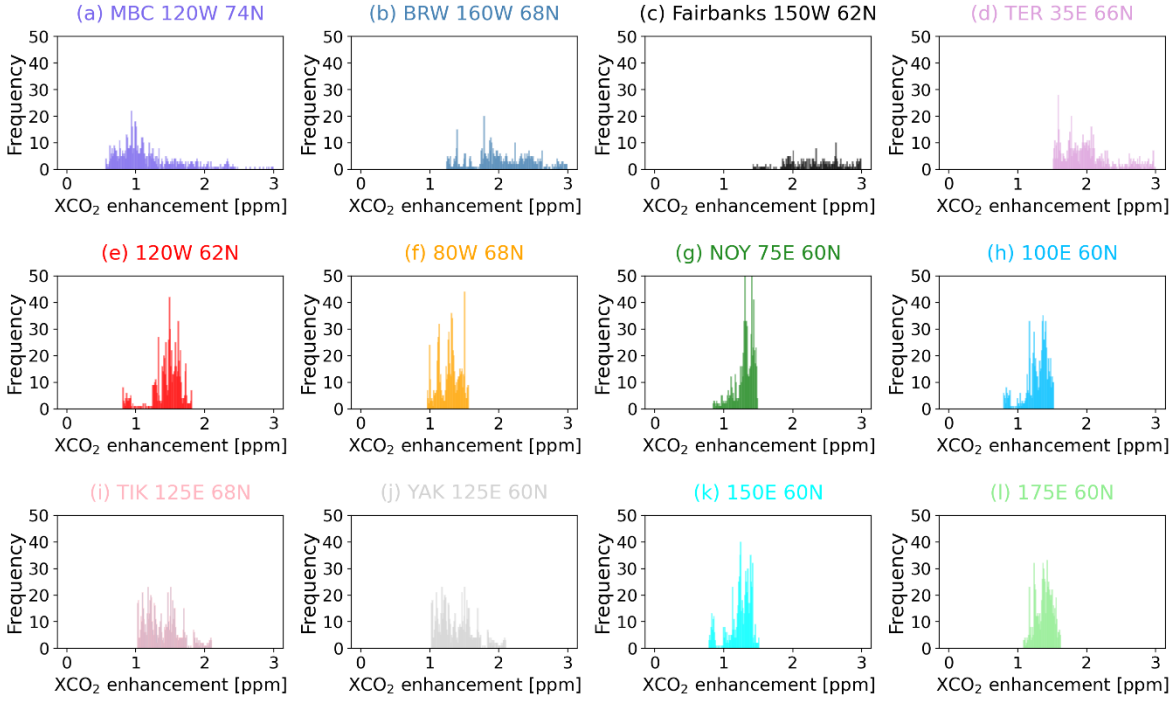

Figure 4.9: *Histogram showing monthly Lower Troposphere CO_2 enhancement of the NA permafrost thawing generated CO_2 enhancement over the selected locations, listed in the order from the west to the east.*

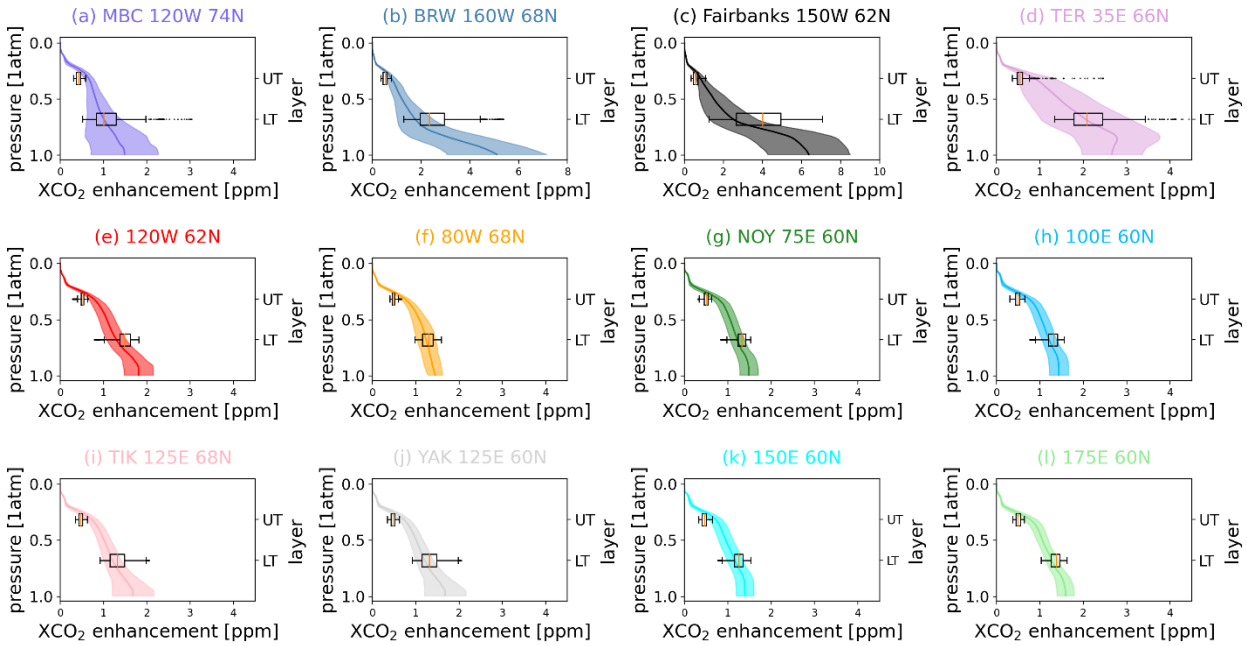

Figure 4.10: *Monthly mean (bold) and STD (shading) of the vertical profile of the permafrost thawing generated CO_2 enhancement over the selected locations, with Comparisons of the mean and STD of CO_2 enhancement between UT and LT over.*

The vertical contrast ΔCO_2 is a sensitive diagnostic for the underlying surface flux (Fig 4.11). XCO_2 (Fig 4.11a) and the lower tropospheric partial column (Fig 4.11b) are both positively correlated with the flux anomaly but also reflect the large-scale flux accumulation (evidenced by the ~1ppm contrast between the January and December values, despite having the same underlying surface flux). The upper tropospheric partial column does not correlate well with the flux anomaly at the surface (Fig 4.11b). In contrast, the ΔCO_2 shows a strong positive correlation (Fig 4.11c) with only a 0.5 ppm difference between December and January when the underlying flux was the same. Nevertheless, over Europe and Siberia, far from the enhanced North American source, the enhancements mirror the pattern over North America with a monthly mean magnitude that can be 75% that of the source region.

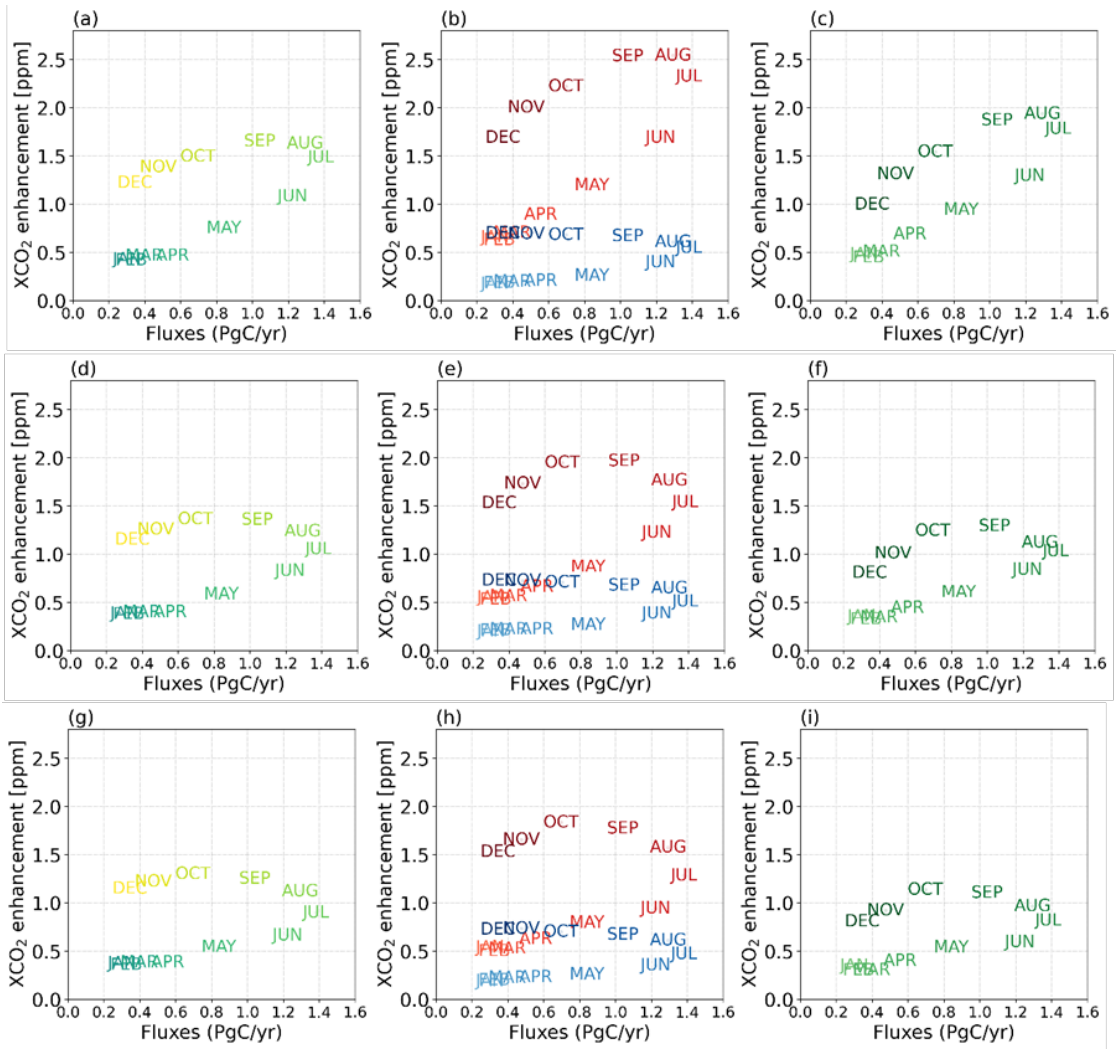

Figure 4.11: *Land-Atmosphere exchange fluxes seasonal cycle vs Simulated Monthly Mean XCO_2 enhancement for 2015 JAN to DEC, with model input fluxes from North America, for Total Column (a,d,g), Lower Troposphere (Blue) and Upper Troposphere (Red), and the difference between Upper and Lower Troposphere (c,f,i). (a)-(c) over NA Arctic, (d)-(f) over EU Arctic, (g)-(i) over SIB Arctic.*

The above analysis reflects perfect sampling, but results appear robust when realistic sampling, with the application of cloud masks and averaging kernels, is applied. In Figure 4.12, during July, the expected satellite detected XCO_2 enhancement due to permafrost thawing at the scale of 3.5ppm, and with the coverage to the northern regions over all continents, the estimated detection error is less than 10% of the idealized detection signal, indicating the latent reliability and precision. In Figure 4.13, during the shouldering season in September, there is still

promising coverage of the XCO_2 signal with only minor loss near the Northern coastal edges, implying the great potential of monitoring the atmospheric CO_2 in the Arctic, which could help fill the vacuums of current observations.

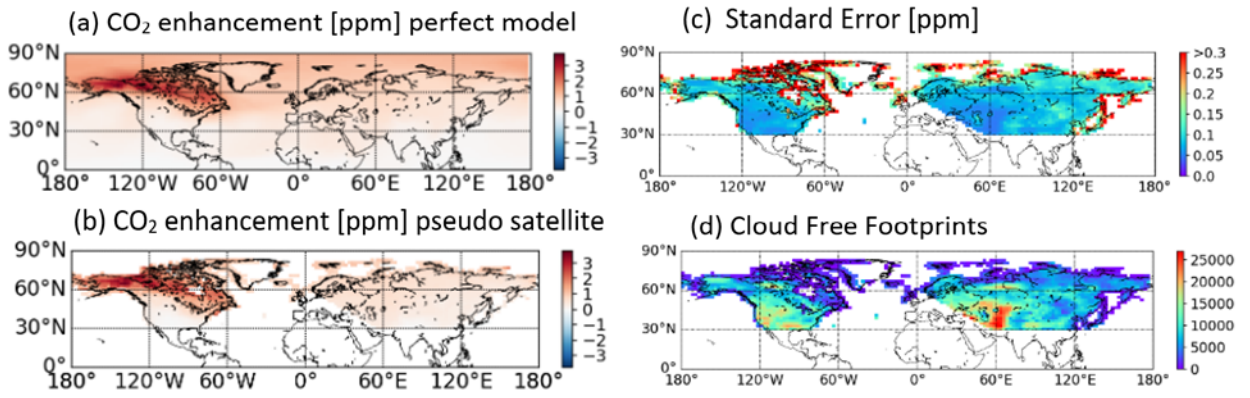

Figure 4.12: *The comparison of the ideal modeled, the expected satellite detected XCO_2 enhancement, and the estimation of detection error due to NA permafrost thawing mirroring the NEE cycle, using 2015 July as an example.*

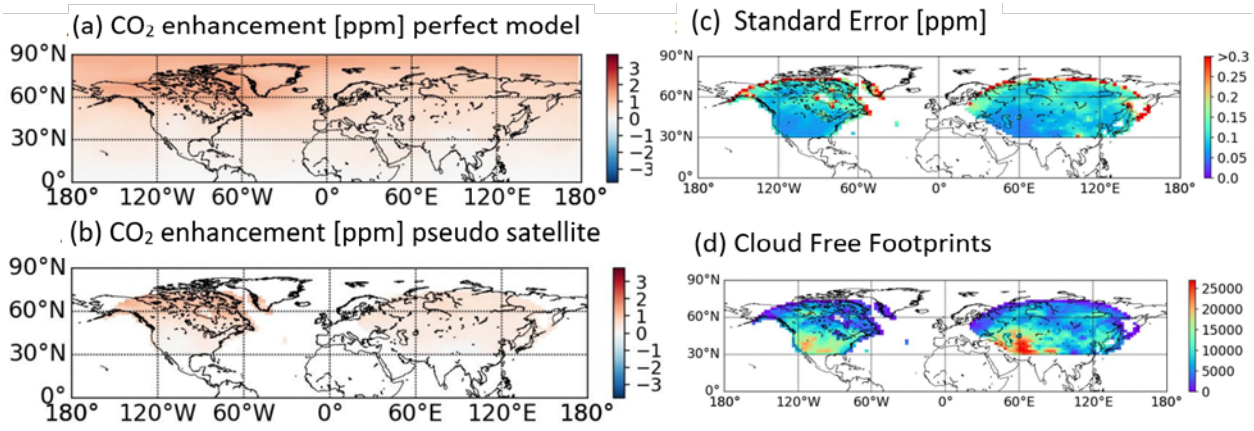

Figure 4.13: *The comparison of the ideal modeled the expected satellite detected XCO_2 enhancement, the estimation of detection error due to NA permafrost thawing mirroring the NEE cycle, using 2015 September as an example.*

4.4 Discussions

TIR has the advantage of providing both day and night continuous measurements in either summertime, wintertime and shouldering seasons. The column averaged CO_2 enhancement from the pseudo satellite observation shows the promising potential capability to capture the atmospheric XCO_2 annual variation (Fig 4.11) which reflects the seasonal cycle of the land fluxes from permafrost thawing and Net Ecosystem Exchange. The ideal 2x2.5 degree high-resolution sounder would help to attain a substantial gain of information mostly due to their broader spectral coverage and finer resolution. Therefore, the ideal XCO_2 from measurements could reach the precision of 0.1 ppm on a monthly time scale, with an estimated error of less than 1 percent (Fig 4.12 and Fig 4.13). The OSSE described in this study demonstrates that TIR retrieved pseudo XCO_2 from a designed mission provides improved constraints on Northern Arctic CO_2 fluxes relative to current satellite missions since it offers better observations during winter months and Northern Arctic Latitudes. Future space instruments could consider this wide range of values to obtain CO_2 concentrations regionally, and possibly extend the CO_2 monitoring system over Southern Hemisphere Antarctica.

Despite the encouraging performance of the perfect model and pseudo satellite observation in estimating CO_2 concentration, we understand that there will be challenges to assimilating the high-temporal-resolution data from the sounding detections, the generates difficulty in rapid evolving processes (e.g. sudden emission events). The spacecraft would only be able to pass the Pan-Arctic only once per day. Although the overpasses occur at various times per day, and we could aggregate the detections into larger gridcells, it would remain challenging to get the XCO_2 diurnal cycle in fine scales from spaceborne observations.

4.5 Conclusions

We quantify permafrost-driven atmospheric CO_2 enhancement using the GEOS-Chem atmospheric transport model originating from permafrost sources in North America. We simulate land-atmosphere CO_2 exchange by adding 1 Pg C/y of additional carbon release following the seasonal cycle of heterotrophic respiration from labile carbon, to quantify the fingerprints on atmospheric partial column CO_2 dry mole fraction in the lower or upper troposphere. During summertime, 1 Pg C/y of additional carbon release from North American permafrost can cause a mean of 3.5ppm and as large as 6ppm partial XCO_2 increase in the lower troposphere, which is potentially detectable from space. The CO_2 release from the permafrost has a much larger influence on the lower troposphere than the upper troposphere - the difference is as large as 3.5 ppm near the source region and as low as 0.5 ppm in a remote area. Our analysis points toward and provides preliminary estimates of observational requirements to identify signals from the Northern Permafrost regions using space-based observations.

4.6 References

Belshe, E. F., E. a. G. Schuur, and B. M. Bolker. "Tundra Ecosystems Observed to Be CO2 Sources Due to Differential Amplification of the Carbon Cycle." *Ecology Letters* 16, no. 10 (2013): 1307–15. https://doi.org/10.1111/ele.12164.

Bey, Isabelle, Daniel J. Jacob, Robert M. Yantosca, Jennifer A. Logan, Brendan D. Field, Arlene M. Fiore, Qinbin Li, Honguy Y. Liu, Loretta J. Mickley, and Martin G. Schultz. "Global Modeling of Tropospheric Chemistry with Assimilated Meteorology: Model Description and Evaluation." *Journal of Geophysical Research: Atmospheres* 106, no. D19 (2001): 23073–95. https://doi.org/10.1029/2001JD000807.

Biskaborn, Boris K., Sharon L. Smith, Jeannette Noetzli, Heidrun Matthes, Gonçalo Vieira, Dmitry A. Streletskiy, Philippe Schoeneich, et al. "Permafrost Is Warming at a Global Scale." *Nature Communications* 10, no. 1 (January 16, 2019): 264. https://doi.org/10.1038/s41467-018-08240-4.

Burke, Eleanor J., Sarah E. Chadburn, Chris Huntingford, and Chris D. Jones. "CO2 Loss by Permafrost Thawing Implies Additional Emissions Reductions to Limit Warming to 1.5 or

2 °C." *Environmental Research Letters* 13, no. 2 (February 2018): 024024. https://doi.org/10.1088/1748-9326/aaa138.

Chevallier, Frédéric, Marine Remaud, Christopher W. O'Dell, David Baker, Philippe Peylin, and Anne Cozic. "Objective Evaluation of Surface- and Satellite-Driven Carbon Dioxide Atmospheric Inversions." *Atmospheric Chemistry and Physics* 19, no. 22 (November 26, 2019): 14233–51. https://doi.org/10.5194/acp-19-14233-2019.

Commane, Róisín, Jakob Lindaas, Joshua Benmergui, Kristina A. Luus, Rachel Y.-W. Chang, Bruce C. Daube, Eugénie S. Euskirchen, et al. "Carbon Dioxide Sources from Alaska Driven by Increasing Early Winter Respiration from Arctic Tundra." *Proceedings of the National Academy of Sciences* 114, no. 21 (May 23, 2017): 5361–66. https://doi.org/10.1073/pnas.1618567114.

Douglas, Thomas A., Merritt R. Turetsky, and Charles D. Koven. "Increased Rainfall Stimulates Permafrost Thaw across a Variety of Interior Alaskan Boreal Ecosystems." *Npj Climate and Atmospheric Science* 3, no. 1 (July 24, 2020): 1–7. https://doi.org/10.1038/s41612-020-0130-4.

Eldering, Annmarie, Chris W. O'Dell, Paul O. Wennberg, David Crisp, Michael R. Gunson, Camille Viatte, Charles Avis, et al. "The Orbiting Carbon Observatory-2: First 18 Months of Science Data Products." *Atmospheric Measurement Techniques* 10, no. 2 (February 15, 2017): 549–63. https://doi.org/10.5194/amt-10-549-2017.

Fisher, Jenny A., Lee T. Murray, Dylan B. A. Jones, and Nicholas M. Deutscher. "Improved Method for Linear Carbon Monoxide Simulation and Source Attribution in Atmospheric Chemistry Models Illustrated Using GEOS-Chem V9." *Geoscientific Model Development* 10, no. 11 (November 15, 2017): 4129–44. https://doi.org/10.5194/gmd-10-4129-2017.

Jin, Xiao-Ying, Hui-Jun Jin, Go Iwahana, Sergey S. Marchenko, Dong-Liang Luo, Xiao-Ying Li, and Si-Hai Liang. "Impacts of Climate-Induced Permafrost Degradation on Vegetation: A Review." *Advances in Climate Change Research*, Including special topic on degrading permafrost and its impacts, 12, no. 1 (February 1, 2021): 29–47. https://doi.org/10.1016/j.accre.2020.07.002.

Kuze, Akihiko, Hiroshi Suto, Kei Shiomi, Shuji Kawakami, Makoto Tanaka, Yoko Ueda, Akira Deguchi, et al. "Update on GOSAT TANSO-FTS Performance, Operations, and Data Products after More than 6 Years in Space." *Atmospheric Measurement Techniques* 9, no. 6 (June 2, 2016): 2445–61. https://doi.org/10.5194/amt-9-2445-2016.

Lin, Xin, Brendan M. Rogers, Colm Sweeney, Frédéric Chevallier, Mikhail Arshinov, Edward Dlugokencky, Toshinobu Machida, Motoki Sasakawa, Pieter Tans, and Gretchen Keppel-Aleks. "Siberian and Temperate Ecosystems Shape Northern Hemisphere Atmospheric CO2 Seasonal Amplification." *Proceedings of the National Academy of Sciences* 117, no. 35 (September 2020): 21079–87. https://doi.org/10.1073/pnas.1914135117.

Magnussen, S., S. W. Taylor, S. Magnussen, and S. W. Taylor. “Prediction of Daily Lightning- and Human-Caused Fires in British Columbia.” *International Journal of Wildland Fire* 21, no. 4 (March 26, 2012): 342–56. https://doi.org/10.1071/WF11088.

Mishra, Umakant, Gustaf Hugelius, Eitan Shelef, Yuanhe Yang, Jens Strauss, Alexey Lupachev, Jennifer W. Harden, et al. “Spatial Heterogeneity and Environmental Predictors of Permafrost Region Soil Organic Carbon Stocks.” *Science Advances* 7, no. 9 (February 24, 2021): eaaz5236. https://doi.org/10.1126/sciadv.aaz5236.

Nassar, R., D. B. A. Jones, P. Suntharalingam, J. M. Chen, R. J. Andres, K. J. Wecht, R. M. Yantosca, et al. “Modeling Global Atmospheric CO_2 with Improved Emission Inventories and CO_2 Production from the Oxidation of Other Carbon Species.” *Geoscientific Model Development* 3, no. 2 (December 15, 2010): 689–716. https://doi.org/10.5194/gmd-3-689-2010.

Natali, Susan M., Jennifer D. Watts, Brendan M. Rogers, Stefano Potter, Sarah M. Ludwig, Anne-Katrin Selbmann, Patrick F. Sullivan, et al. “Large Loss of CO2 in Winter Observed across the Northern Permafrost Region.” *Nature Climate Change* 9, no. 11 (November 2019): 852–57. https://doi.org/10.1038/s41558-019-0592-8.

Natraj, Vijay, Ming Luo, Jean-Francois Blavier, Vivienne H. Payne, Derek J. Posselt, Stanley P. Sander, Zhao-Cheng Zeng, et al. “Simulated Multispectral Temperature and Atmospheric Composition Retrievals for the JPL GEO-IR Sounder.” *Atmospheric Measurement Techniques* 15, no. 5 (March 10, 2022): 1251–67. https://doi.org/10.5194/amt-15-1251-2022.

Neumann, Rebecca B., Colby J. Moorberg, Jessica D. Lundquist, Jesse C. Turner, Mark P. Waldrop, Jack W. McFarland, Eugenie S. Euskirchen, Colin W. Edgar, and Merritt R. Turetsky. “Warming Effects of Spring Rainfall Increase Methane Emissions From Thawing Permafrost.” *Geophysical Research Letters* 46, no. 3 (2019): 1393–1401. https://doi.org/10.1029/2018GL081274.

Pedron, Shawn A., J. M. Welker, E. S. Euskirchen, E. S. Klein, J. C. Walker, X. Xu, and C. I. Czimczik. “Closing the Winter Gap—Year-Round Measurements of Soil CO2 Emission Sources in Arctic Tundra.” *Geophysical Research Letters* 49, no. 6 (2022): e2021GL097347. https://doi.org/10.1029/2021GL097347.

Previdi, Michael, Karen L. Smith, and Lorenzo M. Polvani. “Arctic Amplification of Climate Change: A Review of Underlying Mechanisms.” *Environmental Research Letters* 16, no. 9 (September 2021): 093003. https://doi.org/10.1088/1748-9326/ac1c29.

Scholten, Rebecca C., Randi Jandt, Eric A. Miller, Brendan M. Rogers, and Sander Veraverbeke. “Overwintering Fires in Boreal Forests.” *Nature* 593, no. 7859 (May 2021): 399–404. https://doi.org/10.1038/s41586-021-03437-y.

Schuh, Andrew E., Andrew R. Jacobson, Sourish Basu, Brad Weir, David Baker, Kevin Bowman, Frédéric Chevallier, et al. “Quantifying the Impact of Atmospheric Transport Uncertainty on CO2 Surface Flux Estimates.” *Global Biogeochemical Cycles* 33, no. 4 (2019): 484–500. https://doi.org/10.1029/2018GB006086.

Schuur, E. a. G., A. D. McGuire, C. Schädel, G. Grosse, J. W. Harden, D. J. Hayes, G. Hugelius, et al. “Climate Change and the Permafrost Carbon Feedback.” *Nature* 520, no. 7546 (April 2015): 171–79. https://doi.org/10.1038/nature14338.

Schwab, Melissa S., Robert G. Hilton, Peter A. Raymond, Negar Haghipour, Edwin Amos, Suzanne E. Tank, Robert M. Holmes, Edward T. Tipper, and Timothy I. Eglinton. “An Abrupt Aging of Dissolved Organic Carbon in Large Arctic Rivers.” *Geophysical Research Letters* 47, no. 23 (2020): e2020GL088823. https://doi.org/10.1029/2020GL088823.

Strauss, Jens, Lutz Schirrmeister, Guido Grosse, Sebastian Wetterich, Mathias Ulrich, Ulrike Herzschuh, and Hans-Wolfgang Hubberten. “The Deep Permafrost Carbon Pool of the Yedoma Region in Siberia and Alaska.” *Geophysical Research Letters* 40, no. 23 (2013): 6165–70. https://doi.org/10.1002/2013GL058088.

Trishchenko, A. P., L. D. Trichtchenko, and L. Garand. “Highly Elliptical Orbits for Polar Regions with Reduced Total Ionizing Dose.” *Advances in Space Research* 63, no. 12 (June 15, 2019): 3761–67. https://doi.org/10.1016/j.asr.2019.04.005.

Turetsky, Merritt R., Benjamin W. Abbott, Miriam C. Jones, Katey Walter Anthony, David Olefeldt, Edward A. G. Schuur, Guido Grosse, et al. “Carbon Release through Abrupt Permafrost Thaw.” *Nature Geoscience* 13, no. 2 (February 2020): 138–43. https://doi.org/10.1038/s41561-019-0526-0.

Turner, Alexander J., Jinsol Kim, Helen Fitzmaurice, Catherine Newman, Kevin Worthington, Katherine Chan, Paul J. Wooldridge, Philipp Köehler, Christian Frankenberg, and Ronald C. Cohen. “Observed Impacts of COVID-19 on Urban CO2 Emissions.” *Geophysical Research Letters* 47, no. 22 (2020): e2020GL090037. https://doi.org/10.1029/2020GL090037.

Velazco, V. A., M. Buchwitz, H. Bovensmann, M. Reuter, O. Schneising, J. Heymann, T. Krings, K. Gerilowski, and J. P. Burrows. “Towards Space Based Verification of CO_2 Emissions from Strong Localized Sources: Fossil Fuel Power Plant Emissions as Seen by a CarbonSat Constellation.” *Atmospheric Measurement Techniques* 4, no. 12 (December 21, 2011): 2809–22. https://doi.org/10.5194/amt-4-2809-2011.

Vonk, J. E., S. E. Tank, W. B. Bowden, I. Laurion, W. F. Vincent, P. Alekseychik, M. Amyot, et al. “Reviews and Syntheses: Effects of Permafrost Thaw on Arctic Aquatic Ecosystems.” *Biogeosciences* 12, no. 23 (December 8, 2015): 7129–67. https://doi.org/10.5194/bg-12-7129-2015.

Walter Anthony, Katey, Thomas Schneider von Deimling, Ingmar Nitze, Steve Frolking, Abraham Emond, Ronald Daanen, Peter Anthony, Prajna Lindgren, Benjamin Jones, and Guido Grosse. “21st-Century Modeled Permafrost Carbon Emissions Accelerated by Abrupt Thaw beneath Lakes.” *Nature Communications* 9, no. 1 (August 15, 2018): 3262. https://doi.org/10.1038/s41467-018-05738-9.

Wu, Shiliang, Loretta J. Mickley, Daniel J. Jacob, Jennifer A. Logan, Robert M. Yantosca, and David Rind. “Why Are There Large Differences between Models in Global Budgets of Tropospheric Ozone?” *Journal of Geophysical Research: Atmospheres* 112, no. D5 (2007). https://doi.org/10.1029/2006JD007801.

Chapter 5 Conclusions

The space-based detecting satellites launched in recent years have the potential to provide regional to global measurements of CO_2, can successfully monitor CO_2 from seasonal to interannual timescales over both land and ocean, improve the spatial coverage compared with the currently existing ground-based networks, and help to refine our understanding of Earth's sources and sinks of carbon. This dissertation work has combined the observed atmospheric CO_2 IAV from NASAs OCO-2 satellite mission-which detects the combined imprint of the ocean, terrestrial ecosystem, and human activities, and a three-dimensional atmospheric transport model, to estimate the likely range of IAV in the atmospheric CO_2 owing to air-sea carbon exchange. As a further step, the detectability of the perturbations intrigued by permafrost thawing was quantified based upon a hypothetical satellite mission. The following are the chapter conclusions and recommended next steps for continued research.

Chapter 2 describes interannual variability in atmospheric CO_2, as measured from NASA's Orbiting Carbon Observatory-2. This study shows that IAV in space-based column observations XCO_2 are highly correlated to that of ground-based surface CO_2 from long-term monitoring sites, but that zonal averages of satellite IAV are more correlated than are those of surface CO_2, reflecting an important role for tropospheric transport in XCO_2. Further, XCO_2 IAV timeseries show a strong impact from El Nino conditions, with higher anomalies during El Nino years. Because OCO-2 provides near-global coverage, this study provides a roadmap to study IAV in regions where the surface network is sparse, such as oceans and remote land region

In Chapter 3, I quantify the likely range of IAV in the atmospheric CO_2 mole fraction owing to air-sea carbon exchange by simulating three-dimensional atmospheric CO_2 using the GEOS-Chem atmospheric transport model. The ocean fluxes I use are data products from the Surface Ocean pCO_2 Mapping intercomparison (SOCOM), which interpolate air-sea fluxes from ΔpCO_2 observations through various mapping techniques. I separately label CO_2 from individual ocean regions, aiming to identify the fingerprints of ocean subregions and the whole ocean on atmospheric total column CO_2 dry mole fraction XCO_2. These simulations were analyzed in conjunction with observed atmospheric CO_2 IAV from NASA's OCO-2 satellite mission, which detects the combined imprint of ocean, terrestrial ecosystem, and human activities.

We found that XCO_2 simulated from three SOCOM flux products showed large differences in the magnitude of IAV, although all products showed that the magnitude of ocean-driven IAV was generally less than 0.1 ppm at any location. It is the variabilities in the ocean fluxes that play the dominant role , contributing to more than 70% of the ocean driven XCO_2 IAV, although over certain regions such as the tropical Pacific, XCO_2 IAV is strongly tied to variations in atmospheric transport as well. Over remote ocean regions simulations suggest that ocean fluxes contribute a large proportion of IAV, nevertheless, given precision and bias limitations to the satellite data, our analysis suggests that the XCO_2 IAV signals may be difficult to attribute to regional patterns of air-sea fluxes.

In Chapter 4, I quantify permafrost-driven atmospheric CO_2 enhancement using the GEOS-Chem atmospheric transport model originating from permafrost sources in North America as an case study. The simulation was carried out using land-atmosphere CO_2 exchange by adding 1 Pg C/y of additional carbon release following the seasonal cycle of heterotrophic respiration from labile carbon, to quantify the fingerprints on atmospheric partial column CO_2 dry mole

fraction in the lower or upper troposphere. During summertime, 1 Pg C/y of additional carbon release from North American permafrost can cause a mean of 3.5ppm and as large as 6ppm partial XCO_2 increase in the lower troposphere, which is potentially detectable from space. The CO_2 release from the permafrost has a much larger influence on the lower troposphere than the upper troposphere - the difference is as large as 3.5 ppm near the source region and as low as 0.5 ppm in a remote area. Our analysis points toward and provides preliminary estimates of observational requirements to identify signals from the Northern Permafrost regions using space-based observations.

Next steps for furthering research into the science questions presented here include the following: One of the challenges in Chapter 2 was to investigate the best resolution to aggregate the detection from OCO-2 in order to avoid either noise or large-scale biases. We tried to find the answer by aggregating the OCO-2 detection in different resolution - from 1° resolution to 15° resolution, and compare the difference of these resolutions (In Fig A.1 and A.2) to find the threshold that balanced the two goals of reducing noise yet revealing IAV at sub-zonal resolution. At 5°x5° (lower latitudes and 5°x10° (higher latitudes), the appearance of hotspots is minimized and the IAV amplitudes are spatially smooth, which we interpret as IAV signals emerging above the noise. We further calculated the correlation coefficient among the IAV timeseries in neighboring gridcells of 1° resolution (Fig A.9). The R value decreases as the distance between the gridcell increases in each 10° zonal bands from 70°N to 70°S. We see a rapid decrease in the correlation between gridcells separated by 1° and gridcells separated by 5°, and generally stable correlation coefficient from 5° to 15°separation.

In this study, we consider that the work involved in the suggested model analysis would first require a validation of the model IAV, and the scope of adding a model analysis is beyond

the scale of our current study. As a future step, besides the sensitivity studies with the observations themselves, it would be valuable to make extra sensitivity analysis with high-resolution model data (rather than real data), sampled like OCO-2, which would have sufficient resolution for this purpose.

For Chapter 4, The OSSE described in this study demonstrates that TIR retrieved pseudo XCO_2 from a designed mission provides improved constraints on Northern Arctic CO_2 fluxes relative to current satellite missions since it offers better observations during winter months and Northern Arctic Latitudes. Future space instruments could consider this wide range of values to obtain CO_2 concentrations regionally, and possibly extend the CO_2 monitoring system over Southern Hemisphere Antarctica. Despite the encouraging performance of the perfect model and pseudo satellite observation in estimating CO_2 concentration, it would be valuable to analyze the detectability of rapidly evolving processes - could the projected satellite observe the imprint of a single sudden emission event? This question could be answered by starting an independent nature run and enhanced emissions runs, with pulse input fluxes mirroring the emission such as wildfire combustions, and sample the simulations to produce pseudo-observations. As a final step, error of the CO_2 enhancements based on the synthetic retrieval precisions shall be estimated.

Appendices

Appendix A: Supplemental to Chapter 2

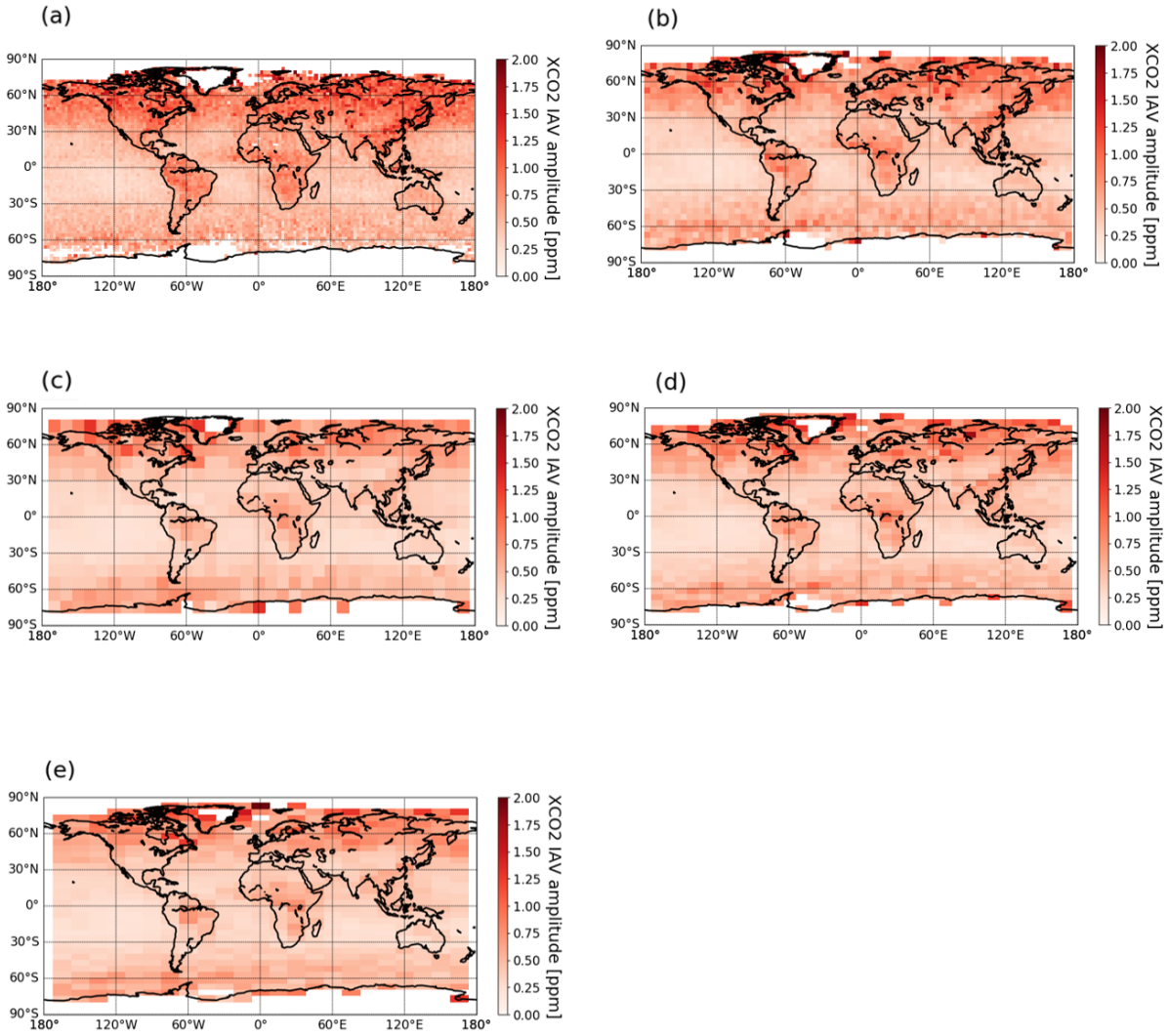

Figure A.1: *The IAV amplitude map, with different resolution from (a) 2.5° longitude by 2.5 ° latitude, to (b) 5 ° longitude by 5 ° latitude, to (c) 10 ° longitude by 10 ° latitude, to (d) 5 ° longitude by 10 ° latitude and (e) 5 ° longitude by 15 ° latitude, each gridbox has at least 5 soundings.*

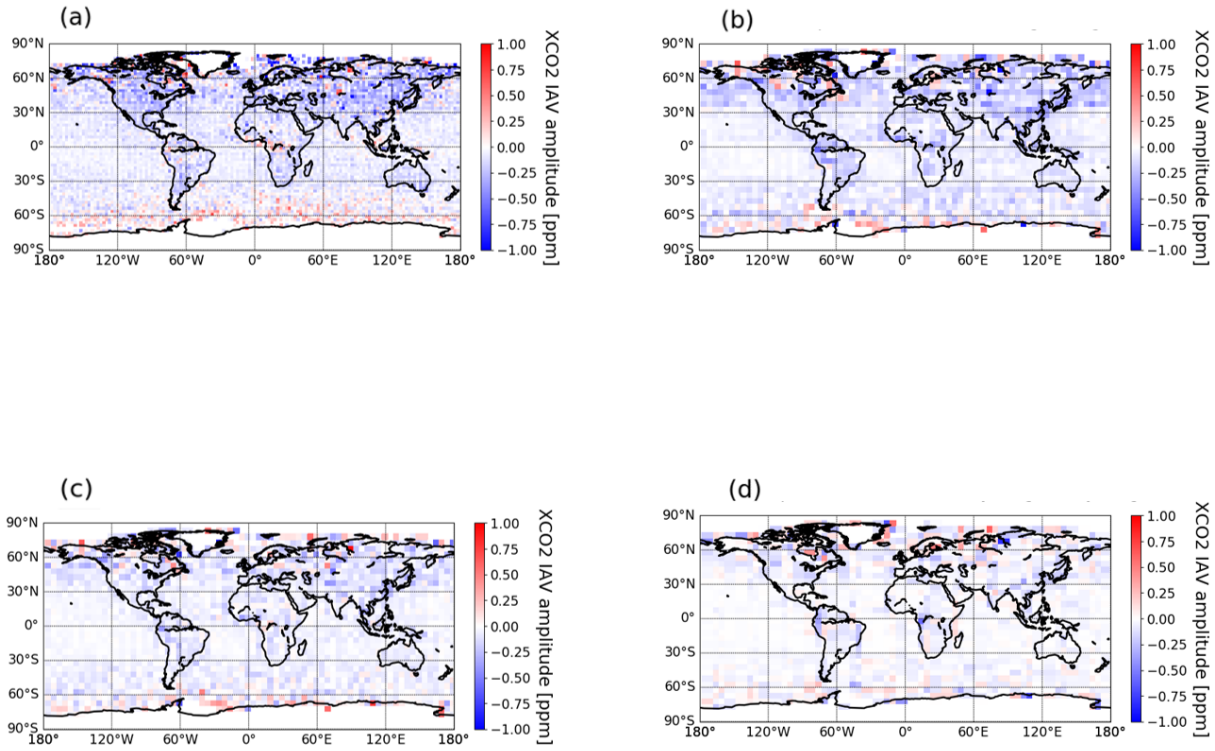

Figure A.2: *The IAV amplitude difference for different resolution. (a) between 5° longitude by 5 ° latitude and 2.5 ° longitude by 2.5 ° latitude, (b) between 10° longitude by 10 ° latitude and 5 ° longitude by 5 ° latitude,(c) between 10° longitude by 5 ° latitude and 5 ° longitude by 5 ° latitude,(d) between 15° longitude by 5 ° latitude and 10 ° longitude by 5 ° latitude.*

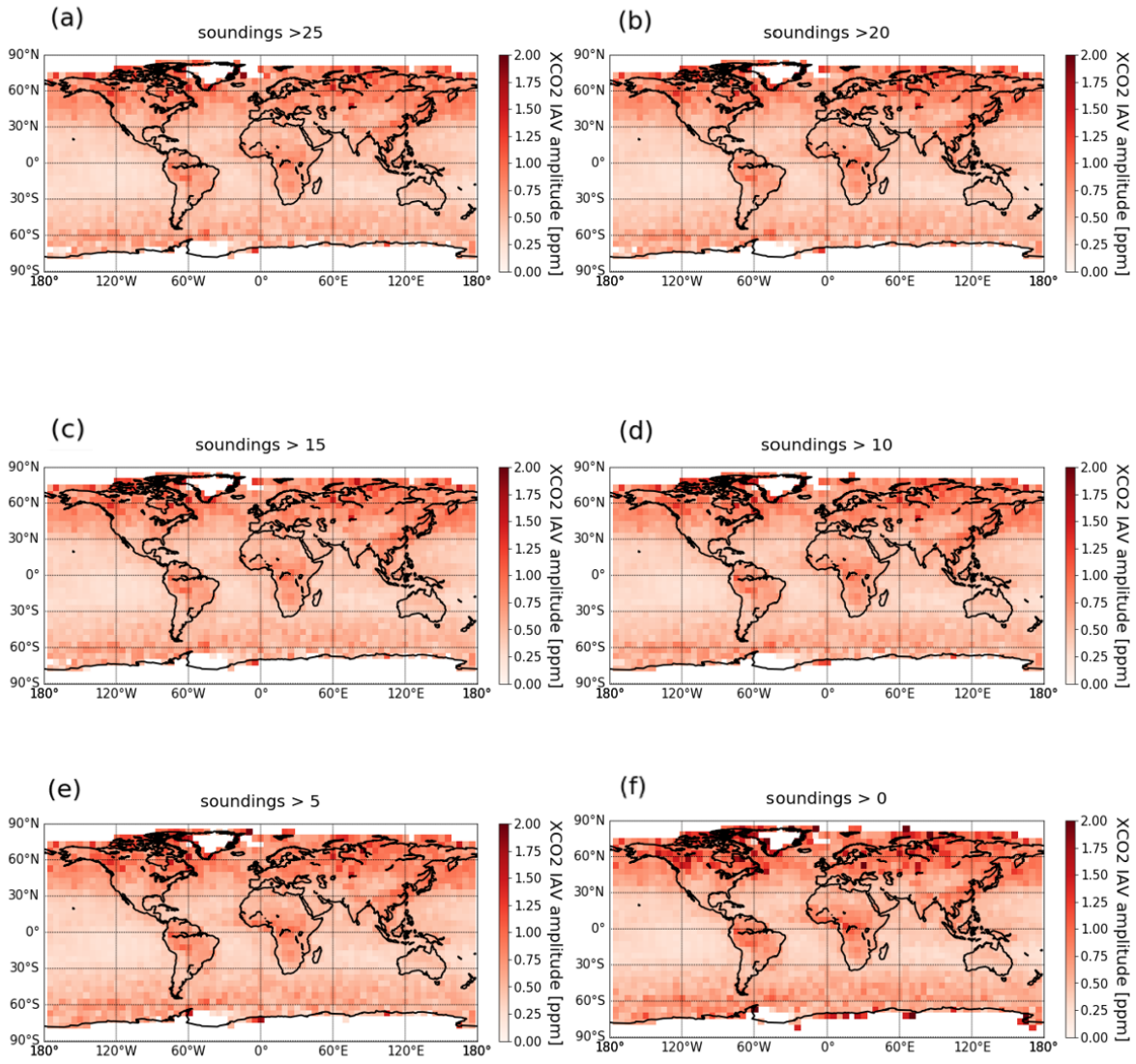

Figure A.3: *The IAV amplitude map, using different sounding numbers as the benchmark to filter and get the aggregated OCO-2 detected* XCO_2.

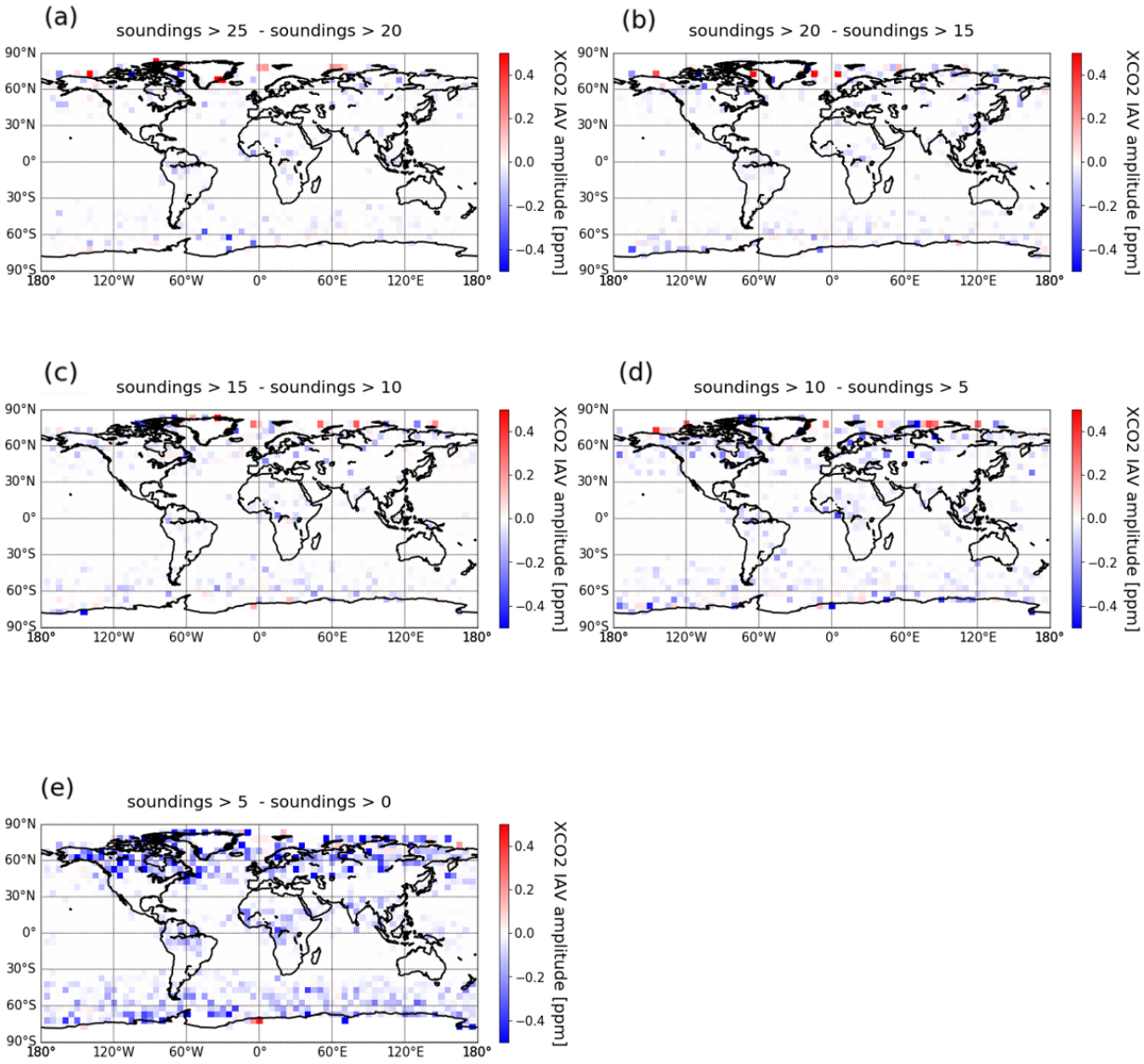

Figure A.4: *The IAV amplitude difference between OCO-2 detected XCO_2 IAV based on different sounding numbers.*

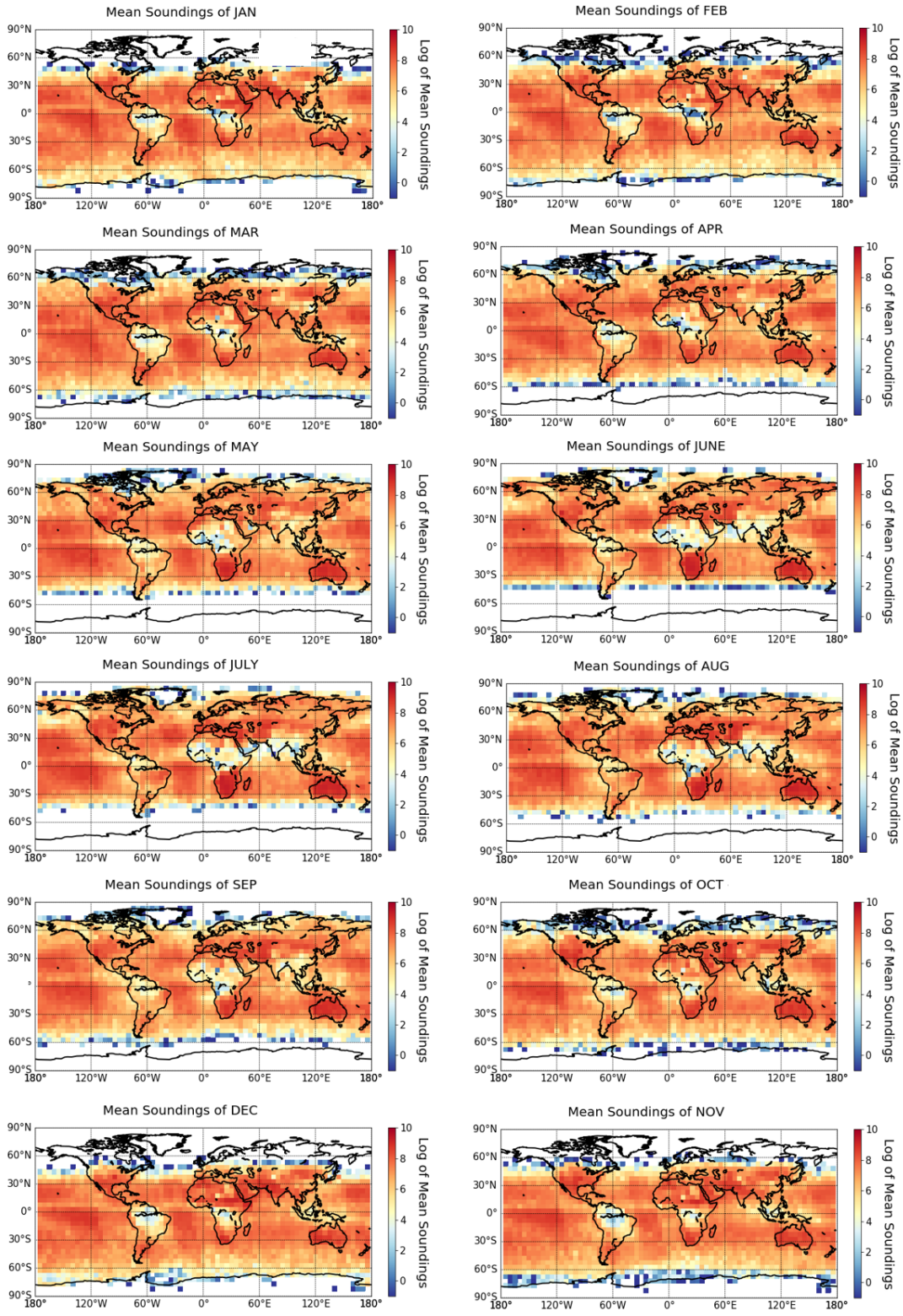

Figure A.5: *The Log of Mean sounding numbers for 12 months for each 5 by 5 ° gridcell all over the world. The colorbar range is set to log -1 to 10 which is equivalent absolute soundings of 0 to 20000.*

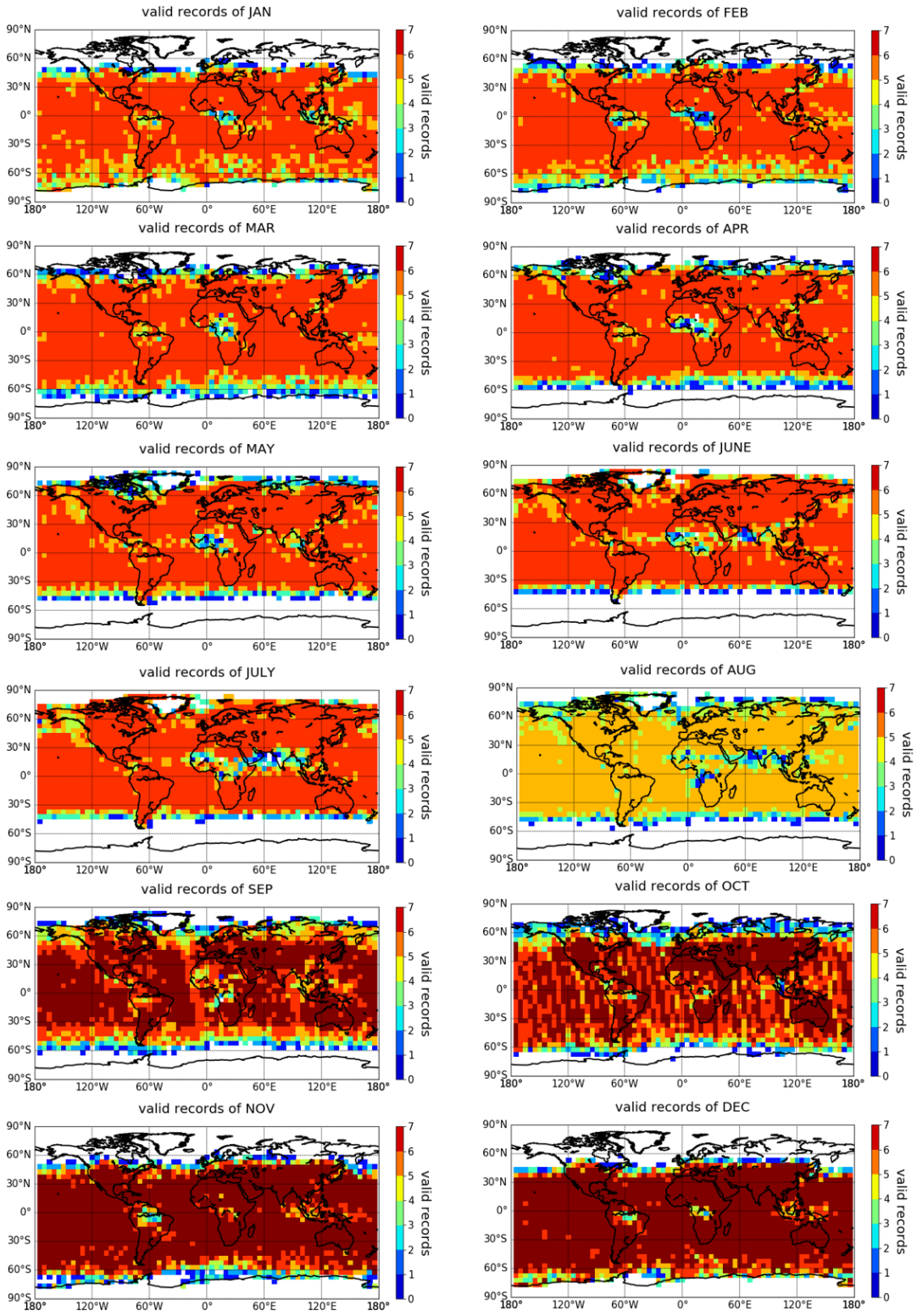

Figure A.6: *The number of valid years (X out of 6 for JAN~JULY, 5 for AUG or 7 for SEP~DEC) for each month (JAN, FEB, etc…) for each 5° by 5° gridcell.*

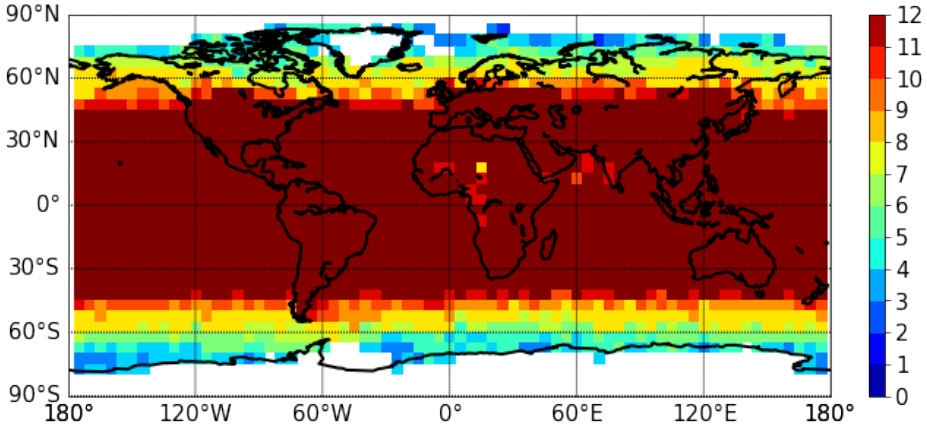

Figure A.7: *The number of months out of 12 months in the year of 2014~2020 (JAN,FEB,MAR…) are available for each grid cell. It shows the OCO-2 XCO_2's capability of detecting, which is related to the validity of our calculated IAV.*

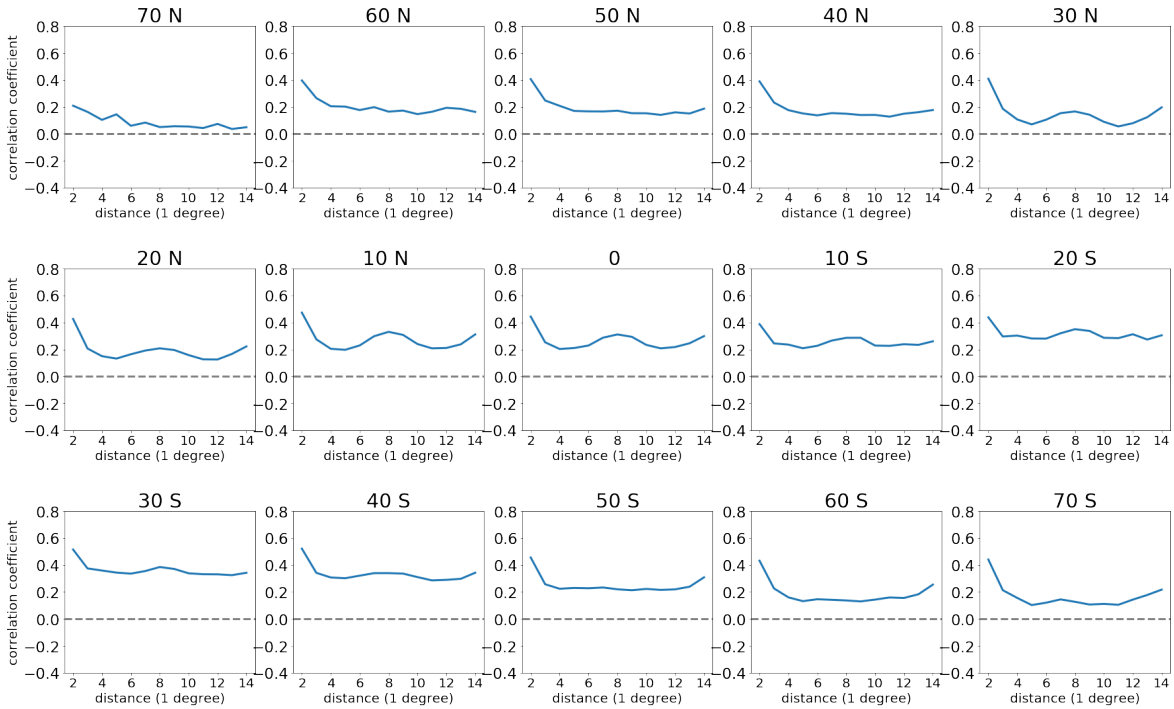

Figure A.8: *Mean Correlation coefficient between the OCO-2 XCO_2 IAV of neighbouring gridcells in each 10° latitudinal band.*

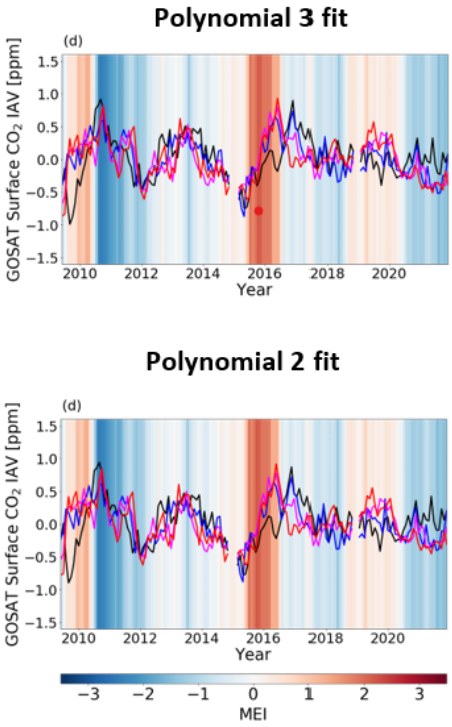

Figure A.9: *Timeseries comparison between the zonal mean GOSAT XCO_2 IAV, based on detrending method using 2nd and 3rd polynomial fit.*

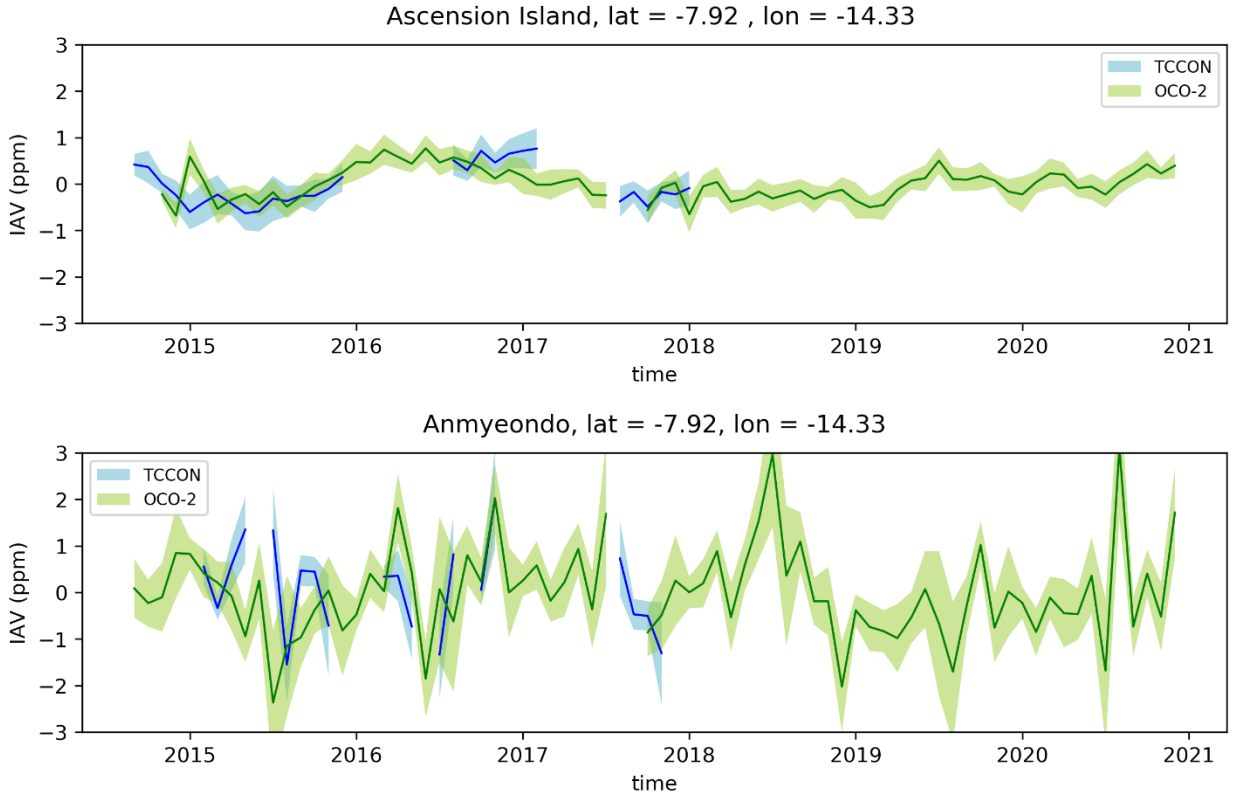

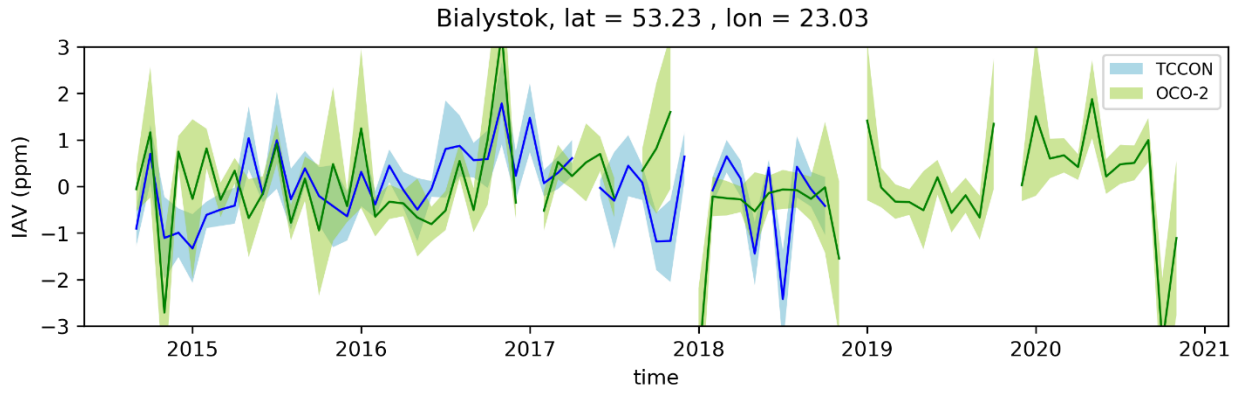
Bialystok, lat = 53.23 , lon = 23.03
TCCON
OCO-2
IAV (ppm)
time
3
2
1
0
−1
−2
−3
2015
2016
2017
2018
2019
2020
2021

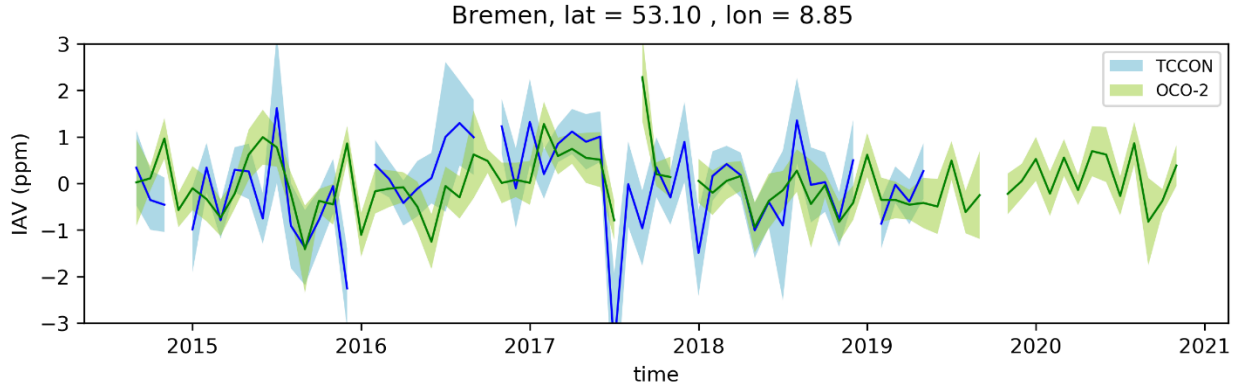
Bremen, lat = 53.10 , lon = 8.85
TCCON
OCO-2
IAV (ppm)
time
3
2
1
0
−1
−2
−3
2015
2016
2017
2018
2019
2020
2021

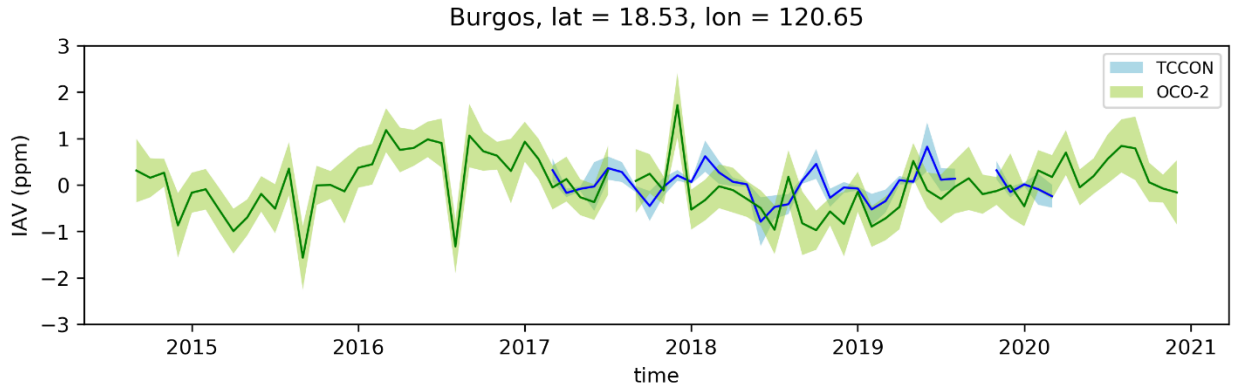
Burgos, lat = 18.53, lon = 120.65
TCCON
OCO-2
IAV (ppm)
time
3
2
1
0
−1
−2
−3
2015
2016
2017
2018
2019
2020
2021

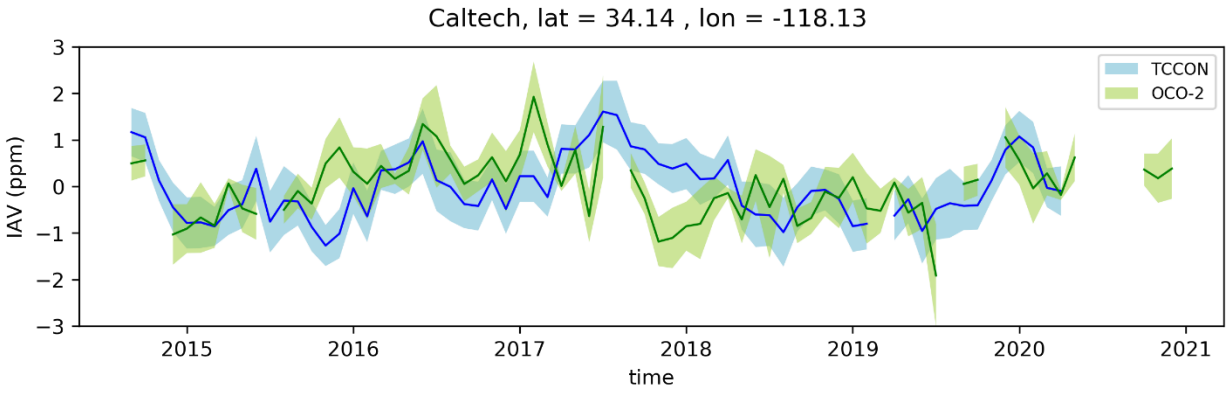
Caltech, lat = 34.14 , lon = -118.13
TCCON
OCO-2
IAV (ppm)
time
3
2
1
0
−1
−2
−3
2015
2016
2017
2018
2019
2020
2021

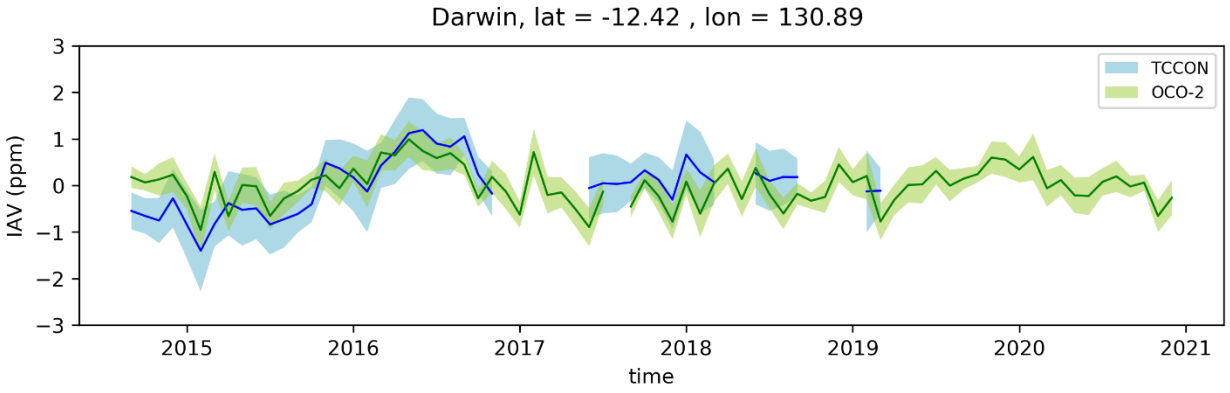
Darwin, lat = -12.42 , lon = 130.89
TCCON
OCO-2
IAV (ppm)
time
3
2
1
0
−1
−2
−3
2015
2016
2017
2018
2019
2020
2021

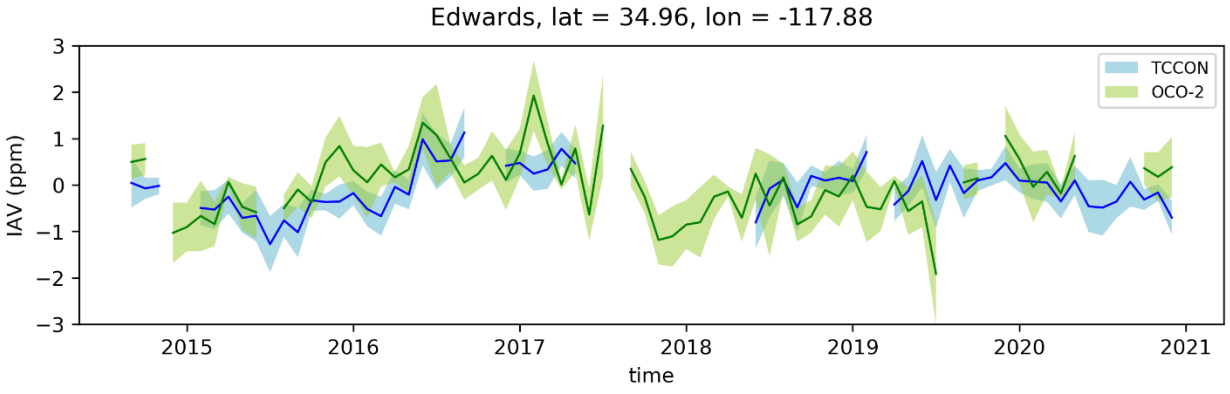
Edwards, lat = 34.96, lon = -117.88
TCCON
OCO-2
IAV (ppm)
time
3
2
1
0
−1
−2
−3
2015
2016
2017
2018
2019
2020
2021

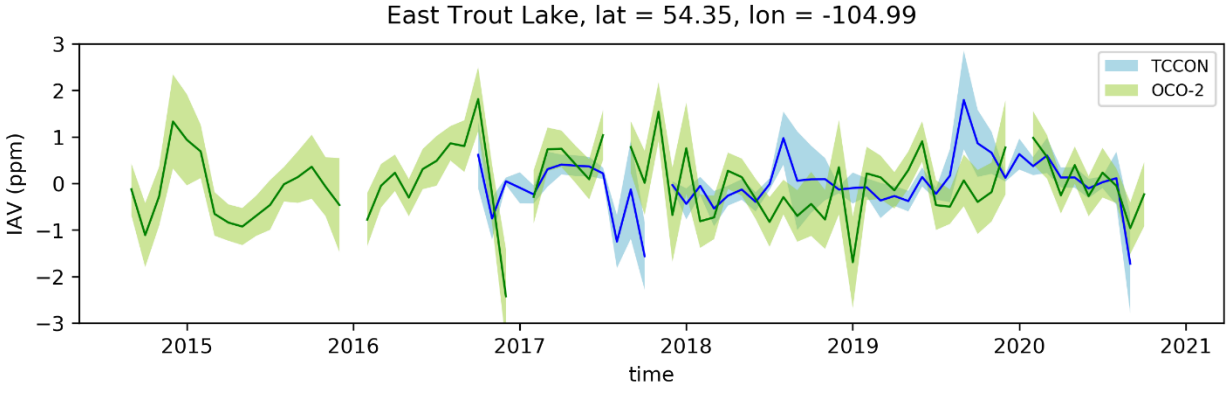
East Trout Lake, lat = 54.35, lon = -104.99
TCCON
OCO-2
IAV (ppm)
time
3
2
1
0
−1
−2
−3
2015
2016
2017
2018
2019
2020
2021

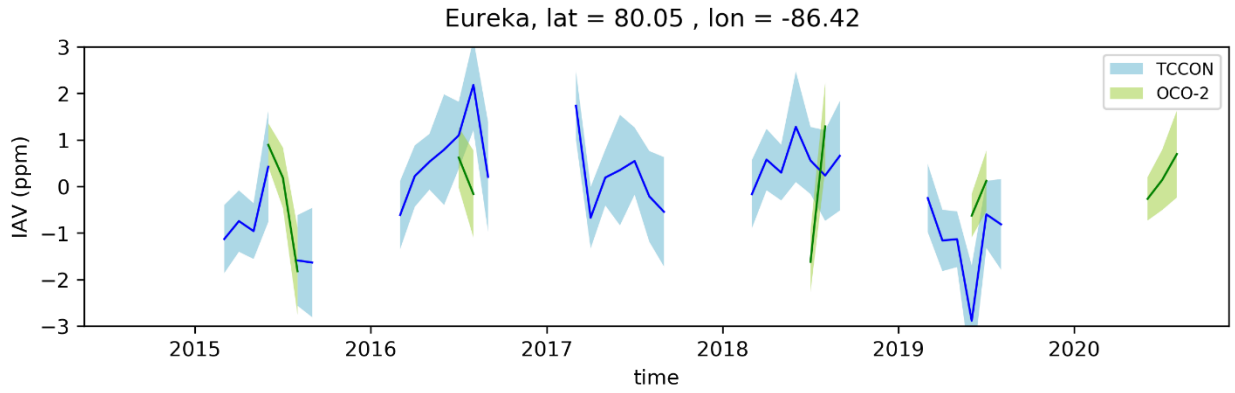
Eureka, lat = 80.05 , lon = -86.42
TCCON
OCO-2
IAV (ppm)
time
3
2
1
0
−1
−2
−3
2015
2016
2017
2018
2019
2020

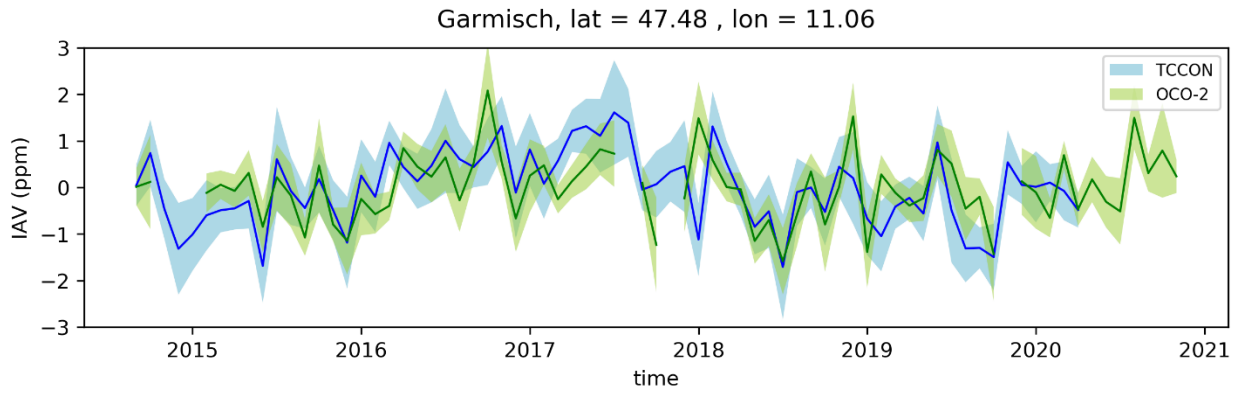
Garmisch, lat = 47.48 , lon = 11.06
TCCON
OCO-2
IAV (ppm)
time
3
2
1
0
−1
−2
−3
2015
2016
2017
2018
2019
2020
2021

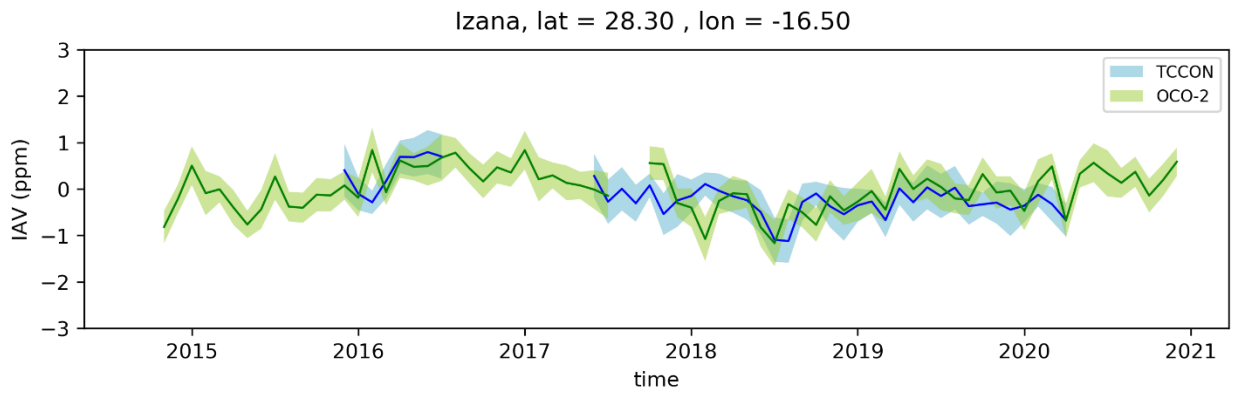
Izana, lat = 28.30 , lon = -16.50
TCCON
OCO-2
IAV (ppm)
time
3
2
1
0
−1
−2
−3
2015
2016
2017
2018
2019
2020
2021

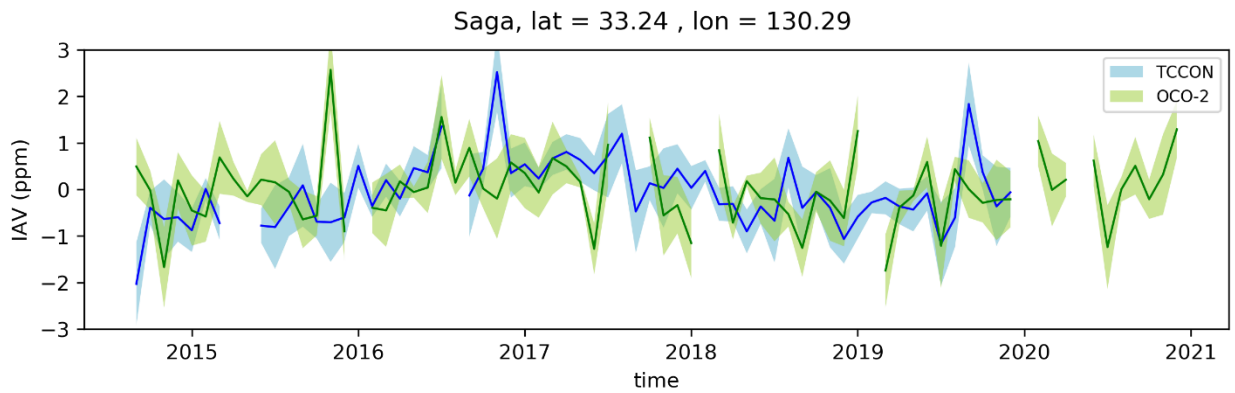
Saga, lat = 33.24 , lon = 130.29
TCCON
OCO-2
IAV (ppm)
time
3
2
1
0
−1
−2
−3
2015
2016
2017
2018
2019
2020
2021

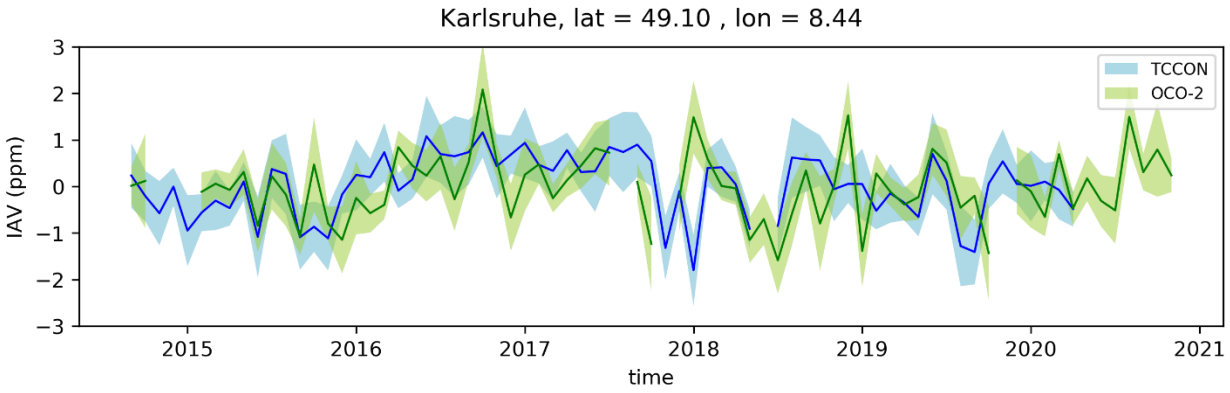
Karlsruhe, lat = 49.10 , lon = 8.44
TCCON
OCO-2
IAV (ppm)
time
3
2
1
0
−1
−2
−3
2015
2016
2017
2018
2019
2020
2021

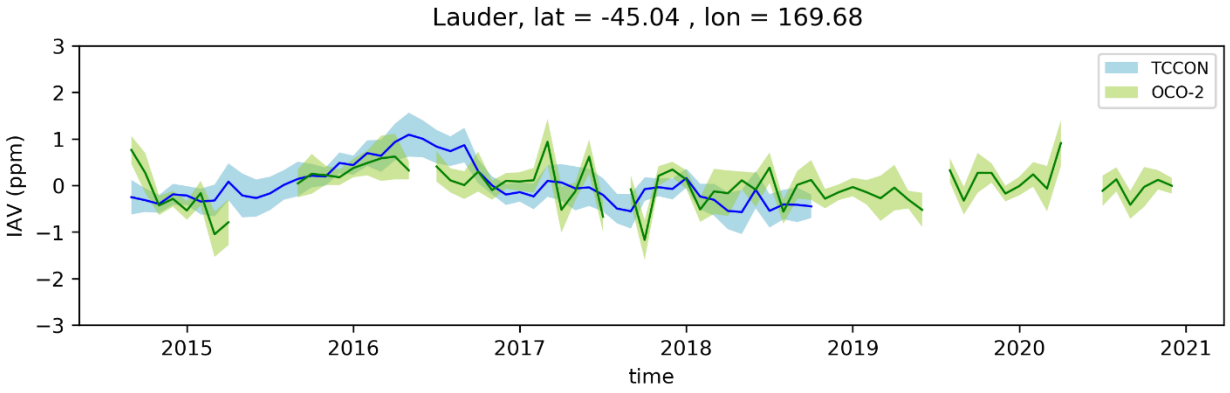
Lauder, lat = -45.04 , lon = 169.68
TCCON
OCO-2
IAV (ppm)
time
3
2
1
0
−1
−2
−3
2015
2016
2017
2018
2019
2020
2021

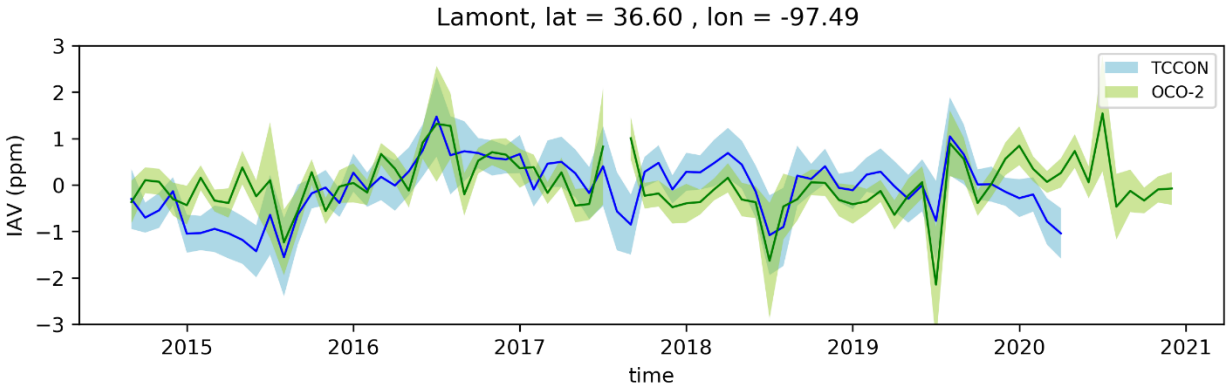
Lamont, lat = 36.60 , lon = -97.49
TCCON
OCO-2
IAV (ppm)
time
3
2
1
0
−1
−2
−3
2015
2016
2017
2018
2019
2020
2021

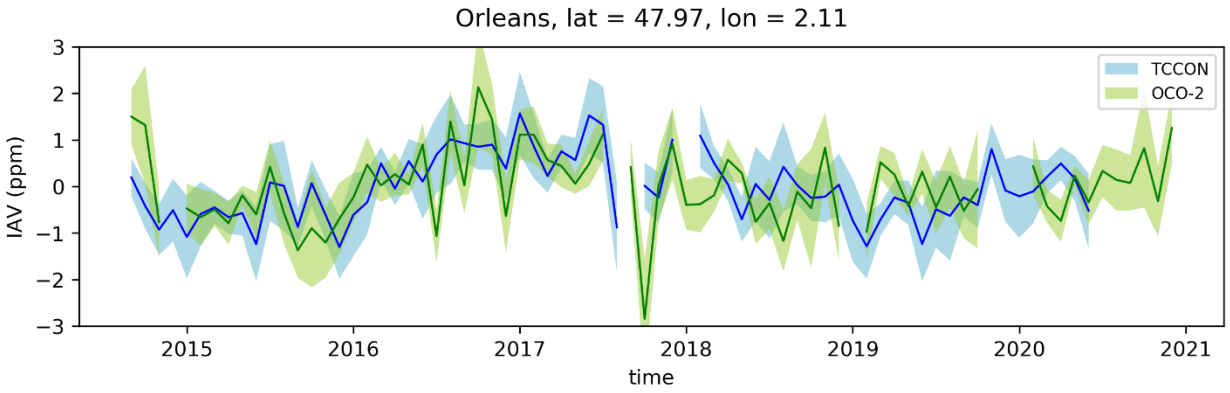
Orleans, lat = 47.97, lon = 2.11
TCCON
OCO-2
IAV (ppm)
time
3
2
1
0
−1
−2
−3
2015
2016
2017
2018
2019
2020
2021

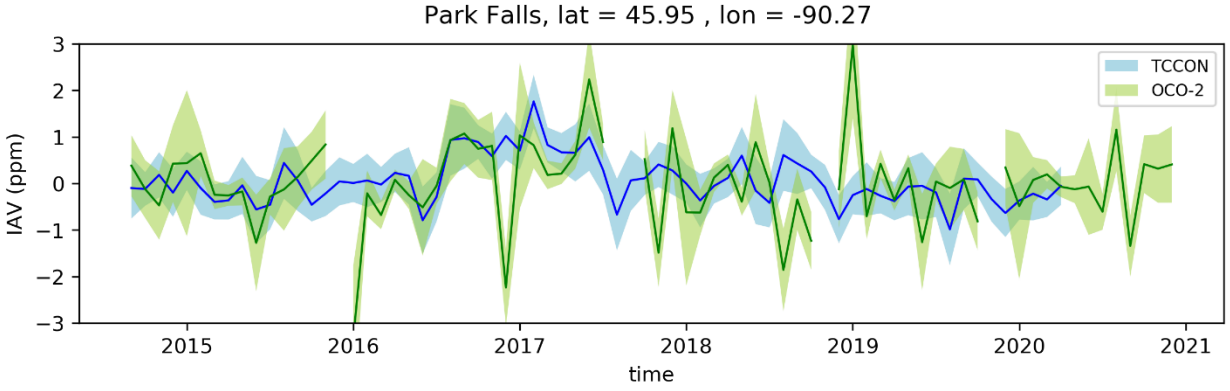
Park Falls, lat = 45.95 , lon = -90.27
TCCON
OCO-2
IAV (ppm)
time
3
2
1
0
−1
−2
−3
2015
2016
2017
2018
2019
2020
2021

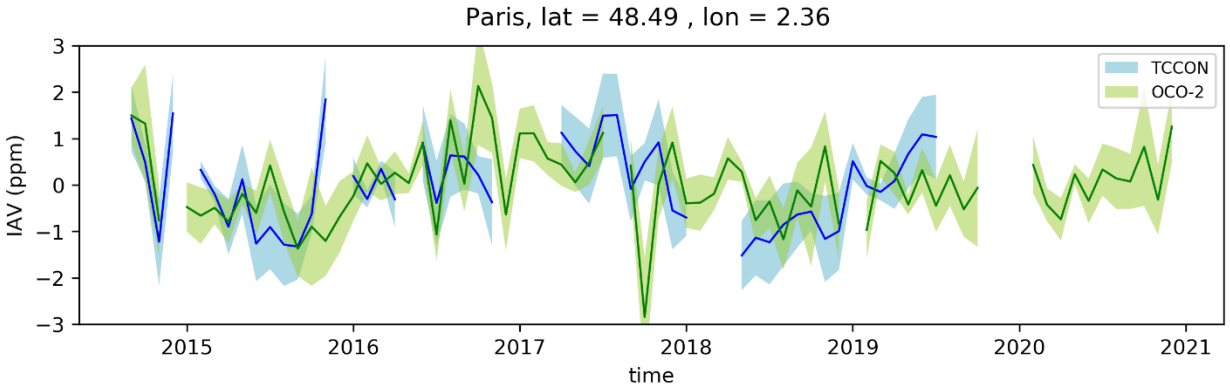
Paris, lat = 48.49 , lon = 2.36
TCCON
OCO-2
IAV (ppm)
time
3
2
1
0
−1
−2
−3
2015
2016
2017
2018
2019
2020
2021

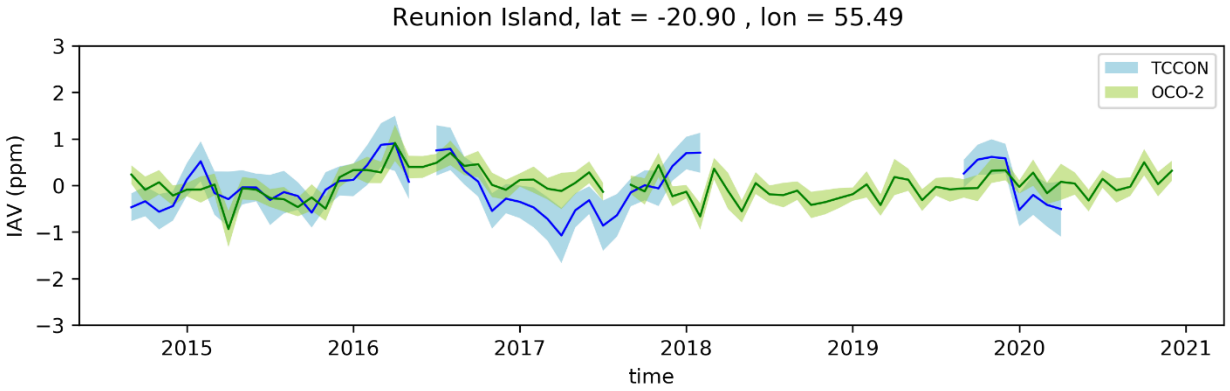
Reunion Island, lat = -20.90 , lon = 55.49
TCCON
OCO-2
IAV (ppm)
time
3
2
1
0
−1
−2
−3
2015
2016
2017
2018
2019
2020
2021

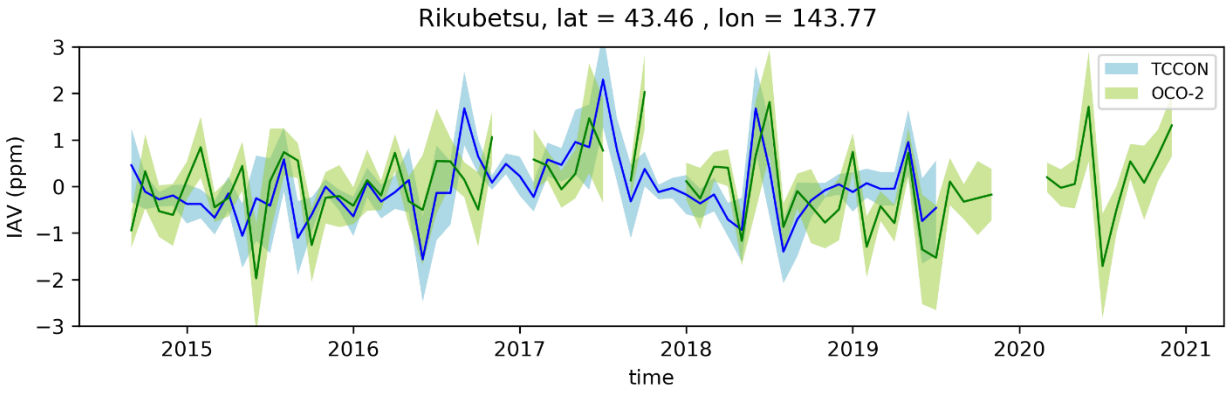
Rikubetsu, lat = 43.46 , lon = 143.77
TCCON
OCO-2
IAV (ppm)
time
3
2
1
0
−1
−2
−3
2015
2016
2017
2018
2019
2020
2021

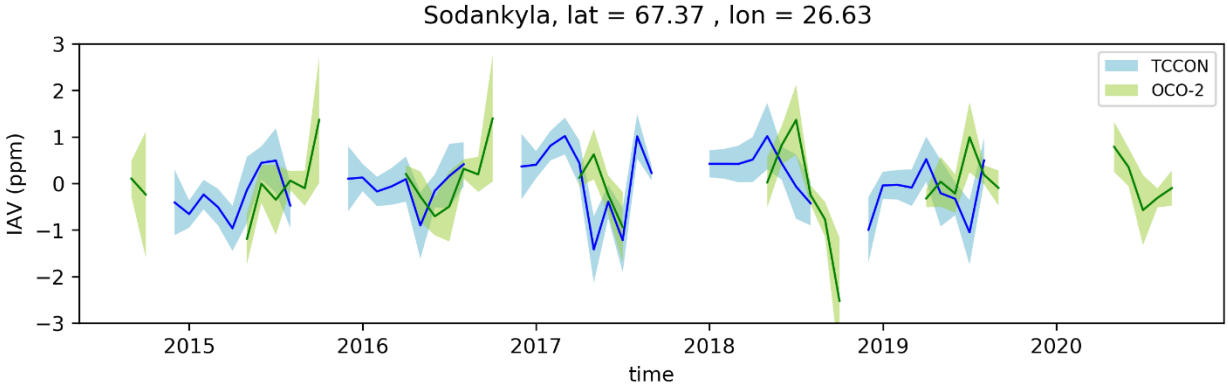
Sodankyla, lat = 67.37 , lon = 26.63
TCCON
OCO-2
IAV (ppm)
time
3
2
1
0
−1
−2
−3
2015
2016
2017
2018
2019
2020

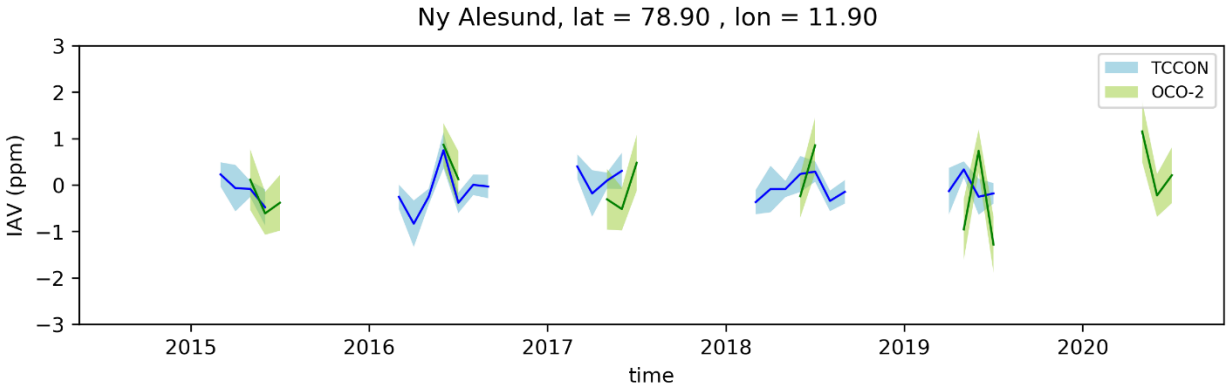
Ny Alesund, lat = 78.90 , lon = 11.90
TCCON
OCO-2
IAV (ppm)
time
3
2
1
0
−1
−2
−3
2015
2016
2017
2018
2019
2020

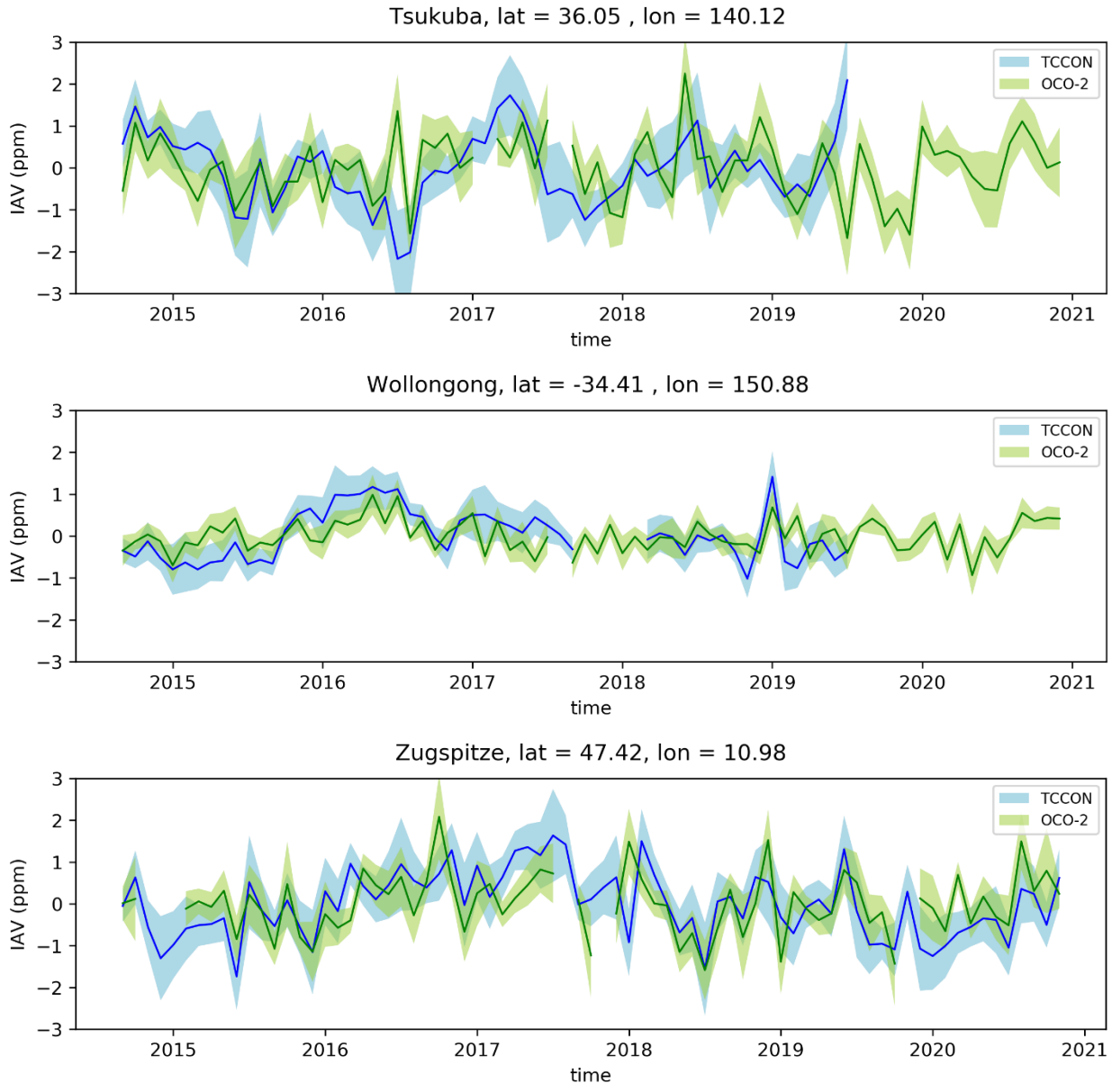

Figure A.10: *Timeseries comparison between the OCO-2 XCO_2 and TCCON IAV, blue shading shows the uncertainty range of TCCON, green for OCO-2.*

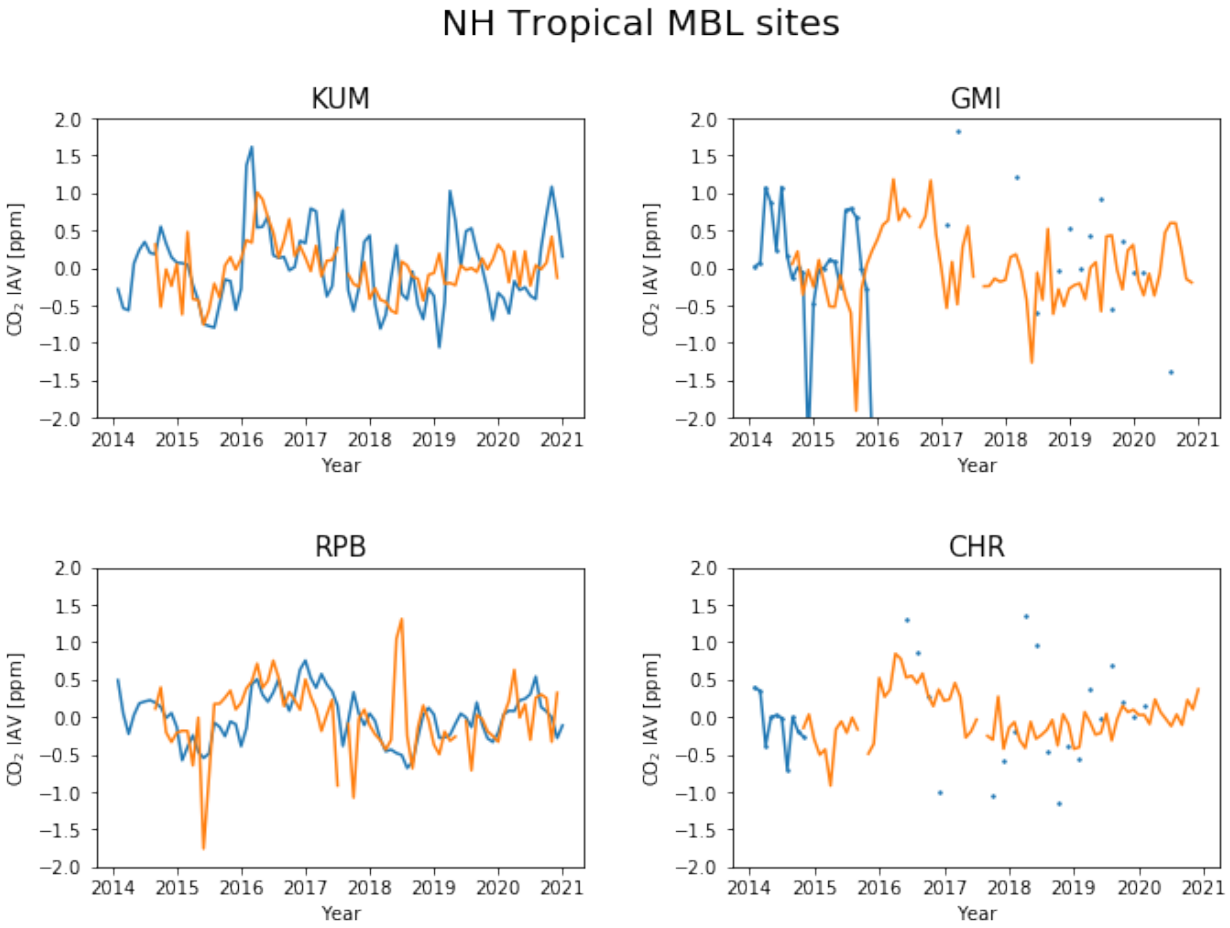
NH Tropical MBL sites
KUM
GMI
RPB
CHR
CO_2 IAV [ppm]
Year
2.0
1.5
1.0
0.5
0.0
−0.5
−1.0
−1.5
−2.0
2014
2015
2016
2017
2018
2019
2020
2021

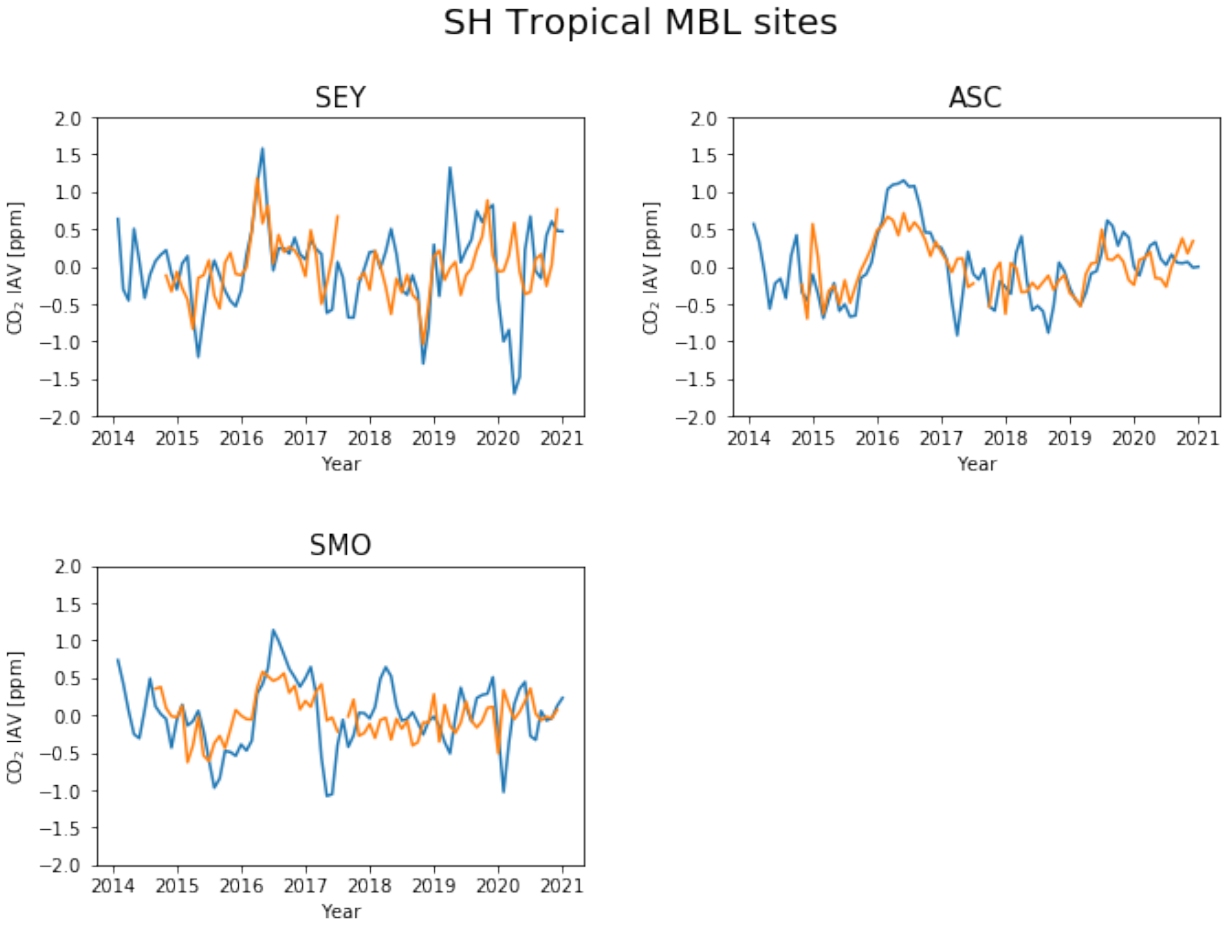
SH Tropical MBL sites
SEY
ASC
SMO
CO_2 IAV [ppm]
Year
2.0
1.5
1.0
0.5
0.0
−0.5
−1.0
−1.5
−2.0
2014
2015
2016
2017
2018
2019
2020
2021

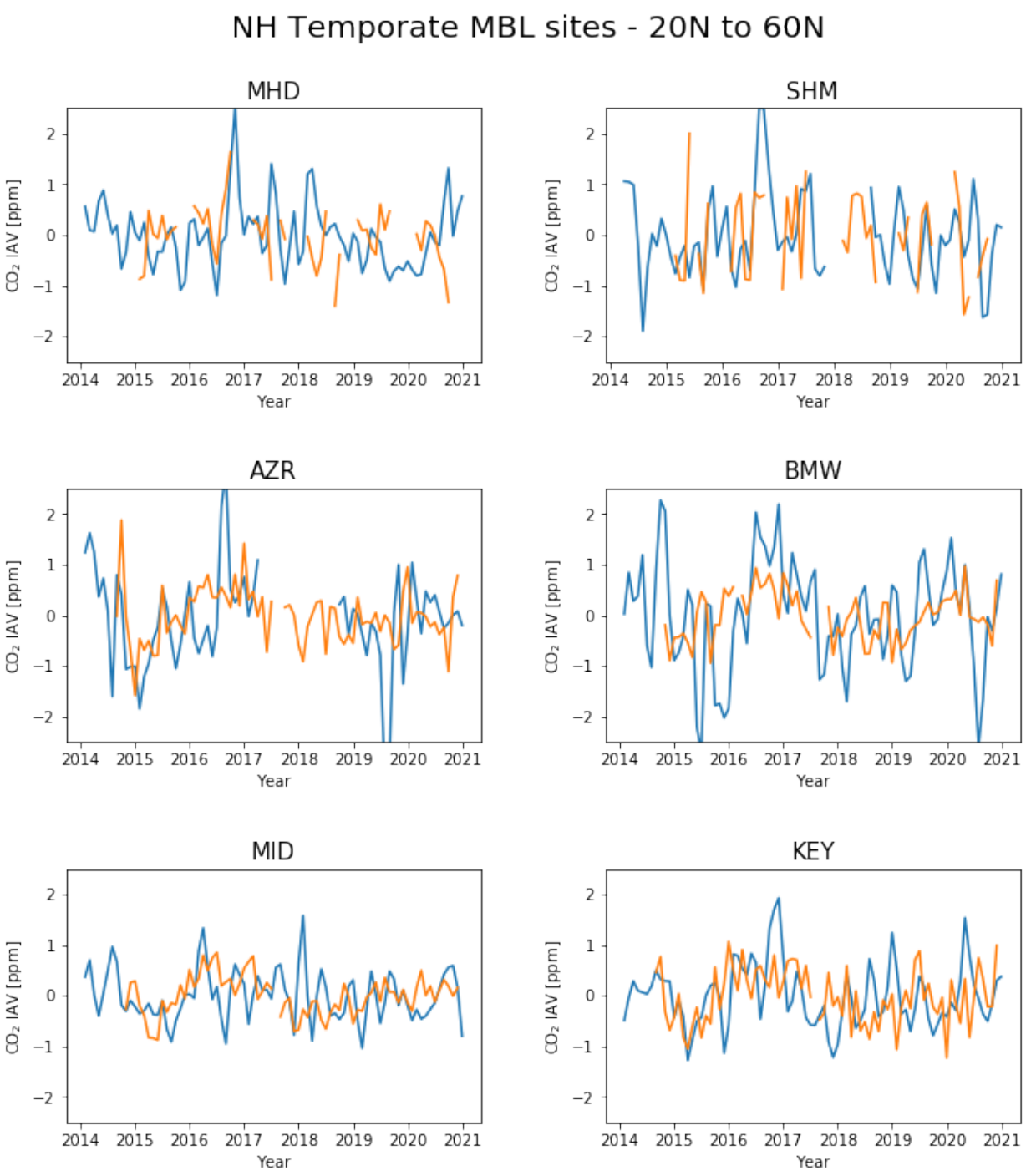
NH Temporate MBL sites - 20N to 60N
MHD
SHM
AZR
BMW
MID
KEY
CO2 IAV [ppm]
Year
2014
2015
2016
2017
2018
2019
2020
2021
2
1
0
−1
−2

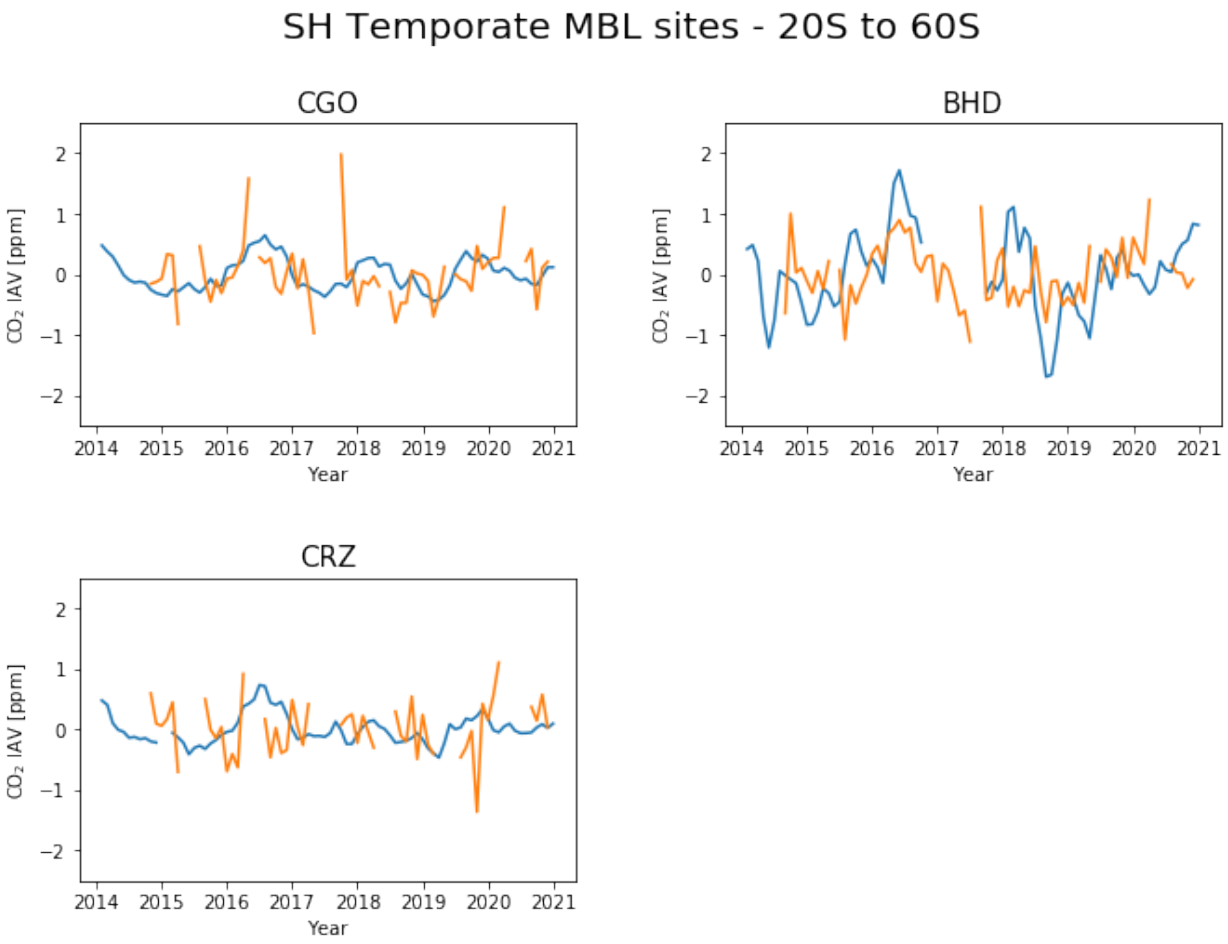

Figure A.11: *Timeseries comparison between surface CO_2 MBL IAV and the co-located OCO-2 XCO_2. Orange lines based on OCO-2 observations while blue lines based on MBL sites.*

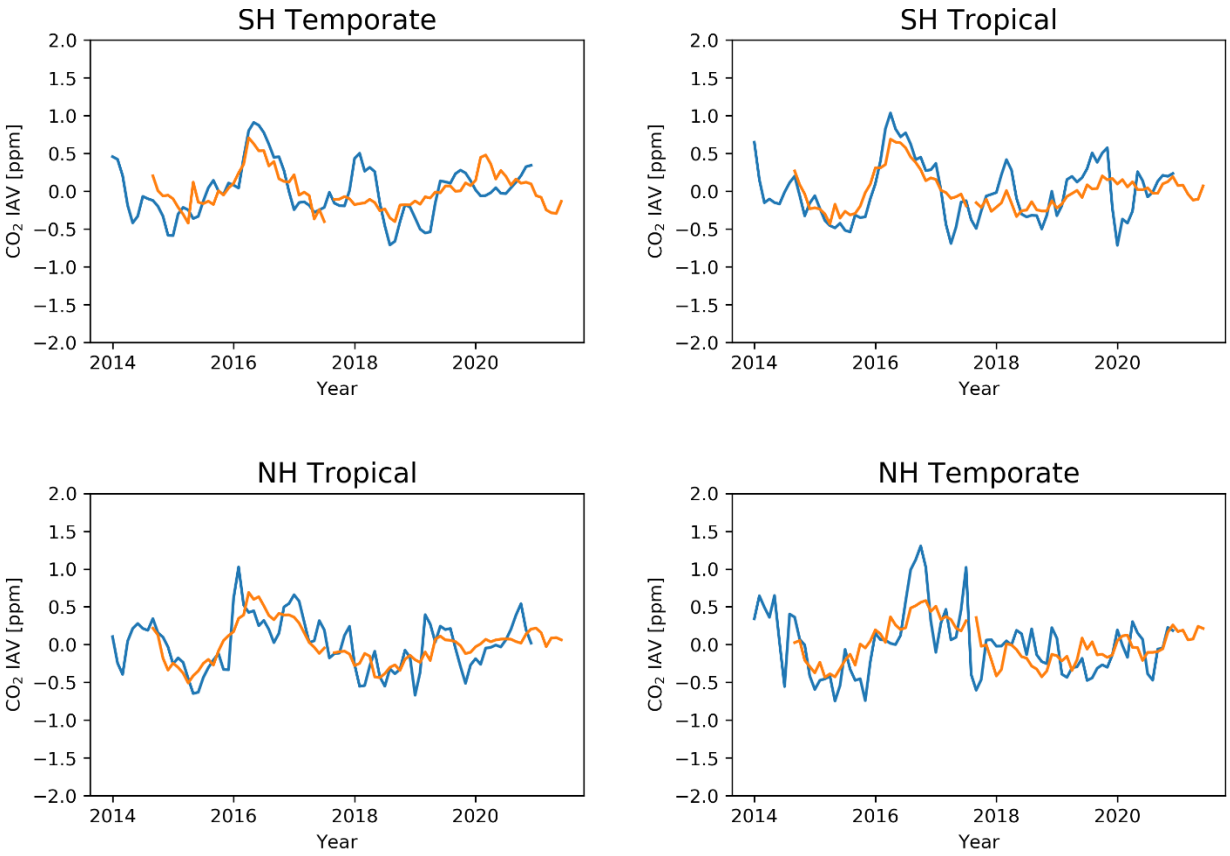

Figure A.12: *Timeseries comparison between the zonal mean OCO-2 XCO_2 and zonal mean MBL surface CO_2 IAV.*

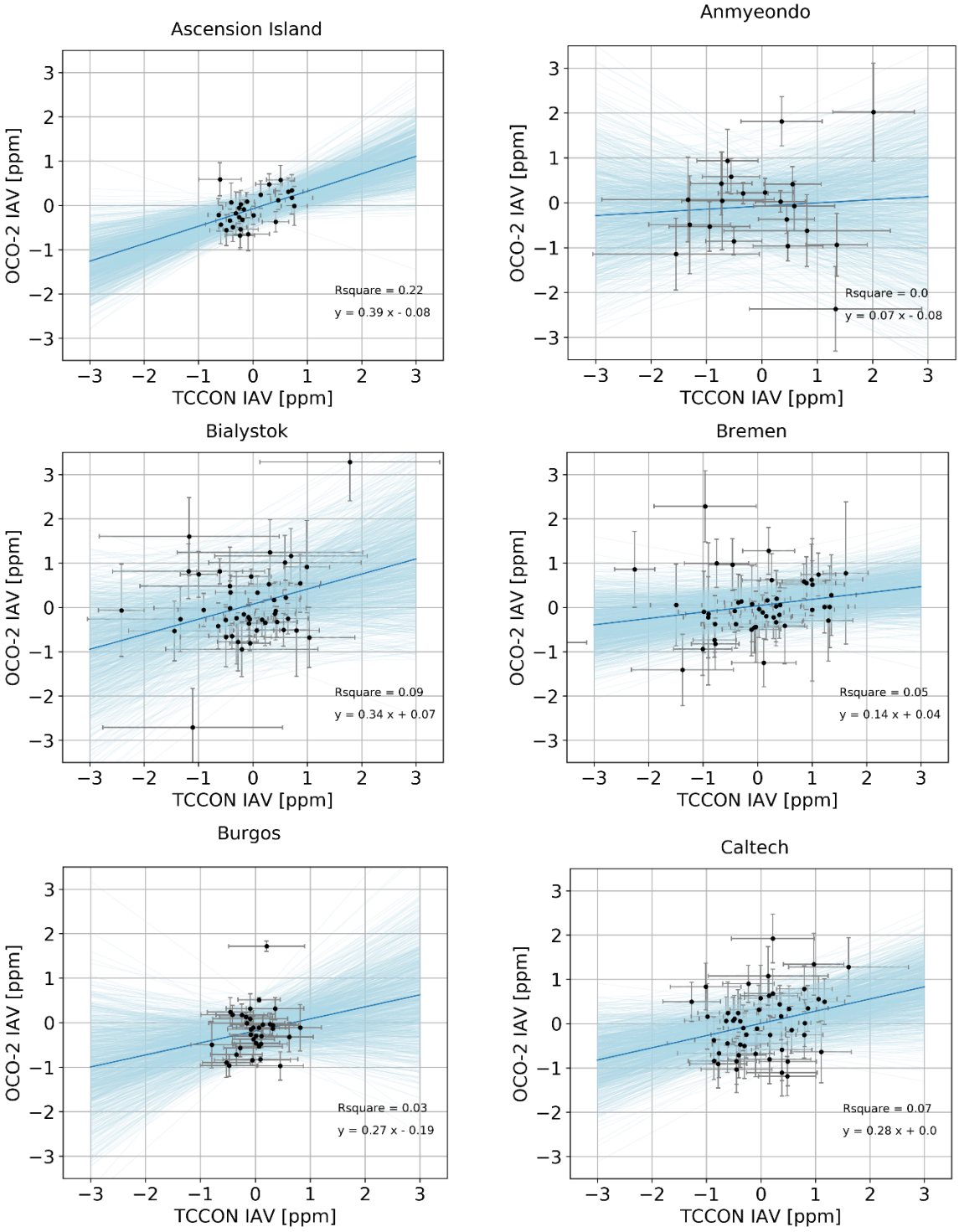
Ascension Island
Rsquare = 0.22
y = 0.39 x - 0.08
Anmyeondo
Rsquare = 0.0
y = 0.07 x - 0.08
Bialystok
Rsquare = 0.09
y = 0.34 x + 0.07
Bremen
Rsquare = 0.05
y = 0.14 x + 0.04
Burgos
Rsquare = 0.03
y = 0.27 x - 0.19
Caltech
Rsquare = 0.07
y = 0.28 x + 0.0
OCO-2 IAV [ppm]
TCCON IAV [ppm]

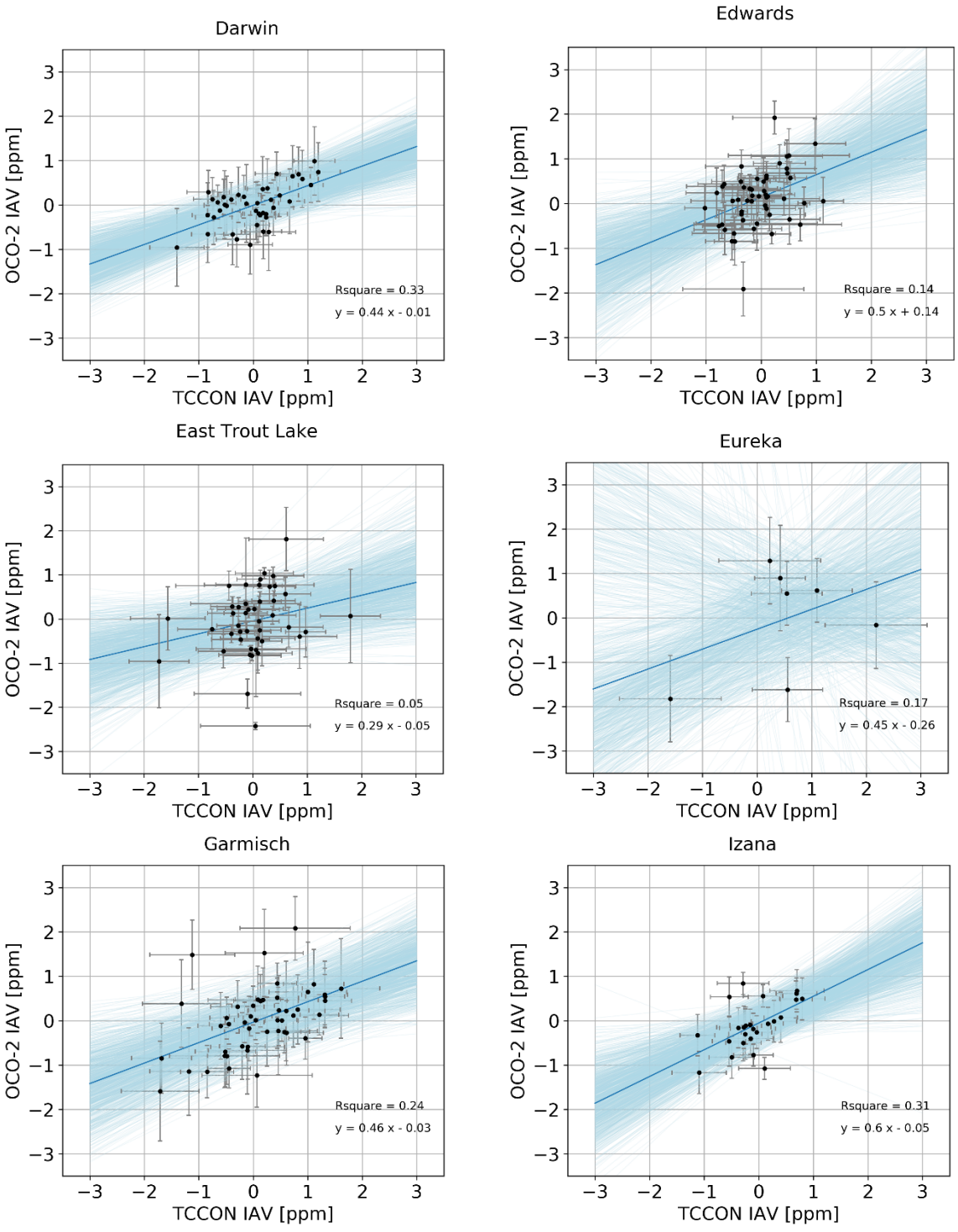
Darwin
Rsquare = 0.33
y = 0.44 x - 0.01
Edwards
Rsquare = 0.14
y = 0.5 x + 0.14
East Trout Lake
Rsquare = 0.05
y = 0.29 x - 0.05
Eureka
Rsquare = 0.17
y = 0.45 x - 0.26
Garmisch
Rsquare = 0.24
y = 0.46 x - 0.03
Izana
Rsquare = 0.31
y = 0.6 x - 0.05
OCO-2 IAV [ppm]
TCCON IAV [ppm]

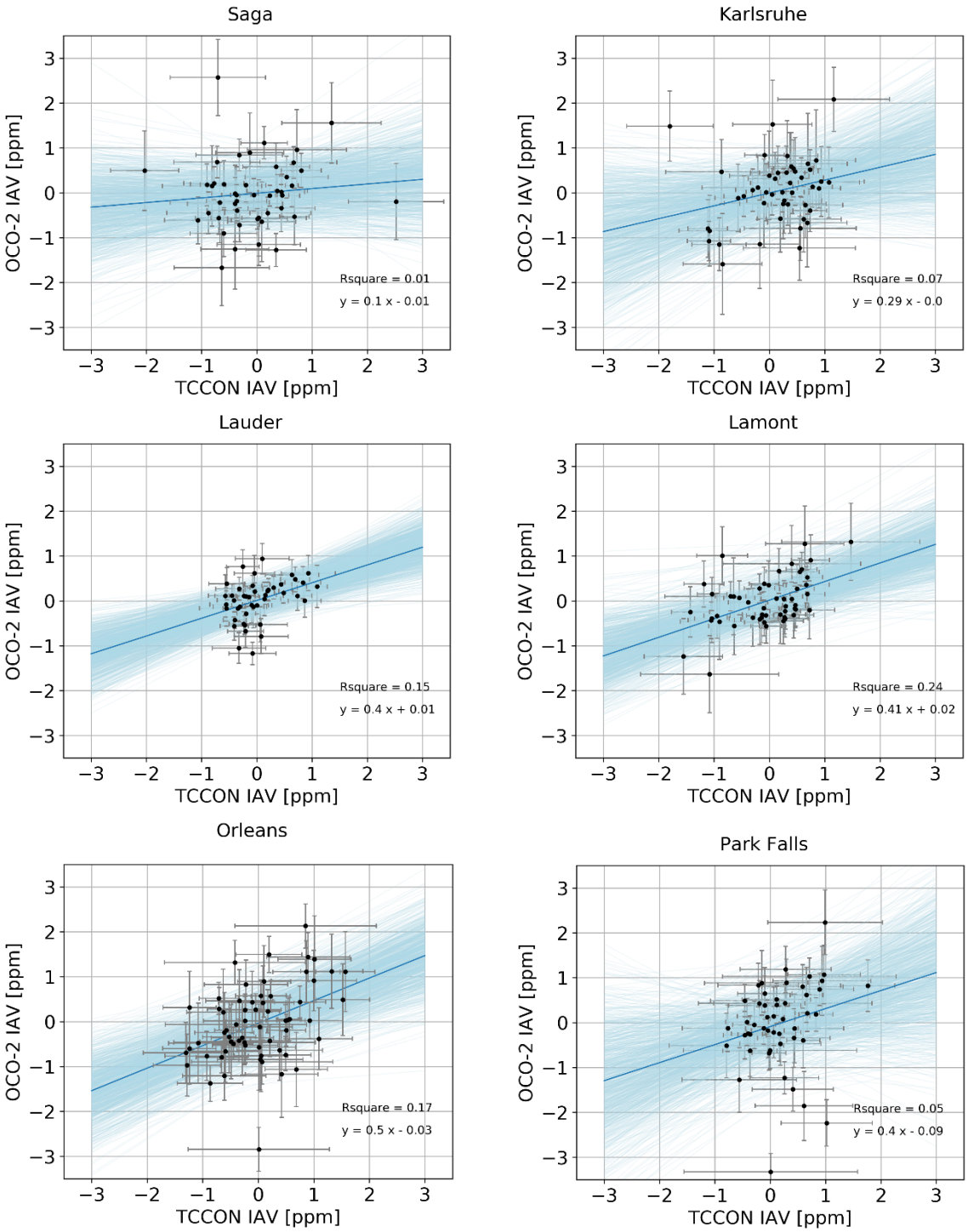
Saga
Rsquare = 0.01
y = 0.1 x - 0.01
Karlsruhe
Rsquare = 0.07
y = 0.29 x - 0.0
Lauder
Rsquare = 0.15
y = 0.4 x + 0.01
Lamont
Rsquare = 0.24
y = 0.41 x + 0.02
Orleans
Rsquare = 0.17
y = 0.5 x - 0.03
Park Falls
Rsquare = 0.05
y = 0.4 x - 0.09
OCO-2 IAV [ppm]
TCCON IAV [ppm]

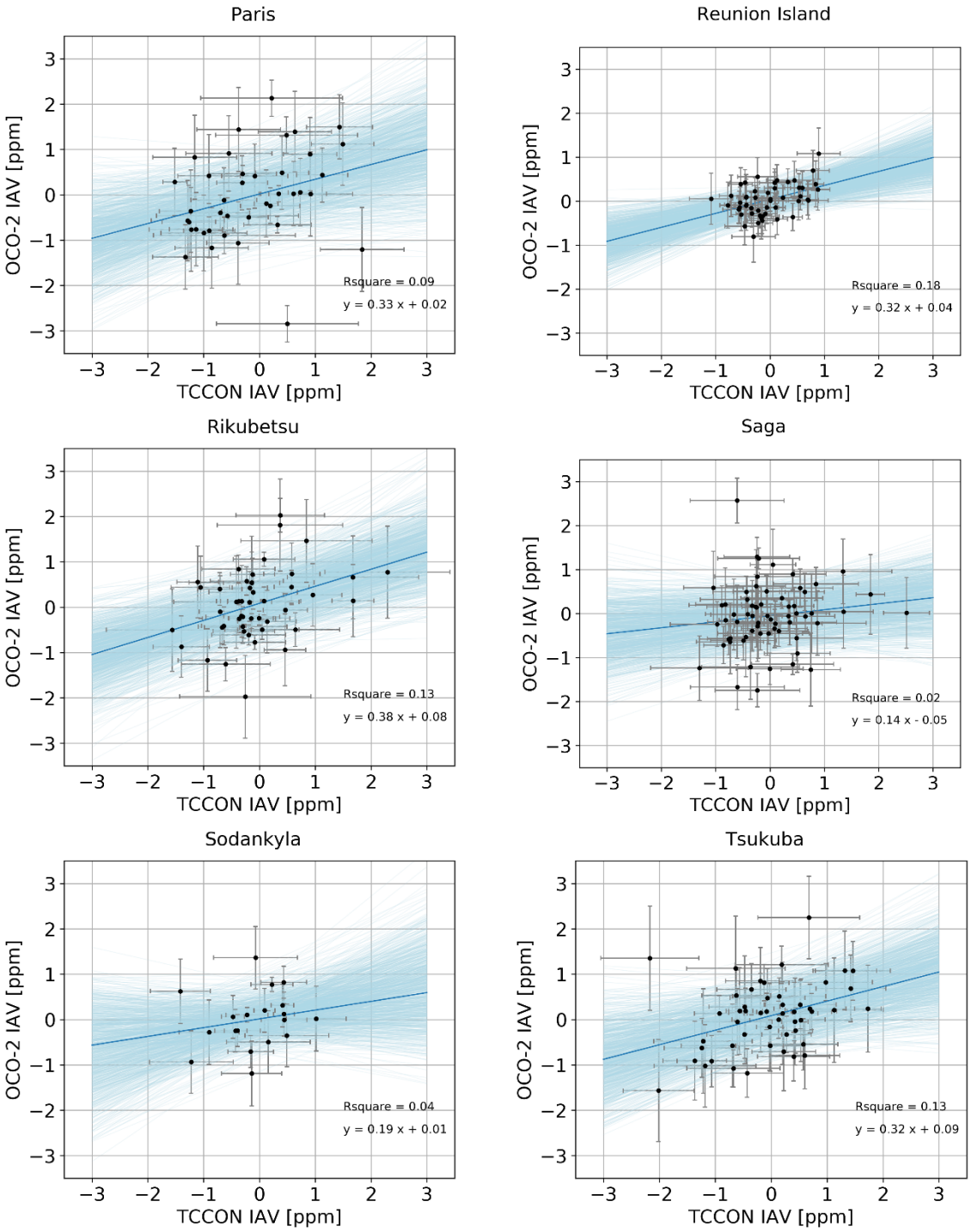
Paris
Rsquare = 0.09
y = 0.33 x + 0.02
Reunion Island
Rsquare = 0.18
y = 0.32 x + 0.04
Rikubetsu
Rsquare = 0.13
y = 0.38 x + 0.08
Saga
Rsquare = 0.02
y = 0.14 x - 0.05
Sodankyla
Rsquare = 0.04
y = 0.19 x + 0.01
Tsukuba
Rsquare = 0.13
y = 0.32 x + 0.09
OCO-2 IAV [ppm]
TCCON IAV [ppm]

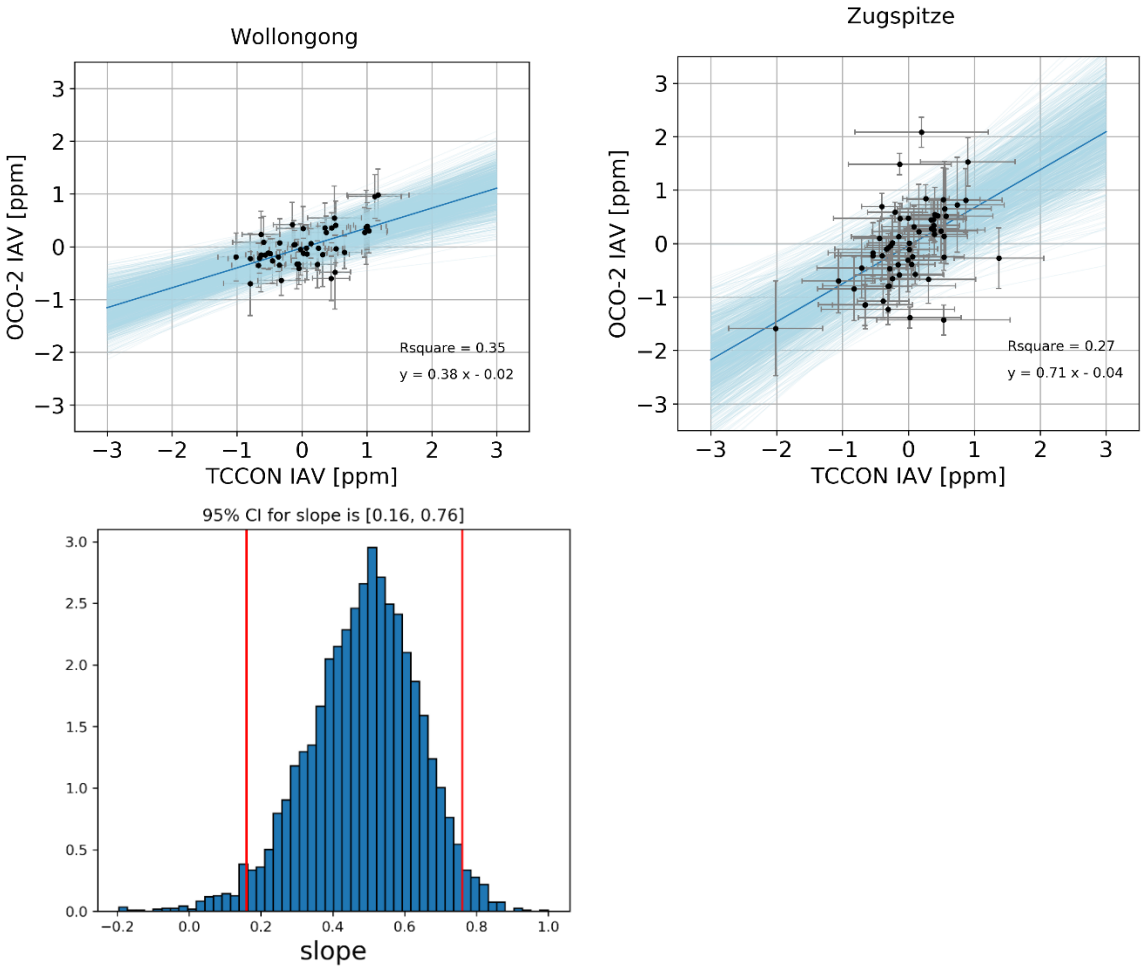

Figure A.13: *Bootsrapping Linear Regression fit between TCCON and OCO-2 monthly averaged XCO_2 IAV over 26 TCCON sites which have records between 2014.09 to 2018.12. Light-blue regression lines in each plot are based on 1000 times 'resampling' of the original OCO-2 vs. TCCON IAV data points. The Steelblue line in each plot is just a simple polynomial fit between y and x. The 95% significant level for regression slope is calculated based on the distribution of the possible 1000 slopes during the bootstrapping process. The last figure, which is the histogram of the 1000 slopes for Lauder, gives an example of how to obtain the range of k-slope.*

Appendix B: Supplemental to Chapter 3

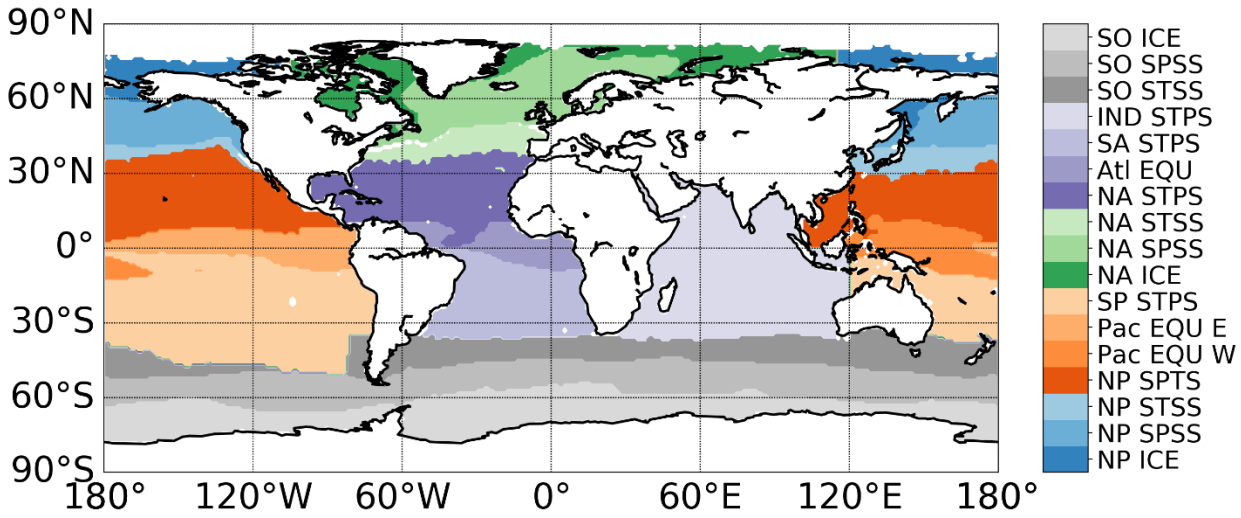

Figure B.1: *Mean biome map created from mean climatologies of maxMLD, SST, summer Chl a, and maximum ice fraction. The acronyms include ice biome (ICE), subpolar seasonally stratified biome (SPSS), subtropical seasonally stratified biome (STSS),subtropical permanently stratified biome (STPS), equatorial biome (EQU). The super-biome we defined and used in the tagged simulations are aggregated based on these open-ocean biomes.*

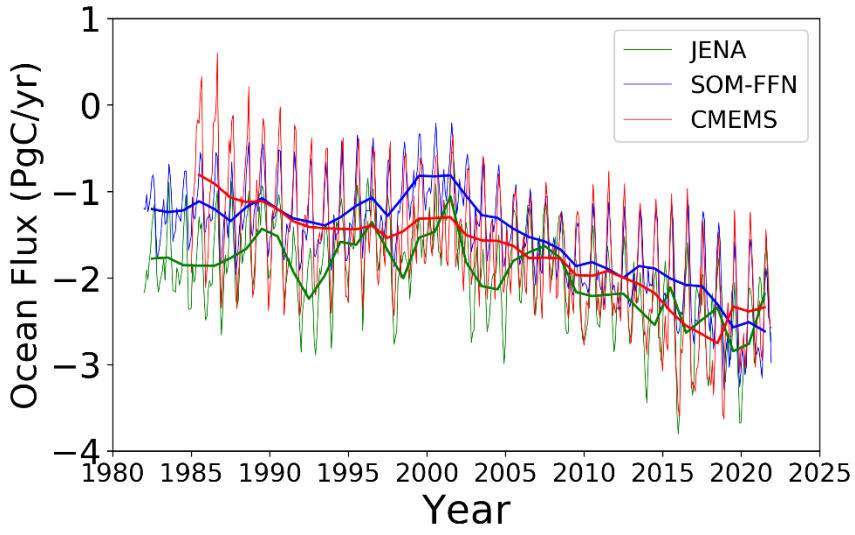

Figure B.2: *The global CO_2 fluxes between the ocean and atmosphere based on three different products.*

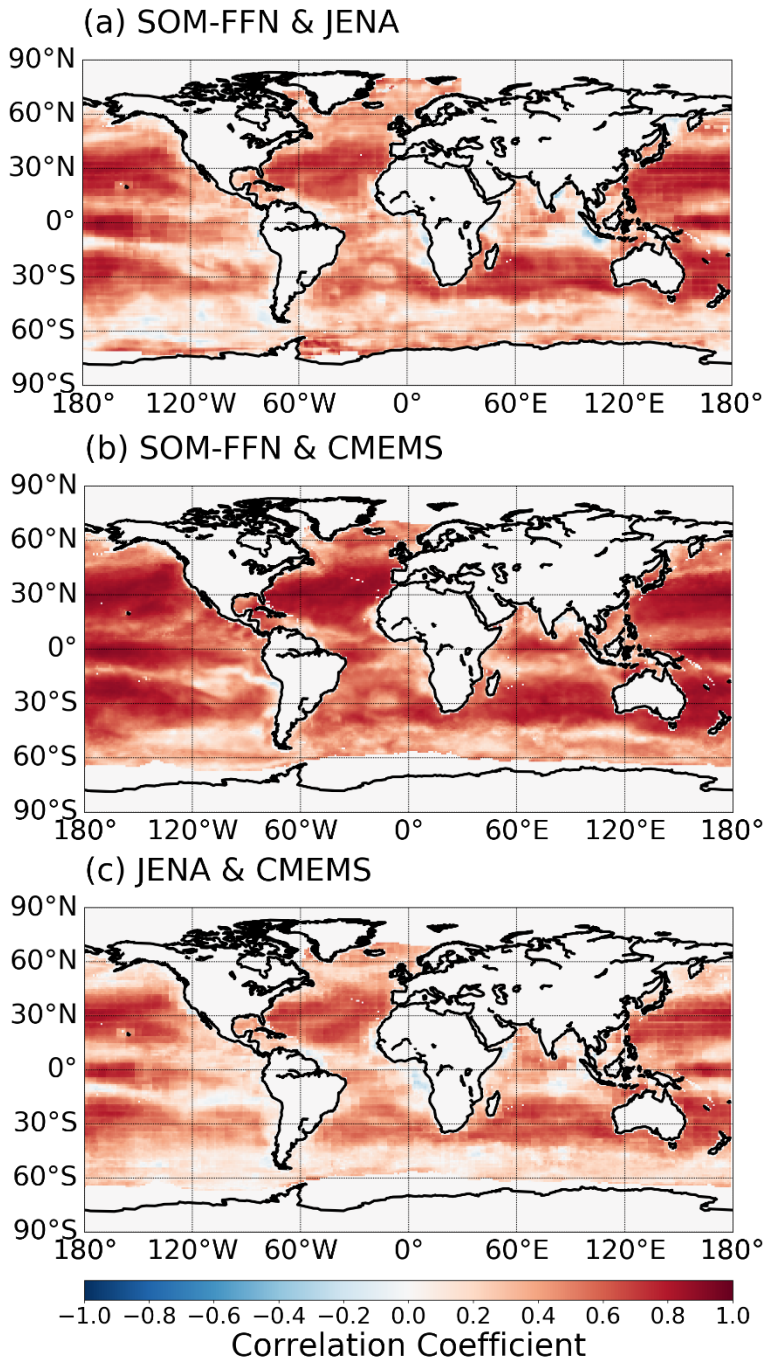

Figure B.3: *The correlation coefficient between the CO_2 fluxes based on different products. (a) between SOM-FFN and JENA, (b) between SOM-FFN and CMEMS, (c) between CMEMS and JENA*

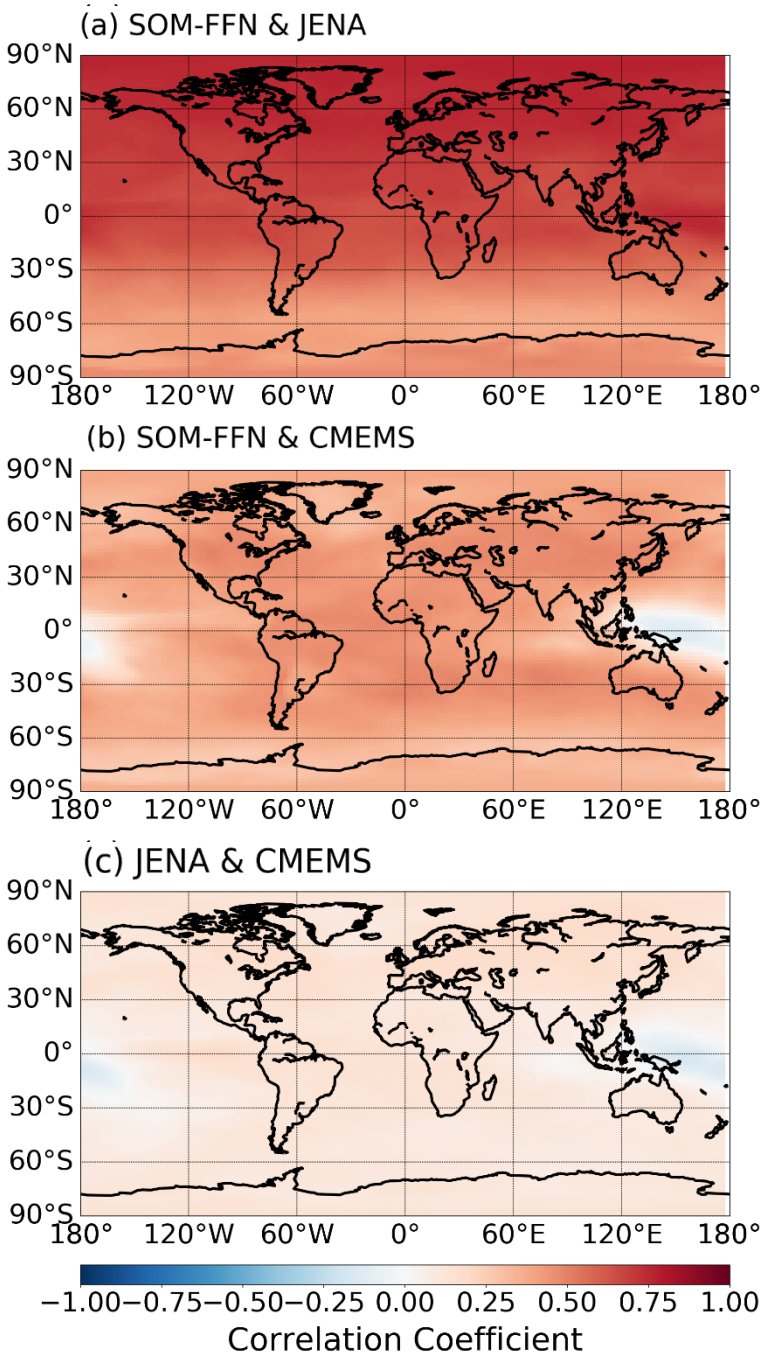

Figure B.4: *Correlation coefficient between the modeled XCO_2 IAV based on dynamic simulation using different products.(a) between SOM-FFN and JENA, (b) between SOM-FFN and CMEMS, (c) between CMEMS and JENA*

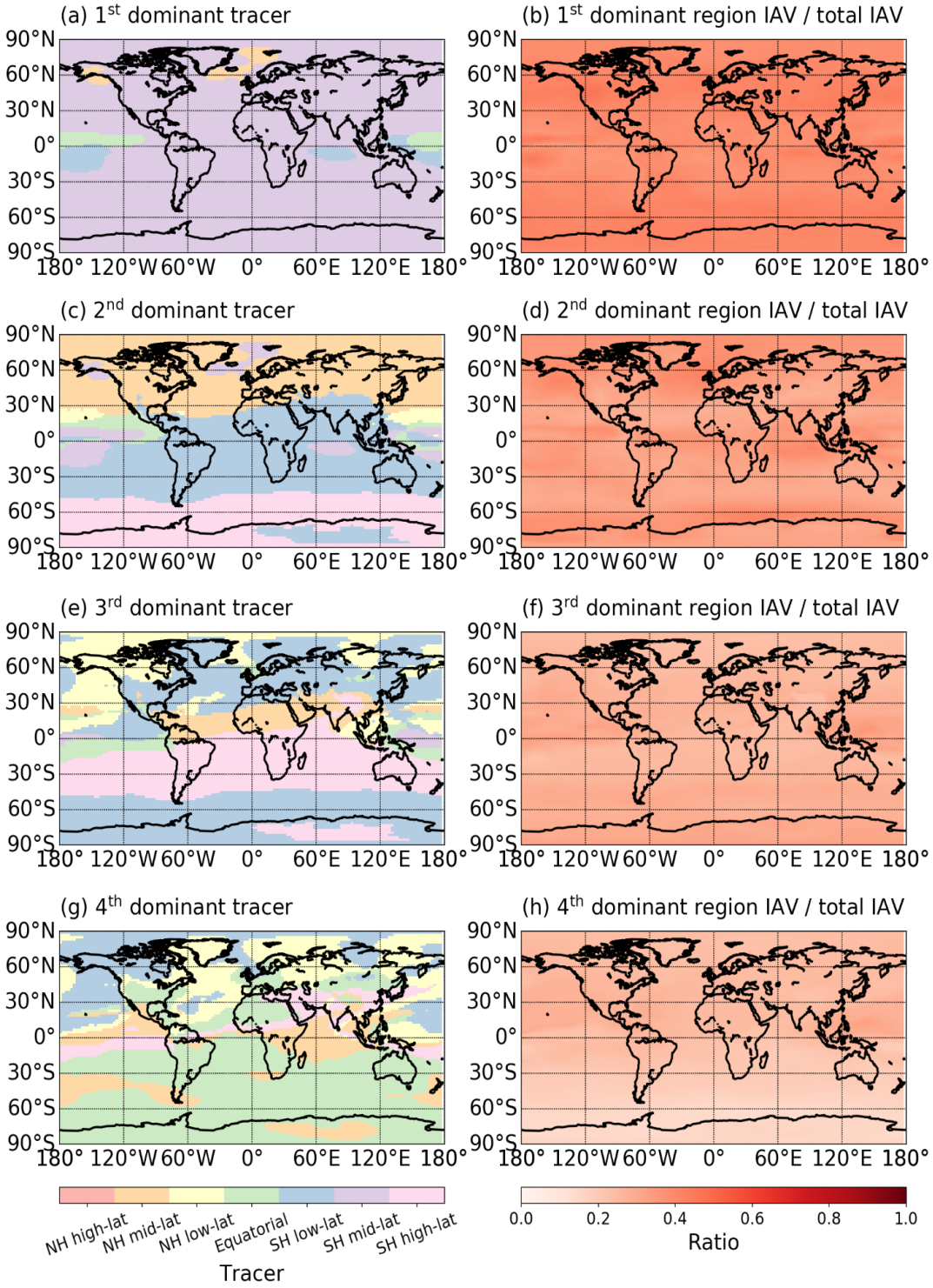

Figure B.5: *First four most important tracers contributing to XCO_2 IAV based on time-varying fluxes from SOMFFN and time-varying transport. The tracers in the left column are determined by calculating XCO_2 IAV amplitude for each gridcell caused by each single tracer and ranking them relative to other tracers. The 'right column shows the ratio of modelled XCO_2 IAV amplitude of the tracer to that of the whole ocean. (a)(b) for first most important tracer,(c)(d) for second most important,(e)(f) for third most important tracer,(g)(h) for fourth most important tracer.*

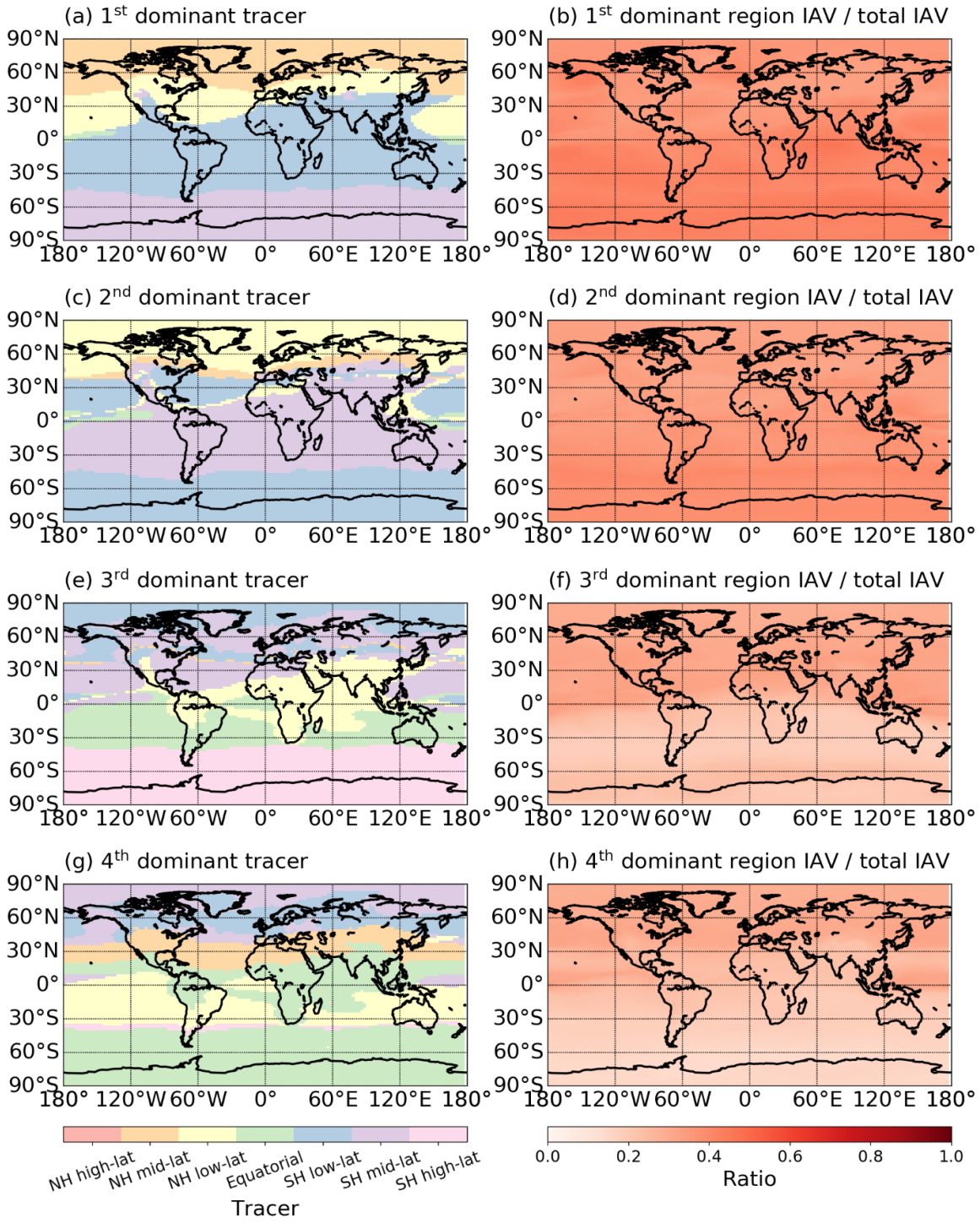

Figure B.6: *First four most important tracers contributing to XCO_2 IAV based on time-varying fluxes from Jena and time-varying transport. The tracers in the left column are determined by calculating XCO_2 IAV amplitude for each gridcell caused by each single tracer and ranking them relative to other tracers. The 'right column shows the ratio of modelled XCO_2 IAV amplitude of the tracer to that of the whole ocean. (a)(b) for first most important tracer,(c)(d) for second most important,(e)(f) for third most important tracer,(g)(h) for fourth most important tracer.tracer,(k)(l) for sixth most important tracer,(m)(n) for seventh most important tracer.*

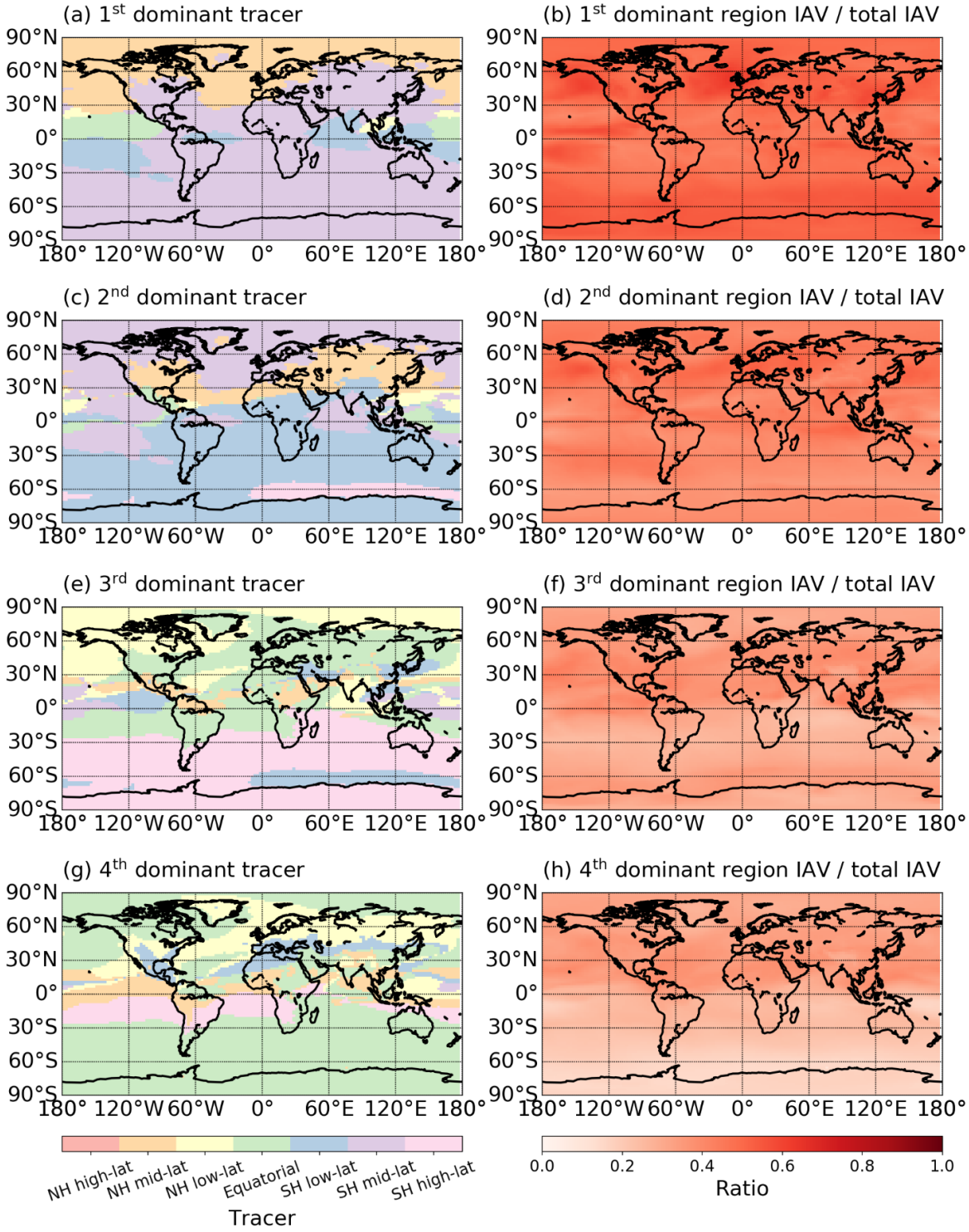

Figure B.7: *First four most important tracers contributing to XCO_2 IAV based on time-varying fluxes from CMEMS and time-varying transport. The tracers in the left column are determined by calculating XCO_2 IAV amplitude for each gridcell caused by each single tracer and ranking them relative to other tracers. The 'right column shows the ratio of modelled XCO_2 IAV amplitude of the tracer to that of the whole ocean. (a)(b) for first most important tracer,(c)(d) for second most important,(e)(f) for third most important tracer,(g)(h) for fourth most important tracer.*

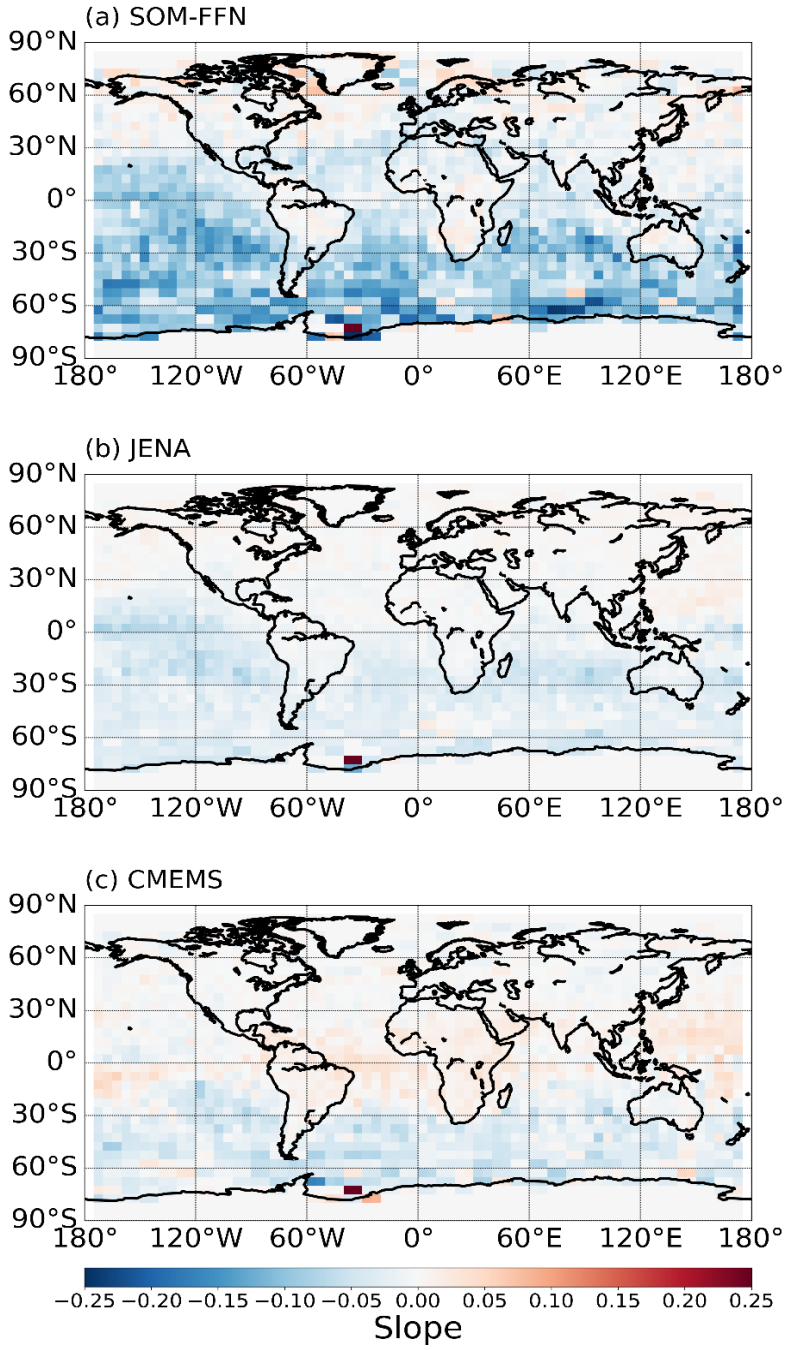

Figure B.8: *The slope of regression between simulated oceanic XCO_2 IAV and OCO-2 detected XCO_2 IAV, (a) for SOMFFN, (b) for JENA, (c) for CMEMS*

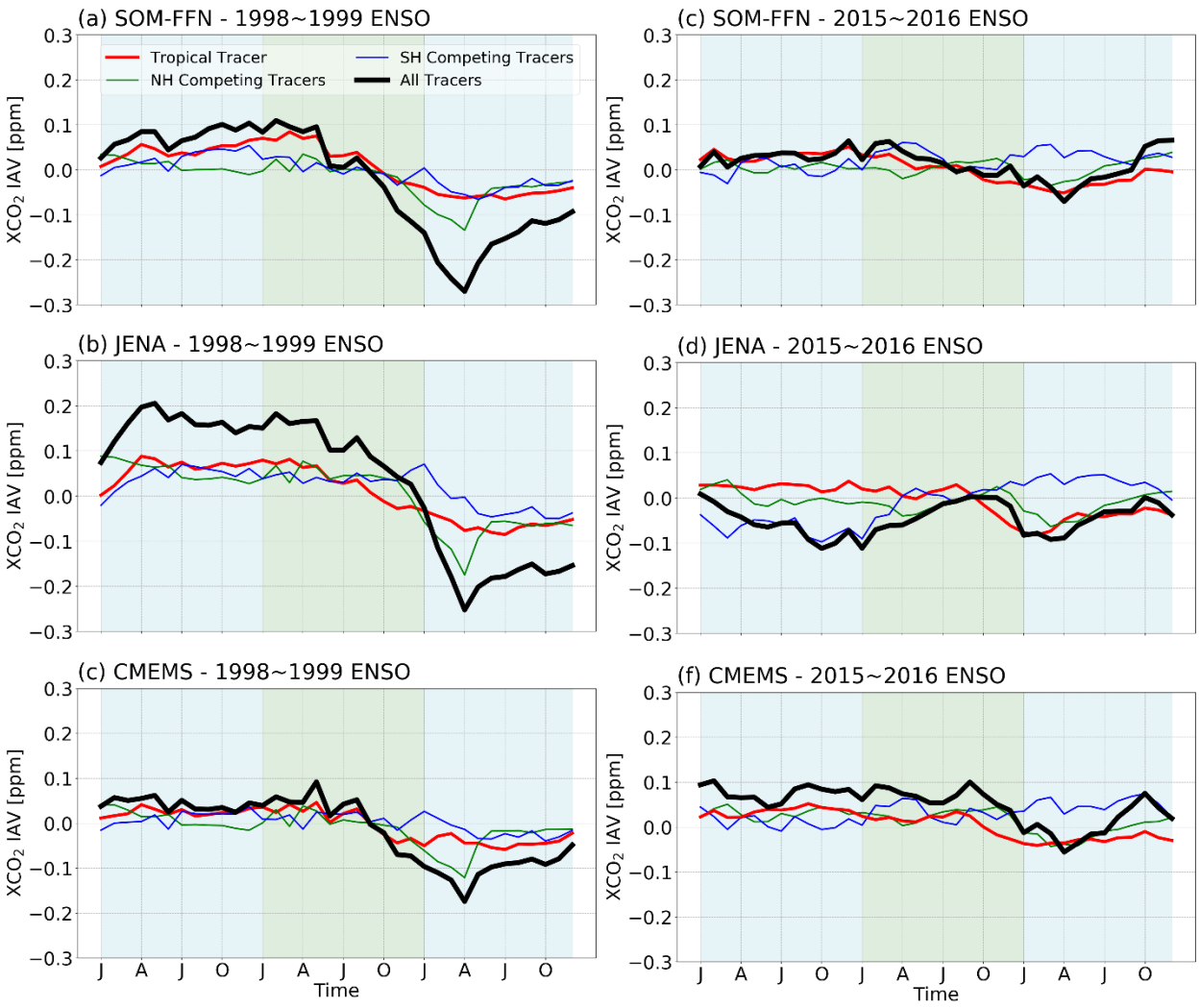

Figure B.9: *The IAV timeseries averaged over the Nino 3.4 region of the key contributing tracers (NH mid-lat, NH low-lat, SH mid-lat, SH low-lat) in driving the XCO_2 IAV during 2 strong ENSO events: 1997-1998 and 2015-2016 - Year1 and Year3 are shaded with blue, Year2 is shaded with green. Tropical Tracer is in red, NH Key Competing Tracers is in green, SH Key Competing Tracers is in Blue, and Sum of All Tracers in black. Left Column is for the 1997-1998 ENSO, Right Column is for the 2015-2016 ENSO. (a)(d)for SOMFFN, (b)(e) for JENA, (c)(f) for CMEMS.*

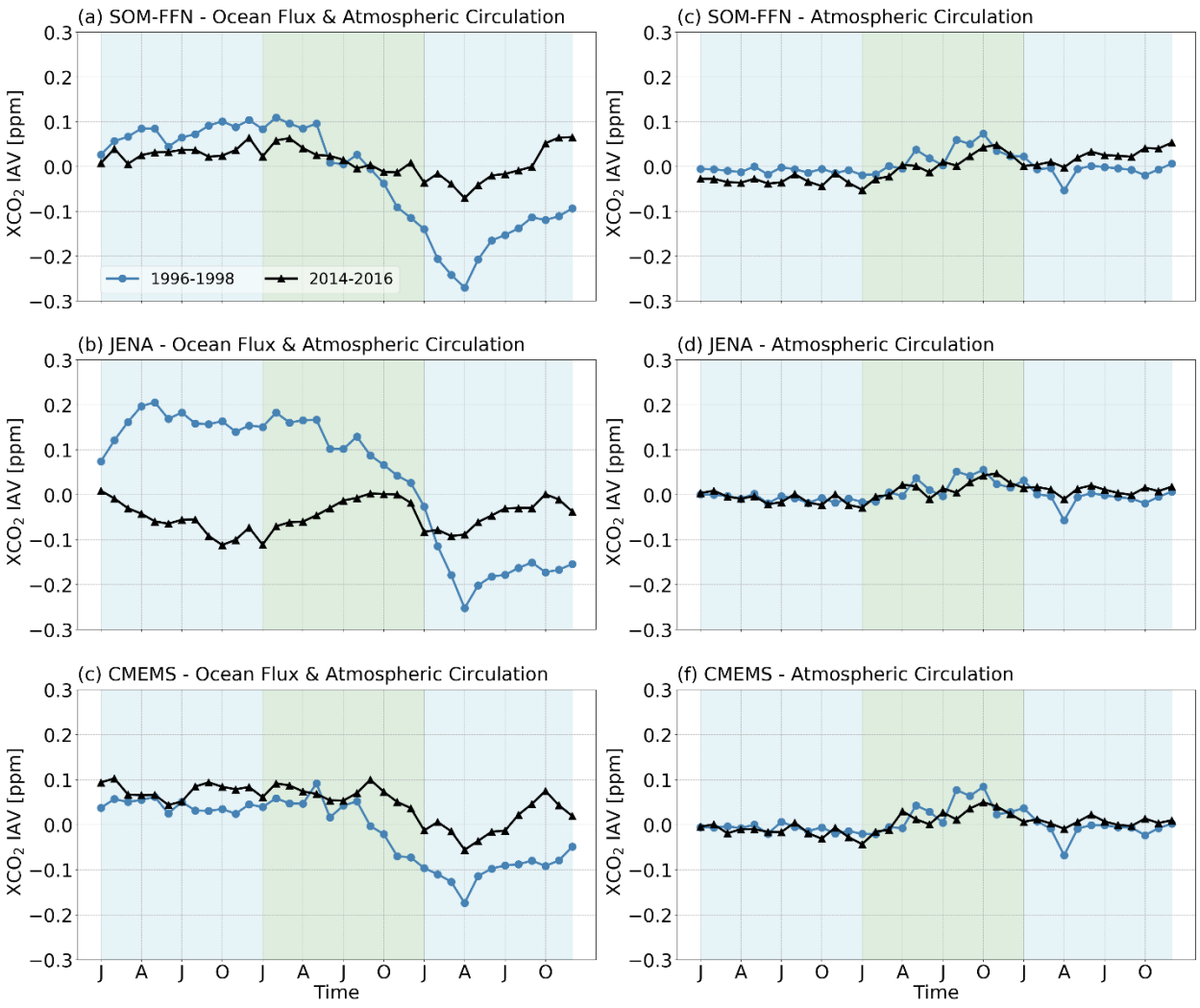

Figure B.10: *The XCO_2 IAV timeseries averaged over the Nino 3.4 region of the key during 2 strong ENSO events: 1997-1998 and 2015-2016 - Year1 and Year3 are shaded with blue, Year2 is shaded with green. The left column is based on the simulation with varying fluxes. The right column is based on the simulation with cyclostationary fluxes. (a)(d)for SOM-FFN, (b)(e) for JENA, (c)(f) for CMEMS.*

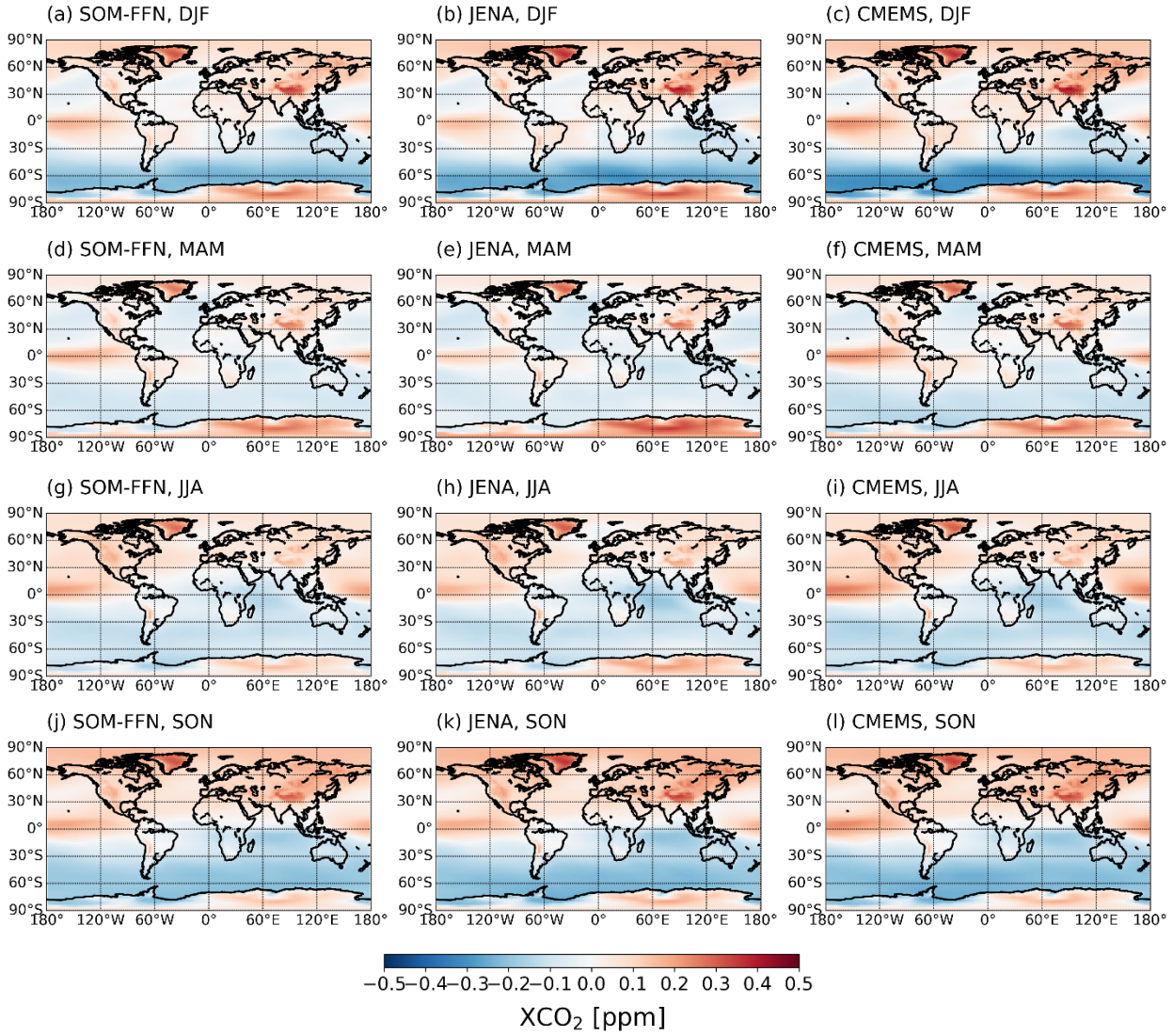

Figure B.11: *Climatological XCO_2 gradients simulated for each observation-based flux product across four seasons. The gradient is calculated by subtracting the global mean seasonal XCO_2 from the simulated XCO_2 at every gridcell averaged over three months. The left column shows results for SOM-FFN, the middle column shows results for JENA, and the right column shows results for CMEMS. The first row shows results for winter (DJF), second row for spring (MAM), third row for summer (JJA) and fourth row for autumn (SON).*